

**Boundary-layer instability on rotating cones  
An experiment-based exploration**

Tambe, S.S.

**DOI**

[10.4233/uuid:40ed5b16-bf5a-409e-a28e-74f115f984cf](https://doi.org/10.4233/uuid:40ed5b16-bf5a-409e-a28e-74f115f984cf)

**Publication date**

2022

**Document Version**

Final published version

**Citation (APA)**

Tambe, S. S. (2022). *Boundary-layer instability on rotating cones: An experiment-based exploration*. [Dissertation (TU Delft), Delft University of Technology]. <https://doi.org/10.4233/uuid:40ed5b16-bf5a-409e-a28e-74f115f984cf>

**Important note**

To cite this publication, please use the final published version (if applicable).  
Please check the document version above.

**Copyright**

Other than for strictly personal use, it is not permitted to download, forward or distribute the text or part of it, without the consent of the author(s) and/or copyright holder(s), unless the work is under an open content license such as Creative Commons.

**Takedown policy**

Please contact us and provide details if you believe this document breaches copyrights.  
We will remove access to the work immediately and investigate your claim.

# Propositions

accompanying the dissertation

## **BOUNDARY-LAYER INSTABILITY ON ROTATING CONES**

AN EXPERIMENT-BASED EXPLORATION

by

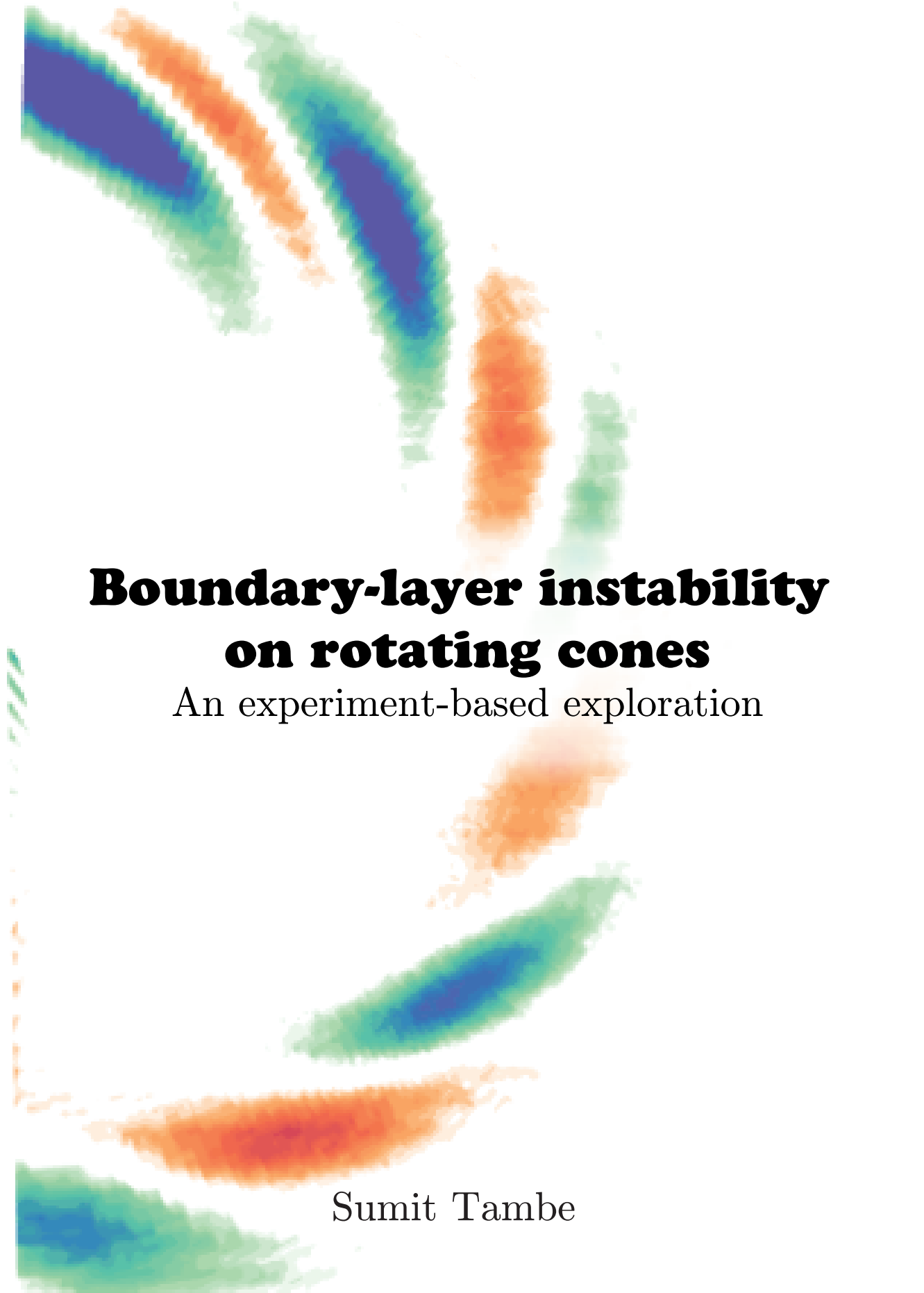
**Sumit Sunil TAMBE**

1. Instability of the boundary-layers on rotating cones can never be observed. Theory predicts the onset of instability, but experiments detect the instability-induced flow features only when they have grown beyond the measurement sensitivity (Chapters 4 and 5).
2. Disturbing the azimuthal coherence will always delay the spiral vortex growth on rotating cones (Chapter 4).
3. In a turbo-fan engine at a transonic cruise, right circular type nose-cones will exhibit instability-induced spiral vortices in the transitional part of boundary-layer (chapter 6).
4. The transitional behaviour of the rotating boundary-layers at hub end-walls will significantly affect the performance of turbo-machinery components (Chapter 8).
5. "Why does a cable entangle?" is a low dimensional version of Heisenberg's question "Why turbulence?<sup>1</sup>".
6. Rapid progress of science benefits from the removal of language-based communications.
7. Judging the value of scientific research is non-scientific itself, until we know it all.
8. Words must be taxed.
9. Life is like mathematics, it's not always real, especially not, during a PhD study.
10. To improve their draft article, one must forget it. Craft breweries catalyse the forgetting, therefore, serve in the interest of science.

These propositions are regarded as opposable and defensible, and have been approved as such by the promotor prof. dr. ir. L. L. M. Veldhuis.

---

<sup>1</sup>"When I meet God, I am going to ask him two questions: Why relativity? And why turbulence? I really believe he will have an answer for the first." — Werner Heisenberg. Similar quote is also attributed to Horace Lamb.



# **Boundary-layer instability on rotating cones**

An experiment-based exploration

Sumit Tambe

# **BOUNDARY-LAYER INSTABILITY ON ROTATING CONES**

AN EXPERIMENT-BASED EXPLORATION

## **Dissertation**

for the purpose of obtaining the degree of doctor  
at Delft University of Technology,  
by the authority of the Rector Magnificus, Prof.dr.ir. Tim van der Hagen,  
chair of the Board of Doctorates,  
to be defended publicly on  
Monday 10 January 2022 at 15:00 o'clock

by

**Sumit Sunil TAMBE**

Master of Science in Aerospace Engineering, Delft University of Technology, The Netherlands  
born in Bhusawal, India

This dissertation is approved by the promotor.

Composition of the doctoral committee:

Rector Magnificus,	chairperson
Prof. dr. ir. L. L. M. Veldhuis	Technische Universiteit Delft, promotor
Dr. A. Gangoli Rao	Technische Universiteit Delft, promotor

Independent members:

Prof. dr. E. M. Greitzer	Massachusetts Institute of Technology, USA
Prof. dr. S. Garrett	University of Leicester, UK
Prof. dr. C. O. Paschereit	Technische Universiteit Berlijn, Germany
Prof. dr. ir. R. A. W. M. Henkes	Technische Universiteit Delft
Prof. dr. F. Scarano	Technische Universiteit Delft, reserve member

Other member:

Dr. ir. F. F. J. Schrijer	Technische Universiteit Delft
---------------------------	-------------------------------



This work was funded by the European Union Horizon 2020 programme: Clean Sky 2-Large Passenger Aircraft (CS2-LPA-GAM-2018-2019-01), and CENTRELINE (grant agreement no. 723242).

*Keywords:* Rotating-boundary-layers, instability, transition, rotating cones, aero-engine-nose-cones

*Printed by:* Proefschriftmaken

*Cover by:* Sumit Tambe. The color patterns are measured thermal-footprints of spiral vortices on a rotating cone in high Reynolds number inflow at Mach  $M = 0.5$ , pertaining to aero-engine-intakes at cruise. The instance is reconstructed from proper orthogonal decomposition modes. The grayscale pattern on the back is sketched to represent typical spiral vortex growth along a rotating broad cone.

Copyright © 2021 S. S. Tambe

ISBN 978-94-6384-289-1

An electronic version of this dissertation is available at <http://repository.tudelft.nl/>.

*Dedicated to my parents Manisha and Sunil.*



# CONTENTS

<b>Summary</b>	<b>ix</b>
<b>Samenvatting</b>	<b>xi</b>
<b>1 Introduction</b>	<b>1</b>
1.1 Motivation . . . . .	1
1.2 Knowledge gap . . . . .	6
1.3 Research aim and methodology . . . . .	8
1.4 Dissertation outline . . . . .	10
<b>2 Background</b>	<b>13</b>
2.1 Introduction . . . . .	13
2.2 Instability . . . . .	13
2.2.1 Centrifugal instability . . . . .	14
2.2.2 Cross-flow instability . . . . .	15
2.2.3 Absolute vs convective instability . . . . .	17
2.3 Boundary-layer instability on rotating bodies . . . . .	17
2.3.1 Rotating disk . . . . .	17
2.3.2 Rotating cones in still fluid . . . . .	20
2.3.3 Rotating cones in axial inflow . . . . .	22
2.3.4 Effect of free-stream turbulence . . . . .	28
2.3.5 Effect of surface roughness . . . . .	28
2.4 Experimental and data processing techniques . . . . .	29
2.4.1 Infrared thermography . . . . .	29
2.4.2 Particle image velocimetry . . . . .	34
2.4.3 Proper orthogonal decomposition . . . . .	35
<b>3 An experimental method to investigate coherent spiral vortices on rotating bodies</b>	<b>39</b>
3.1 Introduction . . . . .	39
3.2 Experimental setup . . . . .	40
3.3 Spatial characteristics of the spiral vortices . . . . .	42
3.4 Data processing procedure . . . . .	43
3.4.1 Spatial characteristics of the POD modes . . . . .	44
3.4.2 Noise reduction . . . . .	46
3.4.3 Physical admissibility of POD modes . . . . .	48
3.5 Comparison to PIV and literature . . . . .	52
3.6 Conclusion . . . . .	54

<b>4</b>	<b>Non-axial inflow</b>	<b>57</b>
4.1	Introduction	57
4.2	Definitions of geometry and flow parameters	58
4.3	Experimental setup	59
4.4	Results and discussion	62
4.4.1	Axial inflow	62
4.4.2	Non-axial inflow	69
4.4.3	Physical interpretation	77
4.5	Conclusion	84
<b>5</b>	<b>The effect of half-cone angle</b>	<b>85</b>
5.1	Introduction	85
5.2	Flow parameters	86
5.3	Experiments	86
5.4	Visualisation of spiral vortex footprints	88
5.5	Spiral vortex growth	92
5.6	Spatial characteristics of the spiral vortices	97
5.7	Conclusion	100
<b>6</b>	<b>Spiral instability modes at transonic flight conditions</b>	<b>103</b>
6.1	Introduction	103
6.2	Description of experiments	104
6.3	Flow field overview	107
6.4	Visualisations of instability modes	109
6.5	Growth of spiral vortices	111
6.6	Spiral vortex angle	114
6.7	Conclusion	116
<b>7</b>	<b>Nose-cone aerodynamics of a low-speed fan under uniform and distorted inflow</b>	<b>119</b>
7.1	Introduction	119
7.2	Experimental setup	121
7.3	Results	124
7.3.1	Uniform inflow	124
7.3.2	Non-uniform inflow	124
7.4	Conclusion	139
<b>8</b>	<b>Relevance of the nose-cone boundary-layer instability to aero-engines</b>	<b>141</b>
8.1	Introduction	141
8.2	Potential effect of nose-cone boundary-layer instability on fan aerodynamics	142
8.2.1	Potential interactions between the spiral vortices and cross-flow in the blade passage	143
8.2.2	Potential interaction of the spiral vortices and the horse-shoe vortex	146
8.3	Expected occurrence of the spiral vortices during a transonic flight	147
8.4	Conclusion	150
<b>9</b>	<b>Conclusions and recommendations</b>	<b>153</b>
9.1	New findings	154
9.2	Limitations	155
9.3	Recommendations	157

---

<b>A</b>	<b>Effect of integration time on the spiral vortex detection using infrared thermography</b>	<b>159</b>
<b>B</b>	<b>Spiral vortex growth from the perspective of a propeller aircraft</b>	<b>161</b>
<b>C</b>	<b>Fan performance under distorted inflow of varying distortion strength</b>	<b>165</b>
	C.1 Fan performance . . . . .	.165
	C.2 Flow unsteadiness . . . . .	.166
<b>D</b>	<b>Effect of nose-cone shape on the distortion transfer through the fan</b>	<b>171</b>
	<b>Acknowledgements</b>	<b>185</b>
	<b>Curriculum Vitæ</b>	<b>187</b>
	<b>List of Publications</b>	<b>189</b>



# SUMMARY

Boundary-layer instability induces spiral vortices on rotating cones. As they grow along the cone, the vortices enhance mixing of high- and low-momentum fluid, and subsequently, cause the boundary-layer to transition into a turbulent state. This transition process is scientifically enticing as it is one of the classical problems in fluid mechanics. In practice, the transitions of rotating cone boundary-layer are relevant in several engineering applications, including rotating nose-cones of aero-engines.

The instability-induced spiral vortices on rotating aero-engine-nose-cones are expected to influence the aerodynamics at the fan root. This will potentially affect the loss mechanism at junctions between fan blades and the hub (the central rotating body of the engine, including the nose-cone). Accurate assessment of these losses requires knowing the boundary-layer instability behaviour on rotating cones in aero-engine-like flow conditions.

The past literature on this classical instability problem has only focused on low-speed (low-Reynolds number incompressible) axisymmetric inflow conditions. In reality, aero-engine-nose-cones often experience high-speed (high-Reynolds number compressible) inflow during a cruise. Moreover, several concepts of future-aircraft feature engines embedded in the airframe, or engines with ultra high bypass ratio with short nacelles. Owing to the associated inflow distortions, the nose-cones of these engines will experience non-axisymmetric inflow. However, limitations of the past experimental techniques pose hurdles in investigating the boundary-layer instability on rotating cones in non-axisymmetric as well as high-speed inflows.

This dissertation explores the boundary-layer instability on rotating cones with the inflow conditions pertaining to a typical aero-engine, i.e. non-axisymmetric as well as high-speed inflow. First, an experimental method is developed to measure the coherent flow structures on rotating cones. This method uses infrared thermography (IRT) with proper orthogonal decomposition (POD) to detect the thermal footprints of the spiral vortices on rotating cones. The POD modes are selectively used to reconstruct different instability-induced flow features. For this selection, a new criterion is formulated to determine the physical admissibility of the POD modes for reconstructing the flow-feature of interest. This method overcomes the limitations of the past experimental methods and has allowed quantitative measurements of spiral vortex growth, angle and azimuthal number, for the first time in complex flow environment, i.e. axial as well as non-axial inflow and high-speed inflow.

The asymmetry of the non-axial inflow has been found to delay the spiral vortex growth on the investigated case of a rotating slender cone (half-cone angle  $\psi = 15^\circ$ ). Here, the spiral vortex growth appears at higher local Reynolds number  $Re_l$  and local rotational speed ratio  $S$  compared to the axial inflow case at same operating conditions. It is postulated that the azimuthal asymmetry of the flow conditions (local  $Re_l$  and  $S$ ) disturbs the azimuthal coherence of the instability characteristics, i.e. angle and wavelength of the dominant mode. This inhibits the spiral vortex growth. However, at high rotational speed ratio  $S$ , when the instability characteristics approach the azimuthal coherence, the spiral vortices are found to be growing in the asymmetric flow field.

Furthermore, the dissertation extends the axial flow investigations from the most addressed case of a rotating slender cone of  $\psi = 15^\circ$  to the broader cones of  $\psi = 22.5^\circ$ ,  $30^\circ$ ,  $45^\circ$ , and  $50^\circ$ . Here, the boundary-layer instability mechanism changes from the centrifugal instability for slender cones  $\psi \lesssim 30^\circ$  to the cross-flow instability for the broad cones  $\psi \gtrsim 30^\circ$ . The exact half-cone angle where this change occurs still remains unclear. While the past literature majorly focused on rotating slender cones in axial inflow, theoretical studies expressed the lack of experimental data for the rotating broad cones in axial inflow. This dissertation has provided this experimental data on the instability-induced spiral vortices for the rotating broad cones of  $\psi = 45^\circ$  and  $50^\circ$  in axial inflow.

The experimental method developed in this work has enabled studying the boundary-layer instability behaviour on rotating cones, for the first time in high-speed conditions, i.e. local Reynolds number  $Re_l = 0\text{--}3 \times 10^6$ , rotational speed ratio  $S < 1\text{--}1.5$ , and inflow Mach number  $M = 0.5$ . These conditions are typically expected on the aero-engine-nose-cones during the transonic cruise of a large passenger aircraft (like A320, A350, etc.). These high-speed measurements revealed that the spiral vortices grow on the investigated rotating cones ( $\psi = 15^\circ$ ,  $30^\circ$  and  $40^\circ$ ) as expected from the low-speed studies. This confirms that the right circular type nose-cones of the transonic cruise aircraft will experience the spiral vortex growth in transitional boundary-layer.

The dissertation also conceptually discusses the potential effects of the spiral vortices on the fan aerodynamics. The spiral vortices are expected to influence the aerodynamics within the blade passage, especially, near the hub. Flow at the hub and fan-blade junction corner often separates on the suction side of the blade. This reduces the total pressure rise and efficiency of the engine. Presence of the spiral vortices is expected to affect the local aerodynamics at the hub, including the hub-corner separation, however, quantifying this effect needs further investigation. Furthermore, the dissertation has also shown a typical asymmetric flow field around the nose-cones when the fan is subjected to an inflow distortion. The fan-driven redistribution of the distorted inflow reduces the flow-field asymmetry near the nose-cone wall in the symmetry plane. This is a favourable condition for the spiral vortex growth.

Overall, this doctoral research has presented a new experimental approach to the classical problem of the boundary-layer instability on rotating cones. This has allowed furthering the fundamental knowledge about the instability-induced spiral vortex growth on rotating cones in following parameters: local Reynolds number  $Re_l = 0\text{--}3 \times 10^6$ , rotational speed ratio  $S = 0\text{--}250$ , inflow Mach number  $M = 0\text{--}0.5$ , inflow incidence angle  $\alpha = 0\text{--}10^\circ$  and half-cone angle  $\psi = 15^\circ\text{--}50^\circ$ .

# SAMENVATTING

Grenslaaginstabiliteit induceert spiraalwervels op roterende kegels. Naarmate deze wervels langs de kegel groeien, versterken de wervelingen de menging van hoge en lage-momentum fluïdum, en veroorzaken zij vervolgens de omslag van de grenslaag naar een turbulente toestand. Dit overgangsproces is wetenschappelijk interessant omdat het een van de klassieke problemen in de vloeistofmechanica is. In de praktijk is de omslag van de grenslaag van roterende kegels relevant in verschillende technische toepassingen, waaronder de roterende neuskegels van vliegtuigmotoren.

De spiraalwervels op roterende neuskegels van vliegtuigmotoren die worden veroorzaakt door de instabiliteit van de grenslaag zullen de stroming bij de wortel van de fan naar verwachting beïnvloeden. Dit zal mogelijk invloed hebben op het verliesmechanisme bij de verbindingen tussen de fanbladen en de naaf (het centrale roterende lichaam van de motor, inclusief de neuskegel). Een nauwkeurige bepaling van deze verliezen vereist kennis van het gedrag van de grenslaaginstabiliteit bij roterende kegels in stromingsomstandigheden zoals bij een vliegtuigmotor.

De literatuur over dit klassieke instabiliteitsprobleem heeft zich in het verleden alleen geconcentreerd op axiaal symmetrische instromingsomstandigheden bij lage snelheid (met een laag Reynoldsgetal en niet samendrukbaar). In werkelijkheid ondervinden neuskegels van vliegtuigmotoren vaak een hogesnelheidsinstroom (indrukbaar stroming en een hoog Reynolds getal) tijdens het vliegen. Bovendien bevatten verschillende concepten van toekomstige vliegtuigen motoren die zijn geïntegreerd met het vliegtuig, of motoren met een zeer hoge omleidingsverhouding en korte motorgondels. Als gevolg van de daarmee gepaarde verstoringen van de instroom, zullen de neuskegels van deze motoren een niet axiaal symmetrische aanstroming ondervinden. Beperkingen van de experimentele technieken uit het verleden vormen echter een hindernis bij het onderzoeken van de grenslaaginstabiliteit op roterende kegels waarbij de stroming zowel niet axiaalsymmetrisch is en een hoge snelheid heeft.

Dit proefschrift onderzoekt de grenslaaginstabiliteit op roterende kegels bij de stromingscondities die horen bij een typische vliegtuigmotor, d.w.z. een stroming die zowel niet axiaalsymmetrisch is en een hoge snelheid heeft. Eerst wordt een experimentele methode ontwikkeld om de coherente stromingsstructuren op roterende kegels te meten. Deze methode maakt gebruik van infrarood thermografie (IRT) met *proper orthogonal decomposition (POD)* om de thermische voetafdrukken van de spiraalwervels op roterende kegels te detecteren. De POD-modi worden selectief gereconstrueerd om verschillende stromingskenmerken die door instabiliteit veroorzaakt zijn te isoleren. Voor deze selectie wordt een nieuw criterium geformuleerd om de fysische aannemelijkheid van de POD-modi te bepalen voor de reconstructie van het stromingskenmerk. Deze methode heeft niet de beperkingen van de vroegere experimentele methoden en heeft voor het eerst kwantitatieve metingen mogelijk gemaakt van de groei, de hoek en het aantal spiraalwervels in azimuthale richting, in complexe stromingsomgevingen, d.w.z. zowel axiale als niet-axiale aanstromingen, en voor aanstromingen en hogesnelheidsinstroom.

De asymmetrie van de niet-axiale instroom blijkt de groei van de spiraalwervels te vertragen bij de roterende slanke kegel (halve kegelhoek  $15^\circ$ ) die onderzocht is in dit onderzoek. Voor dit geval wordt de groei van de spiraalwervel uitgesteld tot een hoger lokaal Reynoldsgetal  $Re_l$  en tot een hogere lokale rotatiesnelheidsverhouding  $S$  in vergelijking met het geval van een axiale aanstroming dezelfde operationele condities. Er wordt verondersteld dat de azimutale asymmetrie van de instroomcondities (lokaal  $Re_l$  en  $S$ ) de azimutale coherentie van de instabiliteitskarakteristieken, d.w.z. de hoek en golflengte van de dominante modus, aanzienlijk verstoort. Dit remt de groei van de spiraalwervels. Echter, bij hoge rotatiesnelheidsverhouding  $S$ , wanneer de instabiliteitskarakteristieken de azimutale coherentie naderen, blijken de spiraalwervels te groeien in het asymmetrische stromingsveld.

Verder breidt het proefschrift het onderzoek naar axiale stromingen uit van het meest besproken geval van een roterende slanke kegel van  $15^\circ$ , naar de bredere kegels van  $22.5^\circ$ ,  $30^\circ$ ,  $45^\circ$ , en  $50^\circ$ . Hier verandert het mechanisme van de grenslaaginstabiliteit van de centrifugale instabiliteit voor slanke kegels van  $\psi \lesssim 30^\circ$  naar de dwarsstroominstabiliteit voor de brede kegels van  $\psi \gtrsim 30^\circ$ . De exacte hoek van de halve kegel waar deze verandering optreedt is nog onduidelijk. Terwijl de voorbije literatuur zich vooral concentreerde op roterende slanke kegels in axiale stroming, wezen theoretische studies op het gebrek aan experimentele gegevens voor de roterende brede kegels in axiale stroming. Dit proefschrift heeft deze experimentele gegevens verschaft over de instabiliteit-geïnduceerde spiraalwervelingen voor de roterende brede kegels van  $45^\circ$  en  $50^\circ$  in axiale stroming.

De experimentele methode die is ontwikkeld in dit werk heeft het voor het eerst mogelijk gemaakt om het gedrag van de grenslaaginstabiliteit op roterende kegels te bestuderen, in hogesnelheidscondities, d.w.z. lokaal Reynoldsgetal  $Re_l = 0-3 \times 10^6$ , rotatiesnelheidsverhouding  $S < 1-1.5$ , en instromend Machgetal van  $M = 0.5$ . Deze condities worden doorgans verwacht op de neuskegels van vliegtuigmotoren tijdens de transsonische kruisvlucht van een groot passagiersvliegtuig (zoals A320, A350, enz.). Deze metingen bij hoge snelheid toonden aan dat de spiraalwervels groeien op de onderzochte roterende kegels ( $15^\circ$ ,  $30^\circ$  en  $40^\circ$ ) zoals verwacht van de studies bij lage snelheid. Dit bevestigt dat bij conische neuskegels van transsonische vliegtuigen de groei van spiraalvormige wervelingen zal plaatsvinden wanneer de grenslaag omslaat.

Het proefschrift bespreekt, weliswaar conceptueel, de potentiële effecten van de spiraalwervels op de aerodynamica van de fan. De spiraalwervelingen zullen naar verwachting de aerodynamica tussen de bladen beïnvloeden, vooral bij de wortel. De stroming bij de wortel van het blad laat vaak los aan kant van het blad waar de druk laag is. Dit vermindert de stijging van de totale-druk en de efficiëntie van de motor. De aanwezigheid van spiraalwervels zal naar verwachting de lokale aerodynamica bij de wortel beïnvloeden, inclusief het loslaat gedrag, maar dit effect moet verder worden onderzocht om een afschatting van dit effect te. Verder laat het proefschrift ook een typisch asymmetrisch stromingsveld rond de neuskegels zien voor het geval waarbij aanstroming naar de fan verstoord is. Vanwege de herverdeling van de verstoring door de fan, vermindert de asymmetrie van het stromingsveld bij het oppervlakte van de kegel in het symmetrievlak voor de groei van de spiraalwervels.

Samenvattend heeft dit doctoraatsonderzoek een nieuwe experimentele benadering gepresenteerd van het klassieke probleem van de grenslaaginstabiliteit op roterende kegels. Deze benadering heeft het mogelijk gemaakt om de fundamentele kennis over de instabiliteitsgeïnduceerde spiraalwervelgroei op roterende kegels uit te breiden met betrekking tot de volgende parameters en hun bereik: lokaal Reynoldsgetal  $Re_l = 0-3 \times 10^6$ , rotatiesnel-

heidsverhouding  $S = 0-250$ , instroom Machgetal  $M = 0-0.5$ , instroominvalshoek  $\alpha = 0-10^\circ$  en halve kegelhoek  $\psi = 15^\circ-50^\circ$ .



# NOMENCLATURE

## VARIABLES

$a$	sound speed
$a_1$	constant
$\mathcal{A}(t)$	time coefficient of POD modes
$\mathcal{E}$	specific heat
$c$	speed of light
$C$	constant
$C_1$	first constant of Planck's law
$C_2$	second constant of Planck's law
$D$	diameter
$d$	diameter of a circle circumscribing a distortion screen cell
$DC_{60}$	distortion index
$dt$	laser pulse separation
$\mathcal{E}$	energy of a photon
$E_b$	total power emitted by a black body
$E_{b,\lambda}$	spectral power emitted by a black body
$E_{signal}$	energy of the signal
$E_{noise}$	energy of noise
$E_{\lambda>\lambda_c}$	cumulative energy of fluctuations with wavelengths greater than a threshold $\lambda_c$
$f$	frequency
$F$	fourier transform
$F_c$	centrifugal force
$F_p$	force related to the pressure difference
$h$	vortex height
$\hbar$	Planck's constant
$\mathcal{I}$	identity matrix
$I$	digital pixel intensity
$I'_{RMS}$	RMS fluctuations of the digital pixel intensity
$k$	POD mode number

$k_{thr}$	threshold of POD mode selection
$l$	meridional length measured from the cone apex
$L$	total meridional length of a cone
$l_{ds}$	depth (axial length) of a distortion screen
$M$	Mach number
$m$	exponent
$M_{avg}$	area-averaged Mach number
$M_l$	local Mach number
$n$	azimuthal number of vortices
$\frac{P_{t,360^\circ}}{P_{t,60^\circ}}$	total pressure averaged over the entire circumferential extent
$Q$	heat
$q$	heat flux
$r$	local radius
$R$	total radius
$Re$	Reynolds number
$Re_l$	local Reynolds number
$Re_L$	inflow Reynolds number
$Re_D$	duct Reynolds number
$Re_{l,c}$	critical Reynolds number
$Re_{l,m}$	maximum amplification Reynolds number
$Re_x$	local Reynolds number ( $Re_l$ ) as per the notation of Kobayashi et al., <a href="#">1983</a>
$Re_{x,t}$	transition Reynolds number as defined by Kobayashi et al., <a href="#">1983</a>
$S$	rotational speed ratio
$S_b$	base rotational speed ratio
$\mathcal{T}$	temperature
$T$	time period
$t$	time
$t_{int}$	integration time
$t_w$	wall thickness of distortion screen cells
$u$	longitudinal velocity component
$u_e$	boundary-layer edge velocity
$U$	inflow velocity
$u'$	fluctuations in the longitudinal velocity
$\mathcal{U}$	matrix containing left singular vectors
$U_{mid}$	mid-span velocity of the blade
$V$	velocity in fan test rig
$\mathcal{V}$	matrix containing right singular vectors
$\mathcal{V}$	volume
$v_\theta$	tangential velocity
$x, y, z, x', y'$	spatial coordinates

$\alpha$	incidence angle
$\alpha_r$	radial angle
$\delta_{RM}$	a criterion for POD modes selection from Raiola et al., 2017
$\epsilon$	spiral vortex angle
$\epsilon_{rad}$	emissivity
$\Gamma$	circulation
$\lambda$	wavelength
$\kappa$	ratio of inflow Reynolds number and base rotational speed ratio
$\mu$	dynamic viscosity
$\nu$	kinematic viscosity
$\omega$	angular velocity
$\omega_z$	vorticity along $z$ direction
$\phi$	flow coefficient
$\phi_k$	$k^{\text{th}}$ POD mode
$\psi$	half-cone angle
$\psi_{load}$	loading coefficient
$\rho$	density
$\Sigma$	matrix containing the singular values
$\sigma$	singular value
$\sigma_{sb}$	Stefan-Boltzmann constant
$\theta$	circumferential coordinate

## SUB- AND SUPERSCRIPTS

$c$	critical
<i>cruise</i>	relating to the aircraft cruise conditions
<i>fan</i>	relating to fan
<i>flight</i>	relating to flight conditions
<i>hub</i>	relating to an aero-engine hub
$\infty$	free-stream conditions
<i>intake</i>	relating to an aero-engine intake
$l$	along the meridional location $l$
$m$	maximum amplification
'	fluctuation over the time-average
$r$	radial component
$t$	total
<i>tip</i>	relating to the fan blade tip
$T$	transpose
$x$	component along $x$ direction
$y$	component along $y$ direction
*	relating to non-axial inflow conditions

## ABBREVIATIONS

2C	two component
3C	three component
BLI	boundary-layer ingestion
BPF	blade passing frequency
DNS	direct numerical simulations
FPA	focal plane array
HSV	horse-shoe vortex
IRT	infrared thermography
LES	large eddy simulations
LWIR	long wave infrared
MCT	Mercury Cadmium Telluride
MWIR	mid-wave infrared
NETD	noise equivalent temperature difference
PIV	particle image velocimetry
POD	proper orthogonal decomposition
RMS	root mean square
RPM	rotations per minute
SV	secondary vortex
TV	tertiary vortex
UHBR	ultra high bypass ratio

# 1

## INTRODUCTION

### 1.1. MOTIVATION

THE century-old riddle of turbulent fluid motion continues to tantalise physicists even today. The path to turbulence is paved by flow instabilities, which often transmute small perturbations into large coherent flow-structures. These structures can further destabilise the flow into an uncontrolled cascade of subsequently small-scale chaotic fluid motions. Studying such instability mechanisms and induced flow-structures not only quenches the scientific curiosity, but also offers potential engineering benefits. Especially in rotating aero-engine components, it is important to know how the flow transitions between stable and unstable states and how coherent flow-structures emerge. Such knowledge will aid in designing efficient aero-engines, which will make aviation more sustainable.

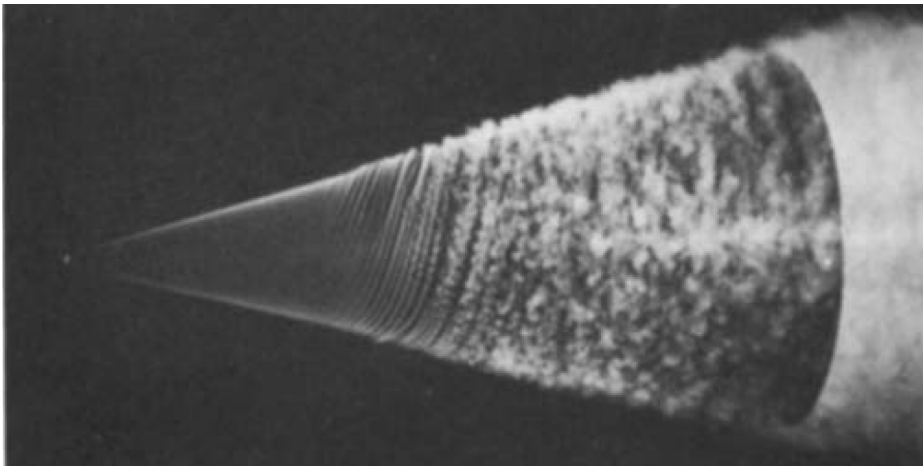


Figure 1.1: Visualisation of the transitional boundary-layer on a rotating slender-cone, with half-angle  $\psi = 15^\circ$ , in axial inflow; taken from Kobayashi et al., 1983.

In an aero-engine, the hub is the central rotating body on which the fan and compressor

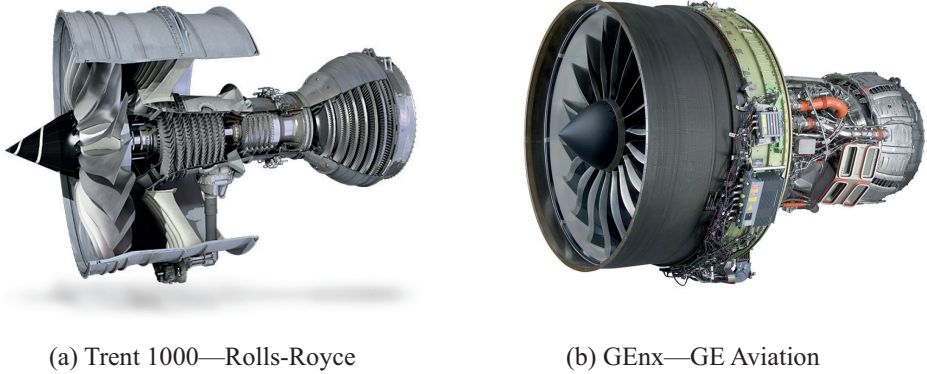


Figure 1.2: Different nose-cone shapes on different aero-engines: (a) Trent 1000 (source: Rolls-Royce) and (b) GEnx (source: GE Aviation).

blades are attached. The boundary-layer on the hub end-wall leads to losses. This boundary layer starts developing right from the tip of the rotating nose-cone, which can be ideally represented by a rotating cone. Kobayashi et al., 1983 showed that, in an axial inflow, the laminar boundary-layer on a rotating cone is unstable and that its primary instability induces spiral vortices (Figure 1.1). Initially, the spiral vortices appear to be azimuthally coherent, i.e. their spacing is almost constant around the azimuth. As they grow downstream, the spiral vortices start to lose their azimuthal coherence and break down into small-scale flow structures. Subsequently, the boundary-layer becomes fully turbulent. This shows that the boundary-layer on an aero-engine-nose-cone can be laminar, can have coherent spiral modes, can be fully turbulent, or can be in a mixed state. As hub end-wall losses depend on the oncoming boundary-layer properties, knowing the state of a nose-cone boundary-layer is necessary to assess and mitigate the losses.

In figure 1.1, it can be seen that the process of spiral vortex formation is a transition of the laminar boundary-layer from a non-modal to a modal state. The break-down of the spiral vortices is followed by the boundary-layer transitioning from a modal to a fully turbulent state. This shows that the boundary-layer undergoes significant transitions in a region between the non-modal laminar and fully turbulent states. Therefore, the boundary-layer is said to be transitional in this region.

In practice, different aero-engine manufacturers choose different nose-cone shapes for the same engine class. For example, figure 1.2 compares different engines designed to power the same aircraft, Boeing 787. Here, Rolls-Royce (figure 1.2a) features a slender nose-cone on its Trent 1000 engine, compared to the broad nose-cone on GE aviation's GEnx (figure 1.2b). Due to the different nose-cone shapes, the transitional behaviour of the nose-cone boundary-layers will be different, with different effects on the fan aerodynamics.

Knowing the transitional behaviour of the nose-cone-boundary-layer is important in aero-engine-fans. These fans are axial compressors and they usually have a corner-flow separation in the near-hub regions of their blades (Gbadebo et al., 2005), see figure 1.3. Generally, the flow separation reduces total pressure downstream of the rotor/stator blades. This reduces the fan efficiency, causing increased fuel consumption. Furthermore, the hub-corner separation can also trigger the rotating stall (Cho et al., 2008). Such stall can cause

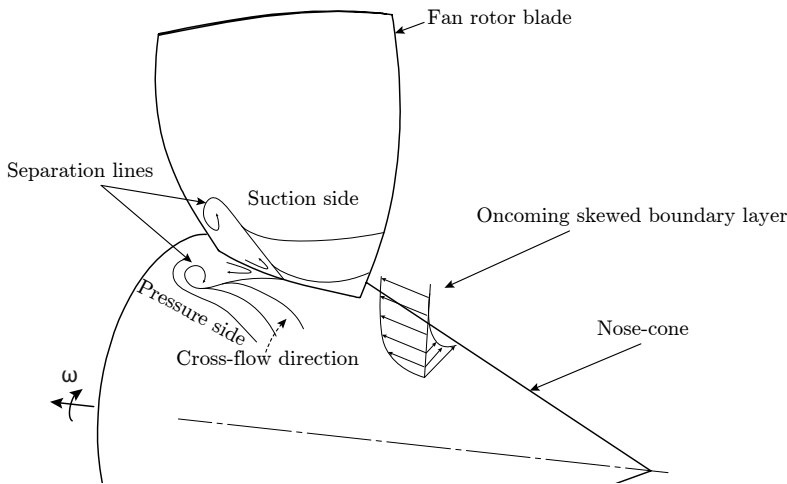


Figure 1.3: Three-dimensional flow separation at the blade-hub junction facing skewed boundary-layer (the concept of hub-corner separation adapted from Lei et al., 2008).

off-design unsteady loads on the blades, reducing their mechanical reliability.

Moreover, in a gas-turbine engine, the hub-flow leaves the fan root and enters the subsequent compressor stages. Therefore, any adversities in the hub-flow, such as total pressure loss, distorted flow angles, etc. can induce losses in subsequent components. For example, in a large gas-turbine-engine with a bypass-ratio  $\approx 10$ , 1% total-pressure-loss at the fan-root can increase the specific fuel consumption by around 0.2% (Zamboni & Xu, 2009). Therefore, it is of interest to minimise the adverse effects of the hub-flow.

However, no past study has addressed the transitional behaviour of the nose-cone boundary-layer at flight conditions and its effects on fan aerodynamics near the hub. The boundary-layer state (laminar, modal or turbulent) is expected to affect the near-wall skewness and flow angles, which have been previously shown to influence the hub-corner separation (Lei et al., 2008). Scillitoe et al., 2017 compared fully laminar versus fully turbulent hub boundary-layers in a linear (non-rotating) compressor cascade. As expected, they observed that the laminar hub boundary-layer separates earlier compared to the fully turbulent case, resulting in a larger corner separation with increased losses. Hergt et al., 2013 applied vortex generator devices upstream of the compressor blade passage to control the hub-corner separation, see figure 1.4 for a conceptual schematic. They observed, for the investigated cases, the generated vortices can reduce the extent of the separated region, mitigating the total pressure loss. Furthermore, Zambonini et al., 2017 reported that the large flow-structures in the on-coming turbulent boundary-layer influenced the hub-corner separation in the linear compressor cascade. Overall, this suggests that the instability-induced flow features in a rotating nose-cone boundary-layer can influence the hub-losses, and therefore, need to be investigated.

To assess and mitigate the hub-flow related losses, it is first necessary to know the locations of boundary-layer transition on a rotating nose-cone at flight conditions. It is also necessary to know what are the instability-induced coherent flow structures along with their typical size and orientation. This requires fundamental investigations on the boundary-layer

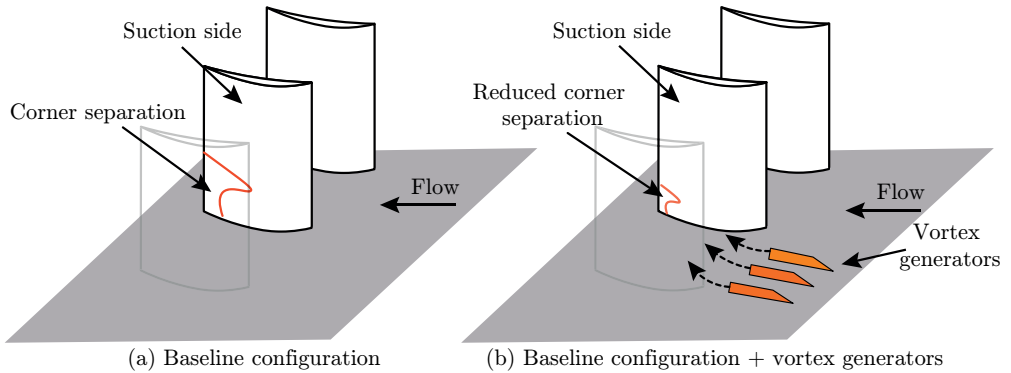
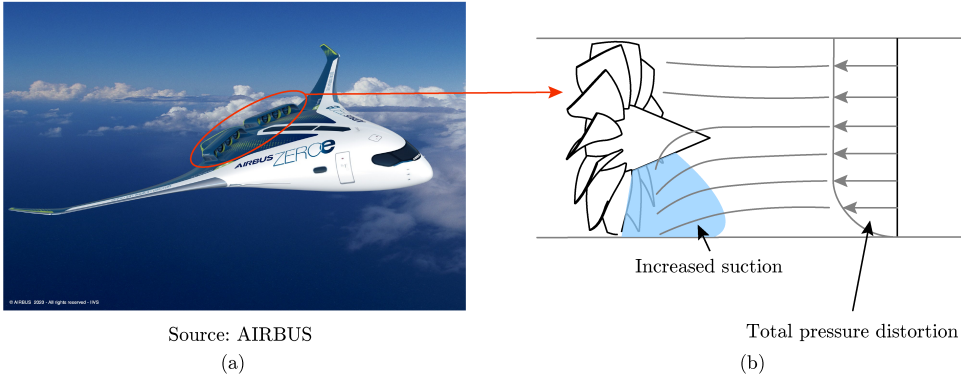


Figure 1.4: Effect of near-wall vortices on the hub-corner separation in a linear compressor cascade. A conceptual adaptation of the results from the experiments of Hergt et al., 2013. (a) Baseline configuration and (b) baseline configuration with a vortex generator row.

instability on rotating cones in aero-engine-like inflow conditions. This knowledge will be useful in assessing how these coherent flow-structures influence the hub-flow related losses.

Fundamental investigations on the nose-cone-boundary-layer instabilities and transition must also be aligned with the global trends in future-aircraft developments. Many of the proposed aircraft concepts, put forth for the future, choose embedded-engines ingesting the airframe-boundary-layer. This type of boundary-layer-ingestion (BLI) can reduce the fuel burn (Felder et al., 2011; Greitzer et al., 2010; Gunn & Hall, 2014) by up to 15% (C. A. Hall et al., 2009). For example, the recent-most aircraft concept unveiled by Airbus, called *AIRBUS ZEROe*, features a blended wing-body aircraft with the hydrogen powered turbofan engines that are embedded in the airframe (figure 1.5a). Here, the fan is ingesting the airframe-boundary-layer which is non-uniform and non-axisymmetric (figure 1.5b). In such cases, the fan accelerates the distorted flow locally, creating an asymmetric suction field. Consequently, the flow three-dimensionally redistributes upstream of the fan and around the nose-cone. During its rotation, a fan blade encounters this three-dimensional flow at varying incidence angle. Especially near the hub, the interaction between the redistributing flow and the rotating nose-cone is currently unknown, but it is expected to influence the losses caused by the distortion (Jerez Fidalgo et al., 2012). Here, the transitional behaviour of the nose-cone-boundary-layer is expected to influence the redistributing flow and associated loss mechanism. But first, it is important to know how the nose-cone-boundary-layer transitions in a non-axisymmetric inflow.

Currently, the use of Ultra-High-Bypass-Ratio (UHBR) engines on existing tube and wing aircraft configuration is gaining attention. This concept offers performance benefits within short implementation times. However, the huge UHBR engines have increased nacelle weight and drag. To minimise this penalty, engineers are exploring the use of short intakes. However, this raises the problem of increased distortion during some flight conditions, such as during take-off/landing or cross-wind operations (Cao et al., 2017; Peters et al., 2015; Vadlamani et al., 2019). In these conditions the inflow is at high incidence angles (figure 1.6). Here, the nose-cone faces a non-axisymmetric inflow. Moreover, the flow separation at the intake lip can add to the distortion, causing upstream flow redistribution as shown in figure 1.5b. Again, here, assessing the hub-loss mechanism becomes challenging due to the



Source: AIRBUS  
(a)

Total pressure distortion  
(b)

Figure 1.5: (a) AIRBUS ZEROe and (b) aero-engine-fan operating with inflow distortion. The boundary layer ingestion (BLI) on the future aircraft causes non-axial inflow on the rotating nose-cone.

unknowns of the nose-cone-boundary-layer transition in non-axisymmetric inflows.

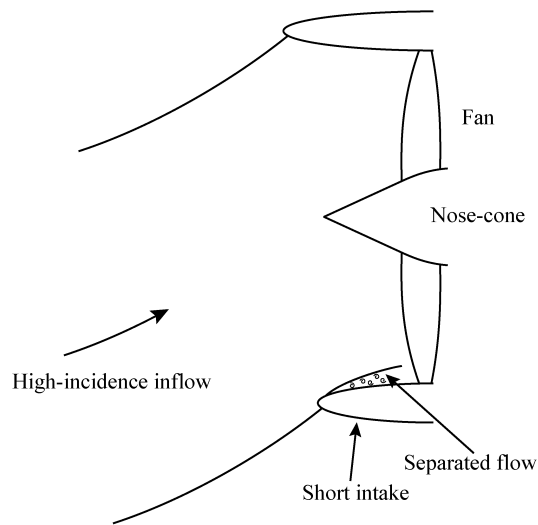
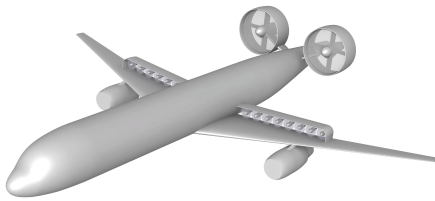


Figure 1.6: A schematic of an UHBR engine with the short intake operating at high-incidence. Due to the inflow incidence angle and the distortion from the inlet-lip flow separation the rotating nose-cone faces a non-axial inflow.

Moreover, the concept of electric flight is gaining serious consideration within the aircraft design community. This comes as a response to the societal need of making serious efforts towards sustainability by reducing the adverse environmental impact of technologies. By burning fossil fuels, aviation alone causes around 1 Gigatonne of  $CO_2$  emissions per year and 5% of the total anthropogenic effective radiative forcing (Lee et al., 2020). This impact can be significantly reduced by shifting to the electric aircraft. However, a fully electric large passenger aircraft (similar to A320 and beyond) is currently infeasible due to the poor energy density of the batteries. Therefore, a hybrid electric propulsion (HEP) is considered as a more

realistic option. Here, electric propulsors are used together with the gas turbine engines.

Figure 1.7 shows examples of the hybrid electric aircraft concepts proposed by TU Delft (Hoogreef et al., 2019) and NASA (Felder et al., 2011). These concepts include the ducted fans ingesting the non-uniform flow over the wings and fuselage. Here, assessing the propulsive losses is extremely important because they can directly impact the feasibility of such hybrid electric aircraft concepts. Knowing the nose-cone-boundary-layer transition in these cases will help in accurately assessing the hub-losses. This will lead to an accurate prediction of the fan performance.



Source: Hoogreef et al. 2019

(a)



Source: NASA

(b)

Figure 1.7: Aircraft concepts with hybrid electric propulsion by (a) TU Delft (Hoogreef et al., 2019) and (b) NASA N3-X (Felder et al., 2011). Both the concepts feature ducted fans ingesting non-uniform inflow over the air-frame.

With these motivations in the background, the present work contributes in the global effort of making aviation more sustainable. This is achieved by adding to the scientific knowledge on the nose-cone-boundary-layer transition. The exact knowledge gaps addressed in this work are described in section 1.2. Section 1.3 details the research aim and methodology. Finally, section 1.4 outlines the dissertation.

## 1.2. KNOWLEDGE GAP

Instability and transition of rotating-boundary-layer-flows has been a classical problem, investigated in several past studies. This section briefly overviews the past literature and presents the identified knowledge gaps. A detailed review of the past literature is presented in chapter 2.

It was Smith, 1947 who first measured the distinct sinusoidal velocity oscillations over a rotating disk in still fluid. Later on, the visualisations of Gregory et al., 1955 revealed that these oscillations pertain to the spiral vortices that are induced due to an instability of the rotating-disk boundary-layer. These spiral vortices have also been observed on other rotating bodies such as cones, spheroids, and ellipsoids (Kobayashi & Izumi, 1983; Kobayashi et al., 1983; Kobayashi et al., 1980; Kobayashi, 1994; Y. Kohama, 1984b, 1987; Y. P. Kohama, 2000). When the spiral vortices grow, they enhance the mixing of high and low momentum flow and significantly change the mean velocity distribution within the boundary-layer (Y. Kohama, 1984a). This changes the boundary-layer skewness which is expected to affect the hub-corner separation as discussed in section 1.1. However, the past experimental investigations were only limited to the low-speed axisymmetric outer-flow conditions.

Several theoretical and numerical studies have investigated the boundary-layer instability

on a rotating disk; these are reviewed in detail by Saric et al., 2003. The studies on a rotating disk are abundant because the similarity solution of its basic boundary-layer flow is known. These studies offer great insights into the onset and growth of different instability modes along with their linear and non-linear behaviours. Similar theoretical analyses have been extended to the cones rotating in still fluid as well as in axial inflow (Garrett et al., 2009, 2010; Garrett & Peake, 2007a; Hussain et al., 2014; Hussain et al., 2016; Hussain et al., 2012; Kobayashi & Izumi, 1983; Kobayashi et al., 1983; Lingwood, 1995; Segalini & Camarri, 2019; Towers & Garrett, 2012; Towers et al., 2016; Towers & Garrett, 2016), discussed in section 2.3. All of these theoretical studies assumed symmetry around the rotation axis. Therefore, the instability behaviour on rotating cones facing non-axisymmetric inflow was unknown. This is of interest for the embedded and UHBR engines as described in section 1.1.

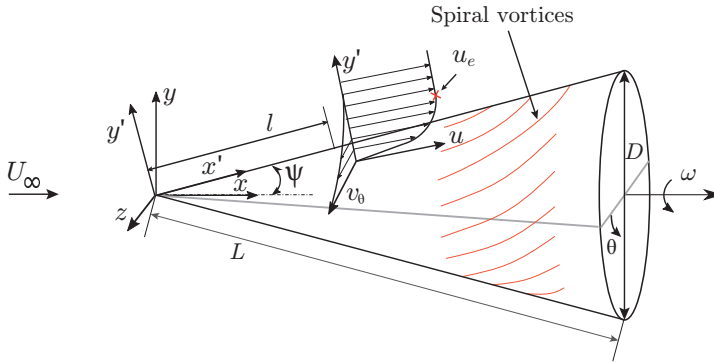


Figure 1.8: A schematic of the spiral vortices on a rotating cone in an axial inflow with the main geometry and flow parameters determining the spiral vortex development.

Figure 1.8 schematically shows a case of a rotating cone in axial inflow. In this case, past studies have shown that the spiral vortex growth depends on two parameters: the local Reynolds number

$$Re_l = \frac{\rho u_e l}{\mu}, \quad (1.1)$$

and local rotational speed ratio

$$S = \frac{r\omega}{u_e} = \frac{l \sin(\psi)\omega}{u_e}. \quad (1.2)$$

Here,  $\rho$  is density,  $u_e$  is the boundary-layer edge velocity,  $l$  is the meridional length along the cone,  $\mu$  is the dynamic viscosity,  $r$  is the local radius,  $\omega$  is the angular velocity of the cone, and  $\psi$  is the half-cone angle.

The parameter space of  $Re_l$  vs  $S$  was not fully explored in the past studies. These studies investigated rotating bodies in incompressible low-speed inflow conditions, i.e.  $Re_l < 10^5$ , Mach number  $M \approx 0$  and  $S > 1-1.5$ , which are not entirely representative of the flight flow conditions. During a typical transonic flight, the aero-engine-nose-cones face the intake flow at Reynolds number  $Re_l$  reaching beyond  $10^6$ , the rotational speed ratio  $S < 1.5$  and Mach numbers  $M = 0.5-0.6$  (In this work, these flow conditions are referred to as *high-speed* conditions). Therefore, the boundary-layer instability behaviour on nose-cones was unknown at

the most-encountered flow conditions in aviation. A few studies have theoretically analysed the instability of a compressible boundary-layer on a broad cone rotating in otherwise still fluid (Towers & Garrett, 2012; Towers et al., 2016; Towers & Garrett, 2016; Towers, 2013), but incorporating the high Reynolds number compressible inflow to this problem is important for the aero-engine applications.

Furthermore, theoretical and numerical studies have investigated a wide range of half-cone angles  $\psi = 15^\circ\text{--}90^\circ$  in axial inflow; however, the past experimental data are only available for  $\psi = 7.5^\circ, 15^\circ$ , and  $30^\circ$ . Garrett et al., 2010 have explicitly expressed the lack of experimental data on broad cones  $\psi > 40^\circ$  for comparing their theoretical predictions of the cross-flow instability.

Investigating nose-cone-boundary-layer instability in asymmetric and high-speed inflow environments requires a new experimental (as justified in section 1.3) approach. Past studies have used particle based visualisation technique which requires a low-turbulent wind-tunnel stream, and such techniques do not yield the required quantification on spiral vortex growth. Past researchers quantified the velocity components using the hot-wire-anemometry, but this intrusive technique does not provide the instantaneous spatial measurements and is time-consuming—which makes it less suitable for the large parametric studies. Therefore, a simple experimental method that would detect the spiral vortices on rotating cones in asymmetric as well as high-speed turbulent inflow is missing in the literature.

Overall, it's well known how the boundary-layer transitions in simplified cases of rotating cones, i.e. in still fluid or axial low-speed inflow. However, such knowledge needs to be expanded to more complex flow scenarios that are relevant in aero-engine applications, aligned with the future developments. Figure 1.9 depicts these knowledge gaps along with the contributions of the present work, discussed in the next section.

### 1.3. RESEARCH AIM AND METHODOLOGY

This research aims to

*Explore the parameter space of boundary-layer instabilities on rotating cones in complex flow environments relevant to aero-engines.*

This includes characterising the onset, growth, and break-down of the instability-induced spiral vortices on rotating cones in different flow environments, i.e. axial, non-axial, and high Reynolds-number compressible inflows. The knowledge gaps discussed in section 1.2 are partially filled by this research, as depicted in figure 1.9. The present contributions will allow future studies to estimate the nature of the transitional nose-cone-boundary-layer and its impact on the engine performance. This would enable devising suitable loss-mitigation strategies.

The following specific research questions are answered in this work:

- *How to detect the spiral instability modes on a rotating cone in complex flow environment?*
- *How does breaking the axial symmetry affect the boundary-layer instability on a rotating cone?*
- *What is the effect of half-cone angle on boundary-layer instability on rotating cones?*

Type of study \ Inflow condition	Experimental studies	Theoretical/numerical studies	Snapshot visualisation of the spiral modes together with growth quantification
still fluid			
low-speed axial inflow			
non-axial inflow			
high-speed inflow			
Type of cones			
Slender cones with inflow			
Broad cones with inflow			

Knowledge from the past studies
 Knowledge gaps addressed by the present work

Figure 1.9: The knowledge gaps and present contribution in the problem of boundary-layer instability on rotating cones.

- *How the instability modes on rotating cones are influenced by an inflow with high-Reynolds and Mach numbers pertaining to aero-engines?*
- *How to use the knowledge of the nose-cone-boundary layer transition for the engineering benefit?*

Historically, fluid dynamic discoveries of flow transitions are led by experimental observations, and later, their underlying physics is explained by theoretical/ numerical analyses. Therefore, fluid dynamic explorations largely rely on experiments due to the lack of general analytical solutions of fluid motion and the bifurcations leading to the multiple solutions for a given flow system. Recent advances in numerical techniques, such as *stability analyses*, *Large Eddy Simulations (LES)*, *Direct Numerical Simulation (DNS)*, show promises in predicting the transitional flow behaviour. However, due to the complexity, stability analyses have been limited to the axi-symmetric cases with incompressible axial inflow on rotating cones. Moreover, LES and DNS require fine spatial resolution with large computational resources, which limits the analyses to very low Reynolds-number flows.

On the contrary, experiments render the natural flow phenomena and remain the primary means of studying the flow instability (Drazin, 2002). Therefore, this exploratory research relies on the experimental approach for investigating the boundary-layer instability on rotating cones in asymmetric and high-Reynolds-number flows. Nevertheless, future theoretical/numerical studies will be essential to further interpret the underlying flow physics of the experimental observations.

To address the knowledge gaps discussed in section 1.2, this research presents a new and simple experimental method that measures coherent flow patterns on rotating bodies. The method can be used in complex flow environments where past methods are not suitable. This method is validated by revisiting the experiments of Kobayashi et al., 1983. Second, the method is applied to study the effect of symmetry-breaking on the instability-induced spiral vortices on a rotating body at low-speed conditions. Furthermore, the effect of varying

the half-cone angle on the instability characteristics is investigated for rotating cones in low-speed axial inflow conditions. The experimental investigations are then extended to the high-speed flow conditions, representative of aero-engine operating conditions. This makes it possible not only to ascertain whether the spiral instability modes observed in low-speed cases exist in this flow regime, but also to characterise their growth in the parameter space  $Re_l$  vs  $S$  for the purpose of prediction. Finally, the dissertation conceptually discusses the possible effects of the instability-induced spiral vortices on the blade-hub junction flow.

#### 1.4. DISSERTATION OUTLINE

The dissertation follows an outline depicted in figure 1.10. Chapter 2 summarizes the background of this dissertation, which includes: concept of instability and review of the past literature on instability of the rotating boundary-layer flows. The chapter also details the working principles of the flow measurement technologies used in this work, along with the data-processing methods.

Chapter 3 presents a new experimental method developed during this work, which makes it possible to measure coherent vortex structures over a rotating body. A simple case of a rotating slender-cone under axial flow (low-speed) is revisited with this method; the results are compared to the past experiments of Kobayashi et al., 1983 as well as to the present measurements, using particle image velocimetry (PIV).

Chapter 4 shows how introducing asymmetry into the flow field affects the spiral vortices induced over a rotating slender-cone. Here, the axial (symmetric) and non-axial (asymmetric) inflow cases are compared to show how the growth and spatial coherence of the spiral vortices are affected by the asymmetry.

Chapter 5 shows how changing the half-cone angle affects the boundary-layer instability on rotating cones in axial inflow. The chapter also provides comparison of present experimental results with the theoretical predictions of Garrett et al., 2010.

Chapter 6 presents the investigations in high-speed flow over three different rotating cones. This chapter demonstrates that high-speed conditions produce spiral waves similar to those observed in past low-speed reports on rotating cones. Confirming that realistic aero-engine-nose-cones can encounter spiral instability modes in the transitional boundary-layer. The chapter also details the characteristics of these modes.

Chapter 7 presents preliminary investigations on nose-cones installed on a ducted fan facing distorted inflow. The results show the typical asymmetric flow-field around different nose-cones that can be expected in embedded and UHBR engines.

Chapter 8 puts the fundamental investigations of the nose-cone-boundary-layer instability in the practical context of real aero-engine applications. The chapter conceptually relates the instability-induced spiral vortices to the possible effects on the fan root aerodynamics.

Finally, chapter 9 presents the combined conclusions of the previous chapters. Highlighting this work's intellectual contributions. Chapter 9 also considers the current limitations and future outlook of this line of research.

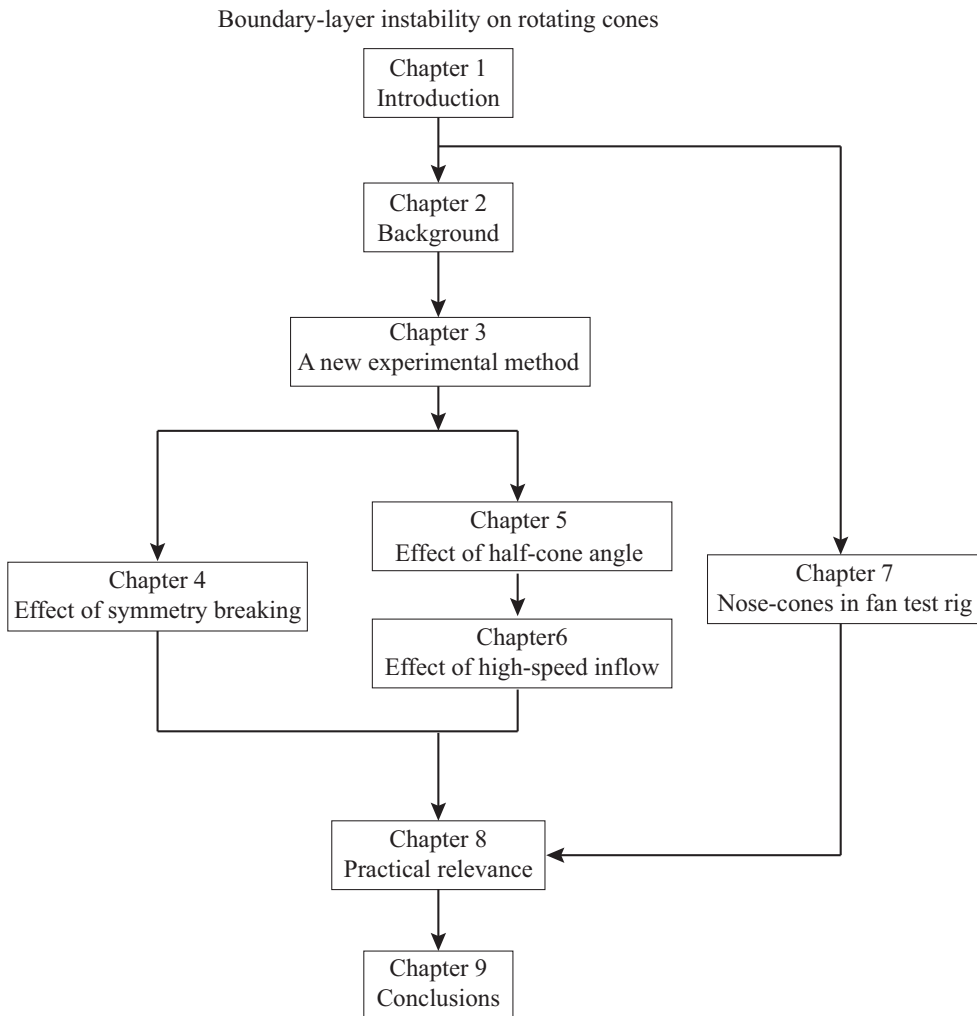


Figure 1.10: Dissertation outline.



# 2

## BACKGROUND

### 2.1. INTRODUCTION

**T**HIS chapter serves as the necessary background for the forthcoming chapters of this dissertation. The chapter starts by explaining the concept of flow instability, and later on, overviews the existing literature on rotating-boundary-layer instabilities. As discussed in chapter 1, the present research largely relies on experiments using state-of-the-art flow measurement techniques: infrared thermography (IRT) and particle image velocimetry (PIV). Therefore, this chapter also presents the working principles behind these flow measurement techniques. Finally, the chapter provides mathematical and conceptual backgrounds of the Proper Orthogonal Decomposition because the POD approach is employed to enhance the flow-measurements of this work.

### 2.2. INSTABILITY

Instability of a system is inability to revert back to its initial state in response to a small perturbation. When a system is unstable, an infinitesimally small perturbation can alter the system-state. Generally, the instability-induced changes in the system-state are observed in experiments.

For example, figure 2.1 shows the flow features in a rising smoke. This is a commonly observed phenomenon of a buoyant jet that has been addressed in several studies (Becker & Massaro, 1968; Mollendorf & Gebhart, 1973; Sreenivas & Prasad, 2000). The rising smoke is initially confined to a vertical column (assuming the absence of meandering). This indicates that small environmental perturbations have not drastically disturbed the fluid motion in this region, thereby exhibiting stability. However, as the smoke rises higher, it suddenly forms the large coherent ring-like patterns. This drastic change in fluid motion is induced by instability, responding to the small perturbations in its environment. Commonly, such formation of large coherent flow-patterns is followed by their break-down due to the secondary instabilities. Subsequently, this results in chaotic broad-spectrum flow fluctuations, also known as turbulence. Generally, in problems concerning flow transitions, it is of interest to know when a given flow system turns unstable, what are the instability-induced coherent flow patterns, and how do they lead to the turbulence. The present work also follows this approach and



Figure 2.1: Instability-induced flow structures in a rising smoke, a common example of a buoyant jet addressed in several studies (Becker & Massaro, 1968; Mollendorf & Gebhart, 1973; Sreenivas & Prasad, 2000). Photographed by Vladuchick, 2010. Instability-induced coherent ring-like flow structures indicate the unstable flow region.

focuses on the onset and growth of coherent structures in unstable boundary-layers on rotating cones.

Generally, a few dimensionless parameters, e.g. Reynolds number, govern the onset, growth and breakdown of instability-induced flow-structures. These parameters are different for different flow systems. Once identified, such parameter space needs to be explored to enable predicting when the instability will induce large coherent structures, how these structures will grow/break-down and what will be their wave-number and wave-angle. Section 2.3 describes the flow parameters relevant to the problem of boundary-layer instability on rotating cones.

Naturally, instability is observed to be of various types, which depend on the underlying mechanisms. Of all the types, centrifugal and cross-flow instabilities are predominantly present in rotating-boundary-layer-flows. Following is their conceptual background.

### 2.2.1. CENTRIFUGAL INSTABILITY

The motion along a curved path requires a centripetal force. In fluid flow, the radial pressure difference provides this necessary centripetal force. For example, consider a fluid element moving on a curved path in figure 2.2, its centrifugal force  $F_c$  is balanced by the centripetal force  $F_p$  provided by the pressure difference. When this fluid element is radially perturbed, its velocity changes due to the conservation of angular momentum; or if its velocity is perturbed, its radial location changes. Consequently, the centrifugal force  $F_c$  required to sustain the curved motion changes. Now, if the local pressure difference at this new

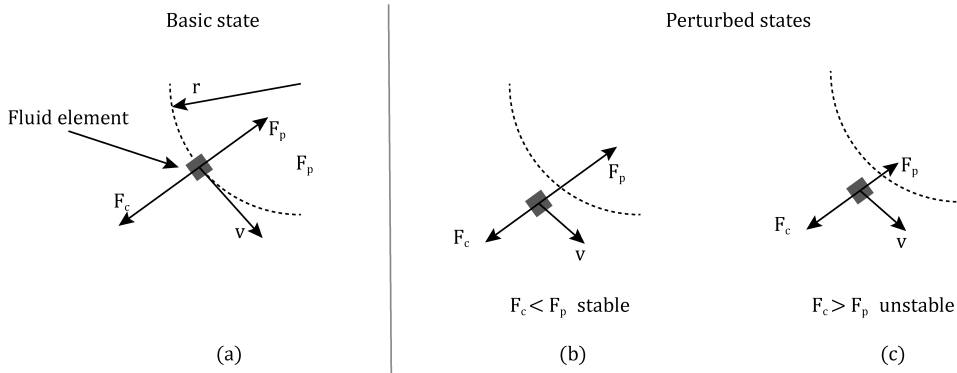


Figure 2.2: Concept of the centrifugal instability shown using a fluid element moving along a curved path in the (a) basic state, and perturbed (b) stable and (c) unstable states.

location is insufficient to curb the perturbation effect or sustain the new curved motion, the perturbation will grow and will drastically change the fluid motion. This type of instability is called as the centrifugal instability. For further reading, refer to Drazin, 2002; Nieuwstadt et al., 2015.

Taylor, 1923 made one of the first observations of the coherent vortices induced by the centrifugal instability. He observed that the viscous flow between the two concentric rotating cylinders exhibits toroidal vortices, see figure 2.3. Görtler, 1954 observed similar vortices due to the centrifugal instability on the concave walls. Later on, Kobayashi and Izumi, 1983; Kobayashi et al., 1983 also observed the vortices induced by the centrifugal instability in the boundary-layer on the rotating slender-cones. All of these observed vortices were counter-rotating in their cross-section.

Generally, the vortices induced by the centrifugal instability are counter-rotating in nature. Recent studies have also shown the existence of the centrifugal instability mode over a spinning cylinder in uniform flow that is orthogonal to the rotation axis (Mittal, 2004; Radi et al., 2013; Rao, Leontini, et al., 2013; Rao, Leontini, et al., 2013), and the vorticity contours associated with this mode suggest the counter-rotating nature of the vortices, which appear as travelling waves (Rao, Leontini, et al., 2013).

Centrifugal instability on rotating cones is discussed in more detail in section 2.3.

### 2.2.2. CROSS-FLOW INSTABILITY

This type of instability exists in an inflectional velocity profile, caused by the cross-wise pressure gradient. Consider a boundary-layer flow shown in figure 2.4, which is typical to the rotating disk in still fluid. Here, the disk surface creates a typical profile of the tangential velocity  $v_\theta$ . As the tangential velocity increases with the radius, a radial pressure gradient appears in the  $u$  direction. This creates an inflectional profile of the radial velocity  $u$ . This type of flow is unstable and causes perturbations to grow and form co-rotating vortices.

The cross-flow instability is commonly present on rotating disks (Y. Kohama, 1984b) and rotating broad-cones with half-cone angles  $\psi > 30^\circ\text{--}40^\circ$  (Kobayashi, 1994). Additionally, cross-flow instability is also present on the swept wings (Y. Kohama, 1987). In all cases, the vortices induced by the cross-flow instability are co-rotating in the cross-section.

2

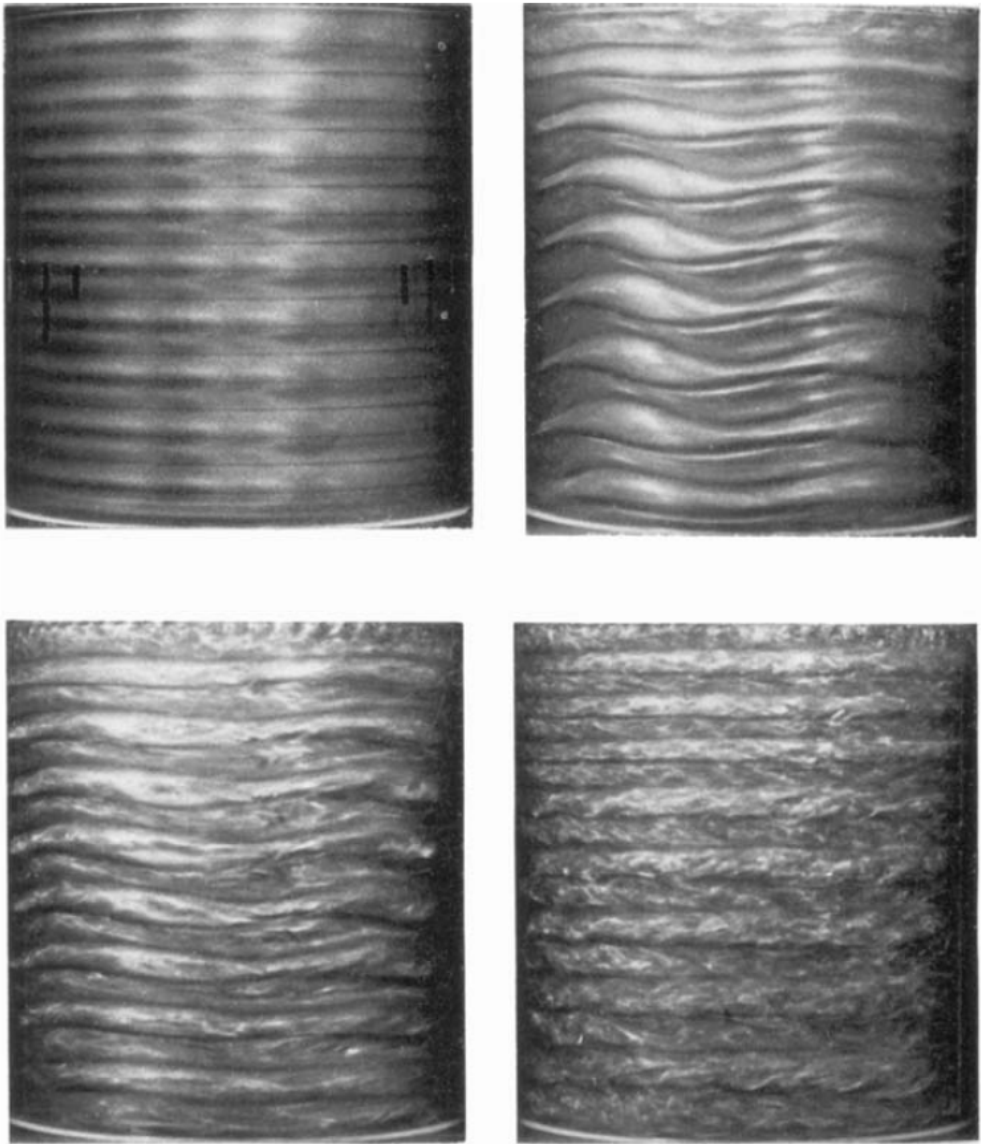


Figure 2.3: Taylor vortices induced by the centrifugal instability of the viscous flow between two concentric rotating cylinders (Fenstermacher et al., 1979).

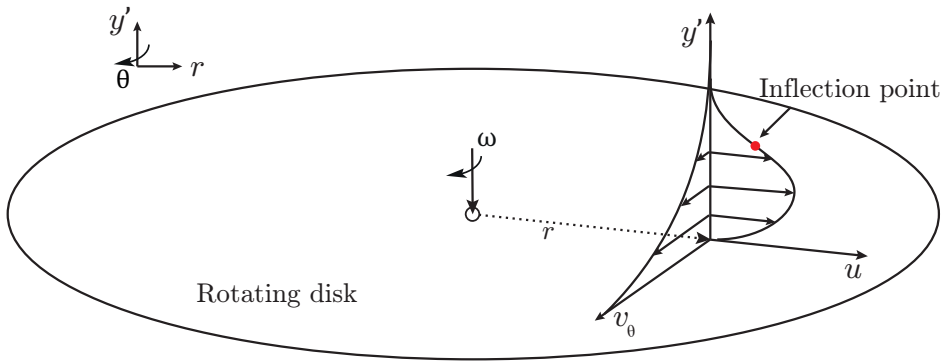


Figure 2.4: Inflectional velocity profile with a cross-flow instability on a rotating disk.

The cross-flow instability on a rotating disk and cones is discussed in more detailed in section 2.3

### 2.2.3. ABSOLUTE VS CONVECTIVE INSTABILITY

Flow instability is also classified as absolute and convective. Lingwood, 1996 has explained this classification with the space-time diagram of an impulse response which is re-created here in figure 2.5. When the flow is convectively unstable a small perturbation impulse grows and gets convected with the flow, see figure 2.5a. When the flow is absolutely unstable, the small perturbation impulse grows with time without any mean spatial convection, see figure 2.5b. Despite of this distinction, some flows may show a combination of both convective and absolute instabilities. As described in section 2.3.1, the spiral vortices on rotating cones are induced by a convective instability.

## 2.3. BOUNDARY-LAYER INSTABILITY ON ROTATING BODIES

In the past, investigations of the flow instability were led by experiments. However, theoretical and numerical studies have played an essential role in explaining the underlying flow-physics of the experimental observations. As discussed in section 1.3, the present work has chosen an experimental approach. Therefore, this section focuses on flow physics related discussion on the boundary-layer instability on rotating bodies, obtained from both experimental and theoretical past studies. The mathematical formulations of the rotating boundary-layer instability problems are beyond the scope of the present work and can be found in the literature, e.g. Hussain, 2010; Towers, 2013.

### 2.3.1. ROTATING DISK

In the past, instability mechanisms in rotating boundary-layer flows were first discovered through studies on a disk rotating in still fluid. Early experiments showed that the laminar boundary-layer on a rotating disk exhibits coherent spiral vortices, before transitioning into a fully turbulent state (Gregory et al., 1955; Smith, 1947). These vortices are better seen in the visualisations by Y. Kohama, 1984b, see figure 2.6.

Here, the radially increasing tangential velocity of the disk surface creates a pressure

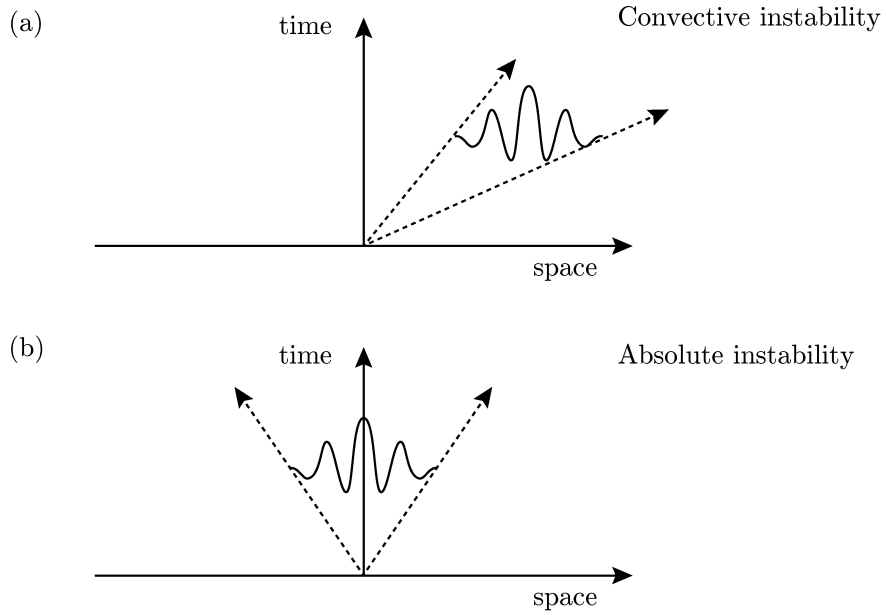


Figure 2.5: (a) Convective and (b) absolute instability. The concept adapted from Lingwood, 1996. The convective instability exhibits spatial growth of an impulsive perturbation, whereas the absolute instability exhibits only temporal growth without any mean convection.

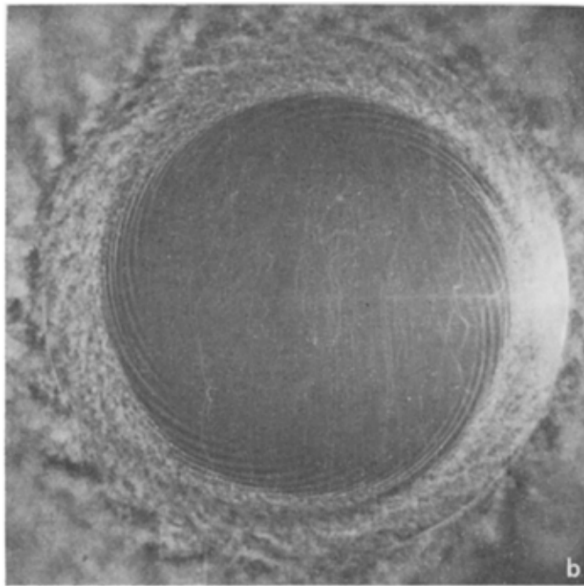


Figure 2.6: Spiral vortices on a disk rotating in still fluid as photographed by Y. Kohama, 1984b.

gradient, leading to an inflectional radial velocity profile. This exhibits the cross-flow instability, as discussed in section 2.2.2, which induces the spiral vortices. These vortices appear co-rotating in their cross sections (figure 2.7a adapted from Y. Kohama, 1984b), and subtend the wave angle  $\epsilon$  of around  $14^\circ$  with the circumferential direction. This angle is the same as an angle between a meridian and a vector normal to the spiral vortex, see figure 2.7b. Here,  $\lambda_\theta$  is the azimuthal wavelength which relates to the azimuthal number of vortices  $n = 2\pi r / \lambda_\theta$ , at a local radius  $r$ . Experiments of Fedorov et al., 1976 and theoretical analyses of P. Hall, 1986; Malik, 1986 showed the existence of another instability mechanism related to the viscous-Coriolis forces over a rotating disk, which can also result in the spiral vortices with  $\epsilon = 20^\circ$ .

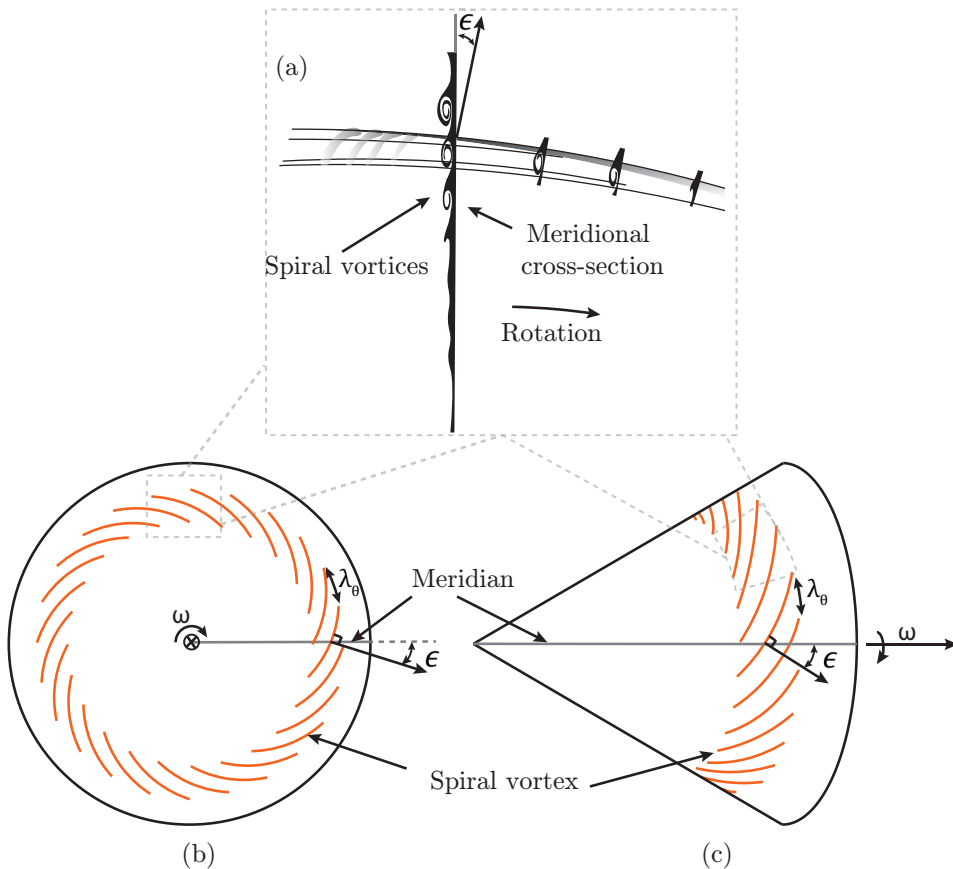


Figure 2.7: Schematics of the spiral vortices. (a) A close-up view showing the co-rotating vortices (adapted from Y. Kohama, 1984b). Spiral vortices on (b) a rotating disk and (c) a rotating cone in still fluid along with the definitions of the spiral vortex angle  $\epsilon$  and azimuthal wavelength  $\lambda_\theta$ .

Both, cross-flow and viscous-Coriolis instabilities are convective instabilities i.e. the perturbations undergo a spatial growth. With the parallel flow assumptions, Lingwood, 1995 proved and later demonstrated with experiments (Lingwood, 1996) that an absolute instability is present in the boundary-layer over a rotating disk. Here, impulsively added

perturbations undergo temporal growth, including the upstream propagation. However, direct numerical simulations of Davies and Carpenter, 2003 showed that with spatial inhomogeneity of the boundary-layer, i.e. without the parallel flow assumption, the convective instability dominates over the absolute instability. Therefore, the rest of the discussion in this dissertation focuses on the convective instability modes.

### CRITICAL FLOW PARAMETERS

The instability and transition of the rotating-disk-boundary-layer depends on the Reynolds number

$$Re = \frac{r\omega}{\nu} \sqrt{\frac{\nu}{\omega}} = r \sqrt{\frac{\omega}{\nu}}. \quad (2.1)$$

Here,  $r$  is the local radius,  $\omega$  is the angular velocity,  $\nu$  is the kinematic viscosity, and  $\sqrt{\nu/\omega}$  is the characteristic length scale.

The critical flow parameter refers to the parameter value beyond which the perturbations start growing in an unstable flow. Various experiments on a rotating disk have observed that the spiral vortices grow beyond the critical Reynolds number  $Re > 290\text{--}294$  (Lingwood, 1995). Furthermore, the rotating-disk-boundary-layer becomes absolutely unstable at  $Re > 510$  (Lingwood, 1996). This suggests that, beyond this Reynolds number, the laminar flow cannot be maintained regardless of any care taken to reduce the perturbations in the environment.

### 2.3.2. ROTATING CONES IN STILL FLUID

Since a disk is nothing but a cone with half angle  $\psi = 90^\circ$ , the boundary-layer instability mechanism on rotating broad-cones ( $30^\circ \lesssim \psi < 90^\circ$ ) is similar to that on a rotating disk (see figure 2.7c). In still fluid, the cross-flow instability on rotating broad-cones induces co-rotating spiral vortices (Garrett et al., 2009; Kato, Alfredsson, et al., 2019; Kato, Kawata, et al., 2019; Kobayashi & Izumi, 1983; Y. P. Kohama, 2000; Towers & Garrett, 2012; Towers et al., 2016; Towers & Garrett, 2016; Towers, 2013), see figure 2.8 for example.

When the half-cone angle  $\psi$  is decreased from  $90^\circ$  to  $15^\circ$ , the wave angle  $\epsilon$  (between the vortex and circumferential directions) decreases from  $14^\circ$  to  $0^\circ$  (Kobayashi & Izumi, 1983; Kobayashi, 1994), see figure 2.9a. This implies that, as the cone becomes slender, the spiral vortices increasingly align towards the local circumferential direction. Additionally, the azimuthal number of vortices decreases with the decreasing half-cone angle, see figure 2.9b. This suggests that the larger azimuthal wavelengths (inversely proportional to the azimuthal number) can grow as the cone becomes slender.

### CHANGE IN THE INSTABILITY MECHANISM

In figure 2.9a, the vortex angle  $\epsilon$  steeply drops within  $\psi \approx 40^\circ - 30^\circ$ . Here, the instability mechanism changes from the cross-flow to the centrifugal type (Kobayashi & Izumi, 1983). For the slender-cones, effect of the centripetal acceleration is stronger, as they are closer to a cylinder than a disk. This results in toroidal vortices (with  $\epsilon \approx 0$ ) on a rotating slender-cone ( $\psi < 30^\circ$ ). These vortices are counter-rotating in the cross-section, similar to those observed in concentric cylinders (Drazin, 2002; Taylor, 1923), concave walls (Görtler, 1954), and rotating cylinders in cross-flow (Mittal, 2004; Radi et al., 2013; Rao, Leontini, et al., 2013).

The exact range of half-cone angles where this change in instability mechanism occurs has not yet been identified. For further discussions, the cones with  $\psi \gtrsim 30^\circ$  are considered

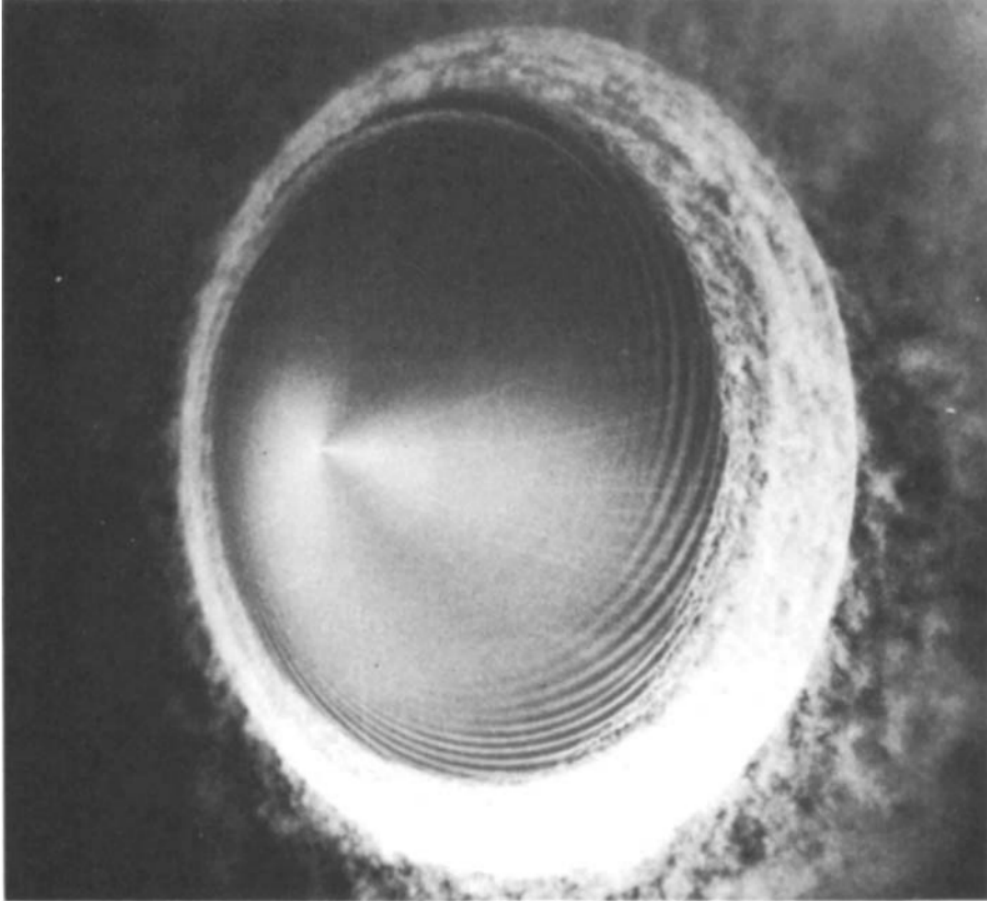


Figure 2.8: Spiral vortices on a broad-cone, with half-angle  $\psi = 60^\circ$ , rotating in still fluid as photographed by Kobayashi and Izumi, 1983.

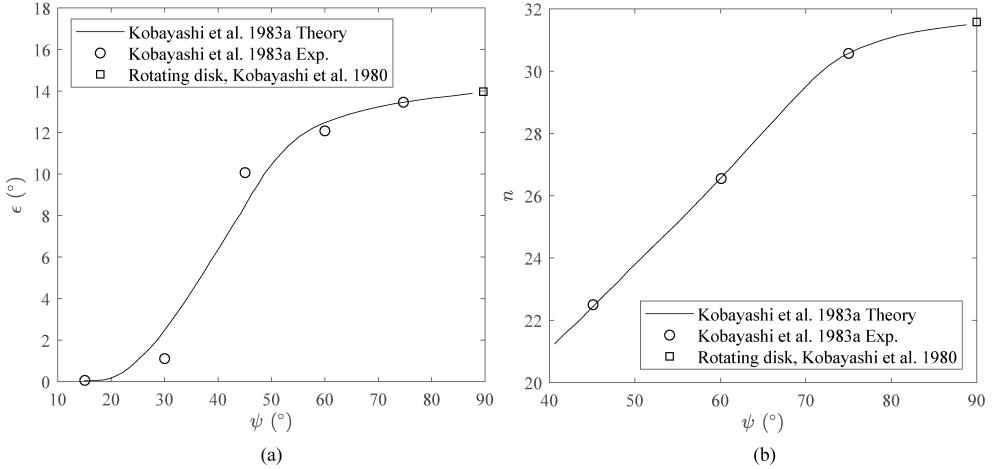


Figure 2.9: Effect of the half-cone angle  $\psi$  on the spiral vortex (a) angle  $\epsilon$  and (b) number  $n$ , as reported by Kobayashi and Izumi, 1983; Kobayashi et al., 1980.

as broad-cones, which are closer to the rotating disk. The cones with  $\psi < 30^\circ$  are considered as slender-cones, which are closer to the case of rotating cylinder.

### CRITICAL FLOW PARAMETERS

Kobayashi and Izumi, 1983 measured the near-wall velocity fluctuations on cones that are rotating in still fluid, using a hot-wire anemometer. They defined the critical point  $x_c$  as the near-most location towards the cone-apex where the hot-wire anemometer detected fluctuations at a single frequency, indicating the existence of spiral vortices. Furthermore, the point where the fluctuation spectrum became wide, resembling a typical turbulent spectrum, was defined as the transition point  $x_t$ . Here,  $x$  is the meridional distance from the cone-apex.

Figure 2.10 shows Reynolds numbers  $Re_x$  corresponding to the critical and transition points versus the half-cone angles, as measured by Kobayashi and Izumi, 1983. Here,  $Re_x = \omega x^2 \sin(\psi) / \nu$ . Both critical and transition Reynolds numbers decrease with the decreasing half-cone angle. This suggests that the slender-cones are more destabilising for the boundary-layer than the broad-cones.

### 2.3.3. ROTATING CONES IN AXIAL INFLOW

When an axial inflow is enforced on rotating cones, both cross-flow and centrifugal instabilities induce spiral vortices that are co- and counter-rotating, respectively. However, only the centrifugal instability on a rotating slender-cone with the half-cone angle  $\psi = 15^\circ$  has extensively been investigated in the literature (Kobayashi et al., 1983; Y. Kohama, 1984a).

#### SLENDER-CONE

Y. Kohama, 1984a closely studied the behaviour, growth, and breakdown of the spiral vortices on a  $15^\circ$  slender-cone rotating in axial inflow. To visualise the spiral vortices, he put the titanium tetrachloride particles on a cone surface which would be carried by the spiral vortices. He imaged these particles using a drum camera with a stroboscope illumination.

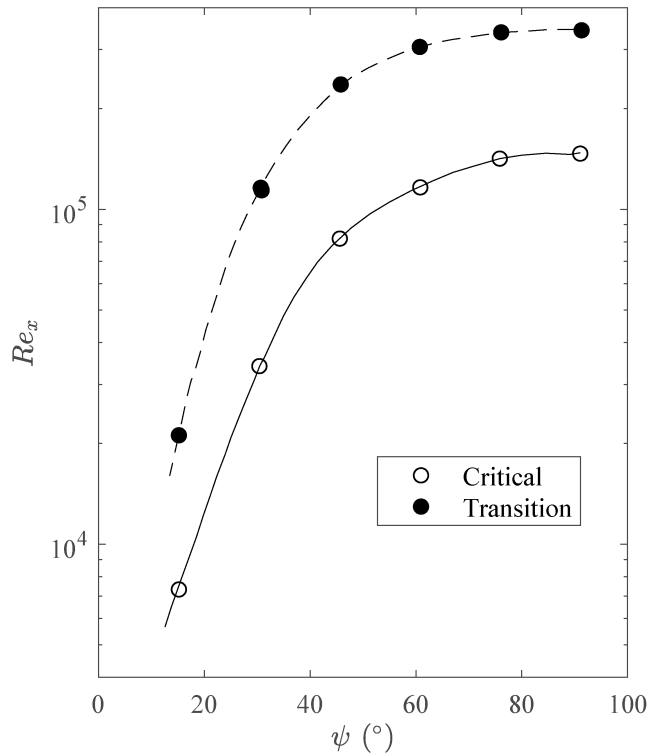


Figure 2.10: Critical and transition Reynolds number for different half-cone angles, as measured by Kobayashi and Izumi, 1983. The transition Reynolds number corresponds to a location on the rotating cone where the hot-wire signal started to resemble a typical turbulent spectrum.

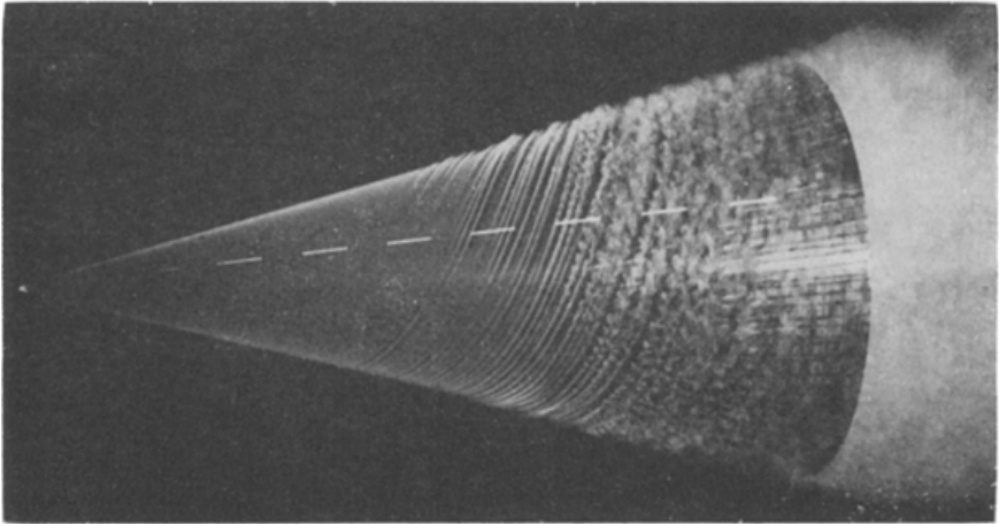


Figure 2.11: Spiral vortices on a rotating slender-cone with  $\psi = 15^\circ$  in axial inflow. The visualisation by Y. Kohama, 1984a.

See his visualisation in figure 2.11. Additionally, figure 2.12 shows a schematic adaption of a spiral vortex, visualised using this method. Figure 2.12 also shows how the vortex height  $h$  was measured from the visualisations. However, his hot-wire measurements showed that the sinusoidal velocity fluctuations corresponding to the spiral vortices were detected at a wall-normal distance larger than  $h$ . Therefore, the actual spatial extent of the vortices is larger than visualised by the particle-based visualisations in figures 2.11 and 2.12.

While tracking the growth of the spiral vortices, Y. Kohama, 1984a observed that past the critical point, the wall-normal height of the spiral vortices increases (figure 2.13). The spiral vortices cause increased stream-wise momentum near the cone-surface, evident from comparing regimes [A] and [B] in figure 2.13. In the present work, this phenomenon is found to be responsible for the increased surface temperature fluctuations on the rotating cone (see figure 4.6). In this region, the mixing of low and high momentum fluid is enhanced, forming shear layers of different scales. Y. Kohama, 1984a suggested that this enhanced activity of mixing affects the mean velocity profiles and could be the leading cause of boundary-layer transitioning to a fully turbulent state. This is interesting for the present dissertation because such modification of the basic flow changes the boundary-layer skewness. This is expected to influence the hub-flow loss mechanisms in a fan or compressor, as discussed in section 1.1.

Recently, Hussain et al., 2016 revisited the rotating  $15^\circ$  slender-cone in axial inflow. They developed a distinct theoretical analyses based on the centrifugal instability mode. They highlighted that even though cross-flow and Tollmien-Schlichting instabilities are present in the flow field, the centrifugal instability is prevalent. Garrett et al., 2009; Garrett and Peake, 2007a also state that for a rotating slender-cone (half angle  $\psi < 40^\circ$ ), the cross-flow and absolute instabilities may not play a dominant role in the boundary-layer transition.

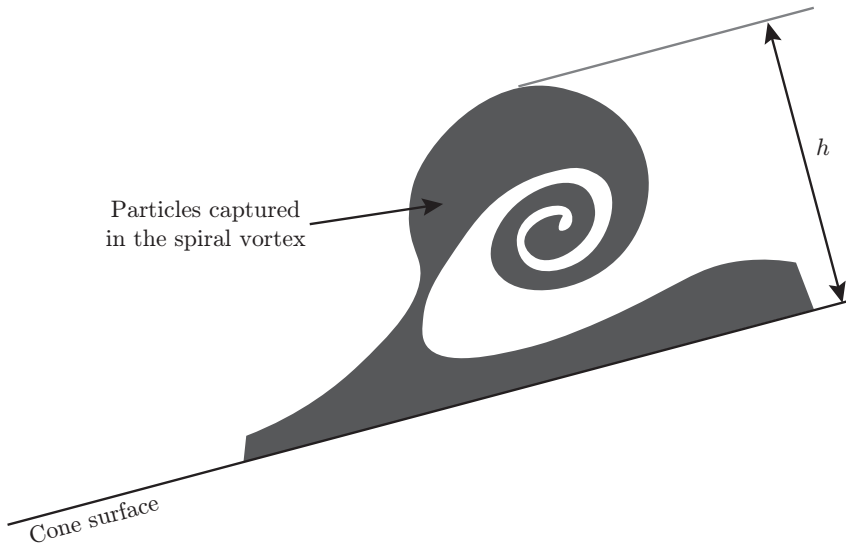


Figure 2.12: A schematic adaption of a spiral vortex visualised by Y. Kohama, 1984a using particle-based visualisation method.

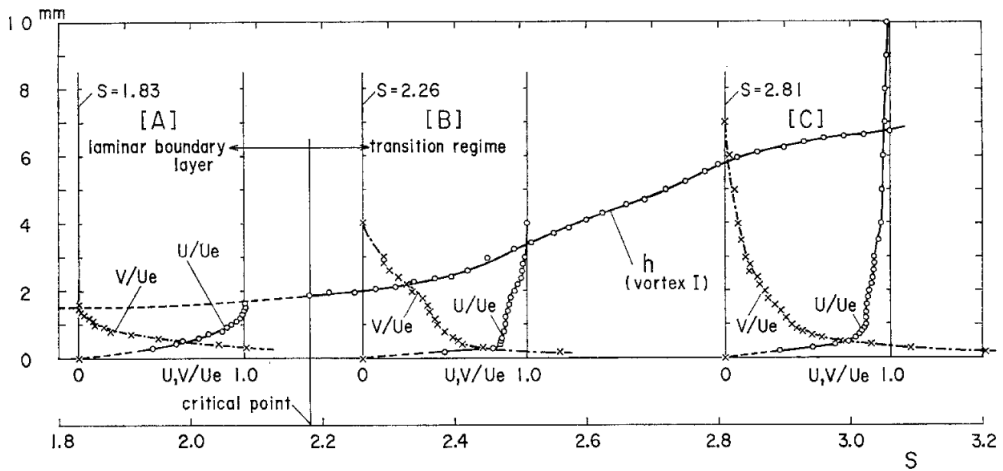


Figure 2.13: Tangential  $V$  and wall-parallel  $U$  velocity profiles during the spiral vortex growth on a rotating slender-cone ( $\psi = 15^\circ$ ) in axial inflow, taken from Y. Kohama, 1984a.

### BROAD-CONES

Theoretical studies performed by Garrett et al., 2010 show that the cross-flow instability mode is dominant on rotating broad-cones (half angle  $\psi > 40^\circ$ ) in axial inflow. As discussed in section 2.3.2, in still fluid, the cross-flow instability on the rotating broad-cones induces co-rotating vortices (Kobayashi & Izumi, 1983)—there has been no such experimental study on broad-cones rotating in axial inflow. However, Kobayashi et al., 1987 observed both co- and counter-rotating vortices on a  $30^\circ$  cone rotating in axial inflow. They suggested that the transition from the counter-rotating to the co-rotating vortices may be continuous with the continuously increasing half-cone angle  $\psi$ . However, in the present author's opinion, this type of speculation is not well-supported by the experimental data of (Kobayashi et al., 1987), as their experiments considered discrete cone angles. Furthermore, as shown later in chapter 5, the spiral vortices on broad-cones ( $\psi = 45^\circ$ – $50^\circ$ ) start as co-rotating vortices but turn into counter-rotating pairs upon their amplification.

### CRITICAL FLOW PARAMETERS

In axial inflow, the onset of instability on rotating cones depends on two parameters, Reynolds number  $Re_l$  and rotational speed ratio  $S$ , as discussed in section 1.2. This applies to both centrifugal and cross-flow instabilities on rotating slender- and broad-cones, respectively (Garrett et al., 2010; Hussain et al., 2016; Kobayashi et al., 1983). Additionally, Garrett et al., 2010 also showed that the absolute instability on rotating broad-cones also depends on the parameters  $Re_l$  and  $S$ . However, for fixed  $S$ , the absolute instability occurs at much higher Reynolds number  $Re_l$  as compared to the convective instability.

Kobayashi et al., 1983 quantified the spiral vortex growth and transition location on a rotating slender cone of  $\psi = 15^\circ$  (figure 2.14). Here, the Reynolds number  $Re_x = Re_l$ , based on the meridional distance  $x = l$ , measured from the cone apex. The free-stream turbulence intensity  $u'_{RMS}$  was low: 0.05-0.15% of the free-stream velocity  $U_\infty$ . Here,  $u'$  is the longitudinal velocity fluctuations. The effect of free-stream turbulence on the critical flow parameters is discussed in 2.3.4.

Apart from the critical and transition points, Kobayashi et al., 1983 also predict the locations where the spiral vortex amplification is maximum. The corresponding Reynolds number is called as maximum amplification Reynolds number  $Re_{x,m}$ . However, they did not provide the experimental measurements of  $Re_{x,m}$  vs  $S$ . These measurements are provided in chapter 4 of this dissertation.

Figure 2.14 shows the region contained within the critical and transition lines as the transition region where the instability induced spiral vortices grow. On a cone, both  $Re_x$  and  $S$  are zero at the cone-apex and start increasing along with  $x$ . At a location on the cone, the parameter values cross the critical line. Hereafter, the spiral vortices can be expected to grow until their maximum amplification. Subsequently, the boundary layer becomes turbulent past the transition line.

The azimuthal number  $n$  and angle  $\epsilon$  depend on the local rotational speed ratio  $S$ , see figures 2.15 and 2.16 for a rotating slender cone  $\psi = 15^\circ$ , respectively. With increasing local rotational speed ratio  $S$  (from  $S = 0$  to 5-6), both  $n$  and  $\epsilon$  decrease as the spiral structure of the vortices starts to approach a toroidal structure. Between  $S \approx 6$  to 8, the vortex structure becomes toroidal, similar to that observed over a rotating cone in still fluid (Kobayashi & Kohama, 1985).

Kobayashi et al., 1987 show that changing the half-cone angle does not change the spiral vortex angle  $\epsilon$ . However, the azimuthal vortex number  $n$  is sensitive to the changes in half-

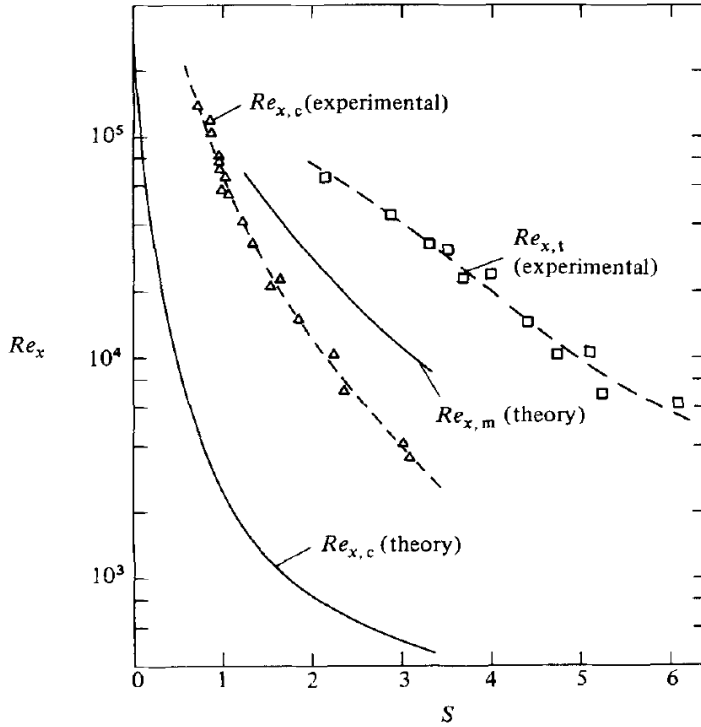


Figure 2.14: Critical  $Re_{x,c}$ , maximum amplification  $Re_{x,m}$  and transition  $Re_{x,t}$  points in the parameter space of Reynolds number  $Re_x = Re_l$  vs  $S$  for a rotating slender cone  $\psi = 15^\circ$ , taken from Kobayashi et al., 1983.

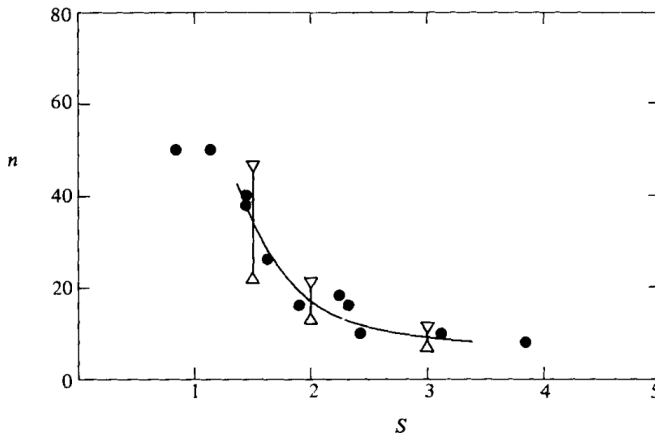


Figure 2.15: Azimuthal number of vortices  $n$  versus the rotational speed ratio  $S$  on a rotating slender cone  $\psi = 15^\circ$ , taken from Kobayashi et al., 1983. • measurements from the visualisations, and theoretical predictions at the  $\Delta$  critical and  $\nabla$  maximum-amplification point.

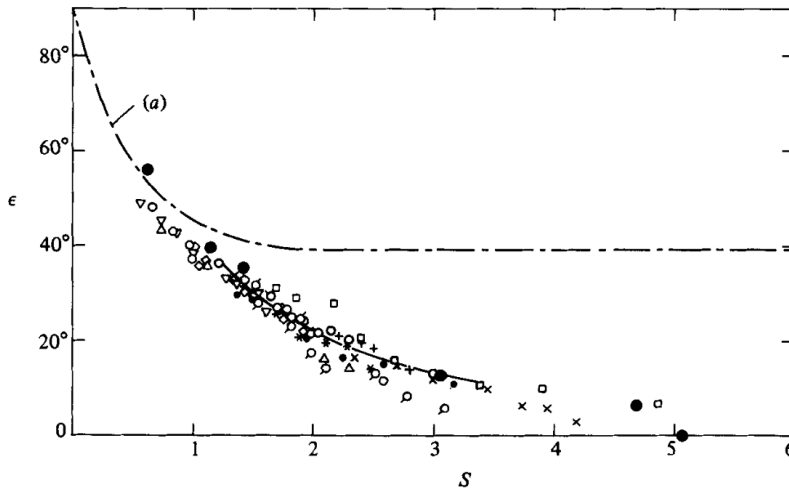


Figure 2.16: Spiral vortex angle  $\epsilon$  versus the rotational speed ratio  $S$  on a rotating slender cone  $\psi = 15^\circ$ , taken from Kobayashi et al., 1983. • are hot-wire measurements, all other symbols are measurements from the visualisations; curve (a) is the predicted wall-shear-stress direction of the laminar boundary-layer.

cone angle. The value of  $n$  decreases with decreasing half-cone angle, suggesting that the slender-cones allow larger azimuthal wavelengths to grow. Similar behaviour was seen in figure 2.9b on cones rotating in still fluid.

#### 2.3.4. EFFECT OF FREE-STREAM TURBULENCE

Generally, the onset of instability-induced flow-structures is significantly dependent on the disturbances in the flow environment, including the free-stream turbulence. Kobayashi et al., 1987 imposed inflow conditions with different turbulence intensity  $u'/U_\infty = 0.04\% - 3.5\%$  on rotating cones of  $\psi = 7.5^\circ, 15^\circ$  and  $30^\circ$ . Here,  $u'$  is the velocity fluctuation over the mean free-stream velocity  $U_\infty$ .

For slender cones ( $\psi = 7.5^\circ$  and  $15^\circ$ ), the critical Reynolds number was not affected by the free-stream turbulence levels of 0.5% and 2.4%, but decreased for the turbulence levels of 2.8% and 3.5%. On a broad cone ( $\psi = 30^\circ$ ), the critical Reynolds number decreased with the increasing free-stream turbulence levels. These differences indicate different receptivity behaviour for different types of cones, which needs further investigations. However, in all the investigated cases, the transition Reynolds number remained unaffected by the free-stream turbulence levels.

#### 2.3.5. EFFECT OF SURFACE ROUGHNESS

Generally, the surface roughness and irregularities also constitute a part of the disturbance environment, which can influence the perturbation growth. Wilkinson and Malik, 1985 observed that the spiral vortices on a rotating disk are induced at a randomly situated dust particles on a rotating disk. In their experiment the spiral vortices were completely established around the rotating disk at the Reynolds number  $Re \approx 350$ .

Wilkinson and Malik, 1985 further observed that an isolated roughness element on a

rotating disk induces wave-packets which grow and exhibit spiral vortices spread over the entire disk-surface. This occurs at Reynolds number  $Re \approx 400$  unlike at  $Re \approx 350$  on a clean disk.

Recently, several theoretical studies have shown that both isotropic and anisotropic roughness elements (combinations of radial and concentric grooves) delay the onset of cross-flow instability on a rotating disk (Alveroglu, 2016; Alveroglu et al., 2016; Cooper et al., 2015; Garrett et al., 2016; Thomas et al., 2020). To theoretically model the roughness, these studies chose two approaches: 1) a partial slip on the wall or 2) a wavy surface. The link between these two roughness models and the real life roughness remains to be investigated. Both theoretical and experimental investigations are needed to understand the instability behaviour on the rough cones.

The roughness elements trigger the spiral modes that are stationary with respect to the rotating body. Recently, Kato, Alfredsson, et al., 2019; Kato, Kawata, et al., 2019 induced stationary spiral vortices on a rotating cone of  $\psi = 60^\circ$  in still fluid. They used 24 equi-spaced roughness elements on a cone because the similar clean cone shows around 20 – 26 vortices. No such investigation is available on the rotating cones facing an inflow. This still remains as an open question.

## 2.4. EXPERIMENTAL AND DATA PROCESSING TECHNIQUES

Past experiments relied on particle-based flow-visualisation methods where particles sprayed on the cone surface get transferred by the spiral vortices, allowing their visualisation. This method is not suitable in high-speed inflows and does not provide any quantification on the spiral vortex growth. To quantify the critical parameters of the spiral vortex growth, these past studies used the hot-wire velocimetry. This technique does not provide any instantaneous visualisation of spiral vortices. Furthermore, the method is challenging to implement in a high-speed flow environment, and its time-consuming nature limits the range of a parametric study. Therefore, as also highlighted in section 1.2, a new experimental approach is required to explore the boundary-layer instability behaviour on rotating cones in complex flow scenarios, i.e. asymmetric and high-speed turbulent inflows.

To fulfill this requirement, this dissertation presents an experimental method which can be used to investigate coherent spiral vortices on rotating cones (chapter 3). This method relies on infrared thermography (IRT) approached with proper orthogonal decomposition (POD) to visualise spiral vortices and quantify their growth. The method is accompanied by particle image velocimetry (PIV) to obtain the velocity fields. Following are the basics of these experimental (IRT and PIV) and data processing (POD) techniques.

### 2.4.1. INFRARED THERMOGRAPHY

Surface temperature measurements often provide insights into complex flow phenomena, e.g. boundary-layer transition. The flow structures usually leave their thermal footprints on a near-by solid surface as they locally affect the surface-heat-transfer. These surface-temperature-patterns can be measured with an infrared camera in a non-intrusive way. This section presents the theory behind the infrared thermography (IRT), as the experimental method presented in this dissertation (chapter 3) predominantly relies on IRT. This section is based on the discussions found in Astarita and Carlomagno, 2013; Mayer, 2000; Schrijer, 2010.

### RADIATION THEORY

The radiative transfer of energy occurs in the form of electromagnetic waves. The spectrum of these waves is divided in several wavelength ( $\lambda$ ) bands, e.g.  $\lambda = 0.38\text{--}0.7\ \mu\text{m}$  is visible light,  $\lambda = 0.7\text{--}1000\ \mu\text{m}$  is infrared, and  $\lambda > 1000\ \mu\text{m}$  is radio band. The infrared band is most commonly used for thermography. Most infrared cameras use  $\lambda = 3\text{--}5\ \mu\text{m}$  of the middle wavelength infrared band (MWIR) and  $\lambda = 8\text{--}12\ \mu\text{m}$  of the long wavelength infrared band (LWIR) (Astarita & Carlomagno, 2013). The following radiation theory clarifies the link between the measured radiation energy and the surface temperature of a body.

When considered as particles, the electromagnetic radiations are photons carrying the energy  $\mathcal{E}$ , which is inversely proportional to their wavelength  $\lambda$  as

$$\mathcal{E} = \frac{\hbar c}{\lambda}. \quad (2.2)$$

Here, the Planck's constant  $\hbar = 6.626 \times 10^{-34}$  Js and  $c$  is the speed of the electromagnetic radiation in a medium.

Every material body absorbs, emits, transmits, and reflects these electromagnetic radiations. However, an ideal body, named black body, absorbs all the incident radiations, irrespective of their incidence angles and wavelengths. For simplicity, the radiation theory starts with a case of an isothermal black body placed in the vacuum. The total power  $E_b$  emitted by a black body is directly proportional to the 4th power of its surface temperature  $\mathcal{T}$ . This relation is known as the Stefan-Boltzmann law:

$$E_b = \int E_{b,\lambda}(\lambda, \mathcal{T}) d\lambda = \sigma_{\text{sb}} \mathcal{T}^4. \quad (2.3)$$

Here, the Stefan-Boltzmann constant  $\sigma_{\text{sb}} = 5.67 \times 10^{-8}$  W/(m<sup>2</sup>K).

The spectral distribution of the radiatively emitted power also depends on the surface temperature  $\mathcal{T}$  of the body. For a black body, the emitted power flux per unit wavelength  $E_{b,\lambda}$ , i.e. spectral hemispherical emissive power (Astarita & Carlomagno, 2013), is related to the surface temperature by the well-known Planck's law:

$$E_{b,\lambda} = \frac{C_1}{\lambda^5 (e^{\frac{C_2}{\lambda \mathcal{T}}} - 1)}. \quad (2.4)$$

Here,  $C_1 = 3.742 \times 10^8$  W/ $\mu\text{m}^4/\text{m}^2$  and  $C_2 = 1.439 \times 10^4$  K $\mu\text{m}$ . Figure 2.17 depicts the Planck's law. With increasing surface temperature, the maximum power is emitted at lower wavelengths, i.e. peak of  $E_{b,\lambda}$  shifts towards the left. Figure 2.17 shows that, at room temperatures, the most-energetic emitted-radiations lie in the infrared band, especially in LWIR.

Scaling the Planck's law by the fifth power of the temperature  $\mathcal{T}^5$  yields:

$$\frac{E_{b,\lambda}}{\mathcal{T}^5} = \frac{C_1}{(\lambda \mathcal{T})^5 (e^{\frac{C_2}{\lambda \mathcal{T}}} - 1)}. \quad (2.5)$$

The scaled emissive power  $E_{b,\lambda}/\mathcal{T}^5$  is a function of  $\lambda \mathcal{T}$ , as depicted in figure 2.18; the single maximum of this curve suggests that the wavelength  $\lambda_{\text{max}}$  at which the maximum power is emitted is related to the surface temperature. The relation is known as the Wien's displacement law:

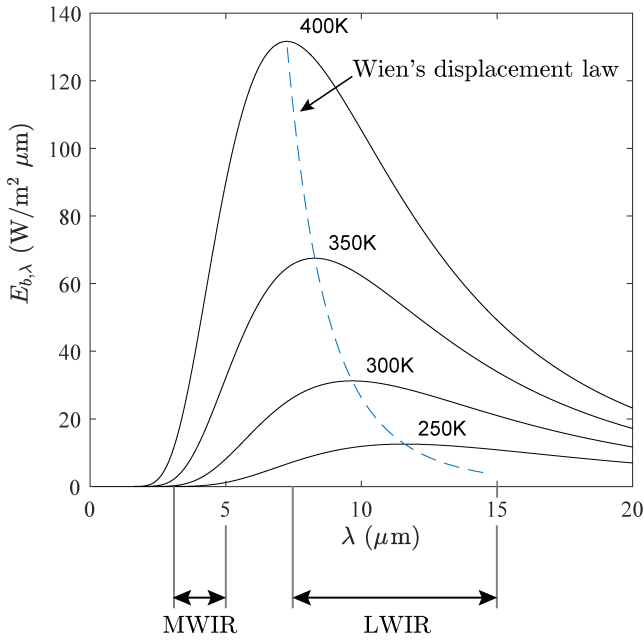


Figure 2.17: Variation of spectral hemispherical emissive power  $E_{b,\lambda}$  with the radiation wavelength  $\lambda$  from an isothermal blackbody for different surface temperatures.

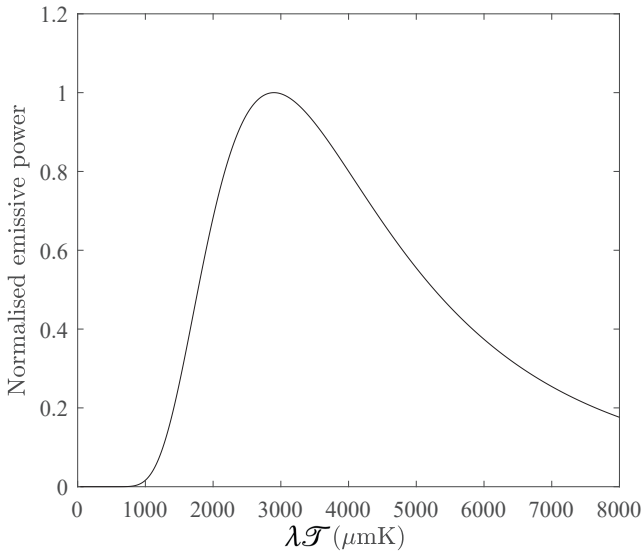


Figure 2.18: Normalised emissive power  $E_{b,\lambda}/T^5$  versus  $\lambda T$ .

$$\lambda_{max}\mathcal{T} = 2898 \text{ K}\mu\text{m}. \quad (2.6)$$

Infrared cameras measure the radiated energy in a fixed wavelength band  $\lambda_1$ – $\lambda_2$ . Such measurements yield the band emissive power as

$$E_{b,\lambda_1-\lambda_2}(\mathcal{T}) = \int_{\lambda_1}^{\lambda_2} E_{b,\lambda}(\lambda, \mathcal{T}) d\lambda. \quad (2.7)$$

For a fixed wavelength band, the band emissive power increases with increasing the surface temperature. This is evident from the Planck's law and Wien's displacement law, see figure 2.17. Therefore, measured radiated energy in a fixed wavelength band can be related to the surface temperature of the black body. Practically, such relation is obtained by calibrating an infrared camera exposed to a black body simulator, simulating various temperatures.

In the present work, the band emissive power is recorded by an infrared camera (described in section 2.4.1) for a fixed duration  $t_{int}$ , called integration time. The present work focuses on detecting the fluctuation patterns of the surface temperature, arising due to the spiral vortices on rotating cones (the method is described in chapter 3). Therefore, the absolute temperature values are not required. The time-integrated band emissive power, representing temperature, is recorded as the digital pixel intensity  $I$ .

Real bodies, unlike black bodies, do not absorb all the incident radiations as part of it is reflected and/or transmitted; the absorption depends on the radiation wavelength and incidence angles. When their absorption is independent of the incident-radiation wavelength, the real bodies are called grey bodies. Real bodies usually behave as grey bodies in the wavelength bands used for the infrared thermography (MWIR, LWIR, etc.).

According to the Kirchoff's law the absorbed radiation power equals the emitted radiation power. The ratio of the power emitted by the real bodies ( $E_r$ ) to that by the black body ( $E_b$ ) at the same temperature is known as the emissivity  $\epsilon_{rad}$

$$\epsilon_{rad} = \frac{E_r}{E_b}. \quad (2.8)$$

The emissivity depends on the viewing angle with respect to the radiating surface. Therefore, as described later (section 3.2), the recorded surface temperature levels (in terms of  $I$ ) vary on a three-dimensional surface of the cone as the viewing angle varies along the circumference. Additionally, the surface treatments, such as coating, finish, may affect the emissivity value. For further readings on the real body radiations and corrections, one can refer to Astarita and Carlomagno, 2013; Mayer, 2000; Schrijer, 2010.

### INFRARED CAMERA

Nowadays, the infrared cameras are composed of an optical system, sensor array and cooling system. The camera gathers radiations using the optical lenses made out of special materials, e.g. Germanium; because commonly used glass lenses are opaque to the infrared radiations. The current work uses a camera named FLIR CEDIP SC7300L Titanium (figure 2.19).

The gathered radiation is focused on a Focal Plane Array (FPA), where the temperature detectors are arranged (similar to the pixels in a camera sensor). Generally, two types of temperature detectors are used: a thermal detector that transduces the temperature change caused by the incident radiation and a photon detector which detects the incident photons.



Figure 2.19: Infrared camera used in this work FLIR CEDIP SC7300L Titanium (image source: FLIR).

The current work uses the photon detector made out of Mercury Cadmium Telluride (MCT). At low temperatures (77–170K), the electrons in photon detectors mostly lie in a valence band. When a photon strikes the detector, it imparts its energy to the electron. This electron jumps to a higher energy level in a conductive band, inducing a photocurrent. By construction, the photon detector can be made sensitive to a narrow wavelength band. The sensor used in the current work is sensitive to  $\lambda = 7.7\mu\text{m} - 9.3\mu\text{m}$ .

The operating temperatures of the photon detectors are extremely low: 77K for LWIR. A dedicated Sterling cooler brings the MCT sensor to its operating temperature. In this condition, the camera noise is at its lowest; with the Noise Equivalent Temperature Difference (NETD) of around 25mK.

#### MATERIAL CHOICES FOR IRT ON ROTATING BODIES

The material choice significantly affects the effectiveness of infrared thermography in measuring unsteady phenomena, such as the boundary-layer transition on rotating bodies. In incompressible low-speed flows, the thermal footprints of the flow structures are usually weak; resulting in sharp temperature gradients with low temperature magnitudes. The Fourier's law of heat conduction states:

$$\mathbf{q} = -\kappa \nabla \mathcal{T}. \quad (2.9)$$

Here, the  $\mathbf{q}$  is the heat flux and  $\kappa$  is the thermal conductivity of the material. For a windtunnel model with high thermal conductivity  $\kappa$ , a sharp temperature gradient will result into high heat flux. A weak thermal footprint of a sharp flow feature will cause high heat conduction within the model and the footprint will quickly disappear before being detected by an infrared camera. Therefore, the low thermal conductivity is desired when measuring complex unsteady flow patterns.

Additionally, the thermal contrast of a footprint depends on the local surface temperature difference caused by the energy transfer to/from the fluid. The energy transferred as heat  $Q$  per unit volume  $\mathcal{V}$  is related to the temperature difference through the material density  $\rho$  and specific heat capacity  $\mathcal{C}$ :

$$Q/\mathcal{V} = \rho\mathcal{C}\Delta\mathcal{T}. \quad (2.10)$$

For a fixed amount of heat transferred by a flow structure, a material with low  $\rho\mathcal{C}$  will host a high surface temperature difference, improving the thermal contrast of the measurement.

In general, the windtunnel model is best suitable for measuring the thermal footprints of unsteady flow structures, when it has low thermal conductivity  $\kappa$  and low volumetric heat capacity  $\rho\mathcal{C}$ , i.e. low thermal product  $\rho\mathcal{C}\kappa$ . Table 2.1 compares the material properties of Aluminium and Polyoxymethylene (POM). Clearly, the thermal product of the POM is three orders of magnitude lower than that of the Aluminium. Therefore, POM is a better choice for the infrared thermography than commonly used aluminium; and most of the windtunnel models in this work are made out of POM.

Material	Density $\rho$ (kg/m <sup>3</sup> )	Thermal conductivity $\kappa$ (W/mK)	Heat capacity $\mathcal{C}$ (J/kgK)	Thermal product $\rho\mathcal{C}\kappa$ (J <sup>2</sup> /m <sup>4</sup> K <sup>2</sup> s)
Aluminium	2700	205	921.096	$5 \times 10^8$
Polyoxymethylene	1420	0.22	1500	$4.68 \times 10^5$

Table 2.1: Comparison of the material properties of Aluminium and Polyoxymethylene. The low thermal product ( $\rho\mathcal{C}\kappa$ ) of Polyoxymethylene makes it a suitable candidate for the present infrared thermography measurements.

#### 2.4.2. PARTICLE IMAGE VELOCIMETRY

Particle image velocimetry (PIV) is an effective non-intrusive tool, which is commonly used for the velocity field measurements. Figure 2.20 depicts a typical PIV setup. Here, the flow is seeded with the tracer particles that closely follow the flow. The test region is illuminated with the laser sheet and the particle images are recorded using a camera. The recorded images are post-processed to obtain the velocity field through the particle-displacement and known time-interval between the two images.

In this work, the particle recordings are obtained as sets of image-pairs obtained within short time intervals  $\Delta t \approx 1\text{--}100\mu\text{s}$ , also called as the pulse separation. The images are then divided into interrogation windows. The cross-correlations with two dimensional shifts are performed to find the particle movement within the interrogation window. A multi-pass approach with decreasing size of the overlapping interrogation windows is used so that the large particle shifts are not missed while resolving the small-scale velocities. All these operations are performed in a commercial software DaVis 8.4.0.

This work uses two types of PIV approaches: two component (2C) PIV and three component (3C) stereo PIV. 2C PIV is a straight forward method of measuring the velocity components within the laser sheet plane. This is achieved by aligning the image plane parallel to the laser sheet and performing a two dimensional geometric calibration.

3C stereo PIV uses two cameras viewing the common region of the laser sheet from two different viewing angles (figure 2.21). Here, the viewing directions  $A$ ,  $B$ , and a coordinate vector  $x$  are assumed to be co-planar, for simplicity. The views are geometrically calibrated with a three-dimensional calibration plate to obtain the viewing angles  $\alpha_A$ ,  $\alpha_B$  and the geometrical scaling. The velocity fields are separately calculated in each image plane as  $u_A$ ,  $v_A$  and  $u_B$ ,  $v_B$ . These fields, along with the geometric calibration, can be used to reconstruct

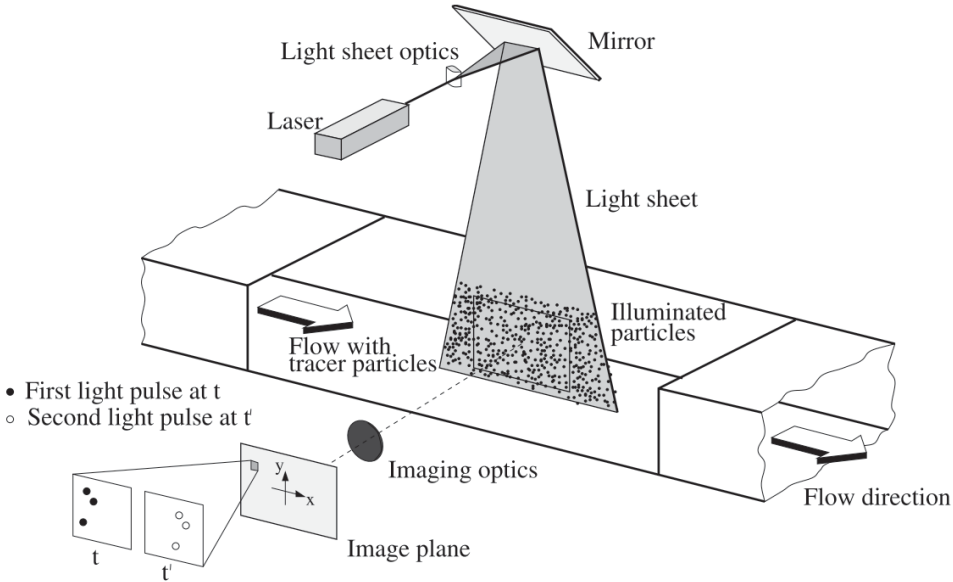


Figure 2.20: Experimental setup of PIV (Raffel et al., 2007).

the real velocity components  $u$ ,  $v$ ,  $w$  in the laser sheet by triangulation. See Raffel et al., 2007 for further details.

### 2.4.3. PROPER ORTHOGONAL DECOMPOSITION

Studying boundary-layer instability and transition essentially involves identifying coherent flow structures in the measurement data (as described in section 2.2). The present work uses a mathematical tool named Proper Orthogonal Decomposition (POD) that allows decomposing a dataset into orthonormal bases, also known as POD modes (chapter 3). Owing to their orthonormality, selected POD modes can be used to reconstruct different low-dimensional representations of the data instances.

The POD was first introduced by Kosambi, 1943 who extended the statistics of random variables to curves. Later, POD was independently developed by many researchers including Berkooz et al., 1993; Lumley, 1967. In different fields, POD is known by various other names, such as, Principal Component Analysis, Empirical Orthogonal Functions, and Karhunen-Loève Expansion. In fluid mechanics, POD is commonly used to identify coherent structures and dominant fluctuation modes in complex flows, such as, transitional or separated flows.

The basic idea of POD is to find a set of orthonormal bases in a multidimensional data, such that, the cumulative distance of the data points to the bases is minimum. In 2D, this is analogous to fitting a line (representing one of the two bases) through a point cloud using the least squares fit. In this sense, the linear combination of POD modes facilitates the closest possible approximation of the data. For example, consider a signal  $u(x, t)$  as a discretised measurement (or numerical simulation) data of a field in space  $x$  and time  $t$ . Then, using POD, it is possible to find the orthonormal spatial modes  $\phi(x)$  along with the time coefficients  $\mathcal{A}(t)$  as:

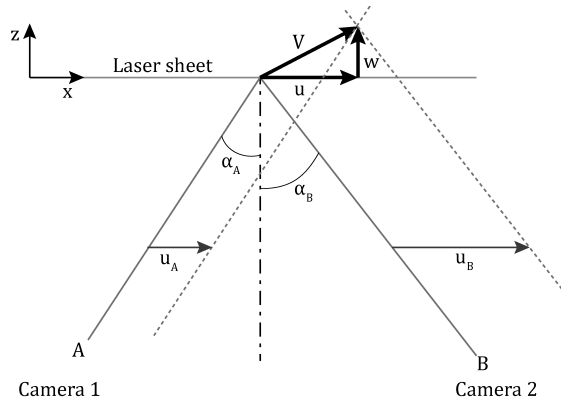


Figure 2.21: Concept of the stereo PIV.

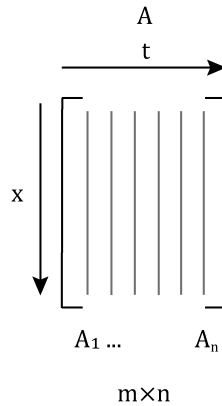


Figure 2.22: Arrangement of a data matrix.

$$u(x, t) = \sum \mathcal{A}(t)\phi(x), \quad (2.11)$$

such that, the projection of the signal on the orthonormal spatial modes is maximum i.e.  $\sum_{k=1}^n \sum_{i=1}^n \langle u_i, \phi_k \rangle$  is maximum. Here,  $\langle, \rangle$  is the inner product. This is analogous to the least-square linear fit through a two dimensional point cloud. Similarly, one can also find the temporal modes  $\phi(t)$  along with the spatial coefficient  $\mathcal{A}(x)$ ; but in practice, such analysis is meaningful only when the temporal resolution is sufficient to capture the phenomenon of interest.

In the present work, the experimental data is available as spatially discretised sets at different time instances. Such dataset is arranged in the matrix  $A(x, t)$  of size  $m \times n$  whose each column is a spatially distributed data at a given time instance; here, the data has  $m$  spatial measurement points (pixels or interrogation windows) and  $n$  time instances with  $m \gg n$ . Figure 2.22 depicts the organisation of the data matrix  $A(x, t)$ .

The POD modes of the data matrix  $A$  can be found using the Singular Value Decompo-

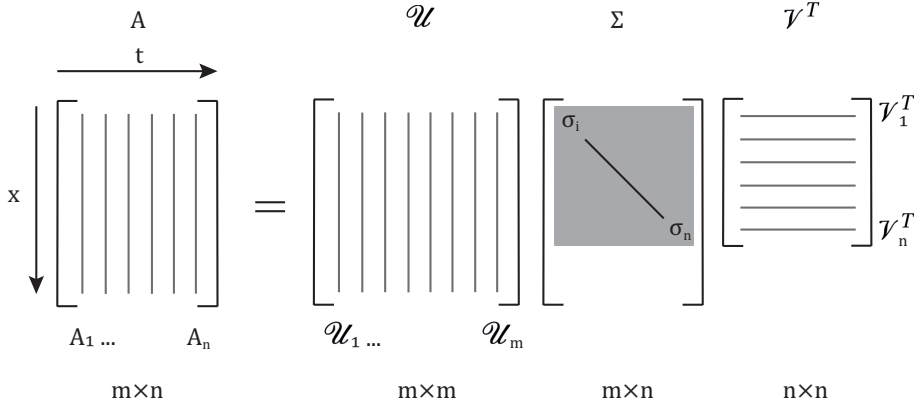


Figure 2.23: Singular value decomposition of a snapshot matrix  $A$ .

sition (SVD). The present work uses a MATLAB function *svds* to compute the SVD. Every rectangular matrix has a Singular Value Decomposition as given by the equation 2.12, which is depicted in the figure 2.23.

$$A = \mathcal{U} \Sigma \mathcal{V}^T \quad (2.12)$$

Here,  $\mathcal{U}$  of size  $m \times m$  and  $\mathcal{V}$  of size  $n \times n$  are unitary matrices, i.e.  $\mathcal{U}^T \mathcal{U} = \mathcal{I}$  and  $\mathcal{V}^T \mathcal{V} = \mathcal{I}$ , where  $\mathcal{I}$  is an identity matrix. Commonly, the columns of  $\mathcal{U}$  and  $\mathcal{V}$  are called left and right singular vectors, respectively. The singular vectors are orthonormal. The  $\Sigma$  is a  $m \times n$  diagonal matrix; its diagonal elements are called singular values which are arranged in a descending order. The singular values represent the relative importance of the singular vectors in the dataset. In the present work, a singular value is regarded as the representative of the fluctuating energy captured in a POD mode. The revised criterion for mode selection uses these singular values to identify the relative importance of a mode in a dataset (discussed in chapter 3).

Physically, the left singular vectors  $\mathcal{U}_i$  are the orthonormal bases for the fluctuations along the columns of  $A$ , and right singular vectors  $\mathcal{V}_i$  represent the dynamics of elements in  $\mathcal{U}_i$  along the rows. In this case, the left singular vectors  $\mathcal{U}_i$  are the spatial modes and the right singular vectors  $\mathcal{V}_i$  represent the time dynamics of  $\mathcal{U}_i$ . The singular values  $\sigma_i$  scale the modes as per their relative importance in the data matrix  $A$ .

The role of singular vectors  $\mathcal{U}_i$  as the spatial POD modes is best seen through a correlation matrix  $AA^T$ . The entries of  $AA^T$  are the correlations between the columns of  $A$  which represent the spatial variation. Using equation 2.12

$$AA^T = \mathcal{U} \Sigma \mathcal{V}^T \mathcal{V} \Sigma^T \mathcal{U}^T = \mathcal{U} \Sigma \Sigma^T \mathcal{U}^T. \quad (2.13)$$

Here,  $\mathcal{V}^T \mathcal{V} = \mathcal{I}$ . The equation 2.13 can also be written as:

$$AA^T \mathcal{U} = \mathcal{U} \Sigma \Sigma^T. \quad (2.14)$$

This is the familiar form of eigendecomposition. Here,  $\mathcal{U}$  contains the eigenvectors of the correlation matrix  $AA^T$  and the  $\Sigma \Sigma^T$  contains the eigenvalues. Therefore, the left singular

vectors  $\mathcal{U}_i$  represent the spatial dynamics in  $A$ . Similarly, one can show that the right singular vectors  $\mathcal{V}_i$  are the eigenvalues of  $A^T A$ , representing the temporal dynamics in this case.

A low-dimensional representation  $\tilde{A}_k$  of a data instance  $A_k$ , can be obtained by the linear combination of the selected  $r$  left singular vectors  $\mathcal{U}_i$  which are the spatial POD modes.

$$\tilde{A}_k = \sum_{i \in r} \mathcal{A}_{i,k} \mathcal{U}_i \quad (2.15)$$

Here, the time coefficient  $\mathcal{A}_{i,k}$  is a projection of the  $i^{th}$  mode on the  $k^{th}$  data instance, i.e.  $\mathcal{A}_{i,k} = \langle A_k, \mathcal{U}_i \rangle$ .

# 3

## AN EXPERIMENTAL METHOD TO INVESTIGATE COHERENT SPIRAL VORTICES ON ROTATING BODIES

### 3.1. INTRODUCTION

WHEN investigating coherent flow structures, flow visualisation is an essential part to understand the underlying physical phenomena. Chapter 1 briefly introduced the requirement of a new experimental approach to detect the coherent flow structures on a rotating body in complex flow environments such as non-axial inflow and high-speed inflow. Along with the visualisations, quantification of spatial properties such as: vortex angle, wavenumber and the location of pairing or amplification are essential for the understanding and theoretical analysis. Experimental techniques which can provide such information have evolved over the years but their applicability to rotating bodies is limited. For example, oil flow visualisation, which is often used to identify flow features such as separation, reattachment, boundary layer transition and the presence of stationary vortices, is not suitable for the rotating case due to the strong centrifugal forces. In the past, flow visualisation was performed based on kerosene smoke filaments (Mueller et al., 1981) or titanium-tetrachloride (Kobayashi et al., 1983) to identify spiral vortices in the transition region over rotating cones. However, smoke flow visualisation works best only at low freestream velocities and low turbulence levels ( $\approx 0.1\%$ ). On the other hand, titanium-tetrachloride is very toxic and requires a highly controlled environment to avoid health issues. In addition, researchers have used hot-wire anemometry to quantify the spiral vortex characteristics and location of the transition region. However, such methods are intrusive in nature and time consuming, which makes them less attractive for parametric studies. These experimental difficulties call for an alternative approach to enable in-depth study of the flow field over rotating bodies of revolution.

A rotating slender cone (half-cone angle  $\psi = 15^\circ$ ) under uniform axial inflow is chosen as a test case since it is well documented in the literature (Kobayashi et al., 1983; Y. Kohama,

---

Parts of this chapter have been published in *Experiments in Fluids*, **60**, 115 (2019) Tambe et al., 2019.

1984b). As detailed in chapter 2, the boundary layer transition mechanism over the rotating cone includes spiral vortices that are induced by the effect of a centrifugal instability. For a fixed cone shape, the characteristics of these spiral vortices (angle, pitch) depend on the local rotational speed ratio  $S = \omega r / u_e$  and local Reynolds number  $Re_l = l u_e / \nu$  (Garrett et al., 2010; Kobayashi, 1994), where  $\omega$  is the angular velocity,  $r$  is the local radius,  $u_e$  is the edge velocity of the boundary layer,  $l$  is the distance from the cone apex along the meridian and  $\nu$  is kinematic viscosity of air. A brief overview of the flow field is given in section 3.3.

Infrared Thermography (IRT) is a non-intrusive technique which can be used to measure surface temperature distribution, as described in section 2.4.1. The overall complexity of the setup and data post-processing is relatively low, which makes it attractive for the parametric studies that span a large number of experimental conditions. IRT has been previously applied to study stationary co-rotating spiral vortices on a rotating disk (Astarita et al., 2002). Limited by the recording frequency due to the scanning mechanism of the camera, the authors used a line scan method to acquire and later reconstruct the time-averaged imprint of spiral vortices. This approach was feasible because the vortices were stationary with respect to the rotating disk. Nowadays, IR cameras use Focal Plane Arrays (FPA) which can record at higher frequencies and more importantly no longer require the scanning system. This allows using IR cameras for measuring high-speed events where the temporal averaging is only limited by the selected integration time. For example in the current application, the vortices are not always stationary but can move along with the flow. Since the signal to noise ratio drops with decreasing integration time and high-speed events typically are less strong, the resulting measurements contain higher noise which degrades the measurement quality.

Recent investigations show that the potential of IRT can be dramatically enhanced by filtering the measurement datasets using Proper Orthogonal Decomposition (POD). For example, Narayanan, 2007 applied this methodology to study the modes of temperature fluctuations of slot jet impingement by filtering IRT data with first 15 POD modes. However, this criterion of modes selection is arbitrary. While it includes the dominant modes, it does not guarantee the reconstruction of the flow structures of interest. Raiola et al., 2017 developed the POD filter for time-resolved IRT measurements of turbulent convective heat transfer. They also proposed a criterion for selecting the optimal number of modes for the low order reconstruction with reduced random noise. However, this criterion does not consider the physical relevance of the modes, and therefore, is not suitable for the reconstruction of the coherent flow structures of interest (as shown in 3.4.3). In the method presented in this chapter, IRT is applied to measure the traces of spiral vortices on a rotating cone and the data is analysed with POD approach. A new criterion is formulated to select the POD modes based on their physical relevance to the flow feature of interest. The resulting reconstructions reveal the detailed spiral vortex footprints with reduced camera noise.

## 3.2. EXPERIMENTAL SETUP

Experiments are performed in the W- tunnel at the Faculty of Aerospace Engineering, TU Delft which is an open jet wind tunnel with an exit cross-section of  $0.6\text{m} \times 0.6\text{m}$ . Figure 3.1 shows the experimental setup. The model consists of a cone with an half-cone angle  $\psi = 15^\circ$  and base diameter  $D = 0.047\text{m}$ . It was connected to a motor in a cylindrical casing mounted on a sting. The cone was rotated by a brushless motor at a constant RPM= 5000. The inflow speed  $U_\infty$  was varied from 2.46 – 12.3 m/s in order to obtain different values of the base rotational speed ratio  $S_b = \omega D / (2U_\infty)$  (5 to 1 respectively, to compare results with

those of Kobayashi et al., 1983). The inflow Reynolds number is defined as  $Re_L = U_\infty L/\nu$  (varied from  $1.5 \times 10^4 - 4.5 \times 10^4$ ). Additional tests are also performed at 15000 RPM to assess the effect of surface rotation during the integration time. The characteristics of the spiral vortices strongly depends on the local value of  $S$  which varies along the cone from zero at the nose to  $\omega D/(2u_e)$  at the base. In the experiments the value of  $S_b$  and  $Re_L$  are used to refer to the operating conditions.

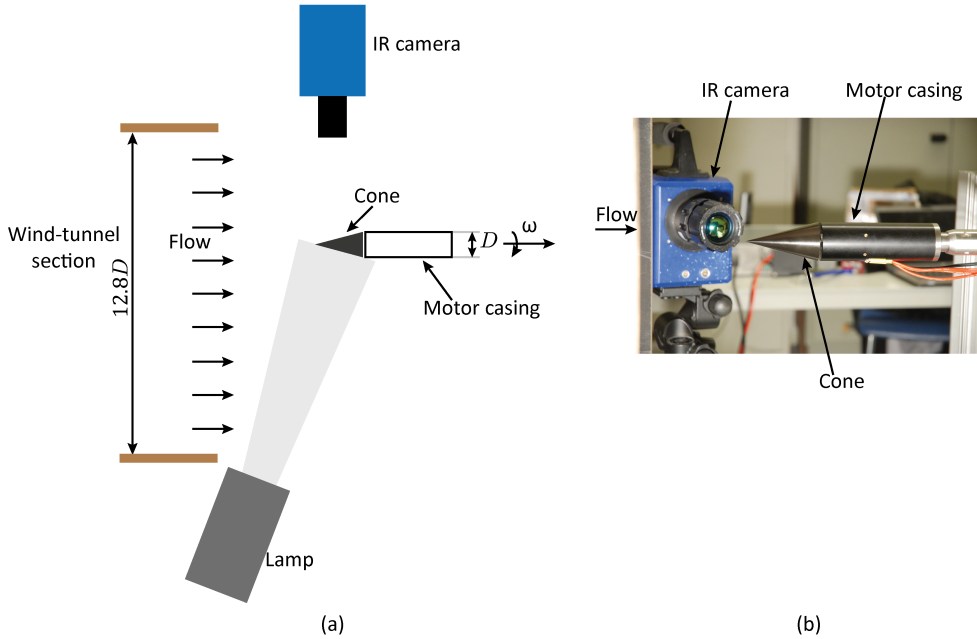


Figure 3.1: (a) A schematic of the experimental setup and (b) a photograph showing the rotating cone setup and an infrared camera.

An Infrared camera FLIR (CEDIP) SC7300 Titanium is used to measure the surface temperature. As the focus of the present study is on the spatial organization of the coherent vortices, the temperature data is processed in the units of digital pixel intensity  $I$  (as described in section 2.4.1). The camera has a  $320 \times 256$  pixel MCT sensor having a nominal Noise Equivalent Temperature Difference (NETD)  $< 25\text{mK}$ . The spatial resolution for the measurements is  $0.28 \text{ mm/px}$ . An integration time of  $t_{int} = 205\mu\text{s}$  is used and 2000 images are acquired at 200 Hz. To improve the thermal contrast, the model was radiatively heated using a white light from a 575W theatre lamp, that is focused on the model.

Considering that the emissivity of the surface is highest in the direction normal to it, the camera (sensor plane) could be placed parallel to the cone meridian. However, this results in a strong reflection of the camera from the model surface (Narcissus effect) and thus reduces the quality of results. The camera placement was adjusted so that the reflections from the model were minimized and the background noise from the light/heat source could be avoided. A schematic of the test setup is shown in the figure 3.1. Once the lamp is switched on, the surface of the rotating model facing the lamp is irradiated and gets heated up. The surface that is not irradiated by the lamp is observed by the IR camera.

The wind tunnel models are made from Polyoxymethylene (POM) which has favourable thermal properties, as discussed in section 2.4.1 (thermal conductivity  $\kappa = 0.22$  W/mK, density  $\rho = 1420$  kg/m<sup>3</sup>, specific heat capacity  $\mathcal{C} = 1500$  J/kgK). Effect of directional emissivity on the observed digital intensity has been estimated by tracking intensity along the cone radius in the average image taken over a dataset. Since the cone surface is three dimensional, the viewing angle varies (with respect to the surface normal vector) from 15° at the axis and 90° at the outermost radial location. It has been observed that within  $R = 0 - 0.9R$ , the intensity gradually drops by 10% (background is subtracted). But from  $0.9R-R$  it steeply drops to the background intensity. This region corresponds to the viewing angles beyond 65.23°. It should be noted that, the main interests in the present investigation are the fluctuations over the time-average for each pixel instead of the absolute magnitude.

It was observed that the overall surface temperature levels are not constant during the measurements because the flow continuously cools down the model. Over the dataset, this difference has been in the order of 5% of the mean intensity levels above the background. This trend is monotonic and has been removed by subtracting a moving average with a kernel size of 20 instances. The resulting temperature fluctuations over the cone surface correspond to the effect of vortices and their magnitude is lower than 1.3 K. Further, the IR measurement data is analysed using Proper Orthogonal Decomposition (POD), which decomposes the data set as a linear combination of spatial modes with time dependent coefficients. A detailed mathematical formulation of POD can be found in section 2.4.3.

Additionally, time-resolved stereo Particle Image Velocimetry (PIV) was used in the symmetry plane using 2 high-speed cameras (Photron Fastcam SA-1) to verify the results from IRT. The PIV cameras have a 12 bit CMOS sensor with  $1024 \times 1024$  pixels. SAFEX smoke particles with diameter  $\approx 1\mu\text{m}$  are used as tracer particles. A Nd:YAG Continuum MESA PIV 532-120-M high speed double pulsed laser is used to illuminate particles. The data is acquired at 2.5 kHz. The cameras were equipped with Nikkor  $f = 200\text{mm}$  and Teleplus 2x lenses resulting in an equivalent focal length of 400mm. The field of view is  $14\text{mm} \times 14\text{mm}$  and the spatial resolution 0.0136 mm/px. The data is processed using Lavision DAVIS 8.40 with a  $48 \times 48$  pixels final window size and 75% overlap, resulting in a vector pitch of 0.16mm. The edge velocity of the boundary layer is obtained from the potential solution found in the study by Garrett and Peake, 2007a as  $u_e(x) = Cx^m$ . Here,  $C$  and  $m$  are obtained by fitting this relation to the PIV data, which results in  $C = 1.84U_\infty$  and  $m = 0.23$ .

### 3.3. SPATIAL CHARACTERISTICS OF THE SPIRAL VORTICES

Before discussing the data processing procedure, it is important to introduce the flow field at a conceptual level. As described in chapter 2, the previous studies of Kobayashi et al., 1983 found that the spiral vortices on a rotating cone appear in the form of counter-rotating vortex pairs. It has been observed in the present study that their foot-print on the surface temperature appears in the form of alternating dark and bright fringes, corresponding to low and high relative temperatures respectively (see figures 3.2 and 3.8). These temperature variations are caused by the up- and downwash created by the vortices which means that there is one vortex pair in between two consecutive bright (or dark) fringes.

Figure 3.2 also shows the definitions of the spiral vortex characteristics such as the components of the wavelength ( $\lambda_l, \lambda_\theta$ ), the number of spiral vortices along the circumference ( $n$ ) and spiral vortex angle ( $\epsilon$ ). The wavelength  $\lambda_l$  can be associated to a wave travelling along the cone meridian in the stream-wise direction. It is defined as the distance between

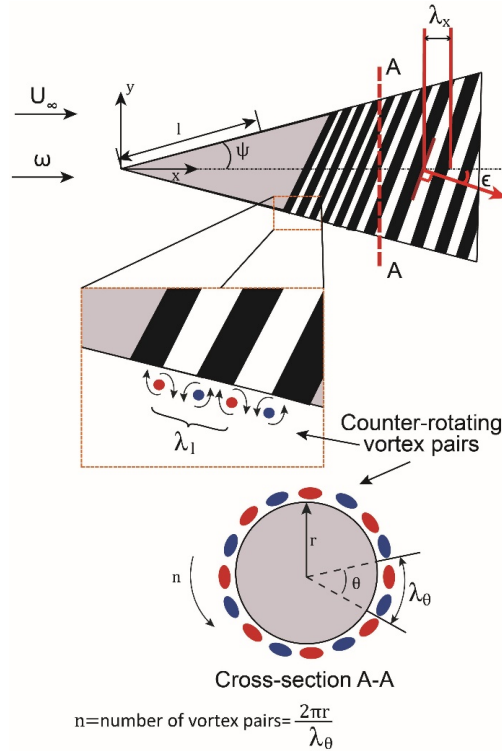


Figure 3.2: Schematic representation of the flow field depicting typical footprints of the spiral vortices on the surface temperature along with the definitions of wavelength components ( $\lambda_l, \lambda_x, \lambda_\theta$ ), number of spiral vortices ( $n$ ) and spiral vortex angle ( $\epsilon$ ). Effects of the surface curvature on the fringes is not shown for simplicity.

two consecutive vortex pairs along the meridian, which is equal to the distance between their consecutive bright (or dark) surface footprints. The wavelength,  $\lambda_\theta$ , is the wavelength along the azimuthal direction. However, in the experiments, we observe the two dimensional projection of a three dimensional cone surface. Therefore, the direct estimation of  $\lambda_l$  and  $\lambda_\theta$  is not possible. The projection of  $\lambda_l$  on to the  $xy$  plane is measured from a two dimensional image as  $\lambda_x$  where  $\lambda_x = \lambda_l \cos(\psi)$ . Whereas,  $\lambda_\theta$  is represented in terms of the number of spiral vortices along the circumference:  $n = 2\pi r / \lambda_\theta$ , where,  $r$  is the local radius. The spiral vortex angle ( $\epsilon$ ) is defined as the angle between the vector perpendicular to the spiral vortex filament and the meridional plane.

### 3.4. DATA PROCESSING PROCEDURE

While the raw IRT data shows traces of the spiral vortices, it also contains footprints of the large scale modulations of these vortices. This includes effects caused by changing vortex states or amplification. This makes it difficult to visualize the underlying structure of the spiral vortices. Additionally, due to the lower integration time and low levels of temperature fluctuations, the measurements also contain noise. These problems are tackled by following a two-step procedure to reconstruct the individual snapshots by a limited selection of the

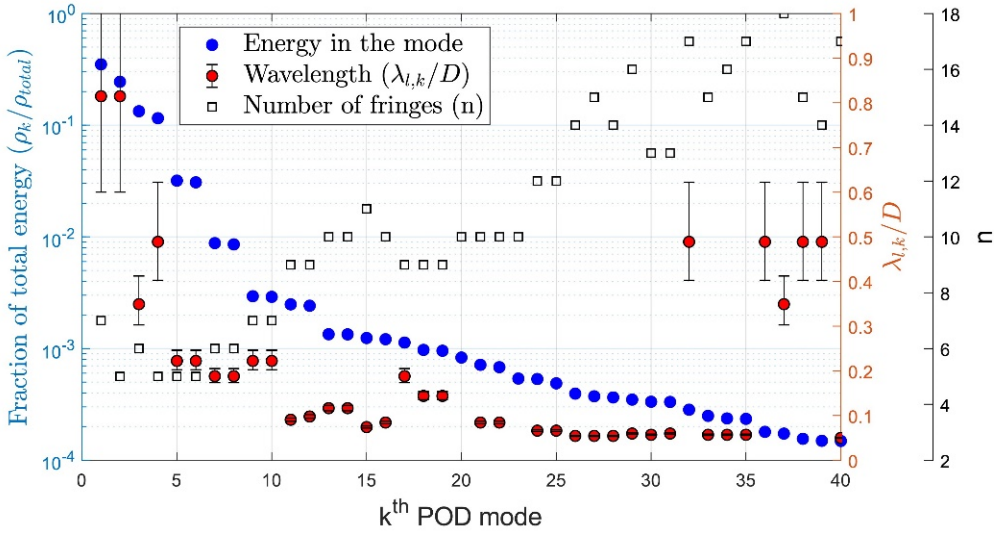


Figure 3.3: Distribution of energy captured in each POD mode compared with the corresponding wavelength ( $\lambda_{l,k}$ ) and the observed number of fringes ( $n$ ) ( $S_b = 5$ ,  $Re_L = 1.5 \times 10^4$ ,  $S = 0 - 4.71$ ,  $Re_I = 0 - 1.58 \times 10^4$ )

POD modes.

At a first step, spatial POD modes, up to a selected mode number, are used to obtain a low order reconstruction with reduced noise (see section 3.4.2). In a second step, the POD modes representing the effects of the large scale modulations are further excluded in the reconstruction to obtain the structure of the coherent spiral vortices (see section 3.4.3). The selection criteria are detailed in sections 3.4.2 and 3.4.3. The spatial POD modes are obtained using a singular value decomposition applied to the empirical correlation matrix of the dataset. The resulting spatial modes are ordered according to the energy content ( $\rho$ ) (in terms of temperature fluctuations) where the strongest modes appear first. Additionally, in the present case, it is also important to obtain the spatial characteristics (similar to  $\lambda_l$ ,  $n$ ) of each POD mode to comprehend the type of spatial periodicity that is captured in it. The detailed discussion on the characteristics of POD modes is presented in the following section 3.4.1.

### 3.4.1. SPATIAL CHARACTERISTICS OF THE POD MODES

The characteristics of a POD mode are captured energy, wavelength, and number of fringes along the circumference. These characteristics are used to comprehend the type of phenomena that it represents. These characteristics are then used while defining selection criteria for the low order reconstruction (see sections 3.4.2 and 3.4.33).

Figure 3.3 shows the energy  $\rho_k/\rho_{total}$  as a fraction of the total energy captured for each POD mode  $k$ . For each corresponding mode, the typical wavelength  $\lambda_{l,k}$  is determined along the meridian of the cone using  $\lambda_{x,k}$  that is calculated by applying a 2D Fourier transform ( $F$ ) on the image matrix of each POD mode. Note, that the wavelength  $\lambda_{l,k}$  is a dominant wavelength in the mode and is not necessarily the wavelength of the spiral vortices ( $\lambda_l$ ) because the flow field, in addition to the spiral vortices, also contains large scale fluctuations

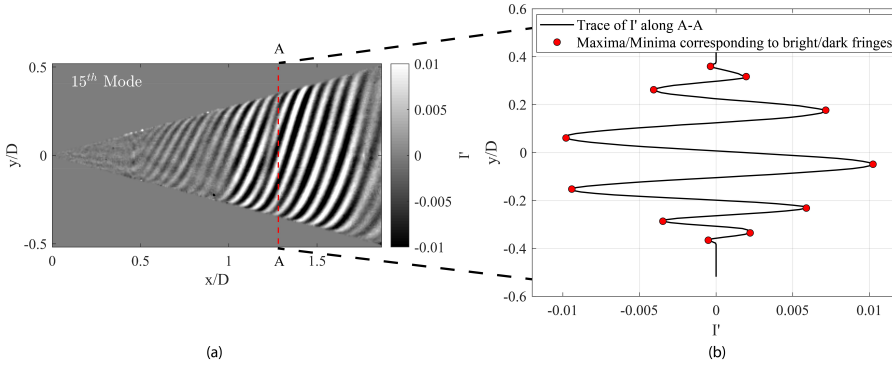


Figure 3.4: Characteristics of a POD mode a) surface temperature field, b) trace of  $I'$  along  $y$  (projected circumference) used to measure the number of fringes ( $n$ ) ( $S_b = 5$ ,  $Re_L = 1.5 \times 10^4$ ,  $S = 0 - 4.71$ ,  $Re_l = 0 - 1.58 \times 10^4$ ).

relating to the vortex strength modulation. The Fast Fourier Transform ( $F$ ) is computed in the region where the alternating fringes appear (in this case the region between  $x/D = 0.6 - 1.8$ ,  $y/D = -0.5 - 0.5$ ).

The plot of normalized Power Spectral Density ( $|F|^2/\sigma^2 M^2$ ) against the spatial frequencies  $f_x$  and  $f_y$  (along  $x$  and  $y$  directions respectively) shows peaks corresponding to the dominant wavelength in the mode (see figure 3.6). Here,  $\sigma$  is Root Mean Square (RMS) of the signal and  $M$  is the number of samples. The spectral resolution in the present case is  $\delta f_x = 0.82/D$  and  $\delta f_y = 0.96/D$ . Uncertainty in wavelength estimation due to the finite spectral resolution is shown by means of error bars in figure 3.3. In a POD mode, the wavelength of the alternating fringes varies slightly when moving from the nose to the base, in proportion to the local cone radius (as seen in figure 3.4a). Also, it can be observed in figure 3.3 that the dominant wavelength in some modes is significantly different from the neighbouring ones (e.g. modes 32, 36) and in the case of modes 20 and 23 it is out of the plot limits (larger than  $1D$ ). Upon inspection of the mode, it appears that there are multiple wavelengths present, see for example figure 3.5. Therefore, the wavelength shown in figure 3.3 by itself is not a reliable measure to determine whether the POD mode directly corresponds to the spiral vortex structure or whether it represents the modulation of the vortex strength or the interaction of vortices. Therefore, it can only be used to qualitatively relate the energy distribution to the spatial periodicity of the fluctuations. Overall, it is observed that the wavelength decreases when the mode number increases (where energy decreases).

Additionally, figure 3.3 also shows the typical number of fringe pairs (bright and dark) ( $n$ , equivalent to vortices as shown in figure 3.2) observed in the corresponding mode along the circumferential direction. As discussed before in section 3.3,  $n$  is representative of the azimuthal wavelength  $\lambda_\theta$ . As shown in figure 3.4b,  $n$  is calculated by tracking maxima/minima of  $I'$  along the  $y$  axis at every axial location. The number of fringe pairs on the back side of the cone (which is not visible) are assumed to be equal to the visible side. The maximum value of  $n$  observed in the POD mode at any axial location is assigned as a characteristic of the respective mode. In other words, it represents the minimum  $\lambda_\theta$  observed. This can be used to determine whether the mode contributes to a physical representation of the spiral vortex or not (see section 3.4.3). As  $n$  has to be an integer and the back side of the cone is not visible, the measurement uncertainty is  $\pm 1$ .

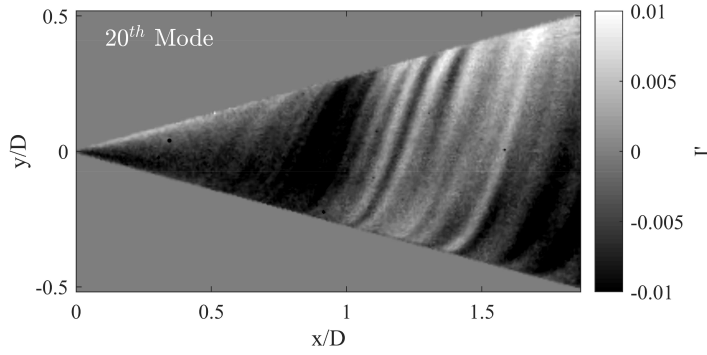


Figure 3.5: The 20<sup>th</sup> POD mode showing multiple wavelengths captured in a single mode ( $S_b = 5$ ,  $Re_L = 1.5 \times 10^4$ ,  $S = 0 - 4.71$ ,  $Re_l = 0 - 1.58 \times 10^4$ ).

### 3.4.2. NOISE REDUCTION

The raw infrared snapshot contains noise arising from the IR camera sensor. This noise persists in the pre-processed image (obtained after the moving mean subtraction), see figure 3.8. This noise is removed by reconstructing the POD modes selected using the following first criterion.

The first criterion is defined such that certain POD modes which contain high noise levels are excluded without having a loss of flow information. In the literature (Raiola et al., 2015; Raiola et al., 2017), a criterion to select the optimal number of POD modes for the reconstruction with reduced random noise has been proposed. This criterion is based on the consideration of the residual error  $\delta_{RM}(k)$  involved in the reconstruction of the measured field using the first  $k$  number of modes. The threshold is set on the relative slope of  $\delta_{RM}^2(k)$  and it has been shown that it reduces the random noise in the low order reconstruction. But the reconstruction still includes the noise due to the focal plane arrays of the Infrared Camera (Raiola et al., 2017), as the POD modes corresponding to such noise usually have higher energy compared to the modes containing the random noise. However, in the present case, the objective of the reconstruction is to obtain the specific flow feature i.e. the thermal footprints of the spiral vortices. Therefore, a different criterion is defined here that is based on the strength of these spiral vortex footprints in a POD mode relative to the measurement noise.

A 2D Fourier transform (as discussed in section 3.4.1) of each mode is used to identify the contribution of noise relative to the wavelengths of interest. For example, figure 3.6 shows the PSD distribution for 15<sup>th</sup> mode, where signal is dominant, and for 39<sup>th</sup> mode, where noise is dominant. It is evident that the 39<sup>th</sup> mode has overall low energy in the peaks as compared to the 15<sup>th</sup> mode. Furthermore, a larger fraction of its energy is distributed among higher frequencies. In the present case, the wavelengths associated with the measurement noise are estimated to be of the order of 4 pixels ( $\approx 0.024D$ ) and below. This is a choice dependent on the experimental conditions, flow structures of interest and acceptable noise levels in the reconstruction. In the present case, temperature footprints of flow structures smaller than  $0.024D$  are not expected to have a sufficient contrast with respect to the measurement noise. Therefore, the energy contained in wavelengths smaller than 4 pixels is regarded as noise ( $E_{noise}$ ). The energy distributed in the wavelengths of interest ( $0.5D > \lambda_x, \lambda_y > 4$  pixels) is

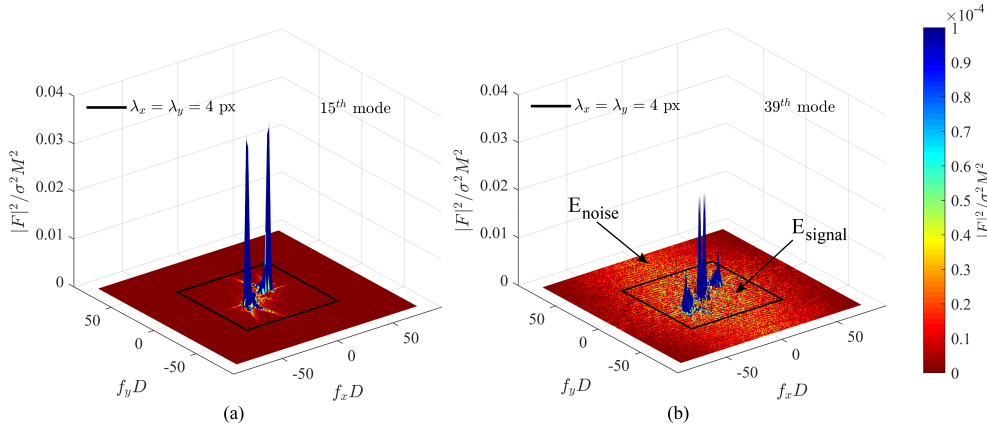


Figure 3.6: Power Spectral Density (PSD) distribution obtained from 2D Fourier transform a) 15<sup>th</sup>POD mode  $E_{signal}/E_{noise} = 66.27$ ,  $\rho_k/\rho_{Total} = 1.24 \times 10^{(-3)}$ ,  $\phi_k = 0.082$  b) 39<sup>th</sup> POD mode  $E_{signal}/E_{noise} = 3.5$ ,  $\rho_k/\rho_{Total} = 1.49 \times 10^{(-4)}$ ,  $\phi_k = 0.00052$  ( $S_B = 5$ ,  $Re_L = 1.5 \times 10^4$ ,  $S = 0 - 4.71$ ,  $Re_l = 0 - 1.58 \times 10^4$ ).

considered as the contribution to the signal ( $E_{signal}$ ). The typical energy corresponding to wavelengths  $\lambda_l$  larger than a certain wavelength  $\lambda_c$  can be obtained as:

$$E_{\lambda > \lambda_c} = \sum_{j=c}^d \sum_{i=a}^b |F_{i,j}|^2 \delta f_x \delta f_y. \quad (3.1)$$

Where  $b$  and  $a$  are indices of  $f_x D$  corresponding to  $\pm(1/\lambda_c - \delta f_x)D$ , respectively. Similarly,  $d$  and  $c$  are indices of  $f_y D$  corresponding to  $\pm(1/\lambda_c - \delta f_y)D$ , respectively.  $\lambda_c = 4px = 0.024D$  for  $E_{\lambda > 4px}$  and  $\lambda_c = 0.5D$  for  $E_{\lambda > 0.5D}$ . The energy associated with noise can be computed as:

$$E_{noise} = E_{Total} - E_{\lambda > 4px} \quad (3.2)$$

while the energy present in the signal can be obtained as:

$$E_{signal} = E_{\lambda > 4px} - E_{\lambda > 0.5D} \quad (3.3)$$

Finally the signal to noise ratio  $E_{signal}/E_{noise}$  can be considered to represent the relative strength of a signal in a mode compared to noise. Additionally, in order to account for the relative importance of each mode in the data-set, the signal to noise ratio is multiplied with the fraction of energy captured in a POD mode with respect to the total energy ( $\rho_k/\rho_{total}$ ). In this way a normalized signal strength  $\phi_k$  may be defined as:

$$\phi_k = \frac{E_{signal}}{E_{noise}} \cdot \frac{\rho_k}{\rho_{total}} \quad (3.4)$$

The order of threshold on  $\phi_k$  in the present case is obtained by defining a threshold on  $\rho_k/\rho_{Total} = 1 \times 10^{-4}$  and  $E_{signal}/E_{noise} = 10$  which results in  $\phi_k = 0.001$ . This ensures that the POD modes with  $\phi_k < 0.001$  have either low signal strength relative to noise or have overall low energy content. It signifies that their effective contribution to the reconstruction of the signal is low, and therefore, their exclusion does not affect the objective of the

reconstruction. The composition of  $\phi_\kappa$  is shown in figure 3.6 for modes above and below the defined threshold  $\phi_\kappa = 0.001$ . It can be observed that the 15<sup>th</sup> mode in figure 3.6a has a high amount of energy distributed in the signal compared to the noise ( $E_{signal}/E_{noise} = 66.27$ ) and its overall importance in the data set is  $\rho_\kappa/\rho_{Total} = 1.24 \times 10^{-3}$ . Together, the relative contribution of the mode in reconstructing the signal is  $\phi_\kappa = 0.082$ . On the other hand, the 39<sup>th</sup> mode in figure 3.6b has a lower fraction of energy distributed in the signal compared to the noise ( $E_{signal}/E_{noise} = 3.5$ ) and its relative importance in the data set is significantly low  $\rho_\kappa/\rho_{Total} = 1.49 \times 10^{-4}$ . Therefore, the relative contribution in reconstructing the signal becomes  $\phi_\kappa = 5.2 \times 10^{-4}$  which is lower by two orders of magnitude compared to that of the 15<sup>th</sup> mode.

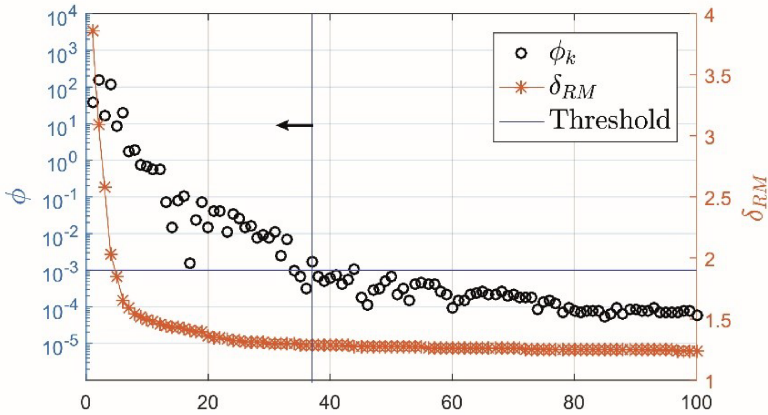
The distribution of  $\phi_\kappa$  among the modes depends on the choice of the wavelengths that are considered as a signal, which depend on the specific flow case and experimental conditions. Figure 3.7 shows the normalized signal strength ( $\phi_\kappa$ ) and the residual error of reconstruction ( $\delta_{RM}$ , represented in terms of  $I'$ ) corresponding to each mode for two different experimental conditions. In the present case, the last POD mode satisfying the criteria  $\phi_\kappa > 0.001$  is defined as the threshold  $\kappa_{thr}$  and the reconstruction is done using the POD modes from 1 to  $\kappa_{thr}$ .

Figure 3.8 shows the filtered image (reconstruction) obtained from the raw image. It can be observed that the camera noise has been effectively removed. However, the effect of large scale modulations of local vortex strength is still present in the filtered image.

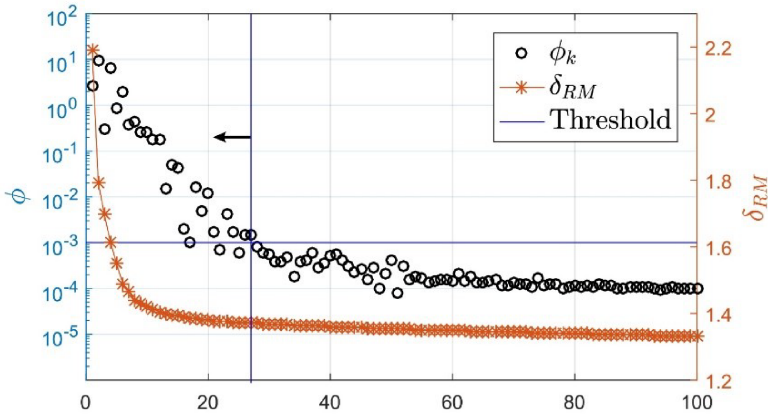
### 3.4.3. PHYSICAL ADMISSIBILITY OF POD MODES

A POD mode is considered as physically admissible for a reconstruction when the periodicity captured in the mode can be directly linked to the flow feature of interest i.e. spiral vortices in the present case. In order to select modes that are physically admissible, the second criterion is defined. This is done based on the physical characteristics of the spiral vortices. As discussed at the start of section 3.4, the POD modes (excluding those containing measurement noise) can be further classified into roughly two contributions. First is the imprint due to the presence of the coherent vortices and secondly the effects caused by the local modulation of the vortex strength.

For the present test case, previous experiments and theoretical analyses from literature show that the number of vortices  $n$  appearing in the boundary layer transition region varies with the local rotational speed ratio  $S$ . From the study by Kobayashi et al., 1983, it is found that the number of vortices around the circumference at an axial location is always greater than or equal to 8. Similar results have also been reported in the theoretical study by Garrett et al., 2010, where they performed linear stability analyses on the range of broad cones (half angles  $40^\circ < \psi < 90^\circ$ ). They observe that  $n$  decreases with increasing  $S$  but stays  $n \geq 8$  even at  $S \rightarrow \infty$ . In these cases, spiral vortices occur due to cross-flow instability, which is different from the centrifugal instability observed in the present case, but still agrees with the lower bound on  $n$ . Similarly, observed and predicted values of  $n$  for rotating spheres and disks are also greater than 8 (Kobayashi, 1994). Physically,  $n \geq 8$  implies that the  $\lambda_\theta/r \leq \pi/4$  or  $\theta \leq 45^\circ$ , where  $\theta$  is the angle subtended by the azimuthal wavelength, see figure 3.2. In other words, these observations show that the perturbations with the azimuthal wavelengths longer than  $\pi r/4$  (and  $\theta > 45^\circ$ ) usually do not grow to form the coherent spiral vortices for the typical spiral vortex angles observed in investigated cases (see figure 3.15). Also having,  $n \ll 8$  implies  $\lambda_\theta \gg \pi/4r$ , and thus depending on the vortex angles would imply much



(a)



(b)

Figure 3.7: Criteria used to define the threshold on the number of POD modes to be considered for a reconstruction a) 5000 RPM,  $\kappa_{thr} = 37$  ( $S_b = 5$ ,  $Re_L = 1.5 \times 10^4$ ,  $S = 0 - 4.71$ ,  $Re_l = 0 - 1.58 \times 10^4$ ) and (b) 15000 RPM,  $\kappa_{thr} = 27$  ( $S_b = 5$ ,  $Re_L = 4.5 \times 10^4$ ,  $S = 0 - 4.71$ ,  $Re_l = 0 - 4.7 \times 10^4$ )

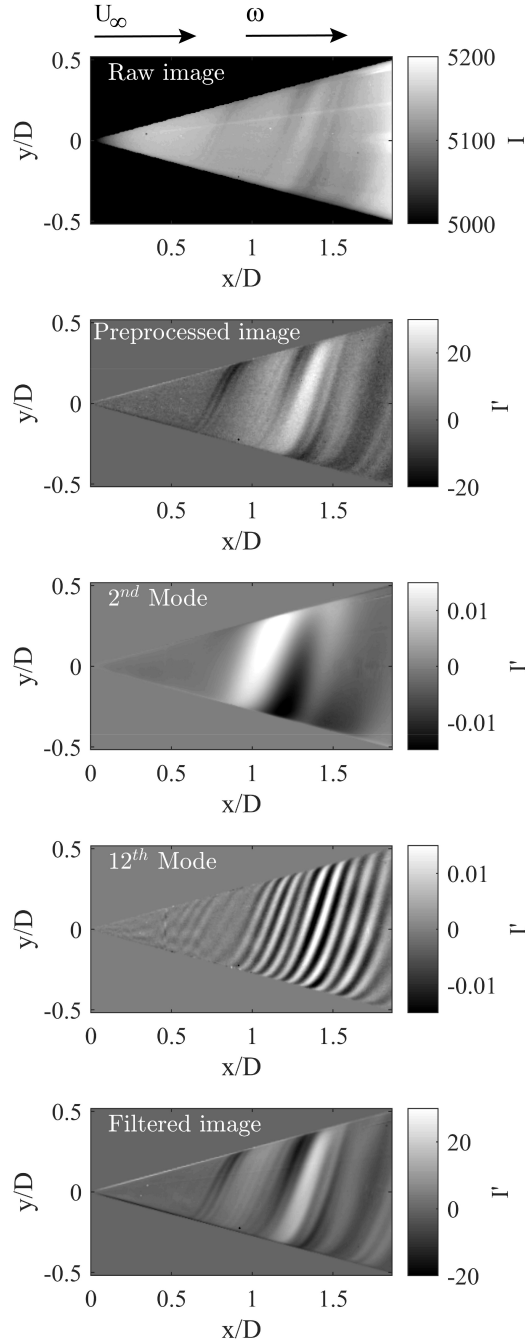


Figure 3.8: POD based reconstruction of spiral vortices from the instantaneous IR Thermography data. Flow from left to right.  $\phi_\kappa > 0.001$ ,  $\kappa_{thr} = 37$ , ( $S_b = 5$ ,  $Re_L = 1.5 \times 10^4$ ,  $S = 0 - 4.71$ ,  $Re_l = 0 - 1.58 \times 10^4$ )

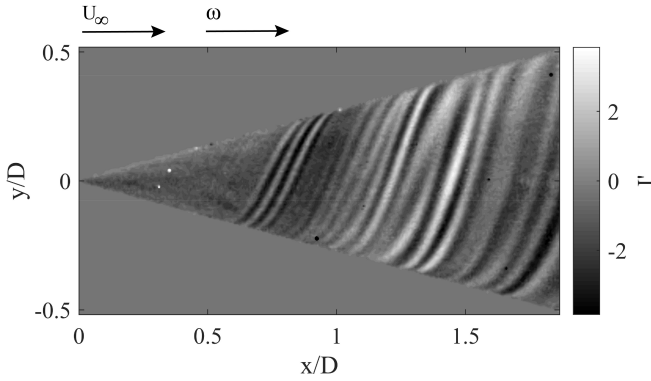


Figure 3.9: Reconstruction using the POD modes satisfying the criteria:  $\phi_\kappa > 0.001$ ,  $n \geq 8$ . Flow is from left to right,  $\kappa_{thr} = 37$  ( $S_b = 5$ ,  $Re_L = 1.5 \times 10^4$ ,  $S = 0 - 4.71$ ,  $Re_l = 0 - 1.58 \times 10^4$ ).

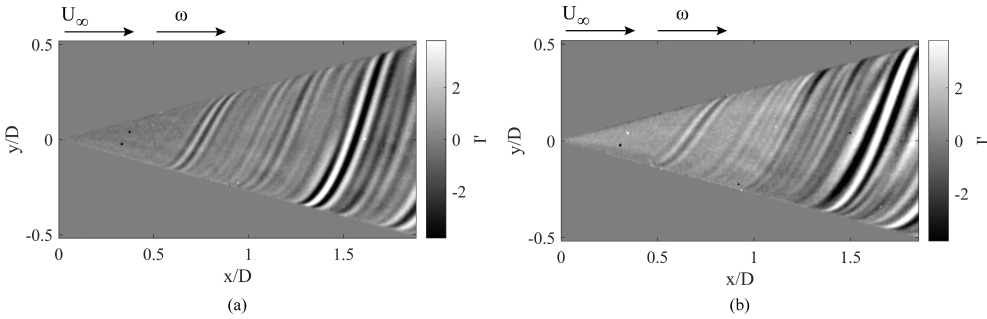


Figure 3.10: Reconstruction using the POD modes satisfying the criteria:  $\phi_\kappa > 0.001$ ,  $n \geq 8$ . Flow is from left to right (a)  $\kappa_{thr} = 39$ ,  $S_b = 4$ ,  $Re_L = 1.9 \times 10^4$ ,  $S = 0 - 3.77$ ,  $Re_l = 0 - 1.97 \times 10^4$ , (b)  $\kappa_{thr} = 44$ ,  $S_b = 3$ ,  $Re_L = 2.5 \times 10^4$ ,  $S = 0 - 2.83$ ,  $Re_l = 0 - 2.63 \times 10^4$

larger vortices with respect to the local radius (e.g.  $n = 2$ , implies  $\lambda_\theta = \pi r$ , which for the typical vortex angles would imply unreasonable vortex size with diameters larger than the local cone radius). However, a more in-depth theoretical study is required to generalise this to any arbitrarily shaped body of revolution.

Based on the past literature, it can be said for the cases of rotating cones ( $15^\circ < \psi < 90^\circ$ ), rotating sphere and rotating disk (which is a rotating cone with  $\psi = 90^\circ$ ) that the POD modes corresponding to  $n < 8$  do not usually resemble the spiral vortices (unless the vortex angle  $\epsilon$  is close to  $0^\circ$ ) but are the effects of large scale modulations in local vortex strength. In order to separate the effect of the vortical structures from other large scale phenomena, only modes with  $n \geq 8$  are considered for the reconstruction. The selectively reconstructed image is shown in figure 3.9 revealing the spatial organization of the spiral vortices in detail. We start observing spiral vortices from around  $x/D = 0.6$ . Their structure remains coherent and they grow in size as they move downstream until approximately  $x/D = 1.2$  where the coherence in the spatial organization starts to decrease. This shows the onset of secondary instability on the vortices as the spacing between the two vortex lines appears to be varying azimuthally.

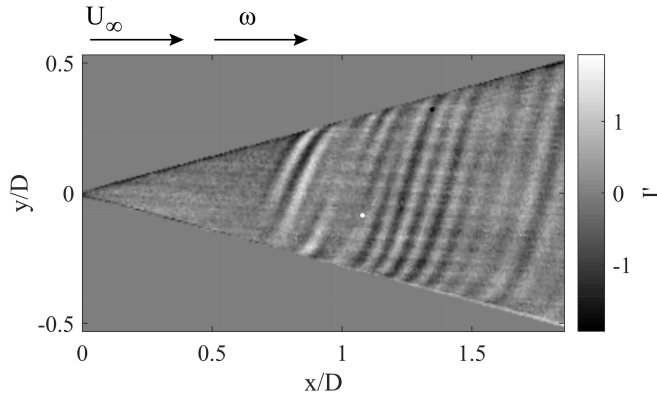


Figure 3.11: Reconstruction using the POD modes satisfying criteria:  $\phi_\kappa > 0.001$ ,  $n \geq 8$  for 15000 RPM Flow is from left to right  $\kappa_{thr} = 27$ . ( $S_b = 5$ ,  $Re_L = 4.5 \times 10^4$ ,  $S = 0 - 4.71$ ,  $Re_l = 0 - 4.7 \times 10^4$ ).

Additionally, selectively reconstructed instances (based on criterion  $n \geq 8$ ) for different combinations of  $S_b$  and  $Re_L$  are shown in figure 3.10. It can be observed that the spiral vortex angle ( $\epsilon$ ) and the number of spiral vortices ( $n$ ) change as the distribution of the rotational ratio  $S$  changes over the cone surface. Figure 3.11 shows the similar result for  $S_b = 5$  at 15000 RPM. It is observed that the surface rotation during the integration time does not cause blur and spiral vortices are still observed. The difference between the vortex structure in figure 3.9 and figure 3.11 is due to the different  $Re_l$ .

As discussed at the start of section 3.4.2, the application of the criterion proposed in the literature (Raiola et al., 2015; Raiola et al., 2017) is not suitable in the present case, as the objective here is to reconstruct the thermal footprints of the spiral vortices. As an example, when this criterion is applied for the case shown in figure 3.11, the threshold mode number increases to  $\kappa_{thr} = 193$ . It is clear in the corresponding distribution of  $\phi_\kappa$  from figure 3.7b that at mode numbers higher than 27, the signal strength drops considerably and there is no significant contribution to the signal relative to noise. Figure 3.12 shows the reconstruction where the criterion from the literature is used for the noise reduction. It is evident from the comparison between figure 3.11 and figure 3.12, that the higher noise is incorporated in the latter and there is no significant change in the structure of the spiral vortices.

When extending the present method to an arbitrarily shaped body of revolution or where the data on expected azimuthal number of vortices is unavailable, values of  $n$  can still be estimated as follows. The typical range of spiral vortex angles ( $\epsilon$ ) can be measured from the filtered image (as shown in figure 3.8). The stream-wise wavelength can be measured by means of other methods like PIV in the symmetry plane. Depending upon the geometry,  $\lambda_\theta$  can be obtained from  $\lambda_x$  and  $\epsilon$ , and thus a lower bound on  $n = 2\pi r / \lambda_\theta$ .

### 3.5. COMPARISON TO PIV AND LITERATURE

Figure 3.13 shows an instantaneous vector field from stereo PIV with the statistical average subtracted. The vector plot shows a crossflow section of the spiral vortices near the wall. Measurement closer to the wall is not possible due to the laser reflection. It is clear from the vector fields that these vortices appear as pairs of counter-rotating vortices with alternating mutual up-wash and downwash regions. Comparing this with figures 3.8 and 3.9 shows that

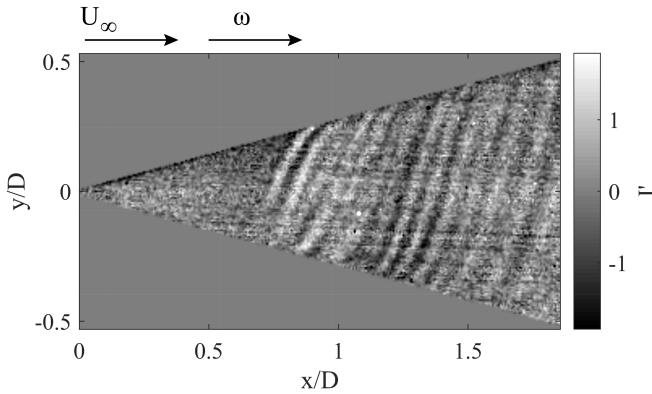


Figure 3.12: Reconstruction using the criterion for noise reduction from the literature and:  $n \geq 8$  for 15000 RPM. Flow is from left to right.  $\kappa_{thr} = 193$ . ( $S_b = 5$ ,  $Re_L = 4.5 \times 10^4$ ,  $S = 0 - 4.71$ ,  $Re_l = 0 - 4.7 \times 10^4$ ).

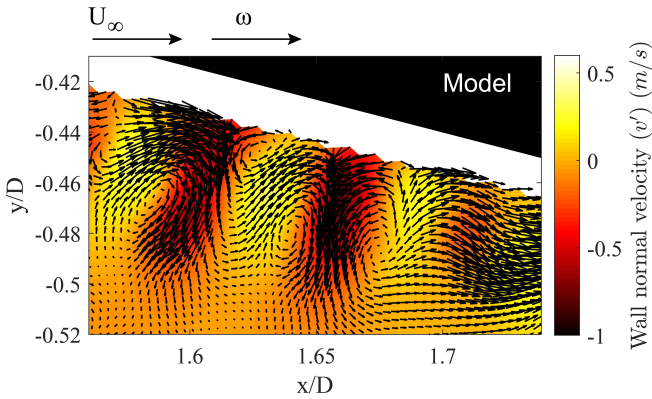


Figure 3.13: Instantaneous vector field and contours of wall-normal velocity from stereo PIV with mean subtracted showing vortices produced over the cone surface. Flow from left to right ( $S_b = 5$ ,  $Re_L = 1.5 \times 10^4$ ,  $S = 0 - 4.71$ ,  $Re_l = 0 - 1.58 \times 10^4$ ).

indeed the alternating dark and bright fringes observed in IRT correspond to the alternating mutual up-wash and downwash regions of the vortices. Thus, between two bright (or dark) fringes in IR images, there is one pair of counter-rotating vortices. The wavelength obtained from figure 3.13 is approximately  $0.06D$ , which is in the same order as the wavelengths in figure 3.3 corresponding to the POD modes with  $n \geq 8$ .

The number of spiral vortices ( $n$ ) and spiral vortex angle ( $\epsilon$ ) are measured from the selective reconstructions for the different combinations of  $S_b$  and  $Re_L$ . They are plotted against the rotational ratio  $S$  and compared with the experimental and theoretical results from the study by Kobayashi et al., 1983 (see figure 3.14 and figure 3.15). The comparison of  $n$  shows good agreement between the present study and the literature (see figure 3.14) confirming that the present reconstruction approach captures the spiral vortex footprints. The trend of spiral vortex angle ( $\epsilon$ ) is in agreement with the literature for small values of  $S$ , but it deviates from literature to higher angles at higher values of  $S$  (see figure 3.15). Note that measurements by Kobayashi et al., 1983 are performed away from the wall, while the angles

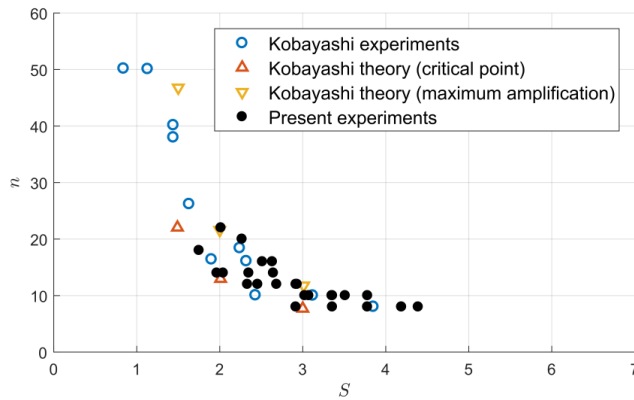


Figure 3.14: Azimuthal number of vortices  $n$  observed at each rotation ratio  $S$  (for all investigated flow conditions) compared with the experimental and theoretical results by Kobayashi et al., 1983.

in the present study are obtained from the measurements at the wall. The angles in the present study deviate towards the wall shear stress direction of the laminar boundary layer which was predicted by Kobayashi et al., 1983 (figure 3.15). The wall shear stress direction depends on the slopes of meridional and tangential velocity profiles at the wall. However, the spiral vortices are generally induced at a location away from the wall (see figure 3.16). Owing to the skewed boundary-layer profile, at high rotation ratio, they are oriented closer towards the rotation direction, and hence their orientation differs from the direction of the wall shear stress.

It shall be noted that the spiral vortices are superimposed on the flow and are convected over the cone surface. It is also evident from figure 3.13 that the vortices are observed only after subtraction of the mean flow. Thus, the limitation imposed on the present method comes from the blur caused by the convective velocity of the vortices during the integration time. The convective velocity is usually lower than the edge velocity. In the present study, the blur is lower than  $0.01D$  to  $0.05D$  for inflow velocities  $2.46 - 12.3$  m/s, respectively. Therefore, reliable measurements of vortex number are only obtained from the flow cases with inflow velocity lower than  $7.4$  m/s (blur lower than  $0.03D$ ).

### 3.6. CONCLUSION

It is shown that IRT coupled together with POD analysis proves to be a useful tool to understand the spatial organization of the non-stationary spiral vortices on rotating bodies of revolution. The criteria based on the signal to noise ratio is used to define the first threshold on the number of POD modes to obtain the reconstruction with reduced measurement noise. The results show that the noise is reduced without altering the structure of spiral vortices.

Furthermore, the POD modes below the first threshold are selectively used to separate the effect of local modulations in the spiral vortex strength and reconstruct the vortex structure based on the physical characteristics. It is observed from past studies that the number of vortices ( $n$ ) along the azimuth is always greater than or equal to 8 for the cases of a rotating cone ( $15^\circ < \psi < 90^\circ$ ), rotating sphere and rotating disk (unless the spiral vortex angle  $\epsilon$  is close to  $0^\circ$ , relating to toroidal vortices on a cone rotating in still fluid). POD modes with the

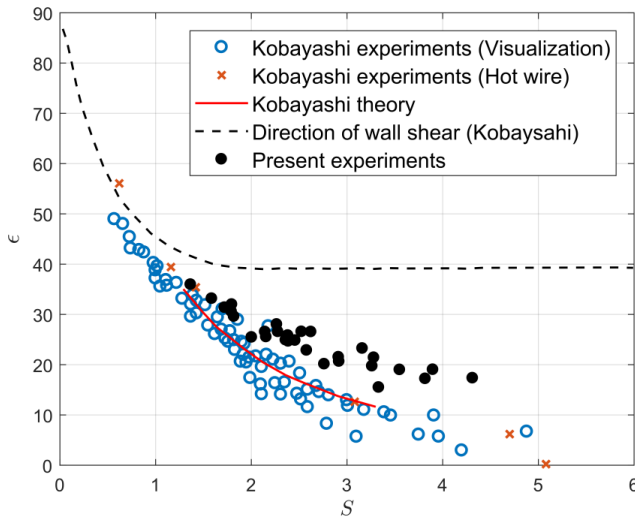


Figure 3.15: Spiral vortex angle  $\epsilon$  observed at each rotation ratio  $S$  (for all investigated flow conditions) compared with the results from the study by Kobayashi et al., 1983.

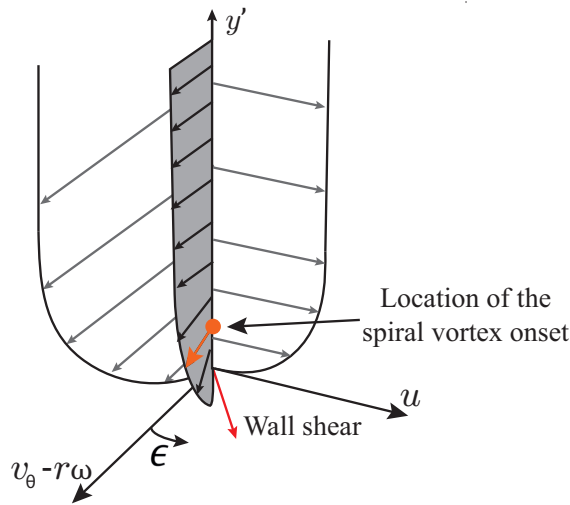


Figure 3.16: A conceptual schematic of a skewed three-dimensional boundary-layer in a reference frame of the rotating cone in axial inflow. As it forms away from the wall, the spiral vortex is oriented closer towards the direction of rotation than the direction of the wall shear.

number of fringe pairs along the circumference ( $n$ ) less than 8 are therefore excluded during reconstruction.

The resulting reconstruction shows the spiral vortex structure, filtering out the effect of modulations in local vortex strength. The number of spiral vortices ( $n$ ) is measured and found to be in a good agreement with the literature. Whereas, the measured spiral vortex angles ( $\epsilon$ ) show good agreement with those from literature at low  $S$ , but deviate towards the direction of the local shear for higher  $S$ . This is a consequence of the measurements at the surface wall. The counter-rotating nature of spiral vortices has been confirmed by PIV measurements.

This method has been used in the forthcoming chapters. These chapters include the investigations on the spiral vortices on rotating cones of different angles in axial flow, non-axial inflow and high-speed inflow. The method has been found useful in detecting spiral vortices in these scenarios.

# 4

## NON-AXIAL INFLOW

### 4.1. INTRODUCTION

SEVERAL past studies have contributed to building our understanding of the boundary-layer instability on a rotating cone, as discussed in chapter 2. But all of these studies are limited to an axisymmetric inflow field. Although the symmetry simplifies analyses, in practice, rotating nose-cones often face non-axial inflows. In aero-engines, the inflows become non-axial due to the design consequences and off-design conditions, e.g. embedded engines ingesting the airframe boundary-layer, ultra high bypass ratio (UHBR) engines with short intakes at take-off and cross-wind operations, etc (see figures 1.5 and 1.6 in chapter 1). In these cases, the boundary-layer instability on a rotating nose-cone can influence the interaction of a non-uniform inflow and the aero-engine fan, consequently influencing the loss mechanisms. Therefore, it is important to investigate how deviations from the symmetry of axial inflow affects the boundary-layer instability on a rotating cone.

Using the experimental method described in chapter 3, this chapter shows how a deviation from a symmetric inflow condition affects the development of spiral vortices, induced by the centrifugal instability, on a rotating cone. A rotating slender cone of half-cone angle  $\psi = 15^\circ$  is chosen for this investigation because it has been previously studied in axisymmetric flow conditions, i.e. still fluid and axial inflow (Kobayashi & Izumi, 1983; Kobayashi et al., 1983). For the ease of analysis, the non-axisymmetric inflow is introduced by changing the incidence angle of the inflow with respect to the rotating cone.

The definitions of the cone geometry and flow parameters are described in section 4.2. The specifications of the experimental setup and data processing methods are detailed in section 4.3. The detailed results and discussions are presented in section 4.4. The measurement approach has been validated by revisiting the axial inflow case, discussed in section 4.4.1. The effect of non-axial inflow on the spiral vortex appearance and growth is discussed in section 4.4.2. A physical interpretation of the observed differences between axial and non-axial inflow cases is presented in section 4.4.3. Finally, the conclusions are discussed in section 4.5.

---

Parts of this chapter have been published in the *Journal of Fluid Mechanics*, **910**, A25 (2021), Tambe et al., 2021

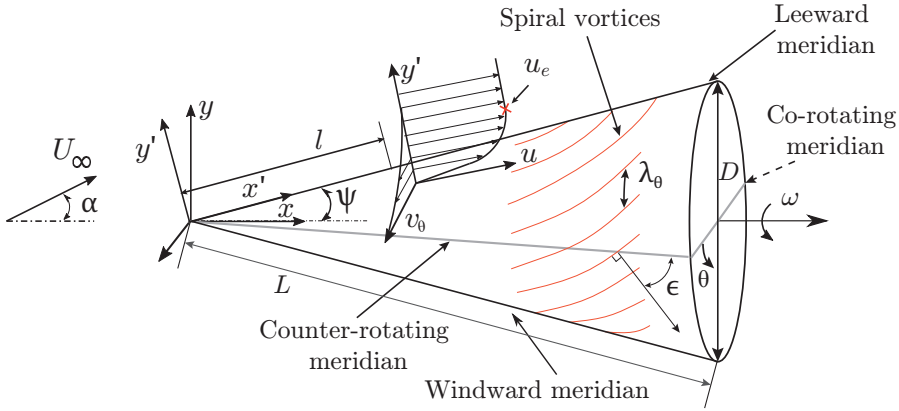


Figure 4.1: Schematic of the rotating cone and coordinate systems.

## 4.2. DEFINITIONS OF GEOMETRY AND FLOW PARAMETERS

A schematic of a rotating cone in the Cartesian coordinate system is shown in figure 4.1. The angular velocity  $\omega$  is aligned with the positive  $x$  axis. The coordinate system  $x', y'$  is used when discussing the velocities in the wall-parallel and wall normal directions, respectively. The cone surface is represented by  $l$  and  $\theta$ , based on cylindrical polar coordinates. Here,  $l$  is the meridional distance from the cone apex, and  $\theta$  is the azimuthal angle measured from the counter-rotating meridian.

The local Reynolds number  $Re_l$  and local rotational speed ratio  $S$  are the important flow parameters which govern the spiral vortex growth (Kobayashi et al., 1987; Kobayashi et al., 1983, chapter 2). Their definitions are as follows:

$$Re_l = \frac{u_e l}{\nu}, \quad S = \frac{r\omega}{u_e}. \quad (4.1)$$

Here,  $u_e$  is the boundary-layer edge velocity,  $\nu$  is the kinematic viscosity of air,  $r$  is the local radius, and  $\omega$  is the angular velocity of the cone.

The boundary-layer edge velocity  $u_e$  is defined as the time-averaged stream-wise velocity, measured at a wall normal location where the magnitude of the vorticity component out of the meridional plane reaches zero. In practice, the vorticity is considered to be zero below the value of measurement uncertainty ( $< 0.24U_\infty/D$ ), where  $U_\infty$  is the free-stream velocity, and  $D$  is the base diameter of the cone. For the axial inflow, the boundary-layer edge velocity over the entire cone is obtained by fitting a power-law form  $u_e = CU_\infty l^m$  (Garrett & Peake, 2007b) to the measured velocity field for  $l/D = 0.8$  to 1.8 ( $C = 1.66$ ,  $m = 0.19$  and RMS fit error  $< 0.02U_\infty$ ).

Although the spiral vortex growth depends on the local scaling  $S$  and  $Re_l$  (Kobayashi et al., 1987), the inflow Reynolds number  $Re_L$  and the base rotational speed ratio  $S_b$  are useful parameters while discussing the experimental conditions. They are defined as follows:

$$Re_L = \frac{U_\infty L}{\nu}, \quad S_b = \frac{D\omega}{2U_\infty}. \quad (4.2)$$

Here,  $L = D/(2\sin(\psi))$  is the total cone length along  $x'$ , and a subscript  $b$  refers to the

Camera	FLIR (CEDIP) SC7300 Titanium
Noise equivalent temperature difference (NETD)	25 mK
Spatial resolution	0.28 mm/px
Integration time	201 $\mu$ s
Acquisition frequency	200 Hz
Number of images per dataset	2000
Heat source	Theatre lamp (575 W)

Table 4.1: Specifications of the Infrared Thermography setup.

cone base. The dependence on the finiteness of a cone is eliminated by defining a parameter  $\kappa$  as

$$\kappa = \frac{Re_L}{S_b} = \frac{U_\infty^2}{\sin(\psi)\omega\nu}. \quad (4.3)$$

Here,  $\kappa$  depends only on the half cone angle, angular velocity and free stream conditions. Since  $\kappa$  is the slope of a line  $Re_L = \kappa S_b$ , it provides a general direction along which the curves of  $Re_l$  vs  $S$  lie for a particular experimental condition. In the subsequent text,  $S_b$ ,  $Re_L$  and  $\kappa$  are used while referring to different inflow conditions and consequently, for the different distributions of local flow parameters  $Re_l$  and  $S$  over the cone.

Figure 4.1 also schematically shows the spiral vortices and their characteristics. Here, the spiral vortex angle  $\epsilon$  is the angle between the meridional line and the direction of the perturbation wave propagation; this is same as the angle between the vortex axis direction and the circumferential direction (Kobayashi et al., 1983). The azimuthal number of vortices  $n$  ideally represents the azimuthal wavelength  $\lambda_\theta = 2\pi r/n$ .

### 4.3. EXPERIMENTAL SETUP

The experimental arrangements and data processing approach is the same as presented in chapter 3. Figure 4.2 describes the setup of IRT and PIV measurements. Tables 4.1 and 4.2 contain the specifications of the IRT and PIV setups, respectively.

Figure 4.3 shows a photograph during IRT measurements with a non-axial inflow. The non-axial inflow is imposed by varying the incidence angle  $\alpha$  between  $0^\circ$  and  $10^\circ$ , within the uncertainty of  $\pm 0.1^\circ$ . Since the present study is focused on deviations from axial symmetry, first, small variations in the incidence angles are considered ( $\alpha = 2^\circ$  and  $4^\circ$ ). A considerably larger value of  $\alpha = 10^\circ$ , which corresponds to a relative incidence  $\alpha/\psi = 0.67$ , is also tested. High values of incidence angles may cause flow separation, and such investigations are beyond the scope of the present study. The inflow velocity of the wind tunnel is varied from 2.46 – 6.15 m/s to obtain different values of the base rotational speed ratio  $S_b$ , and therefore, different distributions of local Reynolds number  $Re_l$  and rotational speed ratio  $S$ . The test matrix is presented in table 4.3.

During the PIV measurements, the laser sheet thickness is kept around 2–2.5mm to ensure that, during a cone rotation, majority of the near-wall particles remain in the laser sheet. However, this results in the velocity field which is averaged over the laser sheet thickness. As schematically shown in figure 4.4, in the case of a slight misalignment (non-zero incidence angle or between the laser sheet and cone axis) or during the non-axial inflow,

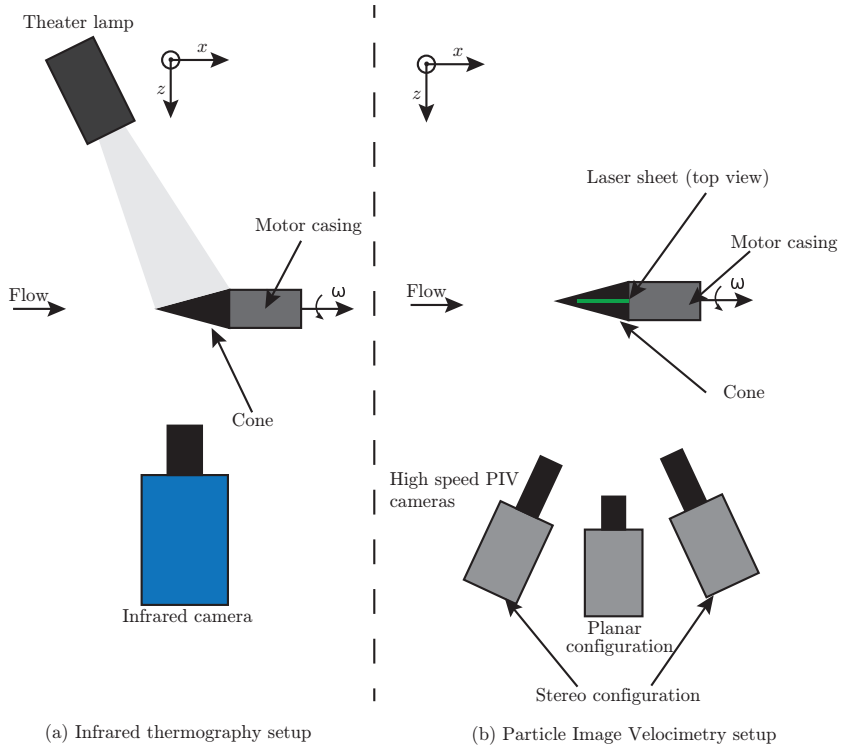


Figure 4.2: Schematics of the experimental setup of (a) infrared thermography and (b) particle image velocimetry.

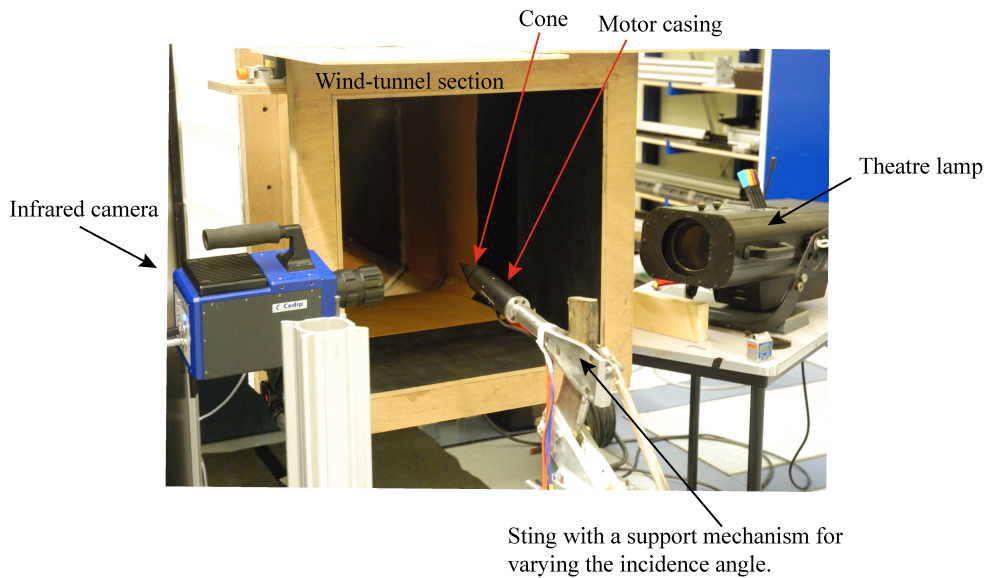


Figure 4.3: A photograph of the experimental setup during infrared thermography measurements.

Camera	Photron Fastcam SA-1
Sensor dimensions	1024 × 1024 px
Vector pitch (3C)	0.16 mm
Interrogation window size	48 px × 48 px
Vector pitch (2C)	0.42 mm
Interrogation window size	24 px × 24 px
Laser	Nd:YAG Continuum MESA PIV 532-120-M
Acquisition frequency	2.5 kHz
Number of image pairs per dataset	1000
Seeding	Smoke particles (diameter ≈ 1 μm)

Table 4.2: Specifications of the PIV setup.

Operating condition no.	$Re_L$	$S_b$	IRT	PIV	$\alpha$
<i>I</i>	$1.5 \times 10^4$	5	✓	✓	0°, 2°, 4° and 10°
<i>II</i>	$1.9 \times 10^4$	4	✓		0°, 2°, 4° and 10°
<i>III</i>	$2.1 \times 10^4$	3.5	✓		0°, 2°, 4° and 10°
<i>IV</i>	$2.5 \times 10^4$	3	✓	✓	0°, 2°, 4° and 10°
<i>V</i>	$3.7 \times 10^4$	2	✓		0°
<i>VI</i>	$1.5 \times 10^4$	0		✓	0°, 2°, 4° and 10°
<i>VII</i>	$2.5 \times 10^4$	0		✓	0°, 2°, 4° and 10°

Table 4.3: Test matrix. Operating conditions *I-V* are chosen to compare the spiral vortex growth with the measurements of (Kobayashi et al., 1983) on a rotating cone in axial inflow. These flow conditions are also used in the non-axial inflow. Velocity field is obtained using PIV for two cases *I* and *IV* of a rotating cone and corresponding cases *VI* and *VII* of a non-rotating cone.

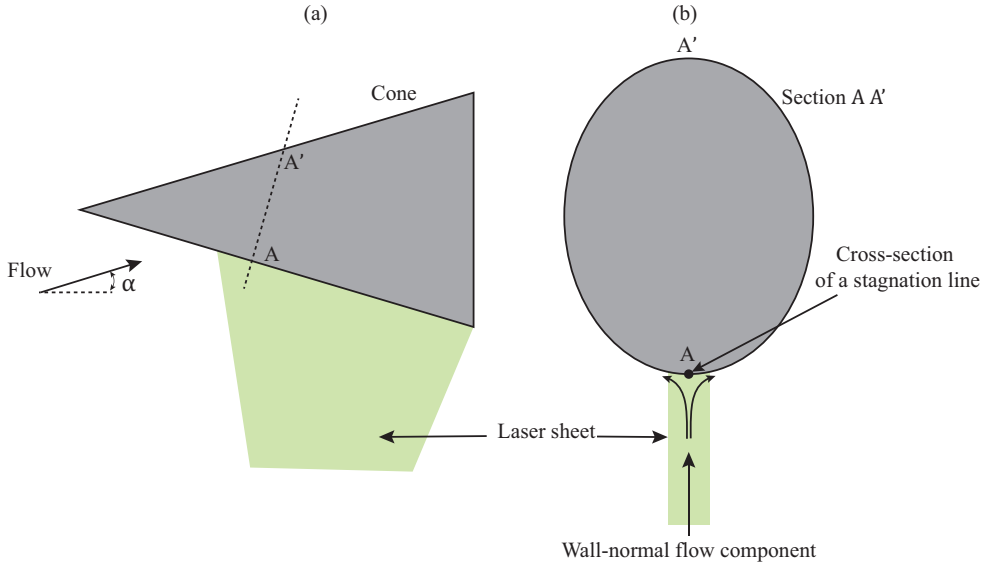


Figure 4.4: Effect of the finite laser sheet thickness on the near-wall velocity measurements on a cone, using PIV. Schematics show (a) side view of a cone and (b) sectional view showing wall-normal velocity component. Laser sheet misalignment and non-axial inflow can measure the near-wall velocity vectors pointing towards the wall, resulting from the averaging over the laser sheet thickness.

a wall-normal velocity component is averaged over the laser sheet thickness. Due to this effect, the near-wall velocity vector appears to be pointing towards the wall. However, this does not significantly affect the velocities away from the wall.

## 4.4. RESULTS AND DISCUSSION

### 4.4.1. AXIAL INFLOW

Under the axial inflow condition, spiral vortices grow in the laminar boundary-layer over the rotating slender cone, leaving footprints on the surface temperature. These instantaneous footprints, which are reconstructed from the POD modes, can be seen in figures 4.5a and b as a projection in  $xy$  plane and on an unwrapped surface, respectively (at  $S_b = 5$ ,  $Re_L = 1.5 \times 10^4$ ). At approximately  $x/D = 0.6$ , the spiral vortices start to appear in a coherent fashion, i.e. the spacing between the vortices is nearly uniform around the azimuth at a constant radius. They grow in the downstream direction until a point of maximum amplification at around  $x/D = 1.2$ , beyond which their footprint deteriorates and the coherence starts to get disturbed. This growth is evident from the statistical RMS of surface temperature fluctuations ( $I'_{RMS}$ , computed from 2000 images acquired at 200 Hz) shown in figures 4.5c and d. Here,  $I'_{RMS}$  starts to increase around  $x/D = 0.8$ , till a maximum value at around  $x/D = 1.2$ , beyond which the fluctuations decrease. No such surface temperature fluctuations were observed for a non-rotating cone ( $I'_{RMS} < 2$ ).

Figure 4.6 allows the comparisons between (a) meridional variation of the surface temperature fluctuations ( $I'_{RMS}$  traced at  $y/D = 0$  from figure 4.5c), (b) the instantaneous footprints

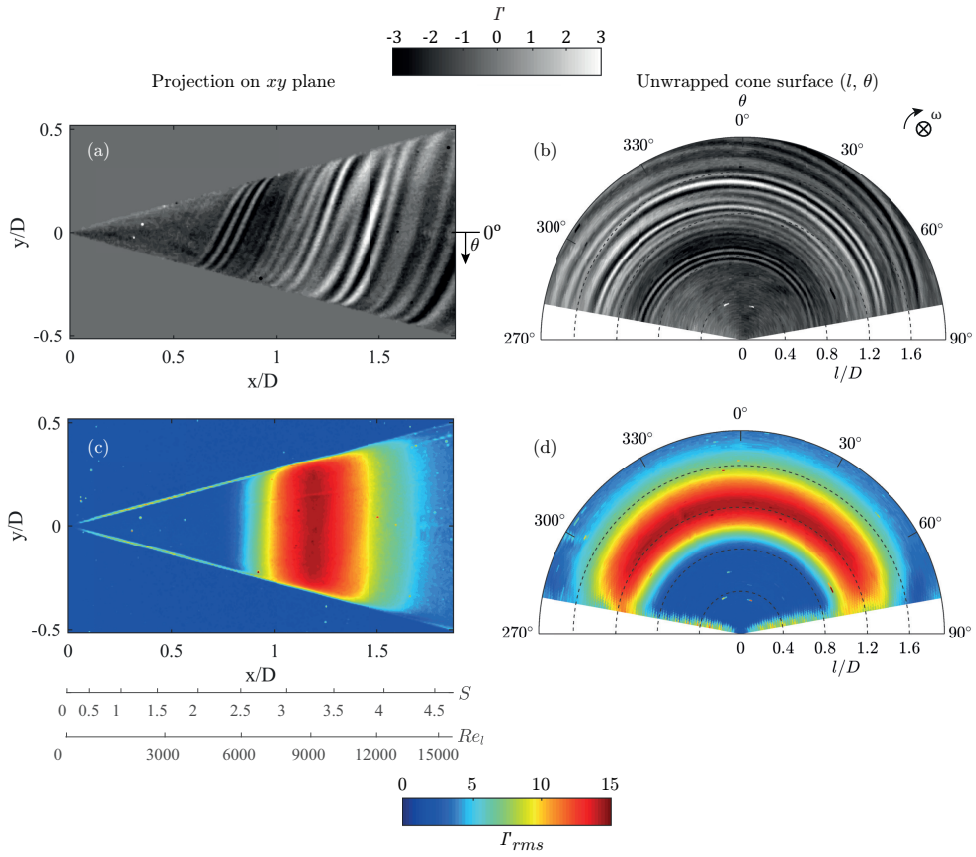


Figure 4.5: (a, b) Instantaneous surface temperature footprints of the spiral vortices and (c, d) the corresponding statistical RMS of the surface temperature fluctuations ( $I'_{RMS}$ ) over a dataset ( $\alpha = 0^\circ$ , operating condition  $I : S_b = 5$ ,  $Re_L = 1.5 \times 10^4$ ).

of spiral vortices on a rotating cone and their influence on (c) the mean flow field compared to (d) the mean flow of a non-rotating case. The flow phenomena occurring at the peak  $I'_{RMS}$  (point  $l_m$  in figure 4.6a) can be further understood by observing the corresponding velocity fields in the wall-normal ( $x'y'$ ) plane. For a non-rotating cone, the time-averaged velocity field shows a region of low streamwise momentum (along  $x'$ ) close to the wall (see figure 4.6d, here the direction of the near-wall vectors is an artifact of the finite laser sheet thickness as shown in figure 4.4). However, for the rotating cone, a similar low momentum region is observed only until around  $x'/D = 1.24$  (see figure 4.6c). Beyond this point, there is a sudden increase in the  $x'$  momentum near the wall. This point coincides with the location of  $I'_{RMS}$  peak. It is clear that as the spiral vortices get amplified, they transport the outer high momentum fluid towards the wall, resulting in increased  $x'$  momentum close to the wall. This mixing process was also observed by Y. Kohama (1984a), see figure 2.13. During the process of amplification, the local shear at the wall is increased as the outer high momentum fluid is transported close to the wall. This increases the surface heat transfer. Consequently, the footprints of the spiral vortices become stronger in the temperature map. The maximum observed surface temperature fluctuations are of the order of 1.3 K. Although not shown here, a similar agreement between the location of increased  $x'$  momentum (obtained from PIV) and the peak of  $I'_{RMS}$  (obtained from IRT) has been observed in all the investigated cases when both PIV and IRT are performed.

Figure 4.7 shows the cross-sections of the spiral vortices in the symmetry plane at  $t_0 + 14.57T$ , where  $t_0$  is the time at the start of acquisition and  $T = 0.012$  s corresponds to the time period of a cone rotation. Additionally, movie 1 (available at <https://doi.org/10.1017/jfm.2020.990>) shows the time series of this vector field. The contours of wall normal velocity fluctuations clearly show the alternating up-wash and down-wash regions near the wall. Together with vectors, this confirms the counter-rotating nature of the spiral vortices which is linked to the centrifugal instability (Görtler, 1954; Kobayashi et al., 1983; Rao, Leontini, et al., 2013; Taylor, 1923).

The growth of the spiral vortices can be seen by tracking their evolution in time. Movie 2 (available at <https://doi.org/10.1017/jfm.2020.990>) shows the spiral vortices evolving over the rotating cone surface. A snapshot from this movie can also be seen in figure 4.8. The flow is from left to right, and the angular velocity is aligned with positive  $x$ . The raw 2C PIV recordings are processed such that the brighter regions signify higher seeding density (in the present 2C PIV setup, the vector pitch of 0.42mm is insufficient to apply quantitative vortex detection methods). The seeding particles, being slightly heavier than air, get ejected outwards from the vortex cores due to the centrifugal force. Therefore, these vortex cores have low seeding density and appear as darker regions (marked as red dots). When tracking the spiral vortices as they move downstream, it appears that they have grown significantly after the maximum amplification point  $l_m$  (corresponding to peak  $I'_{RMS}$ ).

Figure 4.9 shows the spiral vortex evolution using three consecutive instances obtained from infrared thermography measurements. Images on the right are the instantaneous temperature footprints of the spiral vortices. On the left, the traced values of  $I'$  along the  $y/D = 0$  are shown in combination with  $I'_{RMS}$ . In the top row of figure 4.9, a batch of relatively strong vortices has just entered the amplification region at an instance of time  $t_a = t_0 + 22T$ . At  $t_a + 0.42T$ , the footprint of the vortices has grown in amplitude. At the next instance  $t_a + 0.83T$ , the amplitude has further increased. In this region a peak in  $I'_{RMS}$  is observed. Moving further downstream of the  $I'_{RMS}$  peak, the overall coherence decreases i.e. the spacing

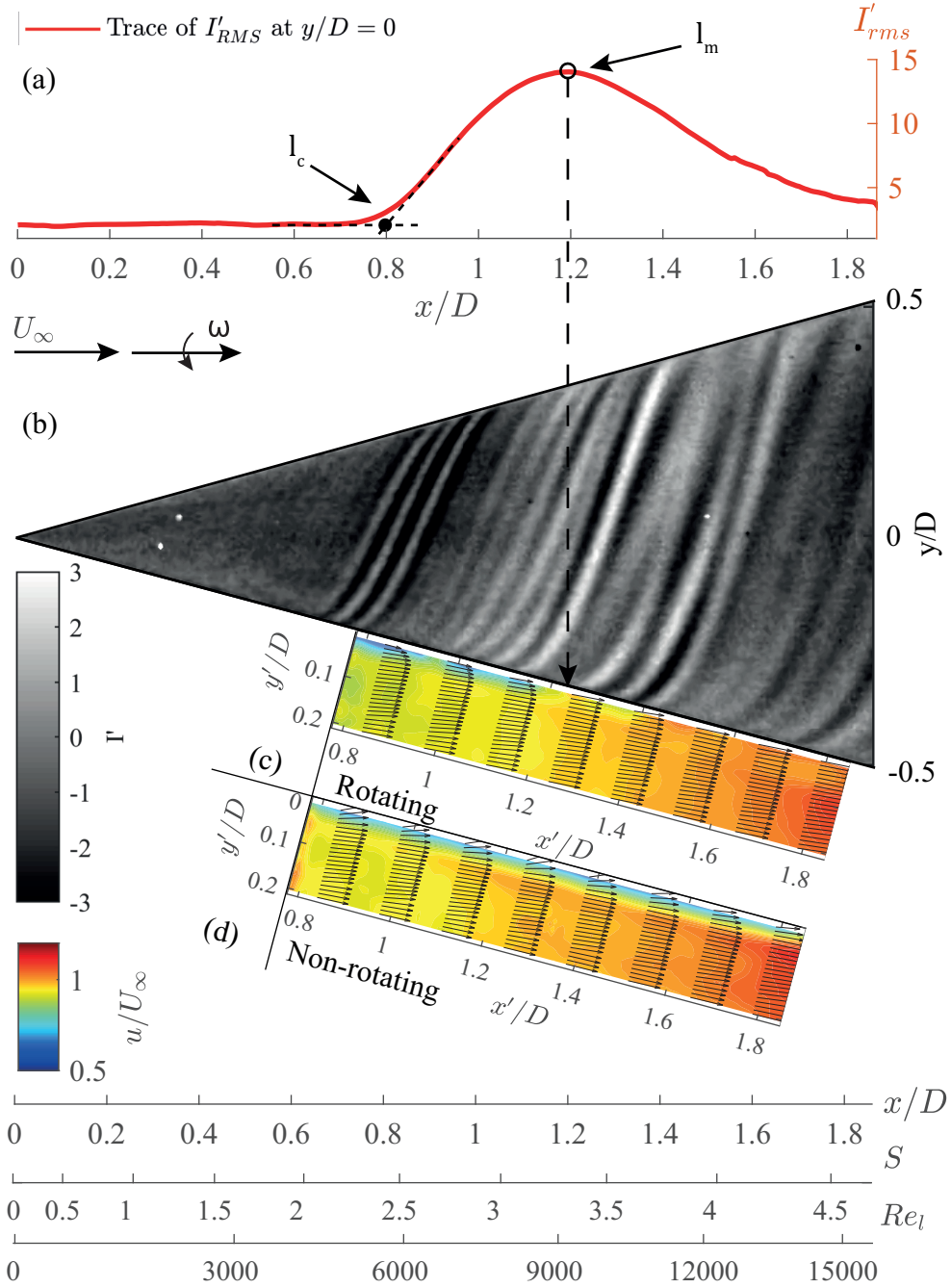


Figure 4.6: Growth and spatial organization of the spiral vortices in axial inflow ( $\alpha = 0^\circ$ ). (a) A trace of  $I'_{RMS}$  at  $y/D = 0$ , (b) instantaneous surface temperature footprints of the spiral vortices on a rotating cone, and time-averaged velocity fields in  $x'y'$  plane for (c) rotating (operating condition I:  $S_b = 5$ ,  $Re_L = 1.5 \times 10^4$ ) as well as (d) non-rotating case (operating condition VI:  $S_b = 0$ ,  $Re_L = 1.5 \times 10^4$ ).

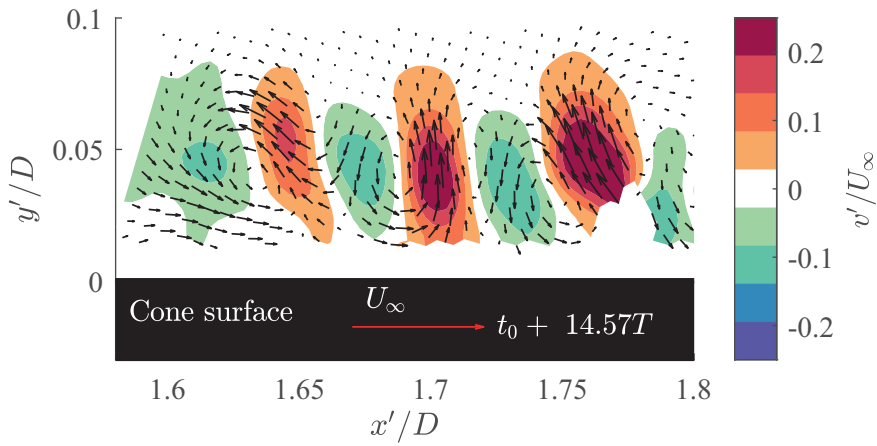


Figure 4.7: Instantaneous wall normal velocity fluctuations with respect to the mean flow showing cross-sections of the spiral vortices ( $\alpha = 0^\circ$ , operating condition I :  $S_b = 5$ ,  $Re_L = 1.5 \times 10^4$ ), also see Movie 1 (available at <https://doi.org/10.1017/jfm.2020.990>).

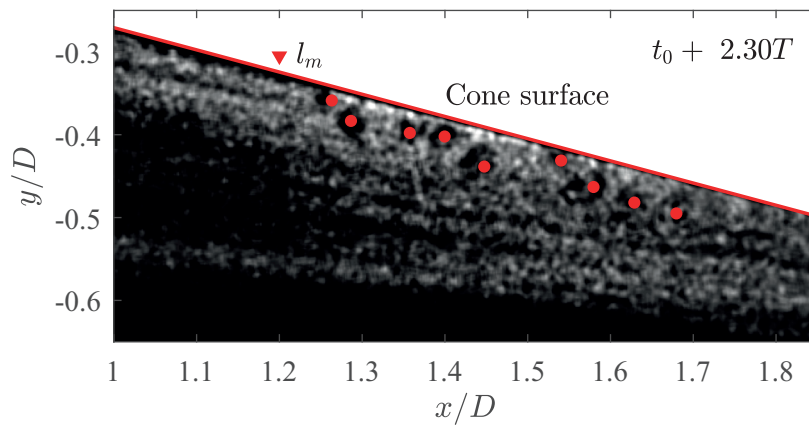


Figure 4.8: Spiral vortices as observed in a PIV recording. Image processing is applied to emphasise seeding density variations. The vortex cores are marked as red dots. Also see Movie 2 (available at <https://doi.org/10.1017/jfm.2020.990>). ( $\alpha = 0^\circ$ , operating condition I :  $S_b = 5$ ,  $Re_L = 1.5 \times 10^4$ ).

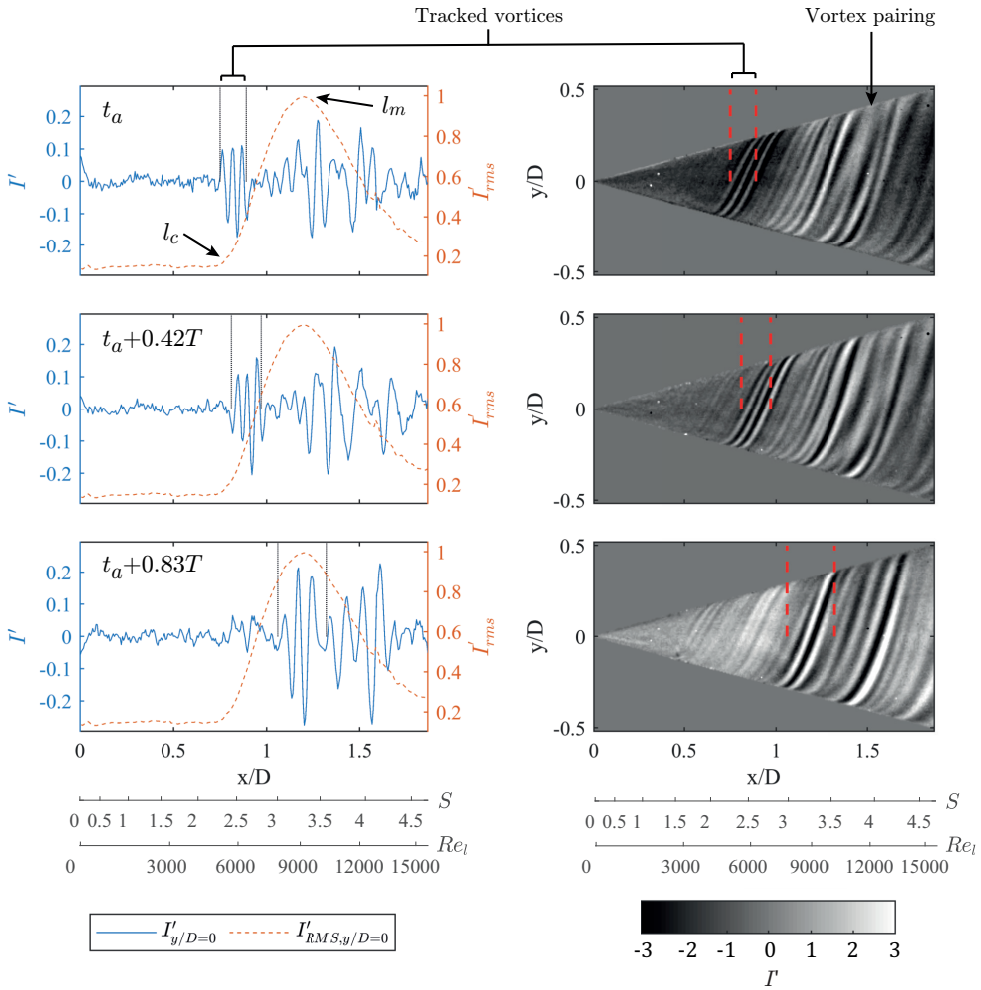


Figure 4.9: Instantaneous surface temperature footprints of the spiral vortices (right column) and corresponding trace of intensity fluctuations  $I'$  at  $y/D=0$  compared with  $I'_{RMS}$  over the dataset (left column) ( $\alpha = 0^\circ$ , operating condition  $I : S_b = 5, Re_L = 1.5 \times 10^4$ ).

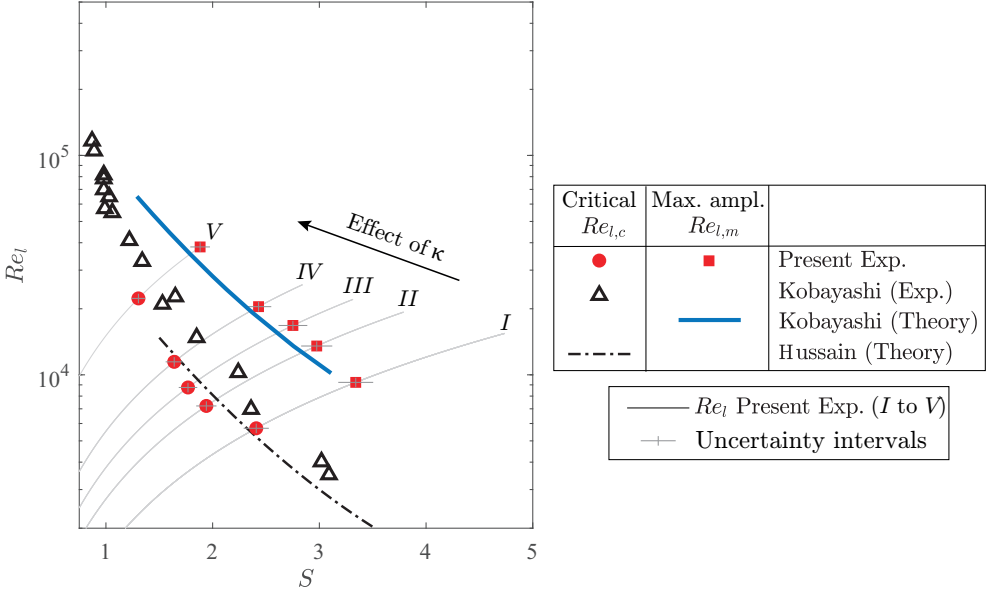


Figure 4.10: Comparison of  $Re_{l,c}$  and  $Re_{l,m}$  measured in the present experiments with the data from literature (Kobayashi et al., 1983, Hussain et al., 2016) for the cases with axial inflow. (I)  $S_b = 5$ ,  $Re_L = 1.5 \times 10^4$ , (II)  $S_b = 4$ ,  $Re_L = 1.9 \times 10^4$ , (III)  $S_b = 3.5$ ,  $Re_L = 2.1 \times 10^4$ , (IV)  $S_b = 3$ ,  $Re_L = 2.5 \times 10^4$  and (V)  $S_b = 2$ ,  $Re_L = 3.7 \times 10^4$ .

between the vortices starts to vary around the circumference at a constant radius. Here, instances of vortex pairing are also observed.

It is clear from figures 4.6 and 4.9 that the  $I'_{RMS}$  peak represents the maximum amplification of the spiral vortices. Therefore, the point  $l_m$  can be associated with the maximum amplification. The corresponding Reynolds number is defined as

$$Re_{l,m} = \frac{l_m u_e}{\nu}. \quad (4.4)$$

The point  $l_c$  at which  $I'_{RMS}$  starts to grow is a critical point that represents the start of spiral vortex growth. The corresponding critical Reynolds number is defined as

$$Re_{l,c} = \frac{l_c u_e}{\nu}. \quad (4.5)$$

In the present study, a closer inspection of figure 4.9 (right columns) shows that the spiral vortices appear at around  $x/D = 0.5-0.6$ , which is before the critical point  $l_c$  (around  $x/D = 0.78$ ) corresponding to the experimental value of the critical Reynolds number  $Re_{l,c} = 5.7 \times 10^3$  for the operating condition I. The accurate detection of the location where the spiral vortices originate is hindered by the measurement limitations, because the spiral vortices are expected to be weak near their origin and their effect on the surface temperature may be below the measurement noise ( $< 25\text{mK}$ ). Therefore, in the present study, the critical Reynolds number  $Re_{l,c}$  is the Reynolds number that corresponds to a critical point at which the spiral vortices start to undergo a rapid growth, rather than a point at which they originate.

Since the spiral vortex growth depends on local Reynolds number  $Re_l$  and rotational speed ratio  $S$ , the critical and maximum amplification locations for all the axial inflow cases are represented in the parameter space spanned by  $Re_l$  and  $S$ , see figure 4.10. The gray lines (numbered as  $I$  to  $V$ ) in figure 4.10 represent the variation of local Reynolds number  $Re_l$  versus rotational speed ratio  $S$  on the cone surface for different operating conditions. These lines can be used to relate the flow parameters ( $Re_l$  and  $S$ ) to the corresponding physical location on the cone surface.

Figure 4.10 shows that the measured values of maximum amplification Reynolds number  $Re_{l,m}$  agree closely with the theoretical predictions of Kobayashi et al. (1983). The values of the critical Reynolds number  $Re_{l,c}$  fall closer to the measurements of Kobayashi et al. (1983), and also agree well with the theoretical predictions of Hussain et al. (2016). However, these values of  $Re_{l,c}$  are nearly an order of magnitude higher than the theoretical predictions of Kobayashi et al. (1983) which were based on the linear stability analysis (see figure 2.14). The theoretical predictions of the critical Reynolds number  $Re_{l,c}$  are sensitive to the accuracy of computing the base flow over which the instability develops (Hussain et al., 2016). With more accurate computations of the base flow, theoretical values of  $Re_{l,c}$ , predicted by Hussain et al., 2016, seem to closely agree with the experimental measurements (figure 4.10).

#### 4.4.2. NON-AXIAL INFLOW

Introducing a non-zero incidence angle disturbs the symmetry of the flow field. Due to the incidence angle, the edge velocity of the boundary-layer (with respect to the cone surface) at a given axial location varies circumferentially, unlike in axial inflow. Figure 4.11a shows the meridional variation of the edge velocity measured by PIV for the cases of rotating and non-rotating cones at  $\alpha = 0^\circ$  and  $\alpha = 4^\circ$ . The comparison shows that due to the incidence angle, the edge velocity is increased on the leeward meridian and decreased on the windward meridian. Consequently, the flow parameters, Reynolds number  $Re_l^*$  and rotational speed ratio  $S^*$ , vary circumferentially at a fixed axial location, unlike in the axial inflow case. Here,  $*$  is used to denote the parameters obtained using the local edge velocities in the case of non-axial inflow. Additionally, there is a component of free-stream velocity in  $y$  direction. This, coupled with the cone rotation, adds to an asymmetry with respect to the  $xy$  plane, dividing the regions into co-rotating and counter-rotating, as shown in figure 4.1. The conceptual difference in the tangential velocity profiles of the boundary-layer at the counter and co-rotating meridians is shown in figure 4.11b for the region, where tangential velocity of the cone surface is greater than the component of the outer flow velocity in  $y$  direction (shown for  $|v_\theta| > |v_e|$ ). As a result, one can observe that the boundary-layer profile is skewed to a larger extent on the counter-rotating meridian than on the co-rotating meridian. Consequently, the relative effect of rotation on the flow is higher in the counter-rotating meridian, analogous to the co-axial cylinders rotating in the opposite direction. Whereas, in the co-rotating meridian, the flow experiences lower relative effect of rotation, analogous to the co-axial cylinders rotating in the same direction. This effect can be accounted as the variation in local rotational speed ratio as  $S^* \approx (v_\theta - v_e)/u_e$ , in the region where  $|v_\theta| > |v_e|$ .

It is clear that due to the asymmetries in the velocity magnitude (leeward and windward meridians) and the relative velocity direction (counter and co-rotating meridians), the local skewness of the boundary-layer profile is distributed asymmetrically around the circumference. Therefore, at a fixed radius, this results in an asymmetric variation of local flow parameters ( $Re_l^*$ ,  $S^*$ ) above and below the values corresponding to the axial inflow case at

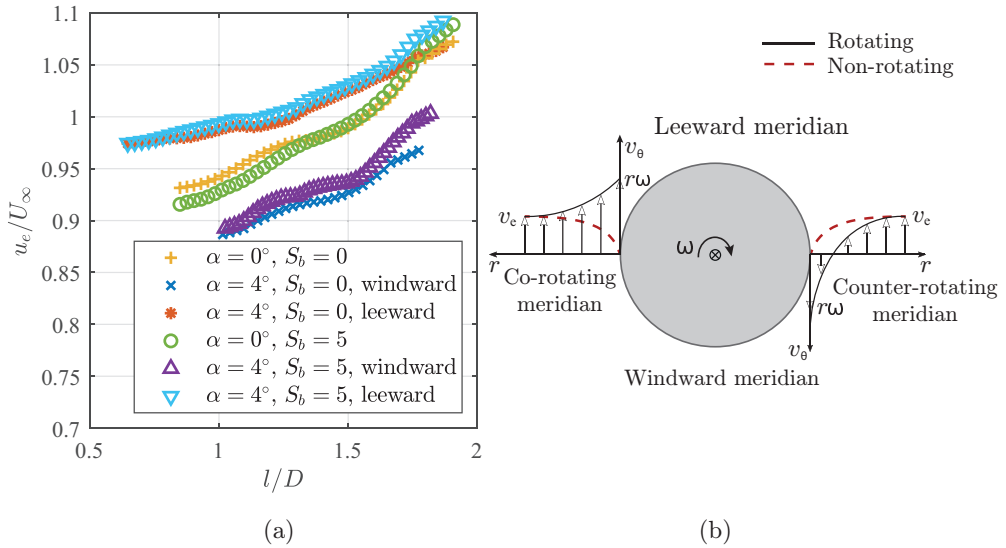


Figure 4.11: Asymmetry in the outer flow field. (a) Meridional variation of the boundary-layer edge velocity. (b) Conceptual sketch of asymmetry in the boundary-layer profiles between co-rotating and counter-rotating meridian, drawn at a cross-flow section of the cone (viewed from the cone apex).

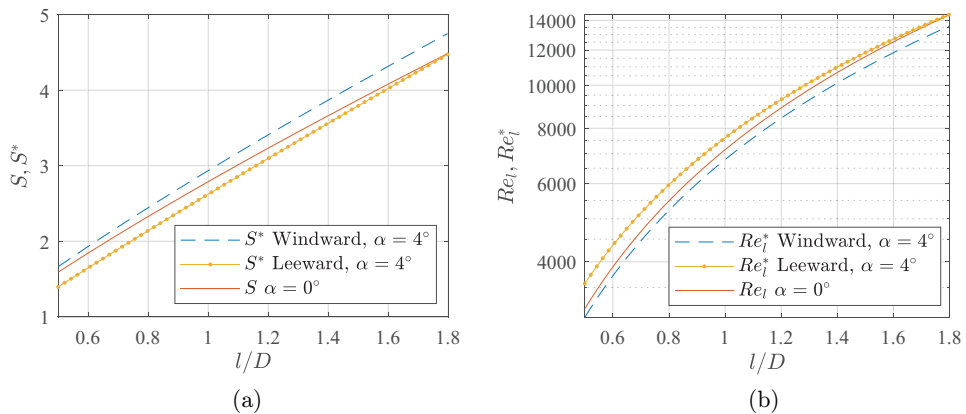


Figure 4.12: Correlation between the flow parameters from axial inflow ( $S, Re_l$  at  $\alpha = 0^\circ$ ) and non-axial inflow ( $S^*, Re_l^*$  at  $\alpha = 4^\circ$ ) along cone meridians (operating condition I :  $S_b = 5, Re_L = 1.5 \times 10^4$ ).

$\alpha$	$C$	$m$	RMS fit error	measurement range	meridian	operating conditions
$0^\circ$	1.66	0.190	$0.02U_\infty$	$l/D = 0.8 - 1.8$	-	$I, IV$
$2^\circ$	1.37	0.136	$0.01U_\infty$	$l/D = 0.83 - 1.8$	windward	$I$
$2^\circ$	1.39	0.135	$0.01U_\infty$	$l/D = 0.83 - 1.8$	windward	$IV$
$2^\circ$	1.35	0.100	$0.011U_\infty$	$l/D = 0.66 - 1.8$	leeward	$I$
$2^\circ$	1.36	0.110	$0.012U_\infty$	$l/D = 0.66 - 1.8$	leeward	$IV$
$4^\circ$	1.53	0.18	$0.01U_\infty$	$l/D = 0.83 - 1.8$	windward	$I$
$4^\circ$	1.66	0.194	$0.01U_\infty$	$l/D = 0.83 - 1.8$	windward	$IV$
$4^\circ$	1.30	0.090	$0.014U_\infty$	$l/D = 0.6 - 1.8$	leeward	$I$
$4^\circ$	1.32	0.100	$0.017U_\infty$	$l/D = 0.6 - 1.8$	leeward	$IV$
$10^\circ$	1.3	0.13	$0.01U_\infty$	$l/D = 0.8 - 1.8$	windward	$I$

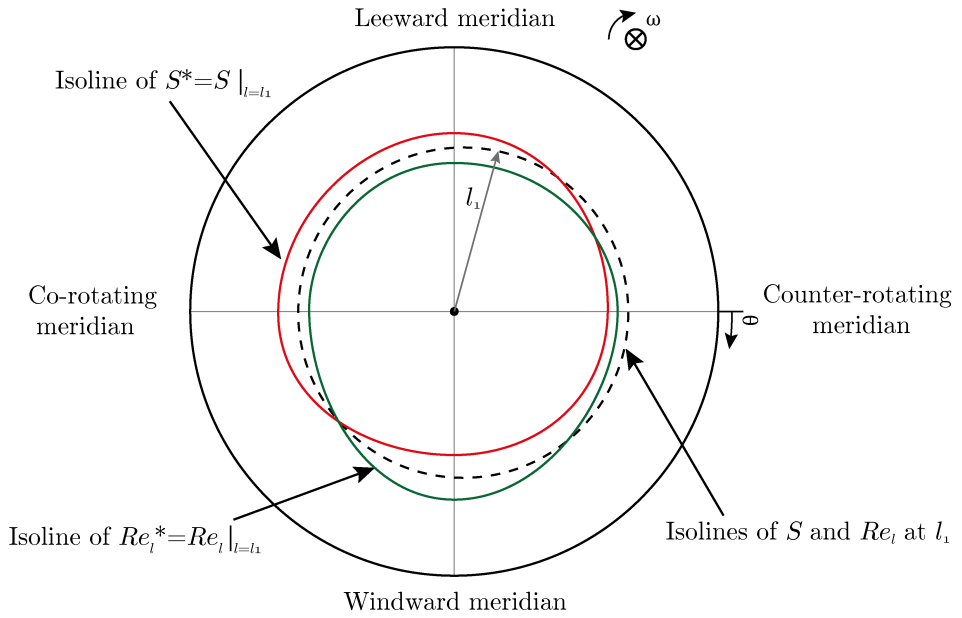
Table 4.4: Fit parameters of the edge velocity  $u_e = CU_\infty l^m$  over the rotating cone.

same operating conditions, i.e. same inflow Reynolds number  $Re_L$  and base rotation ratio  $S_b$ . Figure 4.12 shows these variations in local flow parameters ( $Re_l^*$ ,  $S^*$ ) at windward and leeward meridians in relation to the values from the axial inflow ( $Re_l$ ,  $S$ ) at same operating conditions ( $Re_L$ ,  $S_b$ ). This shows that, along the cone meridians, the  $S^*$  and  $Re_l^*$  follow the general trends of  $S$  and  $Re_l$ , respectively, with small azimuthal variation. Additionally, the edge velocities required to estimate  $Re_l^*$  and  $S^*$  for all other investigated cases can be obtained using the fit parameters  $C$  and  $m$  from Table 4.4 such that  $u_e = CU_\infty l^m$ .

Generally, at constant  $Re_L$  and  $\omega$ , we can write  $S^*(\theta, \alpha, l) = S(l) + \delta_1(\theta, \alpha, l)$  and  $Re_l^*(\theta, \alpha, l) = Re_l(l) + \delta_2(\theta, \alpha, l)$ . Here,  $\delta_1$  and  $\delta_2$  are deviations from the flow parameters for the corresponding axial inflow ( $\delta_1 = \delta_2 = 0$  when  $\alpha = 0^\circ$ ). It is clear that due to the incidence angle, the distribution of the flow parameters ( $Re_l$ ,  $S$ ) around the cone gets distorted. The conceptual sketch of this distortion is shown in figure 4.13. It can be observed that the isolines of  $S$  and  $Re_l$  at a given location  $l_1$  are coincident under axial inflow. At a non-zero incidence angle, these isolines become skewed. Consideration of this distorted distribution of the flow parameters is important for the discussion presented in section 4.4.3.

The asymmetry in the flow field has been found to have a significant effect on the formation and growth of the spiral vortices. Figure 4.14c shows the instantaneous surface temperature map on a rotating cone with the incidence angle  $\alpha = 4^\circ$ . It is important to observe that the spiral vortices are still present in asymmetric inflow conditions. However, their formation and growth are delayed to a location further downstream compared to the corresponding axial inflow case (compare points  $l_c$  and  $l_m$  in figures 4.14c and 4.6a).

Figure 4.14 shows the corresponding time-averaged velocity field for both rotating (b and d) and non-rotating (a and e) cones under the same operating conditions:  $\alpha = 4^\circ$ ,  $Re_L$  and  $S_b$  (here the direction of the near-wall vectors is an artifact of the finite laser sheet thickness as shown in figure 4.4). When the cone is not rotating, the velocity field is asymmetric, with overall lower  $x'$  velocity in the windward meridian. However, both windward and leeward meridians show the low  $x'$  momentum region close to the wall. When the cone is rotating, the mixing of high and low momentum fluid is observed close to the walls in both windward and



$$S^*(\theta, \alpha, l) = S(l) + \delta_1(\theta, \alpha, l) \quad Re_l^*(\theta, \alpha, l) = Re_l(l) + \delta_2(\theta, \alpha, l)$$

Figure 4.13: A conceptual sketch depicting the distorted distribution of the flow parameters  $S$  and  $Re_l$  due to a non-zero incidence angle, shown as isolines of  $S^* = S|_{l=l_1}$  and  $Re_l^* = Re_l|_{l=l_1}$  at a given location  $l_1$ .

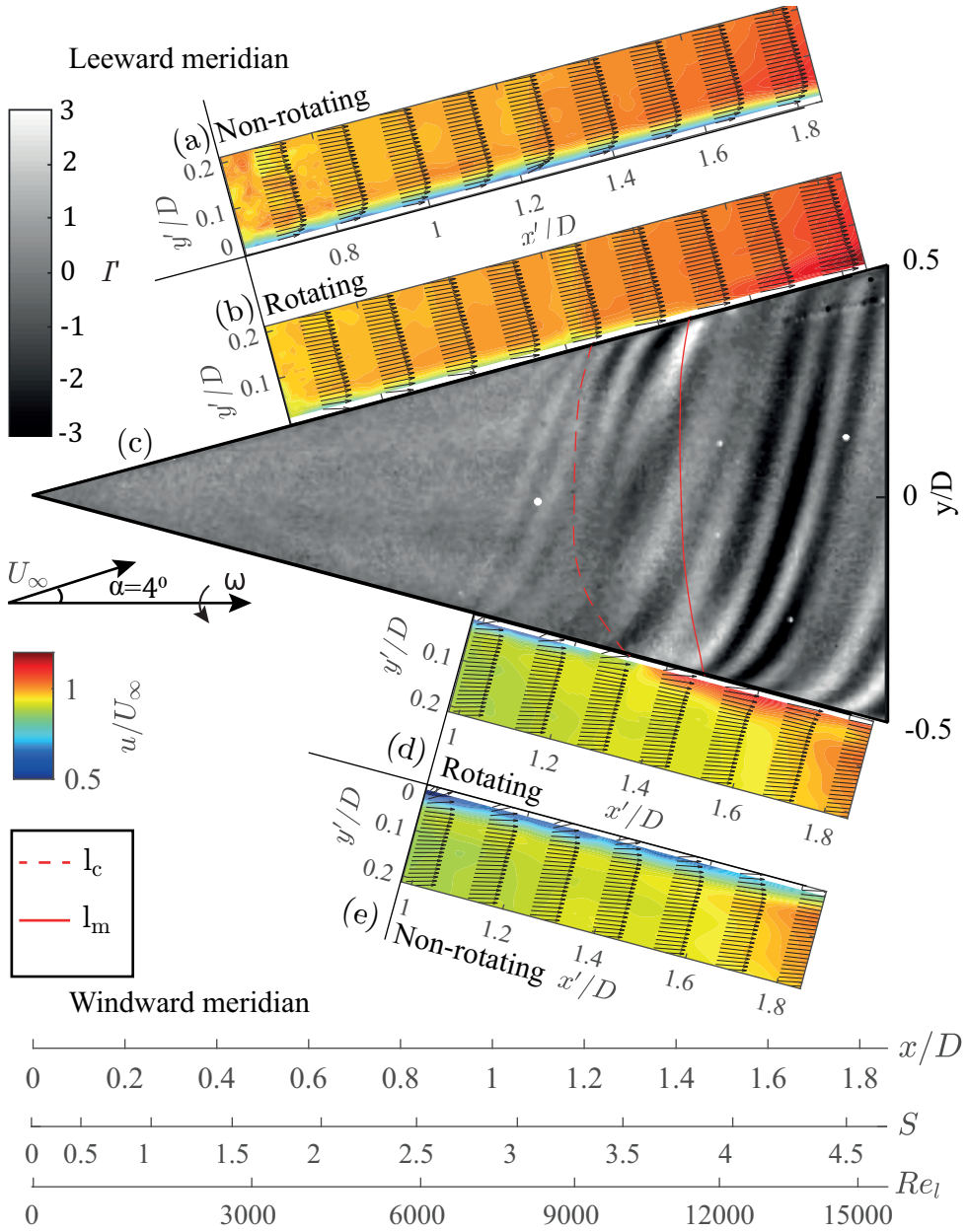


Figure 4.14: (c) Instantaneous surface temperature footprints of the spiral vortices on a rotating cone, and (b and d) time-averaged velocity fields in  $x'y'$  plane for rotating ( $\alpha = 4^\circ$ , operating condition  $I$ :  $S_b = 5$ ,  $Re_L = 1.5 \times 10^4$ ) as well as (a and e) non-rotating case ( $\alpha = 4^\circ$ , operating condition  $VI$ :  $S_b = 0$ ,  $Re_L = 1.5 \times 10^4$ ).

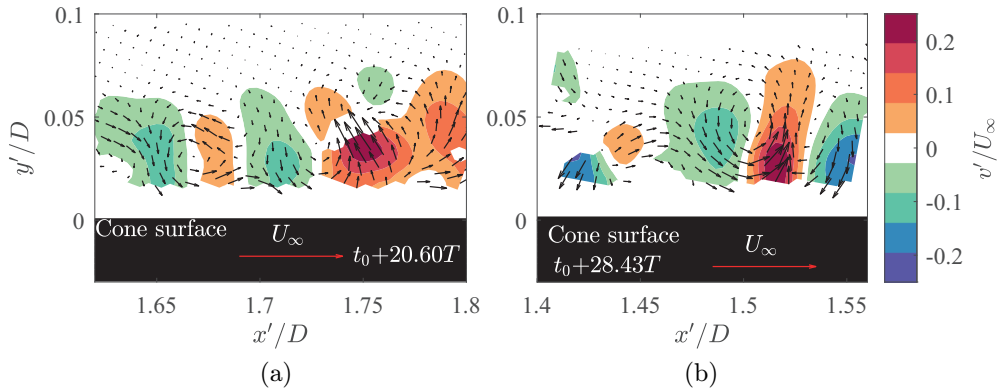


Figure 4.15: Instantaneous velocity fluctuations with respect to the mean flow showing cross-sections of the spiral vortices in (a) windward and (b) leeward meridians ( $\alpha = 4^\circ$ , operating condition  $I : S_b = 5$ ,  $Re_L = 1.5 \times 10^4$ ). Contours represent the wall normal velocity component. Also see movies 4 and 5 (available at <https://doi.org/10.1017/jfm.2020.990>).

leeward meridians, similar to the axial inflow conditions. As a consequence of the delayed growth of the spiral vortices, the mixing is also delayed to the downstream location with respect to the axial inflow case. Additionally, the mixing is gradual in the leeward meridian than the windward meridian. In the windward meridian, the  $x'$  momentum is initially lower due to the incidence angle, but increases after the amplification of the spiral vortices.

Figure 4.14c also shows the loci of critical and maximum amplification points of the spiral vortex growth. These points are distributed at different radii around the cone due to the flow asymmetry, unlike in axial inflow. On the counter-rotating meridian, the critical and maximum amplification points are at lower axial locations ( $x'/D = 1.18$  and  $x'/D = 1.41$  respectively); here, the deviation from the symmetric condition is expected to be highest (see figure 4.11b). The amplification on the leeward meridian occurs at the location with the increased  $x'$  momentum near the wall. However, on the windward meridian, the location where the  $x'$  momentum starts to increase near the wall (around  $x'/D = 1.35$ ) appears to coincide with the critical point of the spiral vortex growth. When comparing the location of amplification for the non-axial inflow to the axial inflow case, the location on the counter-rotating meridian is used.

Figure 4.15 shows the cross-sections of the spiral vortices in the windward and leeward meridians. Contours of wall-normal velocity fluctuations and vectors show the consecutive mutual up-wash and down-wash regions, similar to the axial inflow case (compare with figure 4.7).

Movie 3 (available at <https://doi.org/10.1017/jfm.2020.990>) shows the spiral vortices evolving in the windward meridian; a snapshot from this movie can be seen in figure 4.16. The flow is from left to right, and the angular velocity of the cone is aligned with positive  $x$  axis. The processed PIV images show the vortex cores as dark spots with lower seeding densities (marked as red dots), similar to that shown in movie 2 (available at <https://doi.org/10.1017/jfm.2020.990>). The vortex cores appear to grow significantly around the point  $l_m$  (corresponding to peak  $I'_{RMS}$ ). Comparing movies 2 and 3 (or figures 4.8 and 4.16) shows that, in movie 3 (or figure 4.16), the spiral vortex growth has been delayed to a

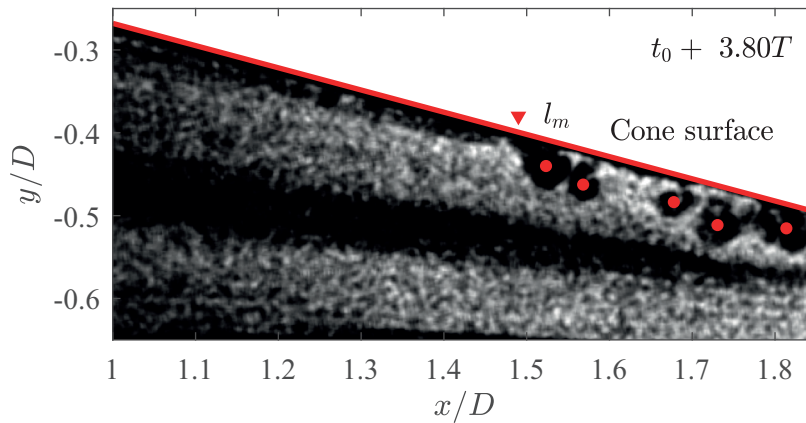


Figure 4.16: Spiral vortices as observed in a PIV recording. Image processing is applied to emphasise seeding density variations. The vortex cores are marked as red dots. Also see Movie 3 (available at <https://doi.org/10.1017/jfm.2020.990>). (Windward meridian,  $\alpha = 4^\circ$ , operating condition I:  $S_b = 5$ ,  $Re_L = 1.5 \times 10^4$ ).

downstream location due to the non-axial inflow. Additionally, movies 4 and 5 (available at <https://doi.org/10.1017/jfm.2020.990>) show the time series of the vector fields shown in figures 4.15a and b, respectively.

Additionally, a comparison of the cases with different incidence angles ( $\alpha = 0^\circ$  to  $10^\circ$ ) is shown in figure 4.17. Note that the spiral vortices appear and get amplified even in the non-axial inflow at investigated inflow Reynolds numbers. The present observations are limited to the measured values of  $Re_L < 2.5 \times 10^4$ .

Figure 4.18 shows the effect of incidence angle on the (a) critical Reynolds number  $Re_{l,c}$  and (b) maximum amplification Reynolds number  $Re_{l,m}$  measured on the counter-rotating meridian, and defined using the edge velocity of the corresponding axial inflow case at same  $Re_L$  and  $S_b$  (Typical correlations between local flow parameters in axial inflow  $S$  and  $Re_L$ , and non-axial inflow  $S^*$  and  $Re_l^*$ , seen in figure 4.12, show that for large meridional shifts (changes in  $l/D$ ) the flow parameters change by similar magnitudes in axial and non-axial inflow). The important observation here is that even a small change in incidence angle delays the critical Reynolds number, and therefore, the amplification of spiral vortices. This is evident by observing that the extent of the delay is much larger when changing the incidence angle from  $0^\circ$  to  $2^\circ$  than  $2^\circ$  to  $4^\circ$ .

In figure 4.18, the critical and maximum amplification points corresponding to the case of  $\alpha = 4^\circ$  appear at slightly lower rotational speed ratio  $S$  as compared to the case of  $\alpha = 2^\circ$ . This is a consequence of using the edge velocity field for the axial inflow case even for the non-axial inflow. Figure 4.19 shows the  $Re_{l,m}^*$  and  $S^*$  computed by using the edge velocity and locations of peak  $I'_{RMS}$  measured by observing windward and leeward meridian separately. Note that, at a meridian, the data points for  $\alpha = 2^\circ$  now appear at lower values of  $S^*$  as compared to the case of  $\alpha = 4^\circ$ . Along a meridian, the effect of increasing incidence angle on the vortices is monotonic, such that with increasing incidence angle the critical and maximum amplification locations appear at higher rotational speed ratios. Overall, the scaling in figure 4.18 can be used to highlight the significant differences between the symmetric and asymmetric flow field.

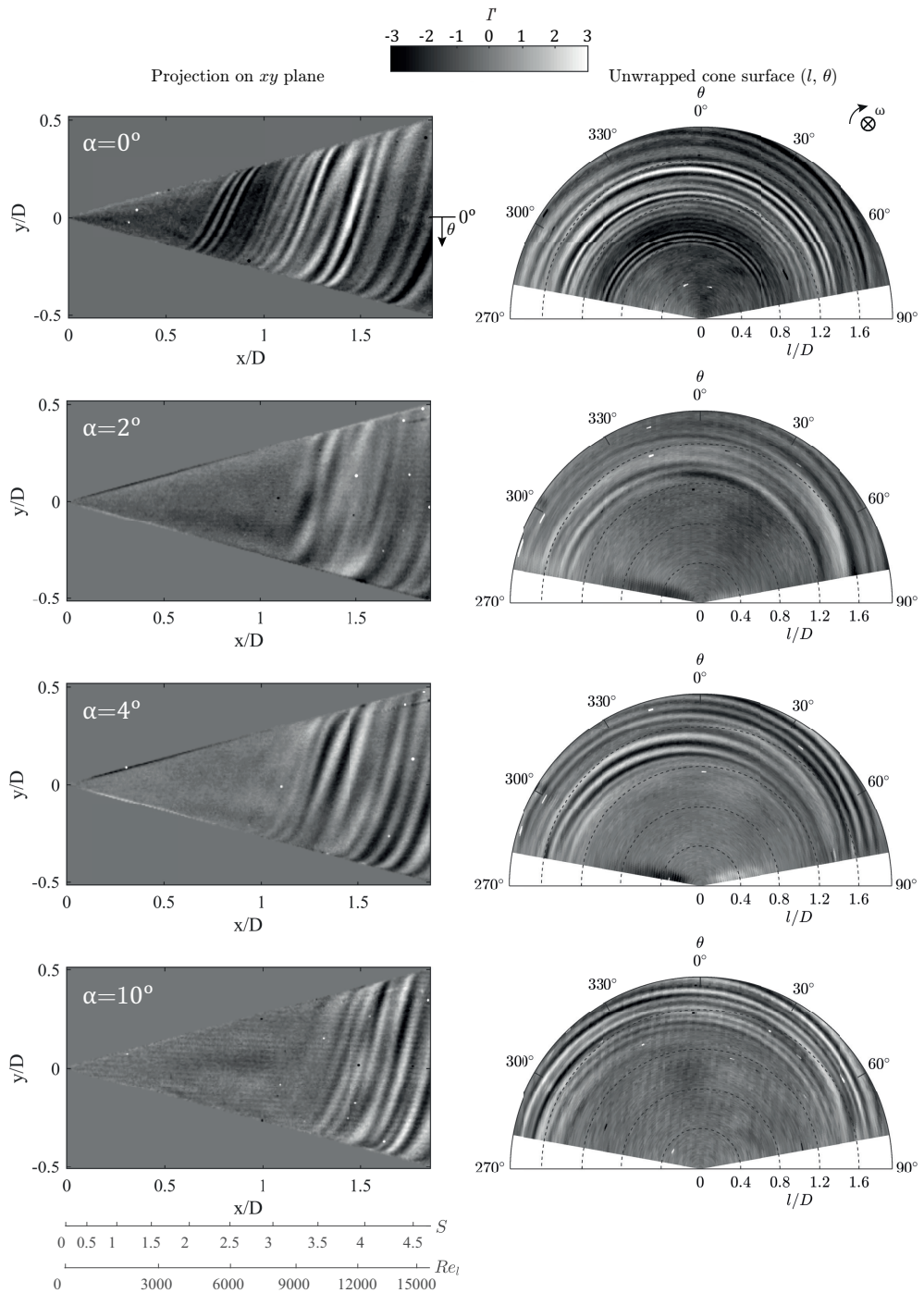


Figure 4.17: Effect of incidence angle variation on the instantaneous surface temperature footprints (at random instances) of the spiral vortices at operating condition  $I$  ( $S_b = 5$ ,  $Re_L = 1.5 \times 10^4$ ), counter-rotating meridian at  $y/D = 0$  (a)  $\alpha = 0^\circ$  (b)  $\alpha = 2^\circ$ , (c)  $\alpha = 4^\circ$ , (d)  $\alpha = 10^\circ$ .

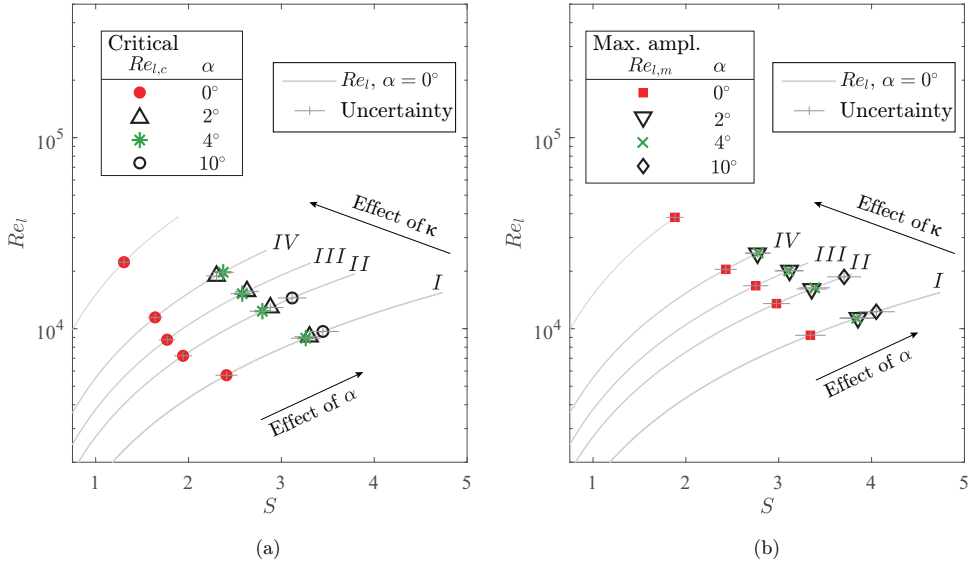


Figure 4.18: Effect of incidence angle on the (a) critical and (b) maximum amplification Reynolds numbers ( $Re_{l,c}$  and  $Re_{l,m}$ ) shown on the scaling from the axial inflow cases ( $Re_l$  and  $S$ ) with the same operating conditions (I)  $S_b = 5$ ,  $Re_L = 1.5 \times 10^4$ , (II)  $S_b = 4$ ,  $Re_L = 1.9 \times 10^4$ , (III)  $S_b = 3.5$ ,  $Re_L = 2.1 \times 10^4$ , and (IV)  $S_b = 3$ ,  $Re_L = 2.5 \times 10^4$ .

**4.4.3. PHYSICAL INTERPRETATION**

The delayed appearance and growth of the spiral vortices in the non-axial inflow can be linked to the following aspects: azimuthal variations (at a constant radius) of the local flow parameters ( $Re_l^*$  and  $S^*$ ), and consequently, the variations in the azimuthal number ( $n$ ) and angle ( $\epsilon$ ) of the most amplified local perturbations that form the spiral vortices.

To obtain the vortex angle  $\epsilon$ , extrema of  $I'$  are tracked along the vortex (within  $y/D = -0.07$  and  $0.07$ ), for example, as shown in figure 4.20a. The azimuthal number of vortices (counter-rotating vortex pairs)  $n$  is obtained from the dark and bright fringes as shown in figure 4.20b. This procedure is repeated at various axial locations for all the cases investigated with IRT to cover a range of rotational speed ratio  $S$ . The invisible side of the cone in figure 4.20 is also investigated separately for all the cases of non-axial inflow.

Figures 4.21 and 4.22 show the variation of azimuthal number of vortices  $n$  and spiral vortex angle  $\epsilon$  with rotational speed ratio  $S$ , respectively, for axial as well as non-axial inflow conditions. Since the rotational speed ratio  $S^*$  circumferentially varies in non-axial inflow, and the complete three-dimensional velocity measurements around the rotating cone are unavailable here, the spiral vortex characteristics ( $n$  and  $\epsilon$ ) are presented against the rotational speed ratio  $S$  from the corresponding axial inflow case (typical correlation between  $S$ ,  $S^*$  and meridional location  $l$  can be found in figure 4.12a). The overall trends of spiral vortex characteristics ( $n$  and  $\epsilon$ ) against the rotational speed ratio  $S$  are similar for axial and non-axial inflows. Importantly, the values of  $n$ ,  $\epsilon$ ,  $|dn/dS|$  and  $|d\epsilon/dS|$  decrease with increasing rotational speed ratio  $S$ .

Generally, a range of perturbations with different wavelengths and orientations can grow in an unstable boundary-layer, but the local flow conditions determine the wavelengths that

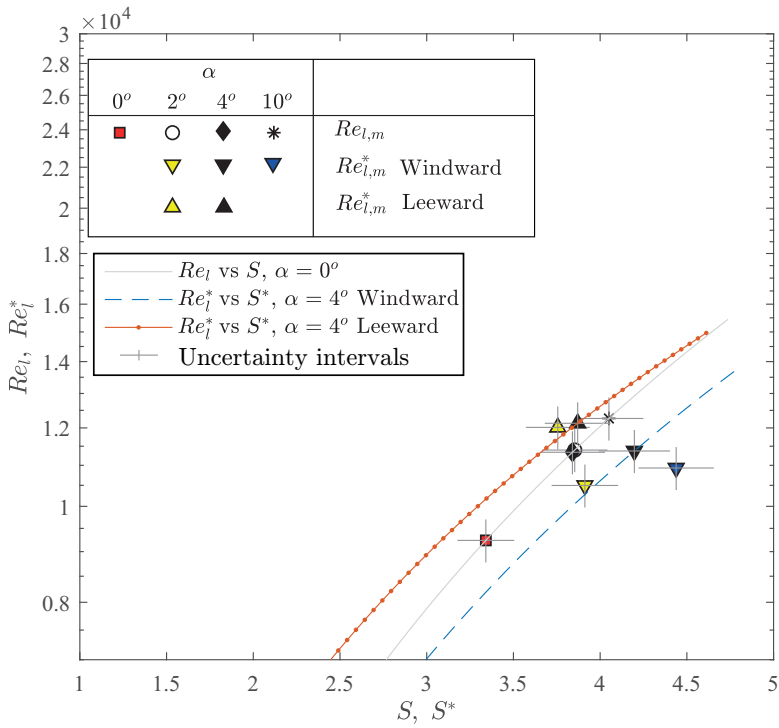


Figure 4.19: Effect of incidence angle on the maximum amplification Reynolds number, with the scaling obtained from the local edge velocity in the symmetry plane.

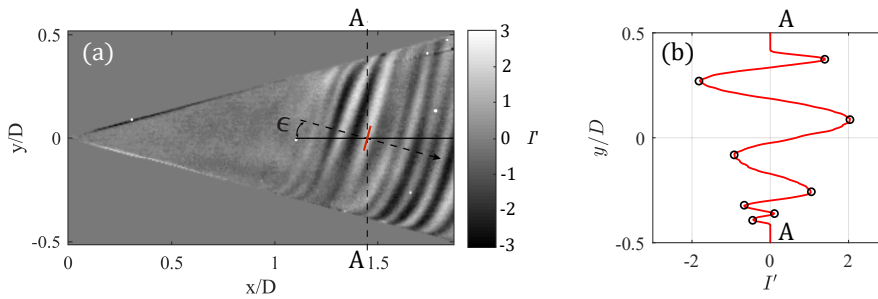


Figure 4.20: An example showing how (a) spiral vortex angle  $\epsilon$  and (b) azimuthal number  $n$  are extracted from the reconstructed surface temperature footprints ( $\alpha = 4^\circ$ , operating condition  $I$ :  $S_b = 5$ ,  $Re_L = 1.5 \times 10^4$ ).

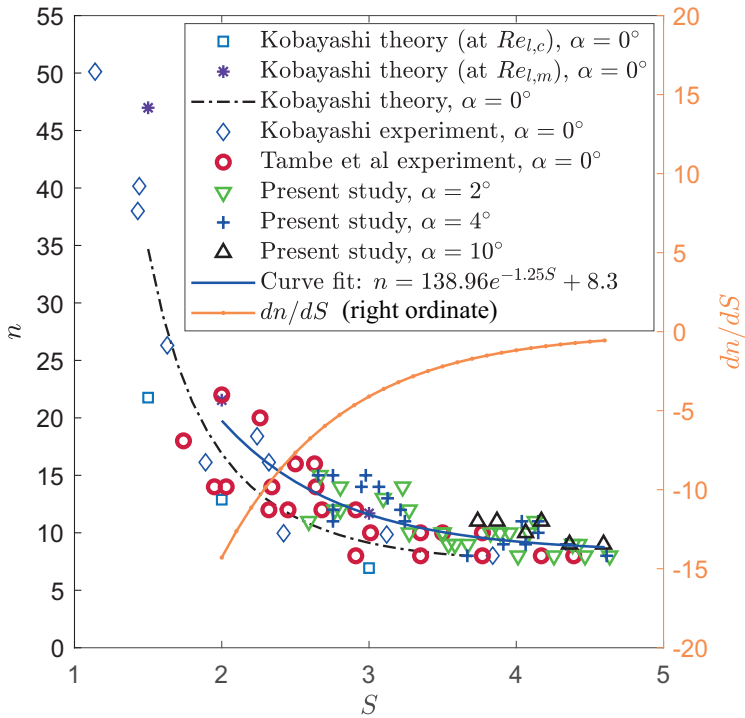


Figure 4.21: Azimuthal number of vortices  $n$  in non-axial inflow compared with the axial inflow cases from Kobayashi et al. (1983) and Tambe et al. (2019).

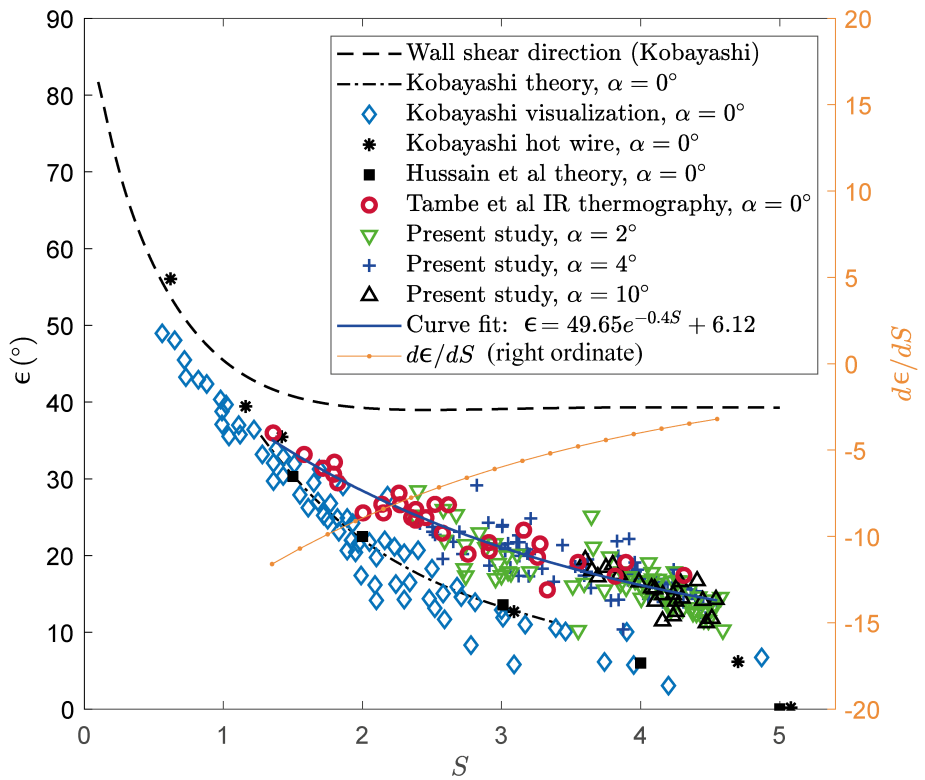


Figure 4.22: Spiral vortex angle  $\epsilon$  for non-axial inflow compared with the axial inflow cases from Hussain et al. (2016), Kobayashi et al. (1983), and Tambe et al. (2019).

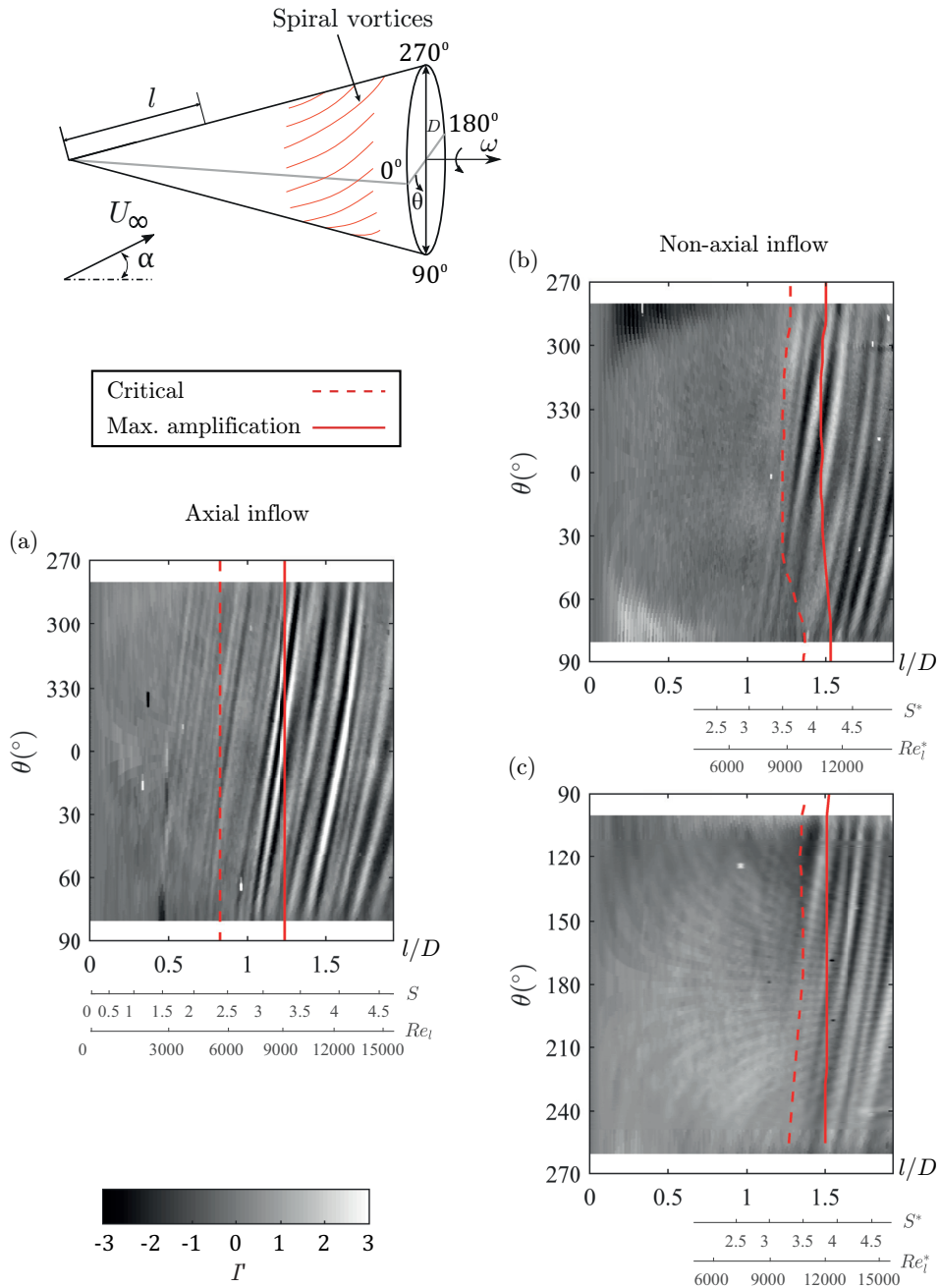


Figure 4.23: Comparison of the spiral vortex footprints over the unwrapped cone surface for (a)  $\alpha = 0^\circ$ , (b),(c)  $\alpha = 4^\circ$  (b and c are instances acquired in separate measurements) at operating condition  $I$ :  $S_b = 5$ ,  $Re_L = 1.5 \times 10^4$ .

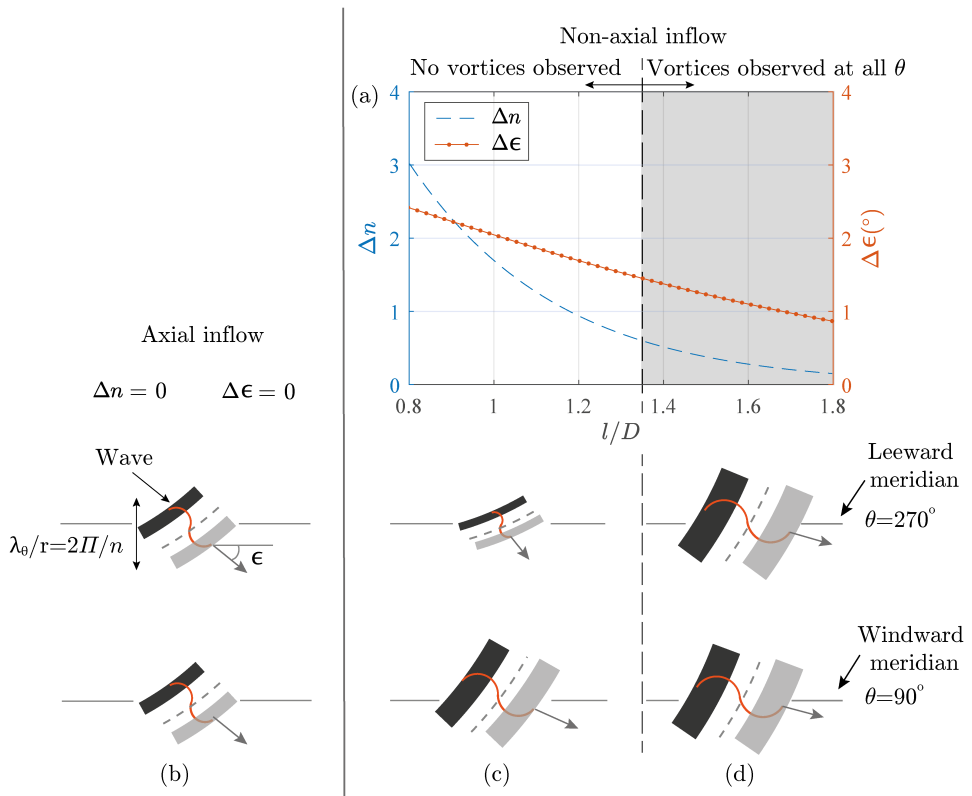


Figure 4.24: Azimuthal differences (between leeward and windward meridians) in vortex number  $n$  and angle  $\epsilon$  shown as (a) estimates for  $\alpha = 4^\circ$ , at operating condition  $I$ :  $S_b = 5$ ,  $Re_L = 1.5 \times 10^4$ , and as schematic waves for (b) axial and (c), (d) non-axial inflow.

can outgrow the rest (Drazin, 2002). On a rotating cone, an additional constraint restricts the azimuthal wavelengths ( $\lambda_\theta$ ) that may grow such that there is an integer number ( $n$ ) of spiral vortices around the cone at a given radius; because any remainder fraction of a wave can not sustain as a vortex. For an axial inflow, the local flow parameters ( $S$  and  $Re_l$ ) are constant along the azimuth for a given radius. Ideally, this condition allows the growth of a same wavelength (such that  $\lambda_\theta/r = 2\pi/n$ ) at a same angle ( $\epsilon$ ) around the azimuth (at a given radius). However, in non-axial inflow, the local flow parameters ( $S^*$  and  $Re_l^*$ ) azimuthally vary at a given radius. Moreover, their isolines are skewed (as shown in figure 4.13). Such locally varying conditions can give rise to different wavelengths at different orientation around the azimuth, which can inhibit the formation of azimuthally coherent spiral vortices.

The non-axial inflow disturbs the azimuthal coherence of the instantaneous spiral vortex footprints. This is evident from figure 4.23, which shows the unwrapped surfaces of a rotating cone for axial and non-axial inflow. In the axial inflow (figure 4.23a), the spiral vortex footprints show strong coherence (less azimuthal variation in spacing and orientation) from  $l/D = 0.6$  to their maximum amplification at  $l/D = 1.24$ , after which the coherence decreases. Figures 4.23 b and c are uncorrelated instances from separate measurements on the opposite sides of the cone at  $\alpha = 4^\circ$ . Here, the local flow parameters  $S^*$  and  $Re_l^*$  vary azimuthally, as shown at the windward ( $\theta = 90^\circ$ ) and leeward ( $\theta = 270^\circ$ ) meridians for figures 4.23 b and c. Consequently, the vortex footprints show an overall weak azimuthal coherence, as their spacing and orientation vary along the azimuth. Additionally, the critical and maximum amplification loci also show azimuthal variations in contrast with the axial inflow where there is no such azimuthal variation.

Relating to the cases from figure 4.23, the azimuthal variations in the local instability characteristics are shown in figure 4.24. The most amplified perturbation waves are schematically shown at leeward and windward meridians (figures 4.24b, c and d). The azimuthal differences (between leeward and windward meridians) of vortex number  $\Delta n$  and angle  $\Delta\epsilon$  (figure 4.24a) are estimated using the experimental data (figures 4.21 and 4.22), where the respective trends of  $n$  and  $\epsilon$  versus the rotational speed ratio  $S$  agree for axial and non-axial inflow (from  $S = 2.5$ -4.6). For the estimation purpose, the local values of  $n$  and  $\epsilon$  are obtained by replacing  $S$  with  $S^*$  in the curve fits (figures 4.21 and 4.22). This approximation is based on the assumption that the local effects of rotation (relative to the edge velocity) on the local instability characteristics are similar in axial and non-axial inflow, e.g. stronger rotation (higher  $S$  or  $S^*$ ) promotes longer azimuthal wavelengths (lower  $n$ ) with their wavefronts oriented more towards the tangential velocity of rotation (lower  $\epsilon$ ). These approximate estimates in figure 4.24a shall only be interpreted for their qualitative trends. Here, both  $\Delta n$  and  $\Delta\epsilon$  are large initially (at  $l/D < 1.35$ ), which suggests a large variation in most amplified perturbation waves around the azimuth as depicted in figure 4.24c. This is the region where no vortices are observed ( $l/D < 1.35$  in figures 4.23 b and c). Further downstream (where overall  $S^*$  values increase), the differences  $\Delta n$  and  $\Delta\epsilon$  decrease, suggesting that similar perturbation waves can grow around the azimuth (see figure 4.24d), similar to the axial inflow case (figure 4.24b). This is the region where the spiral vortices are observed. This shows that at increased rotational speed ratios, the azimuthal coherence is approached, which promotes the growth of the spiral vortices around the cone surface in the non-axisymmetric flow-field.

## 4.5. CONCLUSION

The spiral vortices, induced by the centrifugal instability, over the rotating slender cone ( $\psi = 15^\circ$ ) were visualised by their surface temperature footprints, obtained by the infrared thermography coupled with POD approach. Incidence angles  $\alpha = 0^\circ, 2^\circ, 4^\circ$ , and  $10^\circ$  were investigated. The measured surface temperature fluctuations show the growth of spiral vortices over the rotating slender cone. For axial inflow, the critical and maximum amplification locations of the spiral vortex growth (in parameter space of Reynolds number and rotational speed ratio) agreed with the past literature, validating the approach.

The conclusions are summarised as follows:

1. The asymmetry of the non-axial inflow inhibits the initial growth of the spiral vortices. However, spiral vortices, induced by the centrifugal instability, were detected at a higher local rotational speed ratio  $S$  and local Reynolds number  $Re_l$  as compared to the corresponding axial inflow case.
2. The azimuthal variation of local Reynolds number and rotational speed ratio in non-axial inflow causes azimuthally varying instability characteristics (azimuthal number  $n$  and angle  $\epsilon$  of the most amplified perturbations). It is postulated that these variations may inhibit the growth of azimuthally coherent spiral vortices.
3. However, at a higher local rotational speed ratio, the instability characteristics (azimuthal vortex number  $n$  and vortex angle  $\epsilon$ ) become less sensitive to the changes in local flow parameters, which allows the spiral vortices to grow.

It should be noted that, the present study does not deny other possible phenomenological differences (different instability mechanisms) in asymmetric flow around the rotating cone. However, such phenomena, caused by asymmetry itself, are expected to be azimuthally incoherent. The centrifugal instability appears to be overall dominant in the region with increased azimuthal coherence of its instability characteristics. Understanding other secondary phenomena and their relative importance with respect to the observed centrifugal instability needs a separate investigation.

Although the investigations in this study are of fundamental nature, the results are relevant for various engineering applications in which a rotating slender cone faces non-axial inflow. In novel aircraft propulsion concepts, the aero engine spinners may face non-axial inflow when the embedded engines ingest the airframe boundary-layer, or when the flow separates in the short intakes of the ultra high bypass ratio engines (UHBR). In these cases, the spiral vortices may still appear on a rotating slender cone, but their formation and growth will be delayed to a downstream location compared to the axial inflow at the same operating conditions. These vortices can alter the distortion and blade incidence angles at the blade-hub junction, thus changing the loss mechanisms (as conceptually discussed in section 8.2). However, the inflow Reynolds number ( $Re_L \leq 2.5 \times 10^4$ ) and Mach number ( $M < 0.02$ ) of the present study do not cover the whole range of the flow conditions encountered in aviation. In this regards, investigating the Reynolds and Mach number effects on the boundary-layer instability on a rotating cone is still an open question. Moreover, the boundary-layer instability over the cones of different half angles rotating in axial or non-axial inflow has still not been experimentally investigated. This is particularly challenging because between half angles  $30^\circ - 40^\circ$ , the instability mechanism changes from the centrifugal to the cross-flow (Kobayashi, 1994).

# 5

## THE EFFECT OF HALF-CONE ANGLE

### 5.1. INTRODUCTION

THE centrifugal instability on a slender cone, with half-cone angle  $\psi = 15^\circ$ , rotating in axial inflow has been extensively investigated in the past by Hussain et al., 2016; Kobayashi and Izumi, 1983; Y. Kohama, 1984a (as described in chapter 2). Chapters 3 and 4 investigated the boundary-layer instability on a rotating slender-cone of half-cone angle  $\psi = 15^\circ$ . However, commonly used aero-engine-nose-cones are often not restricted to the slender cones but are found in a wide range of half-cone angles. Therefore, from a wider application standpoint, it is important to know the boundary-layer instability behaviour on rotating cones of different half-cone angles. This chapter shows how changing the half-cone angle  $\psi$  affects the boundary-layer instability on rotating cones in axial inflow.

In still fluid, Kobayashi et al., 1983 have shown that with increasing half-cone angle  $\psi$ , the boundary-layer instability mechanism changes from centrifugal to crossflow. This change occurs at approximately  $\psi \approx 30^\circ$ . Such behaviour was also reported by Kobayashi et al., 1987 when they studied rotating cones ( $\psi = 7.5^\circ, 15^\circ, \text{ and } 30^\circ$ ) in axial inflow with varying turbulence levels. Detailed discussion on these studies has been presented in section 2.3 of chapter 2. However, no such experimental measurements are available for rotating broad cones ( $\psi > 30^\circ$ ) in axial inflow. Garrett et al., 2010 explicitly highlighted the lack of experimental data to compare their theoretical predictions of crossflow instability on rotating broad cones in axial inflow. Such measurements are considered useful for the theoretical analyses which are aimed at investigating the underlying flow physics of the instability. This is useful in understanding the boundary-layer instability on a wide range of slender and broad nose-cones in different aero-engines. Therefore, it is necessary to extend the experimental investigations to larger half-cone angles  $\psi \geq 15^\circ$ .

This chapter provides measurements of the instability-induced spiral vortices on rotating cones in axial inflow. Cones with half-cone angles  $\psi = 15^\circ, 22.5^\circ, 30^\circ, 45^\circ \text{ and } 50^\circ$  are tested using the experimental method described in chapter 3. The present chapter shows how the half-cone angle affects the critical flow parameters of the spiral vortex growth, the spiral vortex angle  $\epsilon$  and azimuthal vortex number  $n$ . The data is compared against the theoretical predictions of Garrett et al., 2010 and the past measurements of Kobayashi et al., 1987.

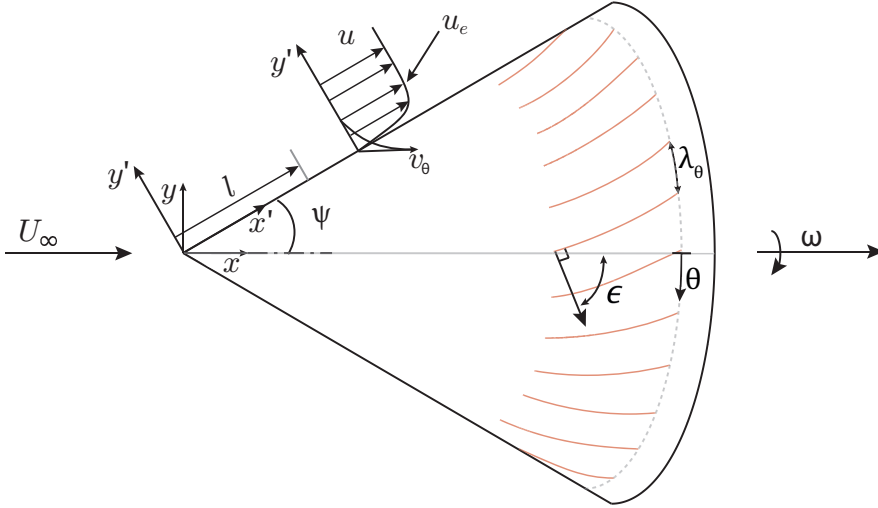


Figure 5.1: Schematic of a rotating cone in axial inflow.

## 5.2. FLOW PARAMETERS

Figure 5.1 shows the schematic of a rotating cone in axial inflow. Here,  $u_e$  is the meridional velocity at the boundary-layer edge,  $l$  is the meridional distance from the cone apex, and  $\omega$  is the angular velocity of the cone. The azimuthal wavelength  $\lambda_\theta$  is the circumferential spacing between the spiral vortices. The spiral vortex angle  $\epsilon$  is the angle of a spiral vortex with respect to the meridian.

Past experiments have shown that parameters  $Re_l = u_e l / \nu$  and  $S = r\omega / u_e$  govern the spiral vortex growth on rotating cones of  $\psi \leq 30^\circ$  (Kobayashi et al., 1987), here  $\nu$  represents the kinematic viscosity. Theoretical predictions of Garrett et al., 2010 suggest that this behaviour can also be expected for the rotating broad cones of  $\psi > 40^\circ$ . Therefore, the present investigation focuses on exploring the parameter space of  $Re_l$  and  $S$  to detect the spiral vortex growth for increasing cone angles.

The inflow Reynolds number  $Re_L$  and base rotational speed ratio  $S_b$  are used while referring to the inflow conditions. These are defined as follows:  $Re_L = U_\infty L / \nu$  and  $S_b = D\omega / 2U_\infty$ . Here,  $U_\infty$  is the free-stream velocity,  $L$  is the total meridional length of a cone, and  $D$  is the cone diameter.

## 5.3. EXPERIMENTS

The measurement and data-processing approaches are the same as presented in chapter 3. The experimental arrangements of IRT and PIV are shown in figure 5.2. Figure 5.3 shows a photograph of the measurement setup. The free-stream velocity  $U_\infty$  is varied from 0.7 – 10.9 m/s. The free-stream turbulence level  $u'_{RMS}$  is typically below 1% of  $U_\infty$ . Here,  $u'_{RMS}$  is the r.m.s. of fluctuations in the free-stream velocity  $U_\infty$ . The cones, made of Polyoxymethylene (POM), are axially aligned with the free-stream and rotated at 2900 – 13500 RPM using a brushless motor. Figures 5.2 and 5.3 show the experimental arrangement. The

experimental procedure is similar to those used in chapters 3 and 4.

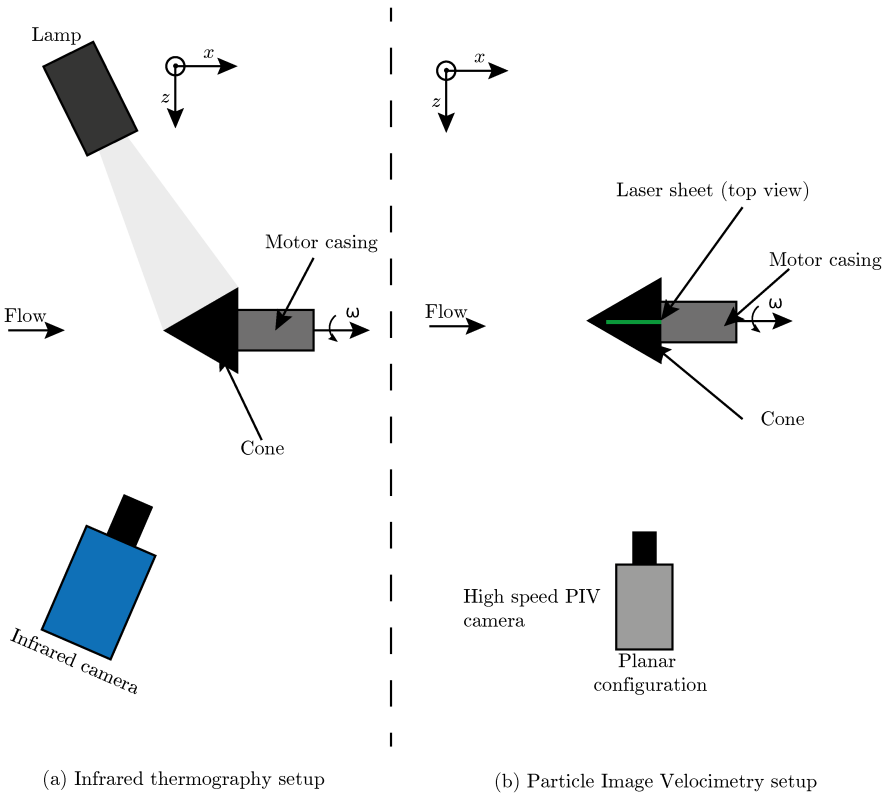


Figure 5.2: Schematic of the experimental arrangements a) infrared thermography and b) particle image velocimetry.

First, the half-cone angles of  $\psi = 15^\circ$  and  $30^\circ$  are chosen for the investigations to compare with the previous measurements and theoretical results of Kobayashi et al., 1987. Additionally, a broad cone of  $\psi = 50^\circ$  is chosen to compare the experimental findings with the predictions of Garrett et al., 2010. Finally, a slender cone of  $\psi = 22.5^\circ$  and a broad cone of  $\psi = 45^\circ$  are also included in order to study intermediate values. All the cones have the same base diameter  $D = 0.1\text{m}$ .

The meridional velocity field is measured using two-component high-speed particle image velocimetry (PIV), see figure 5.2b. The data is acquired and processed using a commercial software DaVIs 8.4.0. A multi-pass cross-correlation approach with decreasing interrogation window size is used to obtain the instantaneous velocity vectors from the image pairs. Table 5.2 details the specification of the PIV setup.

Generally, the instability characteristics of a flow-system depend on its basic flow. As the instability-induced flow features grow upon this basic flow, they can significantly alter the basic velocity profiles. Previous studies (Garrett et al., 2010; Hussain, 2010; Kobayashi & Izumi, 1983) have shown that the boundary-layer edge velocity  $u_e$  of this basic flow can be assumed to be equal to a wall parallel velocity of the potential flow over a cone. This assumption leads to the form of  $u_e = U_\infty C l^m$ , where  $m$  and  $C$  are determined for a given

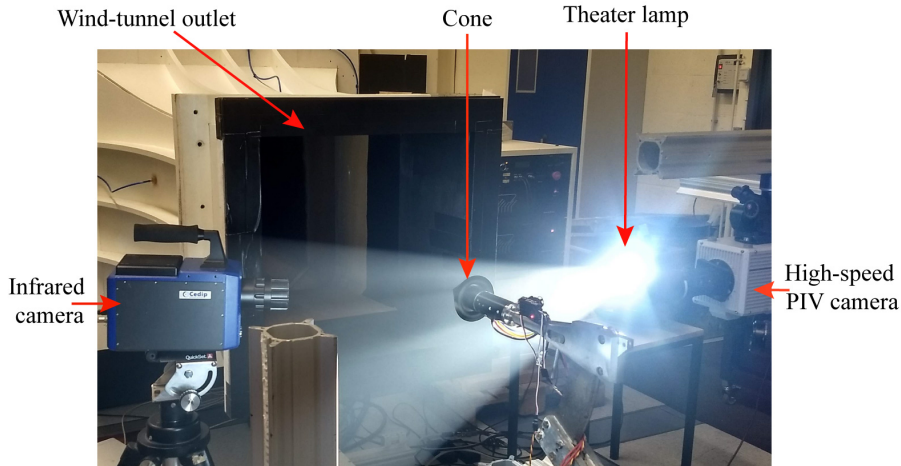


Figure 5.3: A photograph showing the measurement setup.

5

Camera	FLIR (CEDIP) SC7300 Titanium
Noise equivalent temperature difference (NETD)	25 mK
Spatial resolution	0.49 – 0.51 mm/px
Integration time	106 – 205 $\mu$ s
Acquisition frequency	200 Hz
Number of images per dataset	2000
Heat source	Theatre lamp (575 W)

Table 5.1: Specifications of the Infrared Thermography setup.

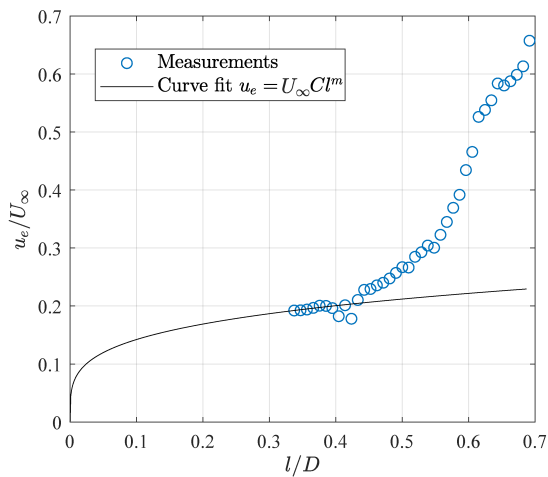
half-cone angle and free-stream conditions. However, Kobayashi et al., 1987 have shown that although the measured  $u_e$  closely follows the form  $U_\infty Cl^m$  for the slender cones ( $\psi = 7.5^\circ$  and  $15^\circ$ ), it deviates near the base of a broader cone ( $\psi = 30^\circ$ ). Here, the measured  $u_e$  tends to be higher than  $U_\infty Cl^m$  towards the base. To facilitate comparisons with theory and past experiments, the boundary-layer edge velocity of the basic flow is assumed to be of the form  $u_e = U_\infty Cl^m$ , where  $C$  and  $m$  are determined by a least-square fit to the measurements away from the base and before the onset of the spiral vortices, for example, see figure 5.4. Here, the boundary layer edge velocity is measured from a time-averaged velocity field; at a location away from the wall where the vorticity value reduces to that of the measurement uncertainty ( $< 0.3U_\infty/D$ ). Figure 5.4 shows that measured boundary layer velocity follows the form  $u_e = U_\infty Cl^m$  at first but deviates from it towards the base of the cone, as expected.

#### 5.4. VISUALISATION OF SPIRAL VORTEX FOOTPRINTS

As described in the chapters 3 and 4, when spiral vortices grow in a boundary-layer, they alter the surface-temperature pattern on a rotating cone. In their down-wash, the vortices increase the shear near the wall. This causes increased heat transfer between the fluid and the cone surface. Contrarily, up-wash decreases such heat-transfer. This causes cold/hot

Camera	Photron Fastcam SA-1
Sensor dimensions	1024 × 1024 px
Vector pitch (2C)	0.26 mm
Interrogation window size	1.04 mm × 1.04 mm
Spatial resolution	30.7 px/mm
Laser	Nd:YAG Quantronix Darwin Duo 527-80-M
Acquisition frequency	2 kHz
Number of image pairs per dataset	2000
Seeding	Smoke particles (diameter ≈ 1 μm)

Table 5.2: Specifications of the PIV setup.

Figure 5.4: An example showing the estimated edge velocity of the basic flow vs the measured edge velocity for  $\psi = 45^\circ$ .

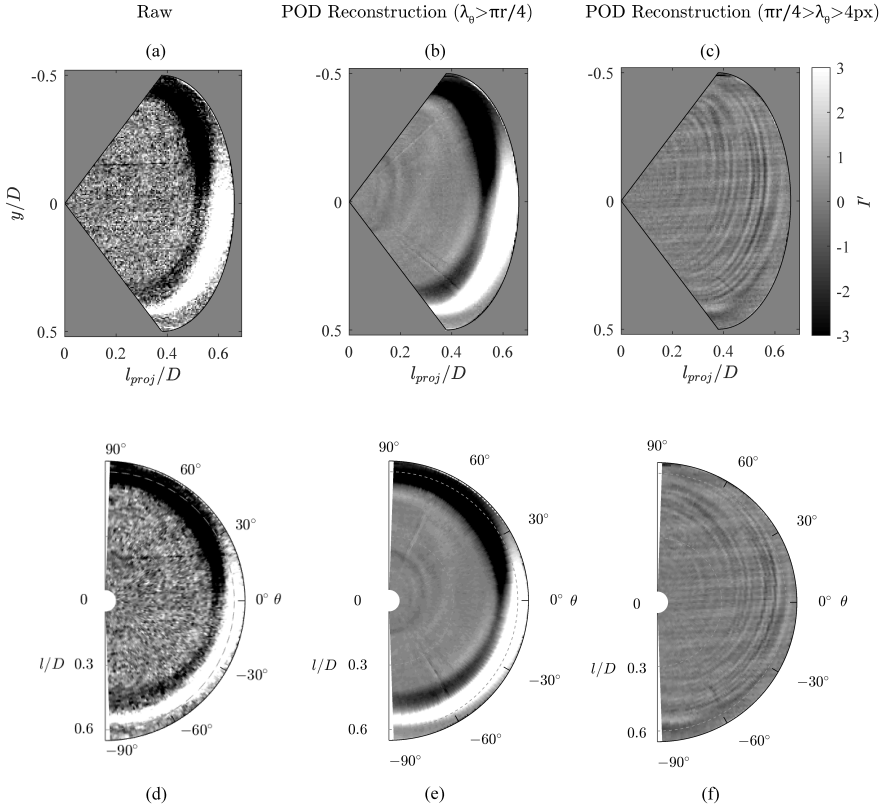


Figure 5.5: Visualisation of the spiral vortex footprints on a rotating cone of  $\psi = 50^\circ$  ( $Re_L = 9.7 \times 10^3$ ,  $S_b = 30.6$ ). (a),(d) raw, (b),(e) POD reconstruction of long wavelengths  $\lambda_\theta > \pi r/4$ , and (c),(f) POD reconstruction of short wavelengths  $\pi r/4 > \lambda_\theta > 4px$ . Top row is as observed in the camera frame and the bottom row contains the respective unwrapped views.

regions on the cone surface that are observed as darker/brighter regions in an infrared image, revealing the footprint of the spiral vortices.

Figure 5.5 visualises different types of temperature fluctuation patterns on a rotating cone of  $\psi = 50^\circ$ . Here, the top row contains the projections of a three dimensional cone in a camera sensor plane and the bottom row contains their unwrapped cone surfaces in polar coordinates  $l$  and  $\theta$ . Figures 5.5a and d show a raw snapshot. Here, the spiral vortex footprints are subtle, because the image is dominated by the noise from the infrared sensor. The spiral vortex footprints become distinctly clear in a low order representation of the snapshot, as seen in figures 5.5c and f. This representation is reconstructed from the POD modes containing the azimuthal wavenumber  $\lambda_\theta$  between  $\pi r/4$  and  $4px$  (see chapter 3 for the detailed selection procedure).

However, the most striking pattern in the raw snapshot (figures 5.5a and d) is the dark and bright spiral with the azimuthal wavenumber  $\lambda_\theta \approx \pi r$ . This pattern is isolated from the raw snapshot by reconstructing POD modes of azimuthal wavenumbers  $\lambda_\theta > \pi r/4$ , as shown in figures 5.5b and e. The temperature fluctuations on the rotating cone involve two distinct

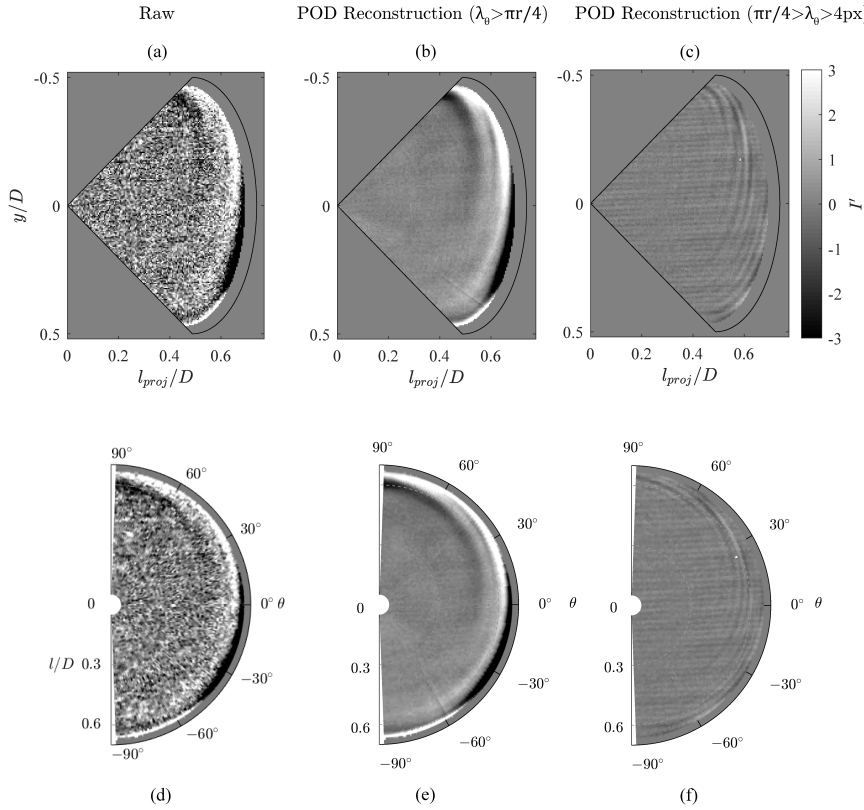


Figure 5.6: Visualisation of the spiral vortex footprints on a rotating cone of  $\psi = 45^\circ$  ( $Re_L = 1 \times 10^4$ ,  $S_b = 27.1$ ). (a),(d) raw, (b),(e) POD reconstruction of long wavelengths  $\lambda_\theta > \pi r/4$ , and (c),(f) POD reconstruction of short wavelengths  $\pi r/4 > \lambda_\theta > 4px$ . Top row is as observed in the camera frame and the bottom row contains the respective unwrapped views.

patterns: a short wavelength pattern ( $\lambda_\theta < \pi r/4$ ) relating to the spiral vortices (figures 5.5c and f) and a long wavelength pattern ( $\lambda_\theta > \pi r/4$ ). Comparing figures 5.5b and c (or e and f) shows that the spiral vortices coexist with the long wavelength pattern but their spacing starts to vary along the azimuth, i.e. their azimuthal coherence is disturbed in this region. The flow phenomena in the region of long wavelength pattern is further discussed in section 5.5 along with the velocity fields.

Figure 5.6 shows that the temperature fluctuation patterns on a rotating cone of  $\psi = 45^\circ$  is similar to that on a rotating  $\psi = 50^\circ$  cone (figure 5.5). Here, both short and long wavelength patterns exist. Together figures 5.5 and 5.6 confirm the existence of the spiral vortices on rotating broad cones ( $\psi > 30^\circ$ ) in axial inflow.

Furthermore, the temperature fluctuation patterns on the rotating slender cone  $\psi = 22.5^\circ$  also show two types of spiral patterns as the broad-cones, see figure 5.7. Figure 3.8 has also shown the existence of the two types of short and long wavelength patterns in the POD modes on a rotating cone of  $\psi = 15^\circ$ . This indicates that the spiral vortices and the long wavelength pattern are distinct universal features that appear in the transitional boundary-layer on both

slender and broad rotating cones.

## 5.5. SPIRAL VORTEX GROWTH

Since the spiral vortex growth on rotating slender cones has been extensively investigated in the past (chapter 4, Kobayashi and Izumi, 1983; Y. Kohama, 1984a), this section first focuses on the case of a rotating broad cone in axial inflow. The growth of the spiral vortices can be tracked through its effects on the surface temperature fluctuations and the velocity fields. To facilitate this, figure 5.8 compares the following quantities on a rotating broad cone of  $\psi = 50^\circ$ : RMS of surface temperature fluctuations  $I'_{RMS}$  along the meridian (figure 5.8a), time-averaged velocity field in a meridional plane (figure 5.8b), instantaneous vorticity field in a meridional plane (figure 5.8c), and a combined POD reconstruction of short and long wavelength patterns (figure 5.8d, relating to the snapshot in figure 5.5). Note that figures 5.8(c) and (d) are uncorrelated instances.

Here, as the spiral vortices start growing in the boundary-layer, their surface temperature footprint starts to get stronger. This is evident from figure 5.8a where  $I'_{RMS}$  starts to increase at around  $l/D \approx 0.4$ . Around this location the vorticity field in figure 5.8c shows an unidirectional wavy pattern suggesting the presence of co-rotating spiral vortices. Such co-rotating spiral vortices have been previously linked to the cross-flow instability, as discussed in chapter 2.

Further downstream in figure 5.8, at around  $l/D \approx 0.5$ ,  $I'_{RMS}$  suddenly increases. This meridional location is defined here as a critical location  $l_c$  where the spiral vortices start their rapid growth, and corresponding critical Reynolds number is defined as  $Re_{l,c} = l_c u_e / \nu$ . Figure 5.8d reveals that the critical location coincides with the onset of the long wavelength pattern, overlaid on the short wavelength footprints of the spiral vortices. This suggests that the long wavelength pattern is linked to the rapid growth of the spiral vortices. Determining its role in the spiral vortex amplification requires a non-linear theoretical analysis.

During their rapid growth, the spiral vortices reach maximum amplification at  $l/D \approx 0.57$ . Here,  $I'_{RMS}$  reaches its peak (figure 5.8a). The meridional location of this peak is defined as the location of maximum amplification  $l_m$ . The corresponding Reynolds number is termed as the maximum amplification Reynolds number  $Re_{l,m} = l_m u_e / \nu$ . The time-averaged velocity field (figure 5.8b) reveals that, around the maximum amplification location, the spiral vortices start to significantly increase the near wall momentum.

The enhanced mixing near the maximum amplification has also been observed for the centrifugal instability on the rotating slender cone of  $\psi = 15^\circ$  (see figure 4.6 in chapter 4). Furthermore, this marks a significant departure from the basic flow on the rotating cones which is usually estimated without considering the effect of instability-induced spiral vortices (as seen in figure 5.4).

The instantaneous vorticity field (figure 5.8c) clearly shows how the vortices have amplified around the maximum amplification location  $l/D \approx 0.57$ . Here, as the spiral vortices amplify and move away from the wall, their counter-rotating part appears as the region of negative vorticity. This observation is similar to that made by Kobayashi et al., 1983 for a  $\psi = 30^\circ$  cone rotating in still fluid. They also observed that the spiral vortices first emerged as co-rotating and further downstream turned into a counter-rotating pair. It is apparent from figure 5.9, taken from Kobayashi et al., 1983, that the direction of rotation of co-rotating spiral vortices is the same as the direction of the positive vorticity observed in the present figure 5.8c. The present observations (for  $\psi \leq 50^\circ$ ) confirm that although on broad-cones

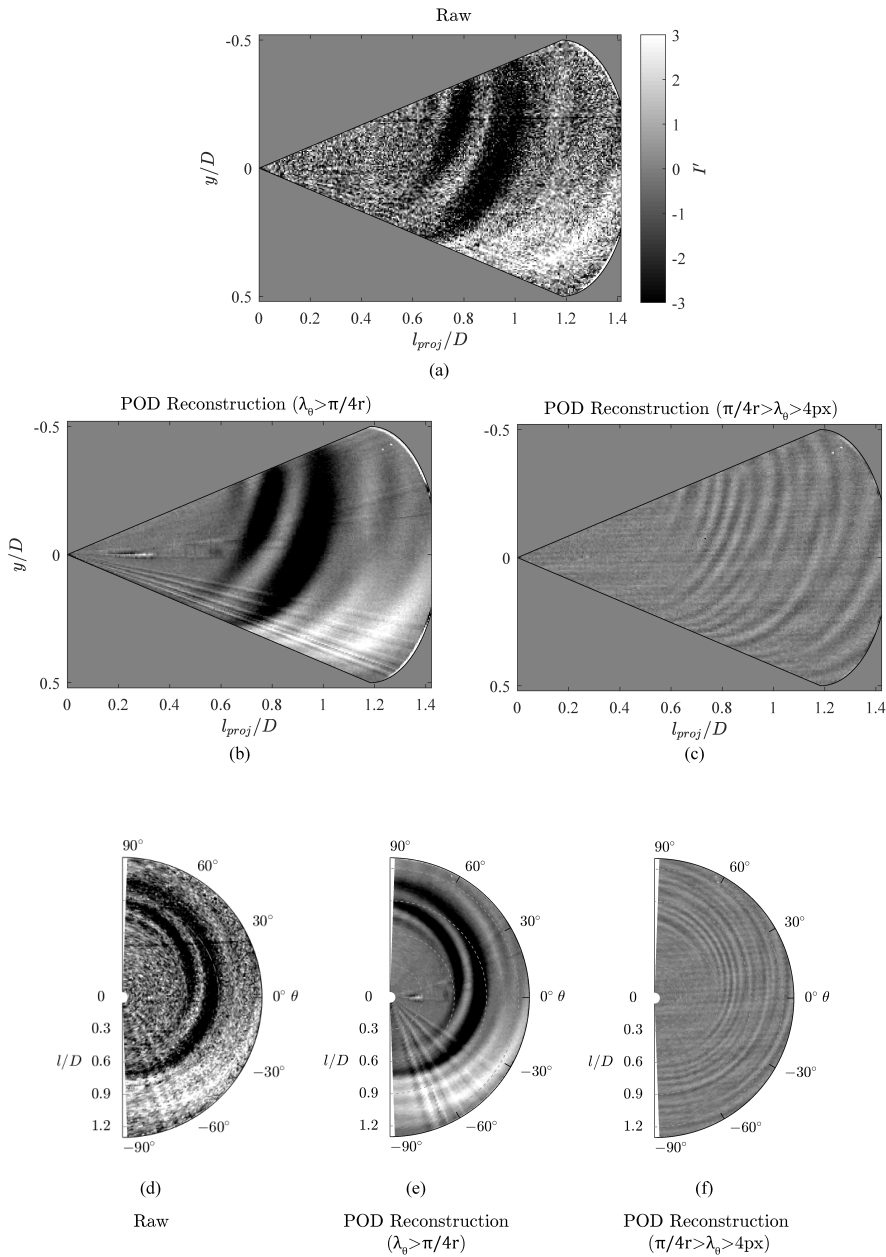


Figure 5.7: Visualisation of the spiral vortex footprints on a rotating cone of  $\psi = 22.5^\circ$  ( $Re_L = 8.1 \times 10^4$ ,  $S_b = 2.9$ ). (a),(d) raw, (b),(e) POD reconstruction of long wavelengths  $\lambda_\theta > \pi r/4$ , and (c),(f) POD reconstruction of short wavelengths  $\pi r/4 > \lambda_\theta > 4px$ . Top row is as observed in the camera frame and the bottom row contains the respective unwrapped views.

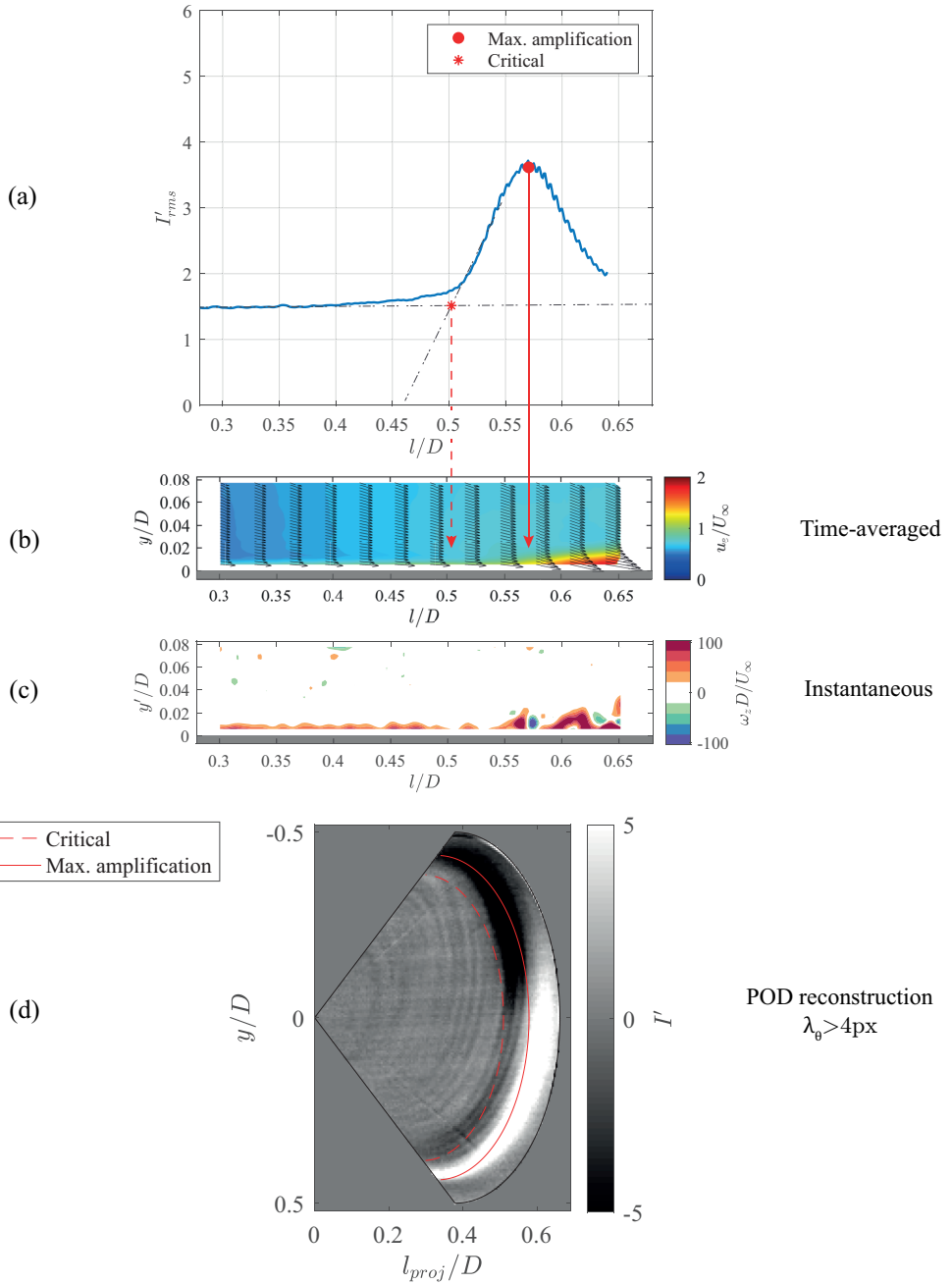


Figure 5.8: Growth of the spiral vortices on a rotating cone ( $\psi = 50^\circ$ ,  $Re_L = 9.7 \times 10^3$ ,  $S_b = 30.6$ ). (a) a meridional trace of surface temperature fluctuations  $I'_{RMS}$ , (b) time-averaged velocity field in a meridional plane, (c) instantaneous vorticity field in a meridional plane, and (d) a combined POD reconstruction of short and long wavelength temperature patterns (criterion  $\lambda_\theta > 4\text{px}$ ).



Figure 5.9: Spiral vortex cross-sections on a rotating cone of half-angle  $\psi = 30^\circ$ , taken from Kobayashi et al., 1983.

rotating in axial inflow the spiral vortices may start as co-rotating, upon amplification they can turn into counter-rotating vortex pairs.

In axial inflow, both, the centrifugal and crossflow instabilities on rotating cones depend on the local rotational speed ratio  $S$  and local Reynolds number  $Re_l$  (Garrett et al., 2010; Kobayashi & Izumi, 1983). For a given rotating cone, the maximum amplification Reynolds number  $Re_{l,m}$  follows an exponential relation with the local rotational speed ratio  $S$ , see figure 5.10. For all cones, higher local rotational speed ratio  $S$  increasingly destabilises the boundary-layer, evident from the fact that the maximum amplification occurs at a lower local Reynolds number  $Re_l$ .

Figure 5.10 suggests that, at first, increasing the half-cone angle stabilises the boundary-layer on rotating cones, i.e. the maximum amplification occurs at higher  $Re_l$  and  $S$  for broader cones. However, for large half-cone angles  $\psi = 45^\circ$  and  $50^\circ$  the maximum amplification is not affected by changing the half-cone angle. Kobayashi et al., 1983 observed the similar behaviour on rotating cones in still fluid. They observed that the critical Reynolds number is highly sensitive to the changes in low half-cone angles ( $\psi \lesssim 40 - 45^\circ$ ), but becomes less sensitive to the changes in high half-cone angles ( $\psi \gtrsim 40 - 45^\circ$ ), see figure 2.10.

Furthermore, figure 5.10 also compares the results of two different tests on the slender cones ( $\psi = 15^\circ$ ) of two base diameters:  $D = 0.1$  m in the present work and  $D = 0.047$  m from Tambe et al., 2021 discussed in chapter 4. All these tests were conducted in the same windtunnel facility (W tunnel). The maximum amplification locations from both the tests show the same trend in the parameter space of  $Re_l$  and  $S$ . This confirms a good repeatability of the present experimental approach in determining the maximum amplification of the spiral vortices.

For all cone types, the critical Reynolds number decreases with the rotational speed ratio  $S$ , see figure 5.11. However, the critical Reynolds number in the present measurements refers to the onset of a rapid growth of the spiral vortices, rather than the location of their origin. Spiral vortices are expected to be weak at their origin and they are detected once their thermal footprint is strong enough to be detected by the infrared sensor. Also, for a same cone, the critical Reynolds number significantly depends on the disturbance environment such as the free-stream turbulence (Kobayashi et al., 1987). The critical Reynolds number is higher

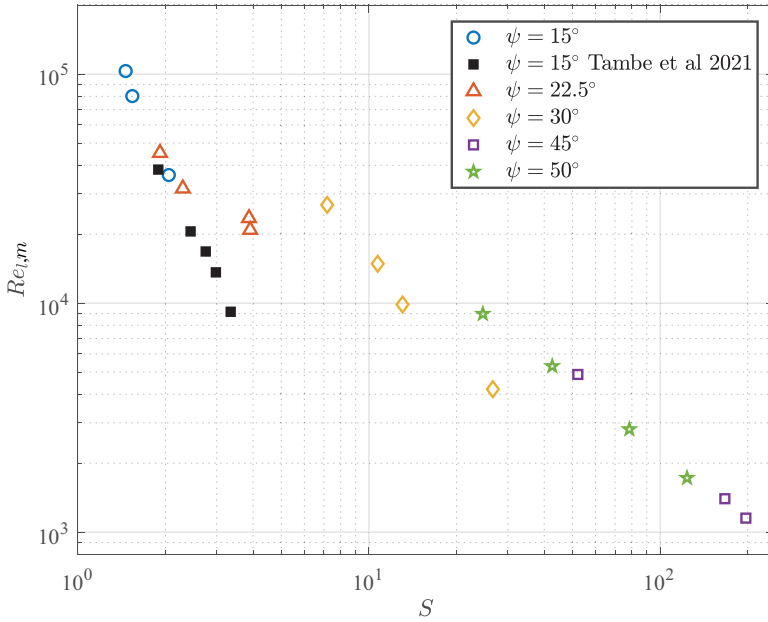
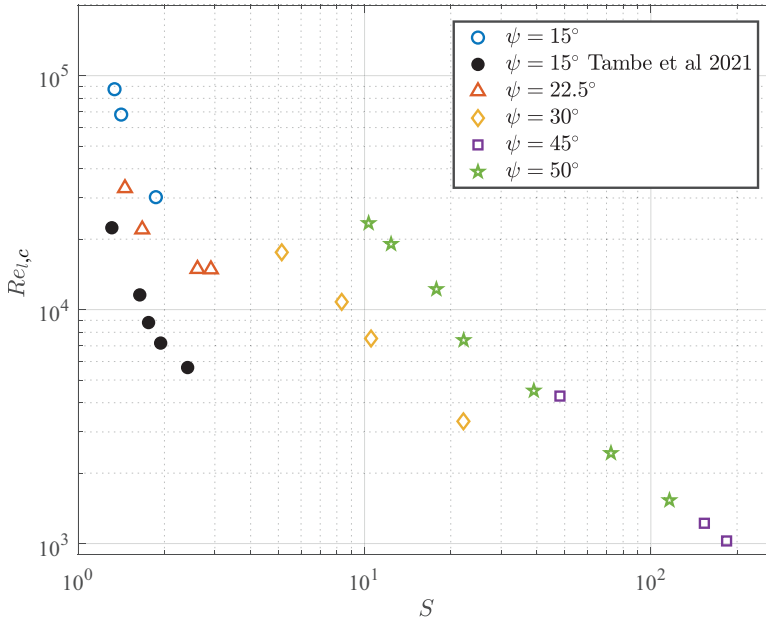


Figure 5.10: Effect of half-cone angle on the maximum amplification of spiral vortices.

in the present case of a slender cone  $\psi = 15^\circ$ , as compared to the previous measurements (Tambe et al., 2021), see figure 5.11. This shows that the repeatability of the present experimental method in measuring the critical Reynolds number is limited by the instrumentation and the uncertainty in the free-stream turbulence, unlike the measurements of maximum amplification.

Similar to the maximum amplification, critical Reynolds number shows high sensitivity to the changes in low half-cone angles ( $\psi \lesssim 45^\circ$ ). The critical Reynolds number is not affected by the changes in high half-cone angles ( $\psi = 45 - 50^\circ$ ). This agrees with the observations made by Kobayashi et al., 1983 on rotating cones in still fluid.

Garrett et al., 2010 have theoretically predicted the onset of convective crossflow instability on a range of broad cones rotating in axial inflow. Garrett et al., 2010 quantified the critical points of the instability in the space of Reynolds number  $Re_{\delta^*} = \delta^* l \sin(\psi) \omega / \nu$  and a parameter  $s = (l \sin(\psi) \omega / u_e)^2 = S^2$ . Here, the length scale  $\delta^* = \sqrt{\nu / \omega}$  relates to the boundary-layer thickness on a rotating cone, without accounting for the effect of axial inflow. Figure 5.12 compares the present measurements of critical and maximum amplification points on a broad cone of  $\psi = 50^\circ$  to the critical points predicted by Garrett et al., 2010 in the parameter space of  $Re_{\delta^*}$  and  $S$ . The comparison shows qualitatively similar trends in experimental and theoretical data. The measured critical Reynolds number is higher than the theoretical prediction. This is expected due to the differences in the definition of the critical point. In theory, the critical point marks the location where the boundary-layer becomes unstable, beyond which the spiral vortices are expected to form. However, the measured critical points in this study mark the onset of the rapid growth of the spiral vortices which



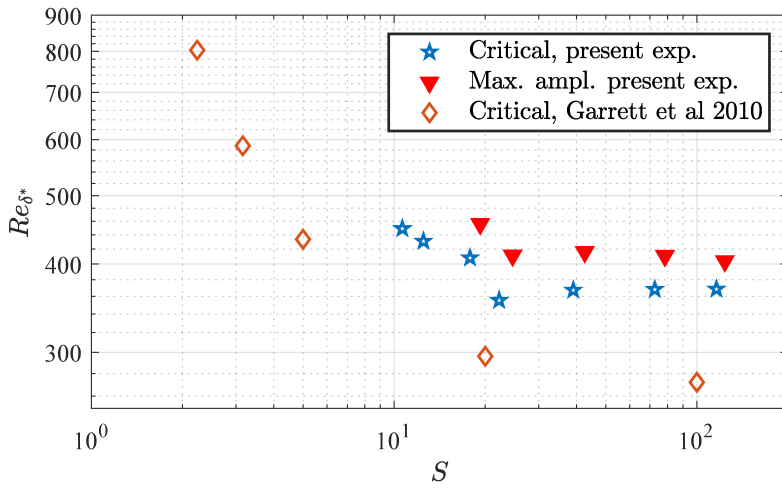


Figure 5.12: Comparison of the present experiments with the theoretical predictions of Garrett et al., 2010 for a rotating broad cone of  $\psi = 50^\circ$  in axial inflow.

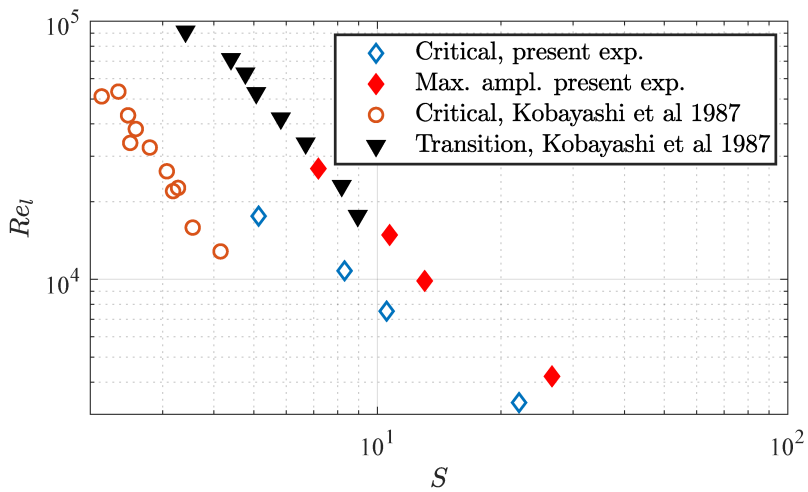


Figure 5.13: Comparison of the present experiments with the measurements of Kobayashi et al., 1987 on a rotating cone of  $\psi = 30^\circ$  in axial inflow.

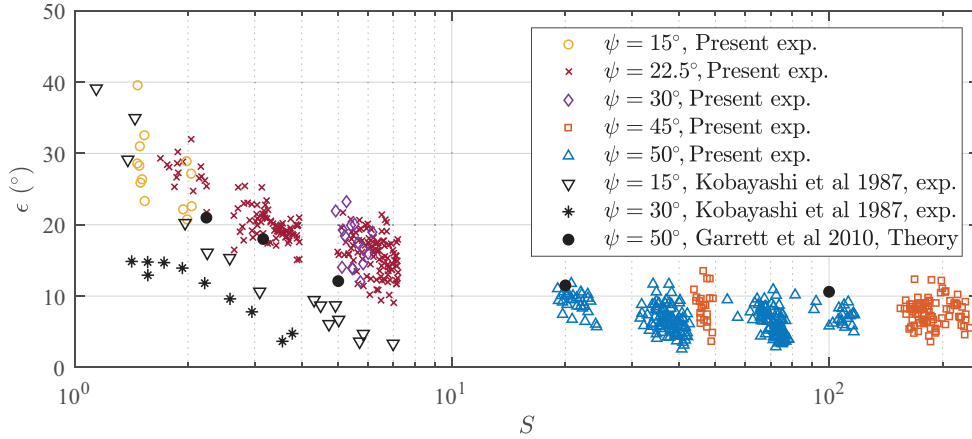


Figure 5.14: Variation of spiral vortex angle  $\epsilon$  vs rotational speed ratio  $S$  for all the investigated cones, compared with past measurements (Kobayashi et al., 1987) and theory (Garrett et al., 2010).

uncertainty is of the order of  $\pm 1^\circ$  for the spiral vortex angle  $\epsilon$  and  $\pm 1$  for the azimuthal vortex number  $n$ .

All investigated cases of rotating cones show a wide range of spiral vortex angles  $\epsilon$  at a given rotational speed ratio  $S$ , see figure 5.14. This relates to the fact that while growing, the azimuthal coherence of the spiral vortices starts to get disturbed, i.e. their azimuthal spacing and orientation varies. Usually, theory predicts the spiral vortex angle of the most unstable mode for a given rotational speed ratio  $S$  at a critical point (Garrett et al., 2010; Hussain et al., 2016; Kobayashi & Izumi, 1983). However, the measurements detect the spiral vortex footprints once they have grown stronger and show a wide range of spiral vortex angle, similar to the past measurements of Kobayashi and Izumi, 1983; Kobayashi et al., 1987.

For all the investigated cones, the spiral vortex angle  $\epsilon$  decreases with increasing rotational speed ratio  $S$ , see figure 5.14. This can be interpreted in the reference frame fixed to the cone surface. Here, the spiral vortices tend to align towards the local direction of the skewed boundary-layer velocity (in the cone reference frame). The trend reasonably agrees with the predictions of Garrett et al., 2010 for  $\psi = 50^\circ$  and measurements of Kobayashi et al., 1987. It should be noted that Kobayashi et al., 1987 measured the angle using a hot-wire stationed at a fixed distance away from the rotating cone surface. On the contrary, the present measurements are performed at the cone surface. Therefore, the quantitative differences are ascribed to the different measurement locations (as described in figure 3.16).

The azimuthal vortex number  $n$  shows scattered measurement data in both present and previous measurements of Kobayashi et al., 1987, see figure 5.15. Generally, the azimuthal vortex number  $n$  decreases with increasing rotational speed ratio  $S$ , for a given cone. This suggests that when the rotation is stronger compared to the axial inflow, larger azimuthal wavelengths  $\lambda_\theta = 2\pi r/n$  grow in the boundary layer.

Figure 5.15 shows that broad-cones  $\psi = 45^\circ$  and  $50^\circ$  exhibit lower azimuthal number  $n$  compared to the predictions of Garrett et al., 2010 but show a similar trend of decreasing  $n$  with increasing  $S$ . The present measurements reasonably agree with those of Kobayashi et al., 1987 for  $\psi = 15^\circ$ . Figure 5.15, including the past measurements and predictions, shows

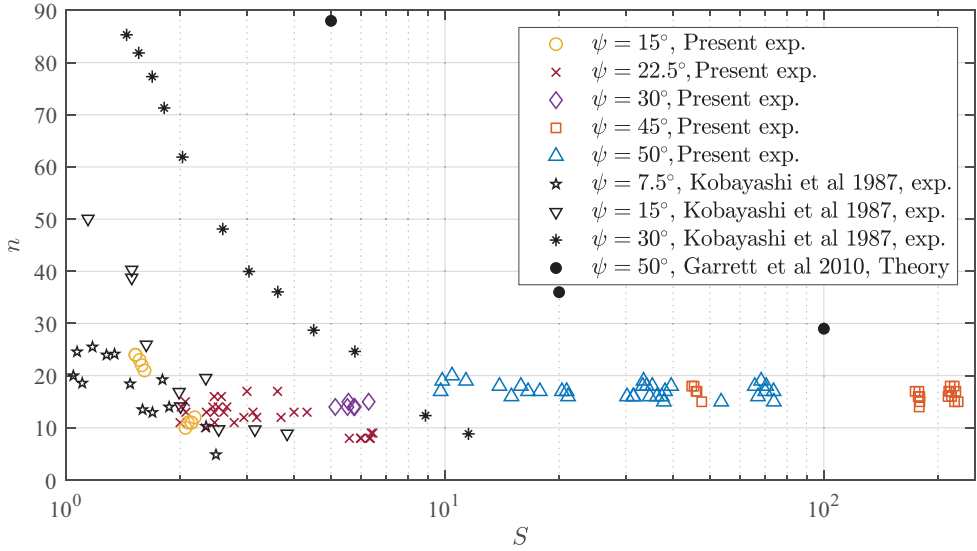


Figure 5.15: Variation of the azimuthal vortex number  $n$  with rotational speed ratio  $S$  for all the investigated cones, compared with past measurements (Kobayashi et al., 1987) and theory (Garrett et al., 2010).

that with increasing half-cone angle the azimuthal vortex number increases  $n$ . However, broad cones of  $\psi = 45^\circ$  and  $50^\circ$  seem to follow a common trend with respect to the rotational speed ratio  $S$ .

## 5.7. CONCLUSION

This study investigated the effect of the half-cone angle on the boundary-layer instability of rotating cones in axial inflow. The rotating slender cones of half-cone angle  $\psi = 15^\circ$  and  $22.5^\circ$ , and rotating broad-cones of half-cone angles  $\psi = 30^\circ$ ,  $45^\circ$  and  $50^\circ$  were tested in axial inflow. The parameter space of local Reynolds number  $Re_l$  and rotational speed ratio  $S$  was explored to detect the spiral vortices on rotating broad-cones of  $\psi = 45^\circ$  and  $50^\circ$  for the first time. The surface temperature patterns on rotating cones were measured using infrared camera and processed with the POD approach. PIV measurements were used to obtain the meridional velocity field. Following are the important conclusions from this study:

- In all the investigated axial inflow conditions, boundary-layer instability is found to induce spiral vortices on rotating cones of  $\psi = 15^\circ - 50^\circ$ .
- The boundary layer transition on all the investigated rotating cones show two distinct types of surface temperature fluctuation patterns: a short wavelength pattern of  $\lambda_\theta < \pi r/4$  relating to the spiral vortex footprints and a long wavelength pattern of  $\lambda_\theta > \pi r/4$  overlaid on the spiral vortex footprints. The latter occurs where the spiral vortices start their rapid growth.
- For all the investigated cones, the spiral vortices are found to start altering the near-wall momentum around the point of their maximum amplification, similar to the past observations in the case of a rotating slender cone  $\psi = 15^\circ$ .

- On rotating broad cones, the spiral vortices appear to start as co-rotating but turn into counter-rotating type upon their amplification.
- For the rotating cones of  $\psi < 45^\circ$ , increasing half-cone angle  $\psi$  has a stabilising effect on the boundary-layer. This delays the spiral vortex growth to higher local Reynolds number  $Re_l$  and higher rotational speed ratio  $S$ .
- For the rotating broad cones of  $\psi = 45^\circ$  and  $50^\circ$ , the change in half-cone angle does not seem to have any significant effect on the location of spiral vortex growth in the parameter space of  $Re_l$  and  $S$ . In both cases, the critical and maximum amplification points coincide on a common trend in the parameter space of  $Re_l$  and  $S$ . Similar observation was reported by Kobayashi et al., 1987 for the rotating cones in still fluid where the critical and transition Reynolds number is less affected by such broad half-cone angles  $\psi \gtrsim 40 - 45^\circ$ .
- For  $\psi = 50^\circ$ , the trends of measured critical and maximum amplification points agree with the trend of critical points predicted by Garrett et al., 2010, supporting their theory. The quantitative differences suggest the need of further investigation with combined experiments and theory.
- The spiral vortex angle  $\epsilon$  varies with the rotational speed ratio  $S$ . The variation is found to follow a common trend for all the investigated cases of rotating cones. The trend shows a qualitative agreement with the past measurements (Kobayashi et al., 1987) and predictions (Garrett et al., 2010).
- The azimuthal vortex number  $n$  decreases with increasing rotational speed ratio  $S$  for each cone. Together with the past measurements and predictions, the increasing half-cone angle results in higher azimuthal vortex number. This suggests that as the cones get broader their instability induces spiral vortices with shorter azimuthal wavelengths.



# 6

## SPIRAL INSTABILITY MODES AT TRANSONIC FLIGHT CONDITIONS

### 6.1. INTRODUCTION

THE past literature and present investigations, discussed in previous chapters 2-5, have explored the boundary-layer instability on rotating cones in low-speed inflow conditions, i.e. low inflow Reynolds numbers  $Re_L = \rho UL/\mu < 10^5$ , high base rotational speed ratio  $S_b = r_b\omega/U > 1$ , and incompressible flow. Here,  $L$  is the total meridional length of a cone,  $r_b$  is the base radius,  $\omega$  is the angular velocity and  $U$  is the inflow velocity. When a transonic civil aircraft is cruising at a free-stream Mach number  $\approx 0.8$ , its engine intakes reduce the inflow Mach number down to 0.5–0.6 (Peters et al., 2015; Uenishi et al., 1990). This, together with the fan design, minimises the supersonic region on the fan blades, reducing the shock-wave related losses. Inside an aero-engine intake, a nose-cone encounters following inflow conditions: high inflow Reynolds number  $Re_L > 10^6$ , low base rotational speed ratio  $S_b < 1.5$  and Mach number  $M \approx 0.5$ –0.6. In this work, these conditions are referred to as *high-speed* conditions, contrasting with the *low-speed* inflow conditions from chapters 3–5. To accurately assess the near-hub aerodynamics of an aero-engine fan, the boundary-layer instability on nose-cones must be investigated at these real flight conditions.

For a rotating cone in axial inflow (figure 6.1), the growth of instability induced spiral vortices depends on the local Reynolds number  $Re_l = \rho l u_e/\mu$  and rotational speed ratio  $S = r\omega/u_e$  (chapters 2-5). Here,  $l$  is the meridional length and  $u_e$  is the edge velocity of the boundary-layer. Past studies have explored the low-speed regime of this parameter space  $Re_l < 10^5$  vs  $S > 1$ , and they detected the growth of instability-induced spiral vortices as the primary instability mode on rotating cones. However, without investigation, one can not extrapolate this instability behaviour to high-speed conditions ( $Re_l > 10^5$  and  $S < 1$ ) that are most common to transonic civil aircraft.

Past studies majorly relied on particle based flow visualisation to detect the instability-induced spiral vortices on rotating cones (Kobayashi et al., 1983; Y. Kohama, 1984a). They deposited particles (titanium tetrachloride) on the cone surface before the experiment and observed their transport during the experiment. This type of methods are not suitable for high-speed experiments in a blow-down tunnel due to several practical challenges. For

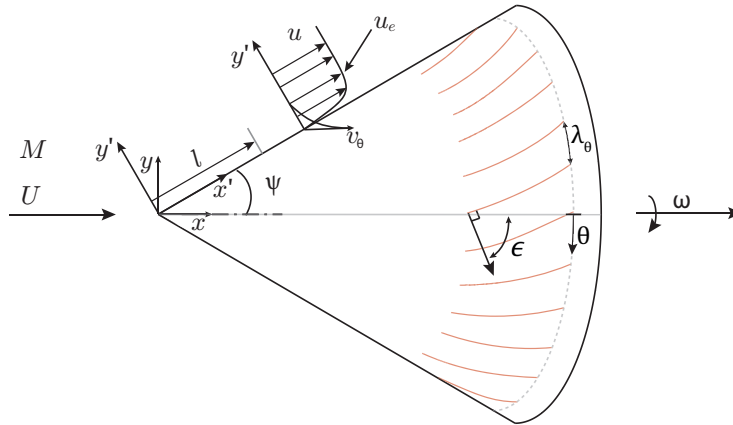


Figure 6.1: Schematic of a rotating cone under axial inflow

example, due to the short durations (around 20s) of each wind-tunnel run, the cones have to be kept rotating before the wind tunnel starts. For a given rotational speed ratio, the angular velocity of a cone is high in a high-speed inflow, causing high centrifugal forces on the deposited particles on the rotating cone surface. This will cause the particle transfer before the operating conditions are achieved, making the spiral vortex visualisation challenging. Therefore, detecting boundary-layer instability on rotating cones remained challenging at flow conditions that are typical for a realistic flight.

The experimental method presented in this work (chapter 3) uses infrared camera to detect the surface temperature footprints of the spiral vortices on rotating cones. This method is relatively easy to implement in high-speed conditions, and overcomes the limitations of the previously used measurement techniques. Using the present method, this chapter explores the boundary-layer instability on rotating cones in high-speed inflow conditions:  $Re_L > 10^6$ ,  $S_b < 1$  and  $M = 0.5$ . Three different cones with  $\psi = 15^\circ, 30^\circ$  and  $40^\circ$  are tested. Section 6.2 describes the experiments. Section 6.3 describes flow fields surrounding the cones in the wind-tunnel test-section. Section 6.4 presents the visualisations of the spiral vortices. Section 6.5 shows the growth and spatial characteristics of the spiral vortices in the parameter space  $Re_l$  vs  $S$ . Section 6.6 presents observed spiral vortex angles. Section 6.7 concludes the chapter.

## 6.2. DESCRIPTION OF EXPERIMENTS

Experiments are performed in TST-27, a transonic-supersonic wind-tunnel at the faculty of Aerospace Engineering, Delft University of Technology (TU Delft). Figure 6.2 shows a schematic of TST-27. This blow-down wind-tunnel uses pressurised air stored in a separate reservoir at a total pressure between 20 and 40 bar. The pressurised air is expanded through a variable area channel to achieve prescribed flow conditions. A variable choke downstream of the test section is used to achieve a desired subsonic Mach number; the desired Reynolds number is determined by varying the total pressure in the settling chamber. The test-section is rectangular with a constant width of 0.28 m and variable height, which for the present case is 0.253 m. To simulate flow conditions within aero-engines, the wind tunnel is operated at

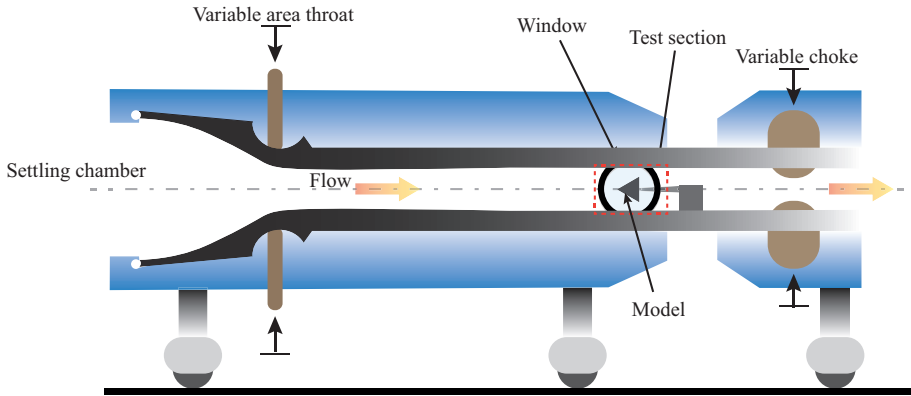


Figure 6.2: A schematic of the transonic-supersonic wind-tunnel TST27.

settling chamber pressures between 1.4 and 1.5 bar resulting in  $Re_L > 10^6$  and at the inflow Mach number  $M = 0.5$ .

Figure 6.3 shows the measurement setup. As contemporary aero-engines are found to use variety of nose-cone shapes, three different cones are chosen for this investigation: a slender cone with half angle  $\psi = 15^\circ$ , and two broad cones with  $\psi = 30^\circ$  and  $\psi = 40^\circ$ . Note that previous chapters 3-5 have investigated cones of  $\psi = 15^\circ$  and  $30^\circ$  in low-speed and therefore, these cases are retained in these high-speed investigations. Broader cones with  $\psi \gtrsim 45^\circ$  are excluded from the test because they experience high drag which is beyond the limit of the current rotating setup. All the models have a constant base diameter  $D = 100$  mm. In the test section, area blockage due to the cone increases from 0% at the tip to 11.1% at the base (excluding the wall boundary-layers), which is comparable to that of a typical aero-engine. The models are rotated by a brushless motor at various rotational speeds (8000 to 36500 RPM) to achieve different combinations of local Reynolds number  $Re_l$  and local rotational speed ratio  $S$ . The models are made of Polyoxymethylene (POM) which has favourable thermal properties for the infrared measurements (as described in section 2.4.1). The surface is smoothed up to the r.m.s. roughness lower than  $1 \mu\text{m}$ . The models are statically balanced around the rotation axis. The tip eccentricity is around  $5 \mu\text{m}$ .

Generally in an unstable system, small environmental disturbances can undergo growth to form coherent flow structures. In the present setup, these disturbances come primarily from three sources: (a) free-stream turbulence of 3.6 to 4% of the mean velocity as measured in an empty test section using particle image velocimetry, (b) surface roughness of the cone  $\approx 1 \mu\text{m}$  and (c) remnant dust particles in the air below the filter size  $< 10 \mu\text{m}$ .

Infrared thermography has been shown to be a useful tool for measuring the spiral instability modes over a rotating disk (Astarita et al., 2002) and a rotating cone (Tambe et al., 2019). This technique is applied in the present study to detect these instability modes from their surface temperature footprints, see figure 6.3 for the measurement setup. The integration times of infrared acquisitions are varied between  $250 \mu\text{s}$  to  $25 \mu\text{s}$  such that the angle swept by the rotating cones during each acquisition is minimized, while retaining a sufficient signal to noise ratio to measure the surface temperature fluctuations. The results show that at the same operating conditions, different integration times do not alter the

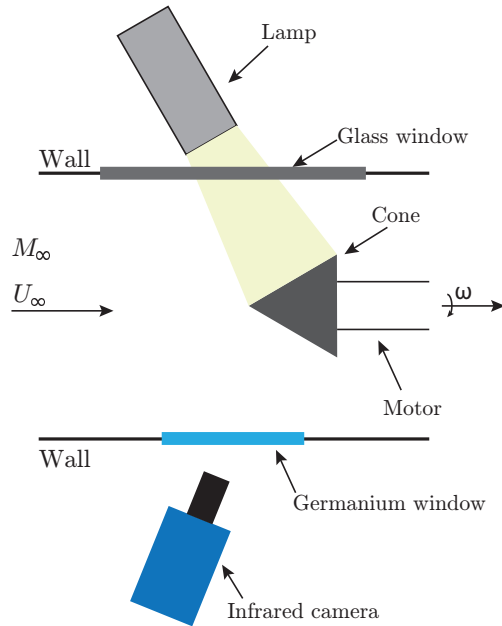


Figure 6.3: Measurement setup.

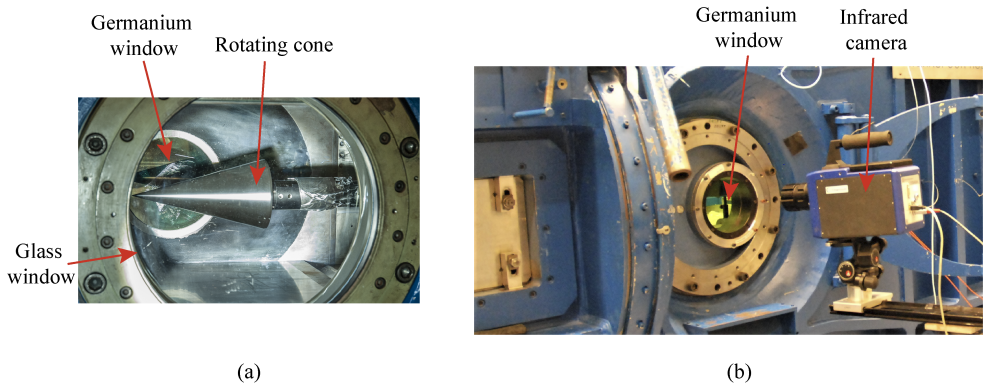


Figure 6.4: Photographs showing (a) rotating cone in the test section of TST-27, a transonic-supersonic wind-tunnel and (b) infrared camera viewing through the germanium window.

Camera	FLIR (CEDIP) SC7300 Titanium
Noise equivalent temperature difference (NETD)	25 mK
Spatial resolution	0.52 mm/px
Integration time	25 – 250 $\mu$ s
Acquisition frequency	200 Hz
Number of images per dataset	2000
Heat source	Theatre lamp (575 W)

Table 6.1: Specifications of the Infrared Thermography setup.

observations of instability modes; an example showing this can be found in appendix A. At high rotation rates (RPM > 30000) of broad cones, the integration times are lowered (50 $\mu$ s to 25 $\mu$ s), and therefore, the signal contrast is increased by using a lamp. Table 6.1 details the technical specifications of the setup.

Before the wind-tunnel test, both the model and the pressurised stagnant air are at ambient temperature. When the tunnel starts, the air expands into the test-section and the static temperature of the air drops, which cools the model surface. During the wind-tunnel operation time (around 20s), the model cools down and its temperature drops continuously. This trend is removed by subtracting a moving average with the kernel size of 20 instances (corresponding to 0.1s) from the dataset. Since this operation is only a precursor to the subsequent modal analysis, the data after moving mean subtraction is referred to as raw data.

To obtain the local flow properties along the cones, static pressure is measured on the non-rotating cones using a sixteen channel Scanivalve DSA3217 pressure acquisition system. The pressures are measured at different circumferential positions of a cone in a rectangular test-section to obtain a circumferential mean static pressure at a given radius. The total pressure and temperature in the settling chamber, and static pressures at the wind-tunnel walls are also recorded.

### 6.3. FLOW FIELD OVERVIEW

The present wind-tunnel configuration features rotating cones in an internal flow, unlike the majority of past studies in low-speed-open-jet facilities. Such internal flow closely represents the most-encountered flow conditions inside an aero-engine. In a symmetry plane, inviscid flow develops between two bounding streamlines near the test-section wall and cone surface, see figure 6.5. Near the cone, the undisturbed oncoming flow slows down upon an encounter with the cone-tip region and turns to follow the cone surface.

Here, estimating flow properties at the edge of a cone boundary-layer is crucial to compute the local flow parameters  $Re_l$  and  $S$  that govern the stability characteristics over the rotating cones. For this purpose, the local Mach number  $M_l$ , just outside the boundary-layer, is obtained using the isentropic relations and measured flow properties: circumferential-mean static pressure along the non-rotating cones and total pressure in the settling chamber. This, along with the measured total temperature, gives the local static temperature at the boundary-layer edge. From this the local air density is calculated using the ideal-gas relation,

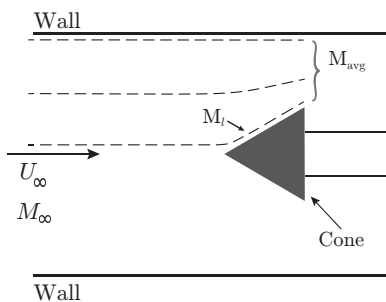


Figure 6.5: Schematic of the internal flow within the test section.

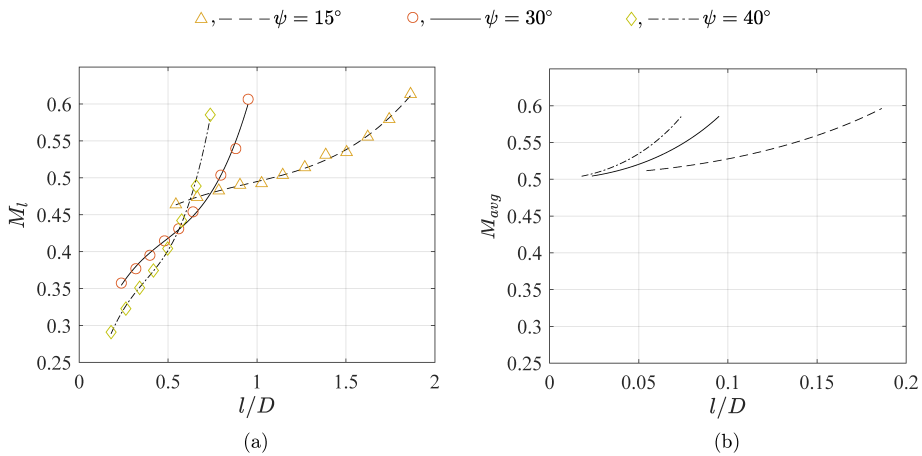


Figure 6.6: Mach number variations over the cone meridians: (a) local Mach number of the potential flow near the cone surface obtained from surface pressure measurements and (b) area averaged Mach number of the flow between a cone and test section walls obtained from the local area ratio.

and local dynamic viscosity is obtained from the Sutherland's law.

The local Mach number  $M_l$  is significantly lower near the cone-tip and increases downstream along the cone beyond the free-stream Mach number, see figure 6.6a. The area-averaged flow Mach number (resulting from one-dimensional-isentropic area-Mach relation) also shows a gradual increase along the cone due to the area contraction, see figure 6.6b. With increasing half-cone-angle  $\psi$ , flow accelerates steeper along the cone, as evident from figure 6.6.

The local Mach number distributions from figure 6.6a are used to obtain the flow parameters: local Reynolds number  $Re_l$  and rotational speed ratio  $S$ . With variable total conditions and rotational speed, different distributions of these parameters are obtained along the cone length to investigate a wider region of the parameter space  $Re_l$  vs  $S$ .

## 6.4. VISUALISATIONS OF INSTABILITY MODES

The instantaneous surface temperature footprints allow visualising the instability modes over the rotating cones. Proper orthogonal decomposition (POD) approach is used to identify the modes of surface temperature fluctuations in the measurement dataset, each consisting of 2000 images. The POD modes corresponding to the measurement noise (wavelength  $\lambda_\theta < 4$  pixels) are discarded. Remaining POD modes are used to selectively reconstruct the instability modes using criteria based on the azimuthal wavelength  $\lambda_\theta$  (see 3 for further details).

Figure 6.7 shows (a) the instantaneous surface temperature fluctuations in the raw data and associated (b and c) POD reconstructions of a rotating broad cone with  $\psi = 40^\circ$ . The top row images are as observed in the camera sensor plane; and corresponding images in the bottom row are unwrapped cone-surfaces (figures 6.7d, e and f). The raw data reveal that a wave pattern ( $\lambda_\theta \approx \pi r/8$ ) appears on a rotating cone, overlaid with a long wavelength modulation ( $\lambda_\theta > \pi r/4$ ). These two types of wave patterns are separated using POD modes. The long wavelength modulation is reconstructed using the POD modes having an azimuthal wavelength  $\lambda_\theta > \pi r/4$ , i.e. an azimuthal number of waves  $n < 8$ , see figures 6.7b and e. The short-wavelength pattern is reconstructed from the POD modes having an azimuthal wavelength between  $\pi r/4 > \lambda_\theta > 4$  pixels, see figures 6.7c and f; this pattern shows nearly constant azimuthal spacing, which indicates azimuthal coherence.

Similar short and long wave temperature patterns have been observed on rotating cones in low-speed conditions (figures 3.8 and 5.8). The low-speed investigations have clarified that the short-wave temperature pattern corresponds to the spiral vortices. The long-wave temperature pattern appears during the rapid growth of the spiral vortices, as they start moving away from the wall and start to enhance mixing of outer and inner fluid within the boundary-layer. This can be viewed as the azimuthal modulation of the strength of spiral vortices. The similarity of the patterns observed in low-speed and present high-speed case suggests that the short-wave pattern in figure 6.7c corresponds to the footprint of the spiral vortices. The long-wave pattern in figure 6.7b appears in the region of spiral vortex growth, where the mixing is enhanced. A theoretical non-linear analysis is required to determine the role of the long-wave pattern in the spiral vortex growth.

Similar wave patterns are observed also for a rotating broad cone with  $\psi = 30^\circ$ , as shown in figure 6.8. Here, a coherent spiral vortex footprints with  $\lambda_\theta \approx \pi r/5$  (figures 6.8c and f) has a major contribution to the raw image (figures 6.8a and d), in addition to the long wave modulation (figures 6.8b and e).

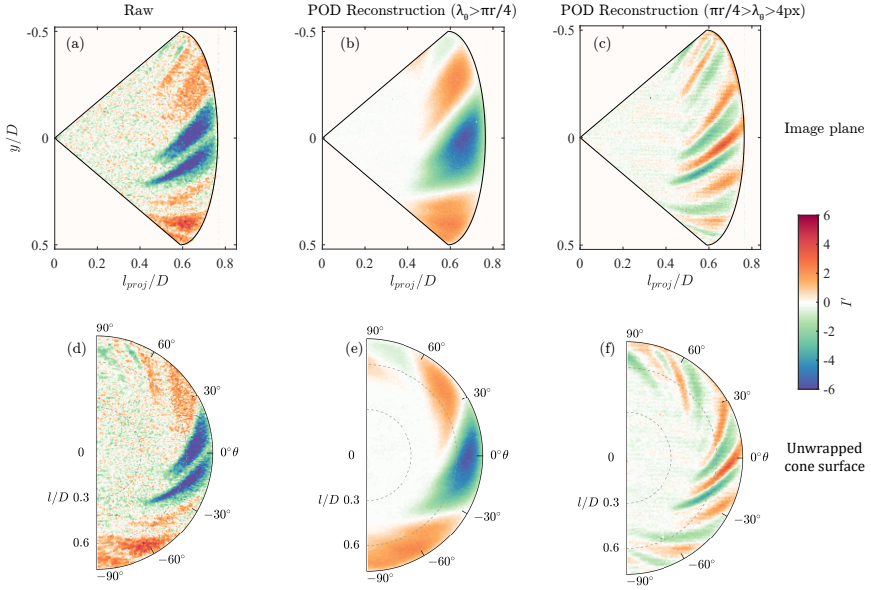


Figure 6.7: Thermal footprints of the spiral instability modes and their POD reconstructions over a rotating broad cone with half angle  $\psi = 40^\circ$  shown in image planes as well as unwrapped cone surfaces.  $Re_L = 1.3 \times 10^6$  and  $S_b = 1.1$ .

6

The stability analyses of rotating broad cones in compressible still fluid (Towers et al., 2016) and with incompressible axial inflow (Garrett et al., 2009) have shown that, with decreasing half-cone angle  $\psi$ , the range of unstable wavelengths gets broadened, and increasingly longer wavelengths can destabilise the flow. Figure 5.15 from chapter 5 agrees with this trend as the azimuthal number decreases (wavelength increases) with decreasing half-cone angle  $\psi$ . A similar trend is observed in the present study, where, for a lower half cone angle  $\psi = 30^\circ$  (figure 6.8), longer wavelengths of  $\lambda_\theta \approx \pi r/5$  are observed as compared to  $\lambda_\theta \approx \pi r/8$  observed for  $\psi = 40^\circ$  (figure 6.7).

Figure 6.9 shows a raw image and the corresponding POD reconstructions for a slender cone with  $\psi = 15^\circ$ . Here, a coherent spiral vortex pattern of  $\lambda_\theta \approx \pi r/4$  (figure 6.9c) is observed along with the long wave modulation (figure 6.9b). However, on the slender cone, other instances with coherent patterns of  $\lambda_\theta \lesssim \pi r/3$  are also observed, see figure A.1 for example. Therefore, the upper bound for the low-order reconstructions in figures 6.9c and f is set at  $\pi r/3$  (relating to the azimuthal number  $n = 6$ ) instead of  $\pi r/4$  (relating to the azimuthal number  $n = 8$ ) used for all other reconstructions in this work. This highlights the need of a separate investigation to identify these vortices by measuring the velocity field.

Overall, the visualizations show that, in high-speed conditions of  $M_\infty = 0.5$  and  $Re_L > 10^6$ , the instability modes over rotating cones appear to be spiral vortices, similar to those observed in low-speed conditions. The spiral vortex patterns on broad cones (figures 6.7 and 6.8) are similar to the spiral vortices observed in the low-speed cases over rotating disks and broad cones; compare figures 6.7 and 6.8 with visualisations of Kobayashi, 1994; Y. Kohama, 1984b; Y. P. Kohama, 2000. On a rotating slender cone, the spiral vortex fronts are oriented

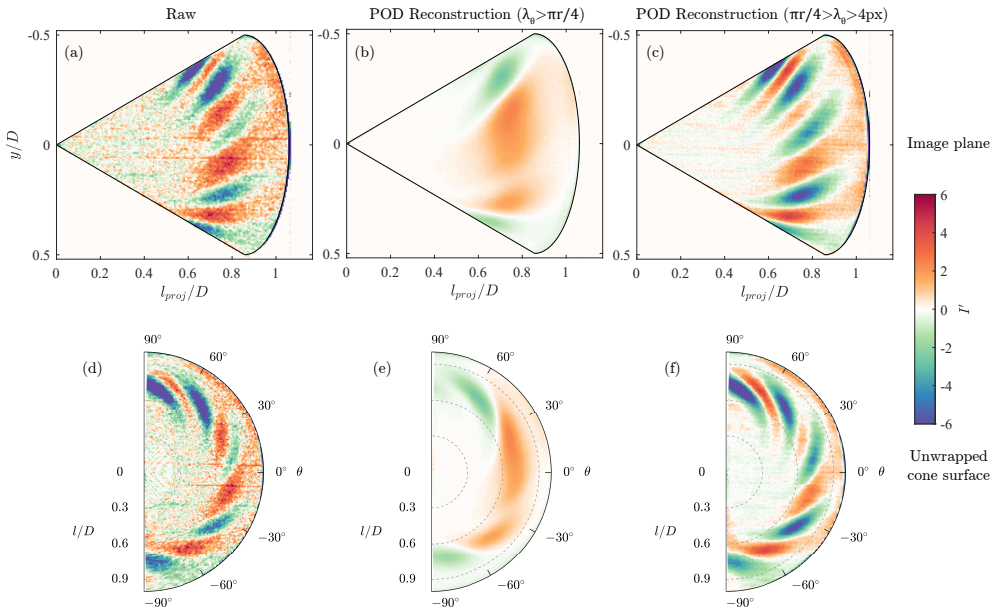


Figure 6.8: Thermal footprints of the spiral instability modes and their POD reconstructions over a rotating broad cone with half angle  $\psi = 30^\circ$  shown in image planes as well as unwrapped cone surfaces.  $Re_L = 1.4 \times 10^6$  and  $S_b = 1$ .

more towards the axial direction as compared to the past low-speed studies (Kobayashi et al., 1983 and chapters 3–5). This is expected as the present observations on slender cones are at low rotational speed ratios  $S < 0.5$ , whereas past low-speed studies encountered high rotational speed ratio  $S > 1$ . This agrees with the previously identified trend where with decreasing rotational speed ratio spiral vortex-fronts become more axial (see figure 3.10).

Flow investigations in a meridional plane are necessary to confirm whether these spiral vortices are co- or counter-rotating. Due to the limitations of the present experiments, i.e. limited optical access for a PIV light-sheet, the cross-sections of the spiral vortices in the meridional plane remains unknown.

## 6.5. GROWTH OF SPIRAL VORTICES

The spiral vortices observed in the present study are convective instability modes. The effect of their spatial growth on the surface temperature fluctuations is observed from the statistical RMS of the thermal footprints  $I'_{RMS}$  on a rotating cone, computed over a dataset (2000 images, acquired at 200Hz). Figure 6.10a shows  $I'_{RMS}$  on a rotating broad cone ( $\psi = 30^\circ$ ), computed over a raw dataset containing the instance shown in figure 6.8a. The region where the spiral vortices appear shows a significantly high levels of temperature fluctuations. The RMS fluctuations are axisymmetric because of the symmetry of axial inflow. Therefore, the spatial growth of the spiral vortices is characterised using a circumferential mean of  $I'_{RMS}$  along the meridional lines (see figure 6.10b). Downstream from the cone apex ( $l/D = 0$ ), the  $I'_{RMS}$  stays low until a critical point ( $l/D \approx 0.57$ ) where it suddenly starts growing. This critical point is ascribed to the onset of the spiral vortex growth. The growth of the spiral vortices continues

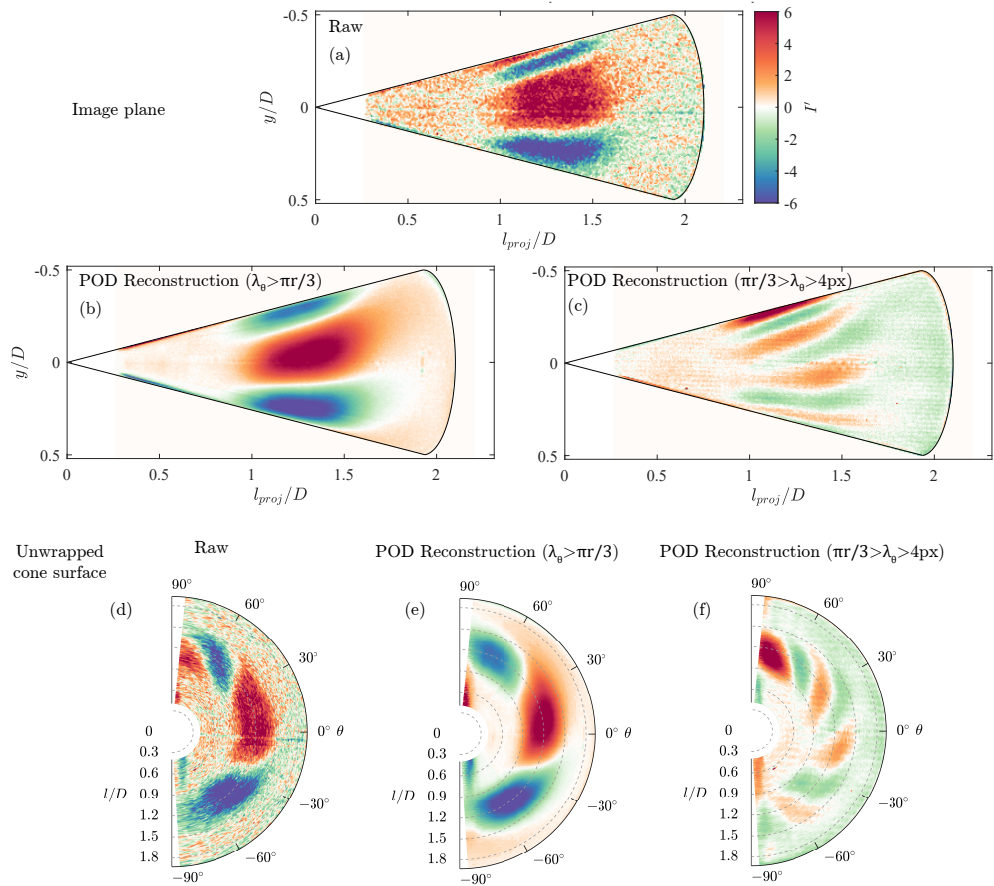


Figure 6.9: Thermal footprints of the spiral instability modes and their POD reconstructions over a rotating slender cone with half angle  $\psi = 15^\circ$  shown in image planes as well as unwrapped cone surfaces.  $Re_L = 3.2 \times 10^6$  and  $S_b = 0.72$ .

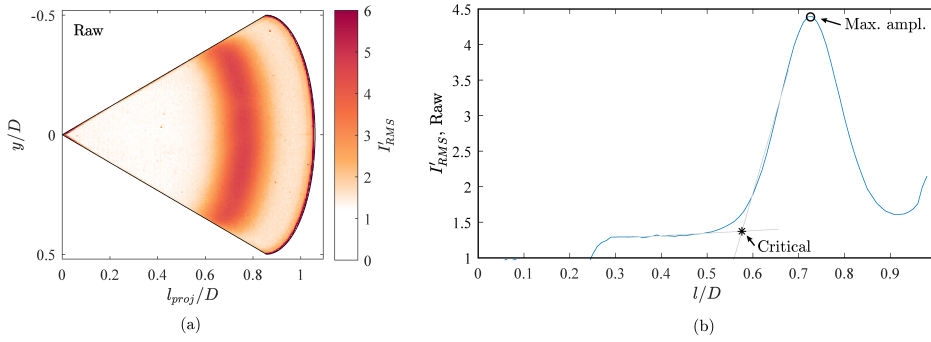


Figure 6.10: RMS of surface temperature fluctuations in a dataset over a rotating broad cone ( $\psi = 30^\circ$ ) shown in an (a) image plane and (b) as a circumferential average along the meridional length for raw data.  $Re_L = 1.4 \times 10^6$  and  $S_b = 1$ .

until a maximum amplification ( $l/D \approx 0.72$ ), after which  $I'_{RMS}$  starts to decrease.

In figure 6.11, the curves of  $Re_l$  vs  $S$  show how these flow parameters vary over a cone at different operating conditions. The critical and maximum amplification points on these curves mark the region spiral vortex growth. The Reynolds numbers corresponding to these points decrease with the rotational speed ratio  $S$ . With increasing half-cone angle, the spiral vortex growth shifts towards the high rotational speed ratios  $S$ .

Figure 6.12 compares the spiral vortex growth region at the present high-speed conditions with the low-speed investigations from the literature. Kobayashi et al. (1987) have tested rotating cones with varying free-stream turbulence level in low-speed conditions. Their observations show that the transition Reynolds number, where the velocity fluctuations start to resemble a typical turbulent spectrum, remains unaltered by the free-stream turbulence level. However, the critical Reynolds number (corresponding to the onset of instability modes) is lowered by a higher intensity of the free-stream turbulence (see figure 6.12). Consequently, the region between the critical and transition points (transition region) becomes broader. The free-stream turbulence level in the present experiments is around 3.5 – 4% of the free-stream velocity  $U$ . Therefore, the present study can be compared to the low-speed results of Kobayashi et al. (1987) with the similar turbulence intensity (3.6% of  $U$ ). The comparison suggests that the transition region reported in low-speed past studies, can be extrapolated to the high-speed (high Reynolds number) conditions of the present study. This shows that the spiral instability modes similar to those studied in the past can be expected on real aero-engine nose-cones.

Figure 6.13 shows the maximum amplification points on rotating cones in low- and high-speed inflows; obtained from chapter 5 and present investigation, respectively. For the investigated cones of  $\psi = 15^\circ$  and  $30^\circ$ , the instability behaviour remains the same in low- and high-speed cases. Here, maximum amplification Reynolds number follows distinct exponential relations with the rotational speed ratio  $Re_{l,m} = CS^{a_1}$ , extending from low-speed to high-speed conditions (shown using dashed and dotted dash lines in figure 6.13). Here, constants  $C$  and  $a_1$  depend on half-cone angle  $\psi$ . For  $\psi = 15^\circ$ ,  $a_1 = -2.62$  and  $C = 2.3 \times 10^5$ . For  $\psi = 30^\circ$ ,  $a_1 = -1.62$  and  $C = 7.1 \times 10^5$ . The present high-speed investigation is performed in a close-test section where the area contraction significantly accelerates the flow along the cone, unlike in the low-speed investigations in open-jet. However, this does not seem

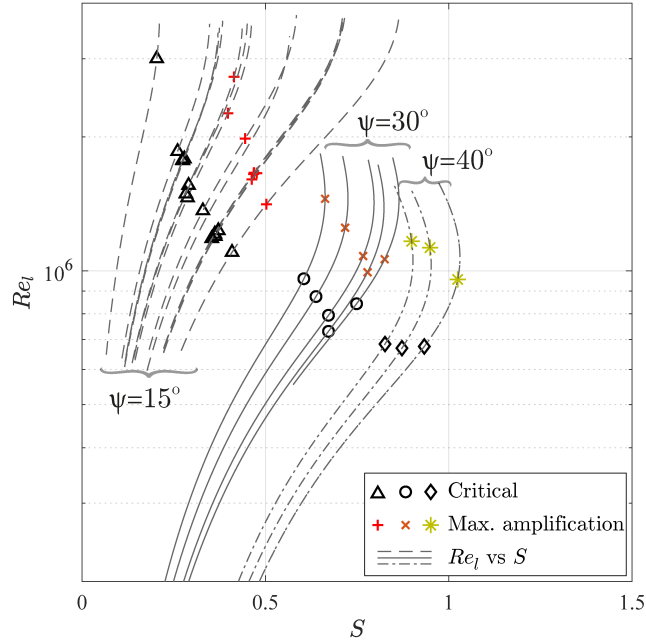


Figure 6.11: Growth characteristics of the spiral vortices

to affect the maximum amplification of the spiral vortices in  $Re_l$  vs  $S$  space (figure 6.13). Moreover, increasing inflow Mach number from  $M < 0.02$  to  $M = 0.5$  has insignificant effect on the trend of maximum amplification points in  $Re_l$  vs  $S$  space (for  $\psi = 15^\circ$  and  $\psi = 30^\circ$ ).

## 6.6. SPIRAL VORTEX ANGLE

Since at low rotational speed ratios  $S$  the stream-wise velocity component is larger than the tangential velocity of the cone, the spiral vortices tend to align towards the axial direction (see figures 6.10-6.12). This contrasts with previous investigations at high rotational speed ratios  $S$  where the spiral vortices are aligned towards the circumferential direction (chapters 3-5). These vortices intersected the projected meridional line  $y/D = 0$  at multiple locations. This allowed a direct extraction of the spiral vortex angle  $\epsilon$  (figure 6.1) as shown in figure 4.20a. However, in the present high-speed investigations, the spiral vortices cross the projected meridian  $y/D = 0$  at far fewer locations, which requires for a different approach.

The spiral vortex angle  $\epsilon$  is obtained from the POD reconstructions as shown in figure 6.14. Here, the spiral vortices appear linear in  $l, \theta$  coordinate system. First, a trace of temperature fluctuations ( $I'$ ) over a  $60^\circ$  sector is obtained along  $\theta$ , at a fixed  $l/D$ . This trace is cross-correlated with temperature fluctuation patterns at an incremented  $l/D$ , sliding along the whole range of  $\theta$  and a cross-correlation peak is found. This procedure is repeated on the new peak location until the whole transition region is scanned. A least-square linear curve (shown as red in figure 6.14a) is fitted to the loci of cross-correlation peaks (shown as circles in figure 6.14a) :  $\theta = ml + c$  (where  $m$  and  $c$  are fit parameters). The spiral vortex angle is obtained as  $\epsilon = \sin^{-1}(1/\sqrt{1 + l^2 m^2 \sin^4(\psi)})$ .

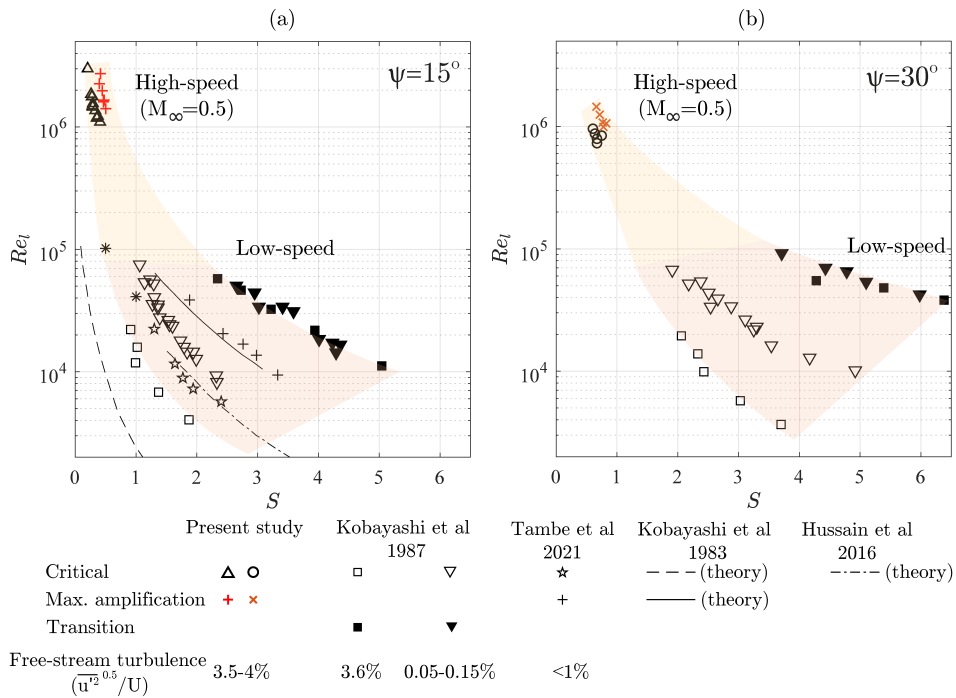


Figure 6.12: Comparisons of the growth characteristics of the spiral vortices at high-speed conditions to those reported in the literature for low-speed conditions (Hussain et al., 2016; Kobayashi et al., 1987; Kobayashi et al., 1983; Tambe et al., 2021). (a)  $\psi = 15^\circ$  and (b)  $\psi = 30^\circ$ .

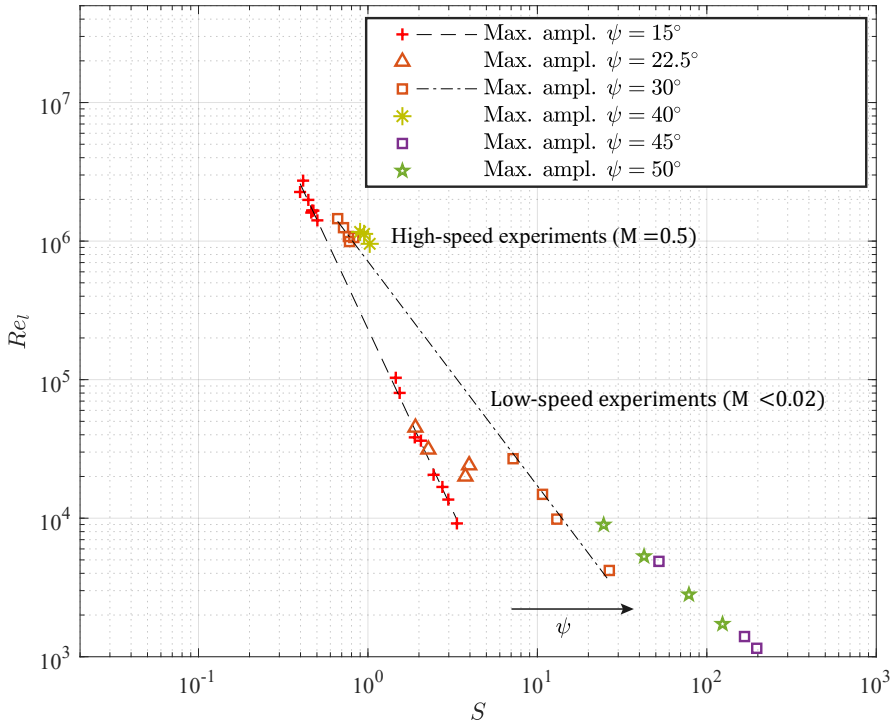


Figure 6.13: Maximum amplification points of the spiral vortex growth on rotating cones in low- and high-speed cases.

As known from low-speed studies, the spiral vortex angle depends on the local rotational speed ratio  $S$  (chapters 2-5). Generally, the spiral vortex angle increases with decreasing rotational speed ratio  $S$ . Physically, this means that as the effect of rotation is reduced, the spiral vortex fronts turn towards the oncoming flow direction. A similar trend is observed at high-speed conditions, as evident from comparing present spiral vortex angles with the low-speed data from Kobayashi et al. (1987) in figure 6.15. In this case, the measured spiral vortex angles in high-speed cases agree well with those from the low-speed studies. This confirms that the Reynolds number does not influence the spiral vortex angles. Figure 6.15b is a zoomed in view of the figure 6.15, showing the measured spiral vortex angle  $\epsilon$ .

## 6.7. CONCLUSION

The instability of the boundary-layers over rotating cones is studied in a high-speed flow at  $Re_L > 10^6$  and  $M = 0.5$ . Two broad cones with half angles  $\psi = 30^\circ$  and  $40^\circ$  and a slender cone with  $\psi = 15^\circ$  are tested in a transonic-supersonic wind tunnel. The instability modes are identified from their surface temperature footprints, measured using infrared thermography. Following are the important conclusions:

1. Visualisations show that instability induced spiral vortices appear on rotating cones facing high-speed inflow at  $Re_L > 10^6$  and  $M = 0.5$ , similar to the inflows in aero-

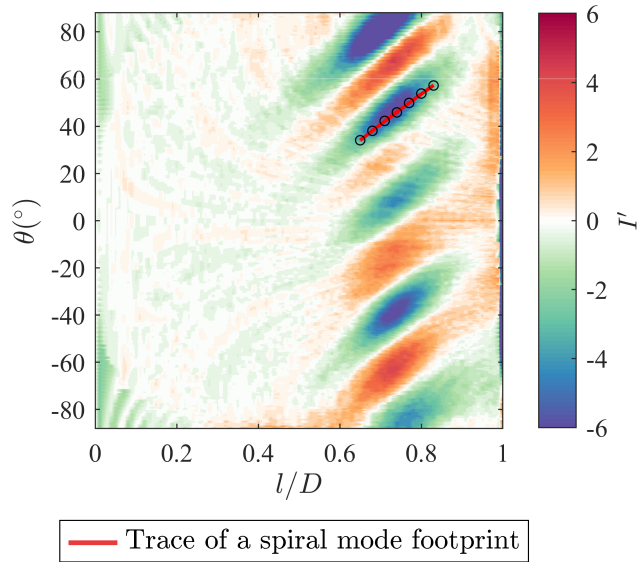


Figure 6.14: Traced wavefront of the spiral modes in  $l$  and  $\theta$  space used to obtain the wave angle  $\epsilon$ .

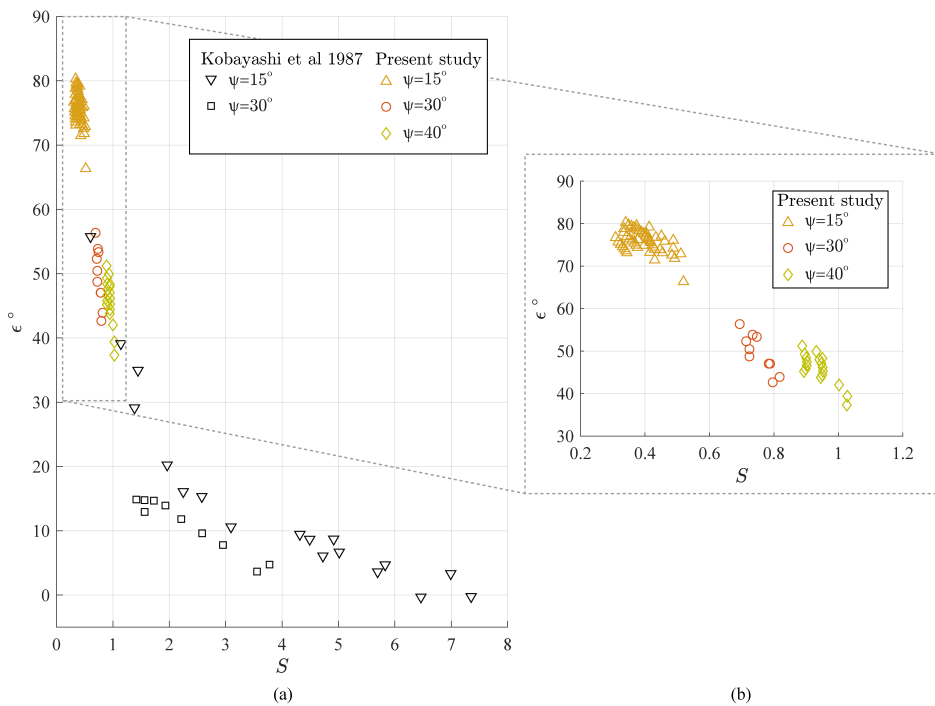


Figure 6.15: (a) Comparisons of the wave angle  $\epsilon$  obtained in the present study to those reported in the literature (Kobayashi et al., 1983) against the local rotational speed ratio  $S$ . (b) A zoomed-in view of the vortex angles obtained in the present study.

engines. Their appearance is similar to the spiral vortices observed over rotating cones in low-speed conditions.

2. In high-speed conditions, the surface temperature fluctuates in two distinct patterns: a short wavelength footprints of spiral vortices and long wavelength modulations of the spiral vortex strength. These patterns show similarities with those observed in the low-speed cases.
3. Local Reynolds number  $Re_l$  and rotational speed ratio  $S$  govern the growth of spiral vortices as expected from low-speed studies.
4. At a fixed local Reynolds number  $Re_l$ , increasing half-cone angle  $\psi$  shifts the growth of the spiral vortices at higher rotational speed ratios  $S$ . This trend was also observed in past low-speed studies.
5. The maximum amplification Reynolds number follows distinct relation with the rotational speed ratio  $Re_{l,m} = CS^{a_1}$ , extending from low- to high-speed conditions. Constants  $C$  and  $a_1$  depend on the half-cone angle  $\psi$ . For  $\psi = 15^\circ$ ,  $a_1 = -2.62$  and  $C = 2.3 \times 10^5$ . For  $\psi = 30^\circ$ ,  $a_1 = -1.62$  and  $C = 7.1 \times 10^5$ .
6. The trend of spiral vortex angle  $\epsilon$  variation w.r.t. the rotational speed ratio  $S$  is common in both low- and high-speed conditions.

## 6

This study has experimentally shown that the instability induced spiral vortices can be expected to appear on aero-engine-nose-cones during a transonic flight. This is evidently observed as the boundary-layer transition region on rotating cones extends to the parameter space of  $Re_l$  vs  $S$  at  $Re_l > 10^6$  and  $S \lesssim 1$  in a similar fashion as expected from the past low-speed studies. Comparison of low- and high-speed investigations shows that the local flow Mach number  $M_l = 0.02-0.6$  does not have a significant influence on the maximum amplification points in the  $Re_l$  vs  $S$  space. However, the cross-sectional view of the spiral vortices remains to be investigated. This information can help in identifying the underlying instability mechanism, as centrifugal instability induces counter-rotating vortices and cross-flow instability usually induces co-rotating vortices (Kobayashi, 1994). Furthermore, the effect of surface roughness on the spiral vortex growth needs to be investigated, as in reality, aero-engine nose cones may experience surface roughness as isolated elements from foreign object impacts, or as distributed roughness arising from, fasteners, manufacturing and coating techniques.

# 7

## NOSE-CONE AERODYNAMICS OF A LOW-SPEED FAN UNDER UNIFORM AND DISTORTED INFLOW

### 7.1. INTRODUCTION

Naturally, the nose-cones affect how the fan encounters the ingested flow inside an aero-engine. Chapters 3–6 have detailed the instability-induced flow features on the rotating cones without a fan. Although extending this analysis to the nose-cones installed on a fan is important, the available fan test rig (described in section 7.2) is limited to the low-Reynolds number ( $Re_l < 2 \times 10^5$ ) and low rotational speed ratio ( $S < 1.5$ ). These conditions are insufficient to simulate the growth of instability-induced spiral vortices. This can be verified from figures 6.13 and 8.5. However, the flow-field outside of the boundary-layer influences the boundary-layer instability on a nose-cone as it depends on the local Reynolds number  $Re_l$  and rotational speed ratio  $S$  (Chapter 4). Therefore, it is important to know how the typical flow-field around different nose-cone shapes develops when the fan is operating with different inflow conditions, i.e. uniform and distorted inflow.

Especially, when the embedded and UHBR engines are operating with distorted inflow (with non-uniform total pressure), the rotating nose-cones face non-axial (asymmetric) flow caused by the fan as described in 1.1, see figure 1.5. Chapter 4 has shown how non-axial inflow affects the instability-induced spiral vortices on a rotating cone. Here, for the ease of analysis, the non-axial flow was imposed by changing the incidence angle of the uniform free-stream on the rotating cone. However, the non-axial flow field around a nose-cone becomes complex when a fan is operating with the distorted inflow. In this case, investigating the boundary-layer instability is beyond the scope of this work due to the limitation on the fan test rig. Moreover, the required numerical approach becomes costly as the simulations need to be performed on a full-annulus fan with Large Eddy Simulation (LES) or Direct Numerical Simulation (DNS) to capture the boundary-layer instability phenomena. Therefore, as a first step towards exploring the boundary-layer instability on nose-cones of embedded and UHBR

---

Parts of this chapter have been presented in ASME TurboExpo 2020, GT2020-14956, Tambe et al., 2020.

engines, this chapter shows how the flow-field asymmetry develops around a nose-cone when the fan is operating with distorted inflow of varying strength.

Previous attempts at studying the fan and distortion interaction date back to mid 20<sup>th</sup> century. Reid, 1969 observed that the circumferential distortion was more detrimental to the stall margin of their compressor than the radial distortion. Furthermore, they observed that the compressor stall was insensitive to the increase in spoiled sector beyond a critical circumferential angle. For their compressor this angle was 60°. The typical effects of the inlet distortion on an aero-engine fan and compressor are discussed in Longley and Greitzer, 1992 along with the computational methods, e.g. parallel compressor theory, hydrodynamic stability analysis of stall. They showed that the value of critical distortion angle is not general. Since past decades, the topic has been revisited with the typical boundary conditions of embedded engines for novel aircraft concepts (Gunn & Hall, 2014; Gunn et al., 2013; Jerez Fidalgo et al., 2012). Although these studies involved different circumferential distortions and different fans, they show that the losses are linked to the upstream redistribution of the distorted flow. This leads to co- and counter-swirling flows at the fan face which pose off-design conditions to the fan around the annuls. A circumferential distortion also arises in high bypass ratio engines with short intakes (Cao et al., 2017; Peters et al., 2015; Vadlamani et al., 2019).

The detailed understanding of flow phenomena in the fan and distortion interaction is important to improve the performance. Such flow interactions have previously been investigated using pressure measurements and numerical simulations. However, these detailed studies are often limited to the investigations around the design point and a fixed distortion strength. The distortion index is used to quantify the strength of the distortion. The present work uses a well-known distortion index  $DC_{60}$ , defined as

$$DC_{60} = \frac{\overline{P_{t,360^\circ}} - \overline{P_{t,60^\circ}}}{\overline{P_{t,360^\circ}}}. \quad (7.1)$$

Here,  $\overline{P_{t,360^\circ}}$  is the circumferential average of the total pressure.  $\overline{P_{t,60^\circ}}$  is the lowest average total pressure over a 60° sector. While some of the past studies have investigated the effect of different distortion patterns on the fan/compressor performance and stability (Frohnafel et al., 2016; Govardhan & Viswanath, 1997; Longley & Greitzer, 1992; Reid, 1969; Yocum & Henderson, 1980), to the authors' knowledge, effect of varying distortion index on the distortion topology (topology of the distorted flow) and up-stream redistribution around the nose-cone has not been addressed in literature. Moreover, only a couple of recent studies have investigated the velocity field in fan and distortion interaction using PIV (Guimarães et al., 2018; Nelson et al., 2014).

This chapter presents experimental investigations of the nose-cone aerodynamics when the fan is operating under uniform as well as distorted inflow. The chapter shows the effect of parametric variation in distortion index on the distortion topology and how the flow-field asymmetry develops around different nose-cones. Although, the embedded and UHBR engines are expected to experience a circumferentially distorted inflow (along with the radial distortion which is less critical for the fan performance), their topology and extent depend on aircraft configurations and operating conditions. To limit the experimental parameters in the present study, a fixed circumferentially spoiled sector, extending 60°, was imposed upstream of a low speed fan. This type of distortion has been investigated in the relevant past literature (Jerez Fidalgo et al., 2012; Reid, 1969). In the present work, Particle Image

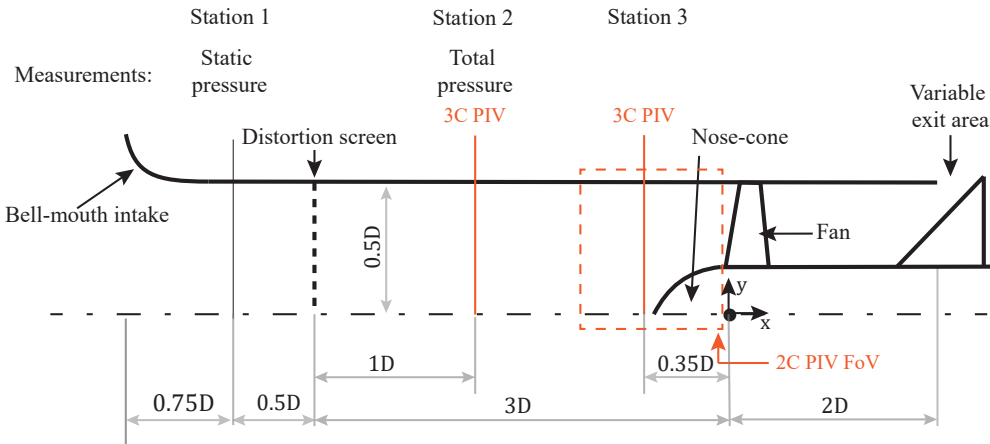


Figure 7.1: Schematic of the fan test rig and the measurement setup (not to scale).

Fan diameter $D_{fan}$ (mm)	112.75
Duct diameter $D$ (mm)	114
Hub to tip ratio $r_{hub}/r_{tip}$	0.42
Number of blades	12
Tip Mach number	< 0.33

Table 7.1: Specifications of the fan used in the experiments

Velocimetry (PIV) is applied to investigate the redistribution of the distorted inflow around the nose-cones.

## 7.2. EXPERIMENTAL SETUP

Figure 7.1 shows a schematic of the fan test rig that is used in the present work. The region upstream of the fan consists of a bell-mouth intake, a distortion screen (without flow straighteners) and a transparent straight duct providing optical access for PIV. The distortion is generated 3 fan diameters upstream of the fan to reduce any coupling effects. The fan specifications are detailed in Table 7.1. The fan is obtained from a commercial company TP Power and had originally an ogival shaped nose-cone. The fan is driven by a 3.5kW brushless motor. The operating conditions of the fan are controlled by controlling RPM and the mass flow. The mass flow is controlled by varying the exit area downstream of the fan. Figures 7.2 and 7.3 show photographs of the fan test rig with a distortion screen.

Figure 7.4 shows the geometries of different nose-cones considered for the present investigations. The slender cone of half-angle  $\psi = 15^\circ$  is chosen as it was also used to study the effect of non-axial inflow on the boundary-layer instability (chapter 4). An ellipsoid of minor axis equal to the half-major axis is chosen to investigate the effect of meridional curvature on the flow-field. Finally, an ogive obtained from the commercial company is also investigated.

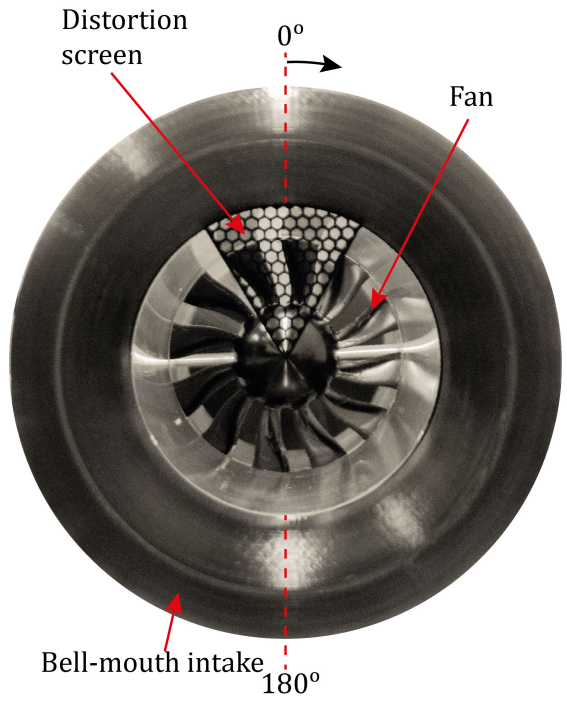


Figure 7.2: Front view of the test rig with a distortion screen.

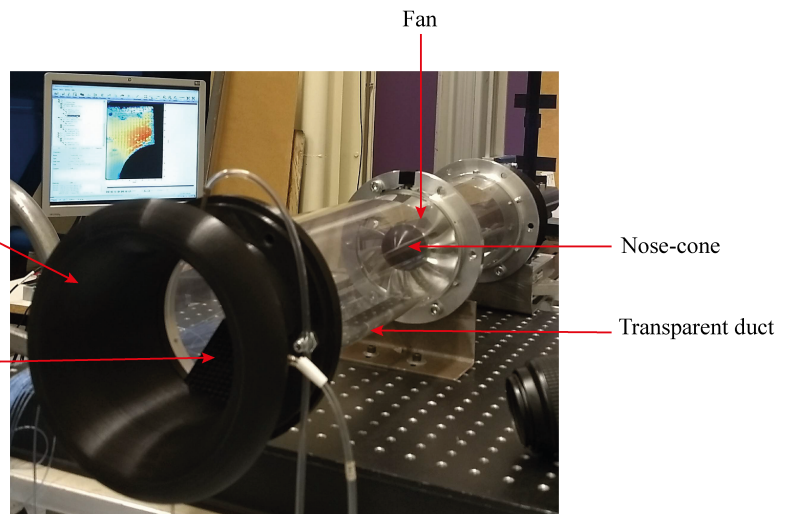


Figure 7.3: A photograph showing the fan test rig.

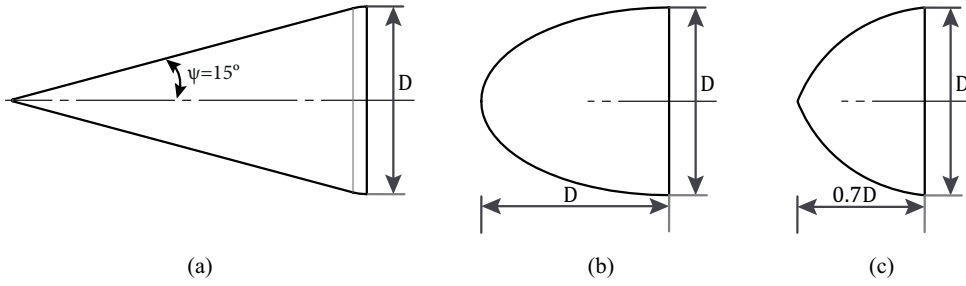


Figure 7.4: Different nose-cones considered in the present investigations: (a) slender cone with the half-angle  $\psi = 15^\circ$ , (b) ellipsoid, and (c) ogive.

Cameras	LaVision Imager 2M (2 nos.)
Camera resolution	1624 × 1236
Pixel size	4.4 μm
Seeding	Smoke (Safex Nebelfluide, 1 μm diameter)
Laser	EverGreen 200
Acquisition rate	15 Hz
Acquisition software	DaVis 8.40
Pixel density (2C)	26 px/mm
Vector pitch (2C)	0.45 mm
Interrogation window (2C)	48 × 48 pixels
Pixel density (3C)	19.5 px/mm
Vector pitch (3C)	0.4 mm
Interrogation window (3C)	32 × 32 pixels

Table 7.2: PIV specifications

Stations 1-3, shown in Figure 7.1, indicate the axial locations at which pressure measurements and PIV are performed. Static pressure at the duct wall is measured at station 1 to compute the incoming mass flow. At station 2, the total pressure is measured to compute the distortion index. Stereo PIV is performed at cross-flow planes (coincident to the duct cross sections) located at stations 2 and 3. This is done to obtain the flow topology of the distortion. Planar 2C PIV is performed in the symmetry plane (coincident with the duct axis) to measure the stream-wise flow development around the nose-cone. The measurements are carried out around the flow coefficient  $\phi = V_x/U_{\text{mid}} = 0.43 - 0.46$ , where  $V_x$  is the mean axial velocity in a duct and  $U_{\text{mid}}$  is the mid-span velocity of the fan. The inflow Reynolds number based on the duct diameter ( $Re_D = V_x D/\nu$ ) is around  $2.3 \times 10^5$ . The inflow Reynolds number based on the diameter of the nose-cone base ( $Re_{D_{\text{hub}}} = V_x D_{\text{hub}}/\nu$ ) is around  $1 \times 10^5$ . The base rotational speed ratio relating to the nose-cone ( $S_b = r_{\text{hub}}\omega/V_x$ ) is around 1.3. Specifications of the PIV setup are detailed in Table 7.2.

Intense laser reflections from the duct wall and the fan blades pose several challenges when conducting the PIV measurements. The fan blades and nose-cone are painted black to

reduce the reflections. Each particle image is pre-processed to increase the dynamic range by following a three step procedure: subtract the minimum over a dataset, multiply by a constant (100), and divide by the average over the dataset. This reduces the background light and reflections. Particle images are further enhanced by subtracting the Butterworth filter (Stephen Butterworth, 1930) (in DaVis 8.40) computed over a kernel size of 7 images. This procedure effectively eliminated the reflections. Vector calculations are performed on these pre-processed images (see Table 7.2 for details).

The total pressure is measured by a total pressure rake consisting of eight pitot probes (inner diameter 1mm) distributed radially. The pressures are scanned by NUB pressure sensor with a 2.5 kPa module. Two hundred samples are acquired at the rate of 10Hz at each circumferential location. The statistical uncertainty (Benedict & Gould, 1996) of the time-averaged pressure is below 1%.

## 7.3. RESULTS

### 7.3.1. UNIFORM INFLOW

Naturally, the nose-cone shape affects how the fan encounters the inflow in an aero-engine. Figure 7.5 shows planar views of axial (left column) and vertical (right column) velocity fields around two different nose-cone shapes: a slender cone (top row) and an ellipsoid (bottom row). The flow around the conical nose-cone undergoes a gradual contraction (figure 7.5a) with the high vertical velocity near the cone surface (7.5b). However, the blunt tip of an ellipsoid, followed by the meridional convex curvature, causes rapid changes in the axial and vertical velocity fields along a meridian (7.5c and d). These differences in flow-field will cause different boundary-layer instability behaviour on the rotating nose-cones. However, there is no infrared access in the current fan-test rig as the plexi-glass duct is opaque to the infrared radiations. Furthermore, as shown in figure 8.5, the low Reynolds number of the current fan test rig is insufficient to promote the detectable spiral vortex growth on the nose-cone. Therefore, the boundary-layer instability on rotating nose-cones has not been investigated here.

Figure 7.6 compares the velocity profiles at the Aerodynamic Interface Plane (AIP, defined here at  $x/D = -0.05$ ) for two different nose-cones: a slender cone and an ellipsoid. The difference in total velocity (resultant of axial and radial, see figure 7.6c) distribution arises due to the fact that, at AIP, the cross-sectional area is higher for the cone as compared to the ellipsoid. The difference appears in the radial velocity profiles (figure 7.6c). As expected, the radial velocity is higher near the slender nose-cone surface compared to the ellipsoid.

The difference in radial velocity results in the difference in the radial angle  $\alpha_r$ , see figure 7.7. The radial angle is overall higher for the slender nose-cone. This suggests that with the slender nose-cone the fan will encounter higher span-wise velocity as compared to the ellipsoid. This, together with the different axial velocity, will change the fan performance. However, quantifying this performance change needs high resolution total pressure measurements downstream of the fan, which were not obtained in the present setup.

### 7.3.2. NON-UNIFORM INFLOW

This section shows how the asymmetrically distorted inflow gets redistributed around the nose-cone. As discussed in chapter 4, the asymmetry of the outer flow affects the growth of the instability-induced spiral vortices on rotating cones. As depicted in figure 8.5, the low

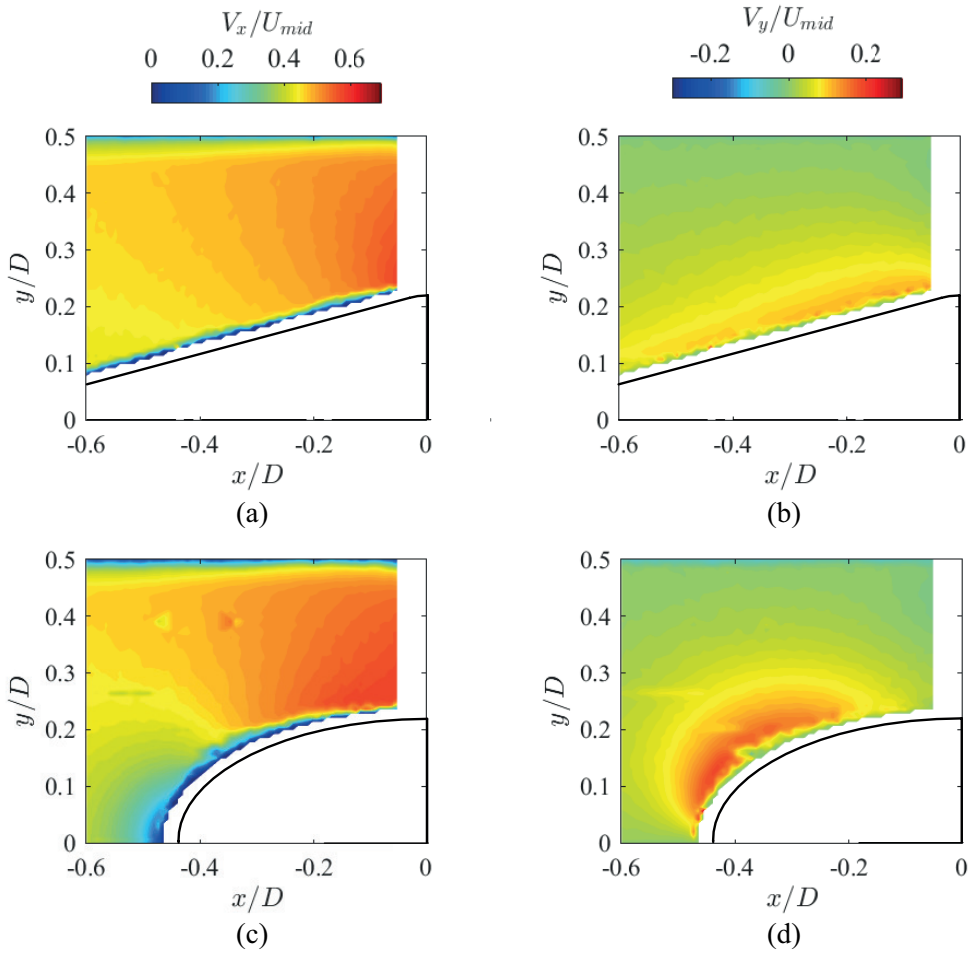


Figure 7.5: (a and c) Axial and (b and d) vertical velocity contours for two different nose-cones: (a and b) a slender cone and (c and d) an ellipsoid. The nose-cones are attached to a fan ingesting the uniform inflow at the flow coefficient  $\phi = 0.44$ . Near-wall velocity field is spoiled by the PIV laser reflections.

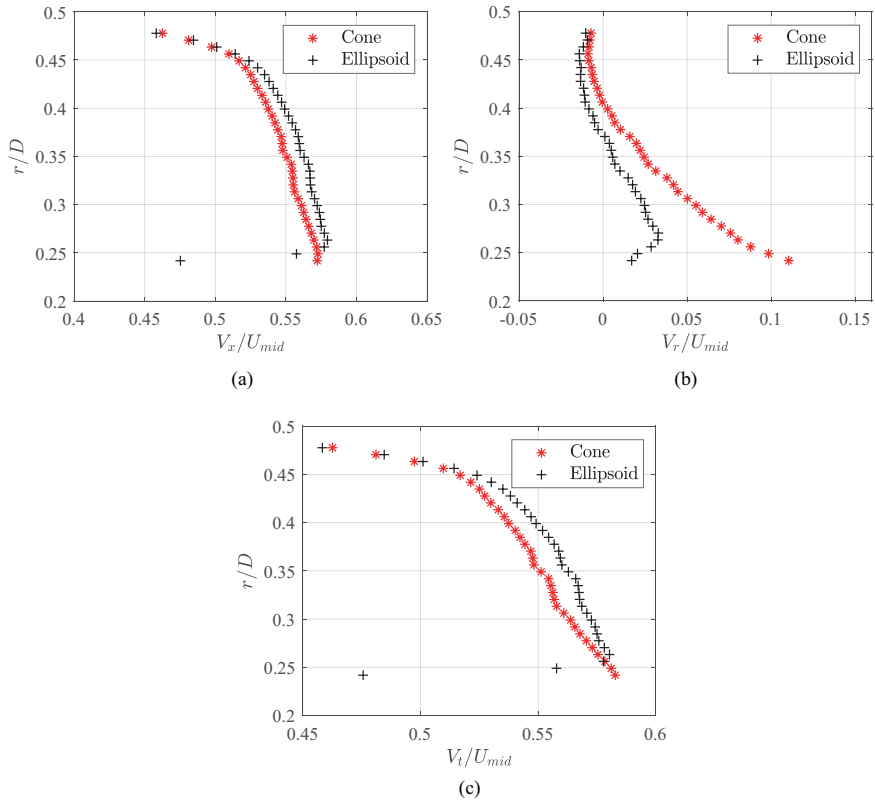


Figure 7.6: (a) Axial, (b) radial, and (c) total velocity at the AIP of the fan for two different nose-cones: a slender cone and an ellipsoid. The fan is ingesting the uniform inflow at the flow coefficient  $\phi = 0.44$ .

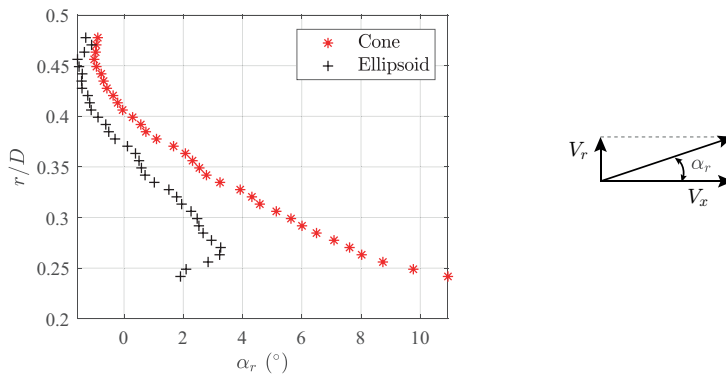


Figure 7.7: Radial angle at the AIP of the fan operating with the uniform inflow at the flow coefficient  $\phi = 0.44$ .

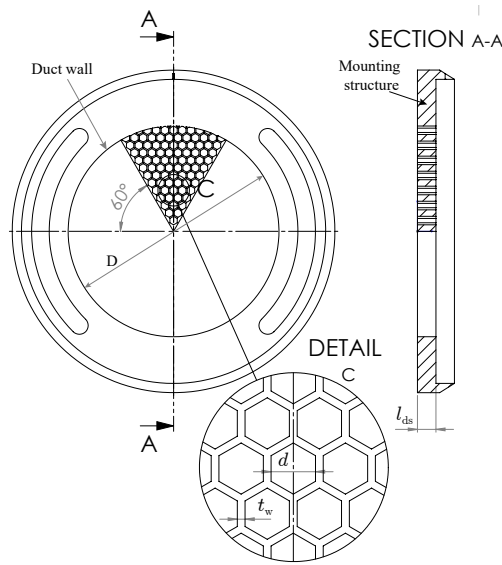


Figure 7.8: Schematic of a distortion screen.

Reynolds number fan test rigs (including the present rig) do not simulate the exact instability behaviour of the nose-cone-boundary-layer as expected in the cruise condition. Therefore, the present discussion is limited to how the asymmetry develops around the nose-cones when the fan is operating with the inflow distortion.

First, the section describes how the inflow distortion is generated and how the distortion index  $DC_{60}$  varies with the distortion screen geometry. Second, it is discussed how the distortion topology is affected by the distortion screen geometry. Finally, the section discusses how the distortion undergoes redistribution around the nose-cone and how it affects the flow field asymmetry in the symmetry plane of the nose-cone. The effect of distortion on the fan performance and flow unsteadiness are detailed in appendix C.

### DISTORTION GENERATION

The distortion was generated by means of 3D printed screens with honeycomb cells spanning circumferentially, over a  $60^\circ$  sector. Figure 7.8 shows the schematic of a distortion screen, along with the definition of its geometry parameters: diameter  $d$  of a circle inscribed in an hexagonal cell, axial depth  $l_{ds}$ , wall thickness  $t_w$ , and duct diameter  $D$ .

Table 7.3 details the geometry specifications of the five distortion screens that are used in this study. Figure 7.9 shows the diametric views of these distortion screens. The value of  $DC_{60}$  was varied by changing the grid porosity, defined as the ratio of unblocked area to the total area of the grid. The grid porosity was varied by changing the inner diameter ( $d$ ) of each hexagonal orifice while maintaining the same depth ( $l_{ds}$ ) to diameter ( $d$ ) ratio  $l_{ds}/d$  (see Table 7.3), as recommended in literature (Idelchik, 1986). The inner cell diameter  $d$  is increased from the screen DS1 to DS4 while maintaining constant  $l_{ds}/d$  and wall thickness  $t_w$ . For the screen DS5, both inner cell diameter  $d$  and wall thickness  $t_w$  are increased.

Figure 7.10a shows that  $DC_{60}$  monotonically varies with the inner cell diameter  $d$ . The

Screen	Grid porosity	$l_{ds}/d$	$t_w/D$	$d/D$
DS1	60.5%	2.5	0.0061	0.024
DS2	64.5%	2.5	0.0061	0.029
DS3	68.2%	2.5	0.0061	0.035
DS4	78.0%	2.5	0.0061	0.061
DS5	72.7%	2.5	0.0088	0.070

Table 7.3: Distortion screen specifications

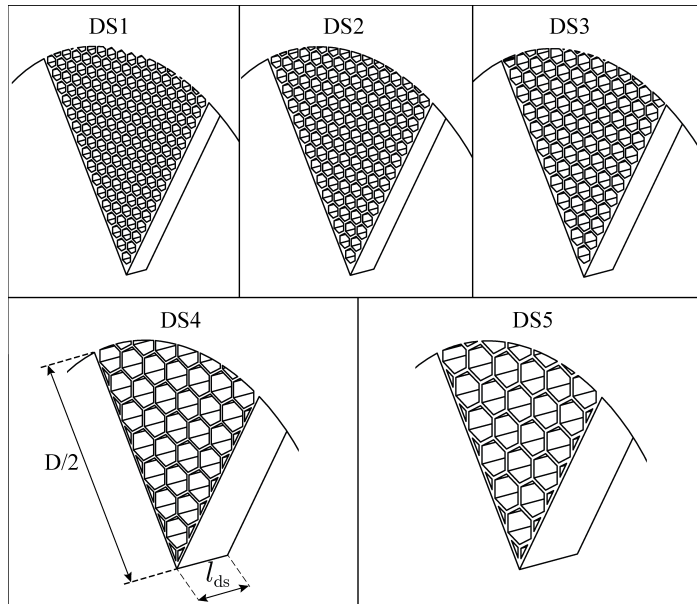


Figure 7.9: Diametric views of the distortion screens.

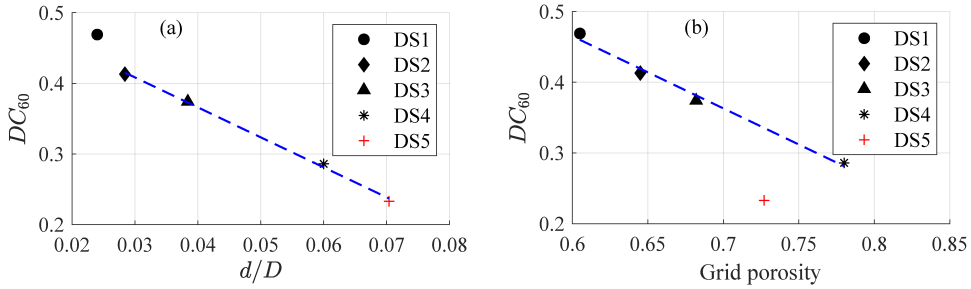


Figure 7.10: The variation of  $DC_{60}$  with respect to (a) inner cell diameter  $d/D$  and (b) grid porosity.

variation is linear except for the stronger distortion of the screen DS1. However, for a constant  $l_{ds}/d$  and wall thickness  $t_w$ ,  $DC_{60}$  is found to scale linearly with the grid porosity (see Figure 7.10b). A deviation from the linear trend is observed when the wall thickness  $t$  of cells is changed (see DS5 in Figure 7.10b).

### DISTORTION TOPOLOGY

The distortion topology and transfer from the screen to the fan face is observed to be different for different distortion screens. Figure 7.11 shows the distortion transfer from the screen to the nose-cone in terms of the velocity fields obtained using stereo PIV (3C) in cross-flow planes. For the distortion screen DS1, the topology of the distortion is distinctly different than that of DS4, even though they correspond to the linear trend of  $DC_{60}$  in Figure 7.10b.

Figure 7.12a shows the axial vorticity field at station 2, downstream of the screen DS1. The region with concentrated positive and negative vorticity suggests that there exists a counter-rotating vortex pair with the mutual velocity in radially outward direction. This drives the high momentum flow from the clean region (defined here as the circumferential location of  $180^\circ$ , opposite to the distortion screen) towards the distorted region. This results in a two lobed distortion pattern observed in velocity fields and total pressure measurements from Figure 7.11a. Such vortex pairs are also observed for screens DS2 and DS3. However, no vortex pairs are observed for screens DS4 and DS5.

Comparing figures 7.12a and b shows that the vorticity field is weaker for screen DS3 than that of screen DS1. The vortex strength is quantified by the circulation  $\Gamma$  present in each vortex (together, the circulation is zero for a vortex pair).  $\Gamma$  is estimated by the area integration of the vorticity  $\omega_x$  over the half sectors of the cross-flow planes from Figure 7.12. Table 7.4 shows the circulation estimates for screen DS1 and DS3, normalized by scales relating to the fan rotation at the midspan. The vortex pair is stronger for the higher  $DC_{60}$ . The order of magnitude of the circulation in the vortex pair is much lower than the magnitude of the circulation corresponding to the fan rotation, suggesting that the vortex pairs are weak.

There are primarily two reasons why the vortex pair is present for DS1, DS2 and DS3, but not for DS4 and DS5: increased total pressure loss, and reduced depth  $l$  as a consequence of same  $l_{ds}/d$ . The longer depth  $l_{ds}$  of screens DS4 and DS5 (see Figure 7.9) constrains the streamlines to be parallel to a longer axial extent, resulting in more uniform static pressure field downstream of the distortion screen. This, combined with the lower total pressure differences, suppresses the formation of a stream-wise vortex pair downstream

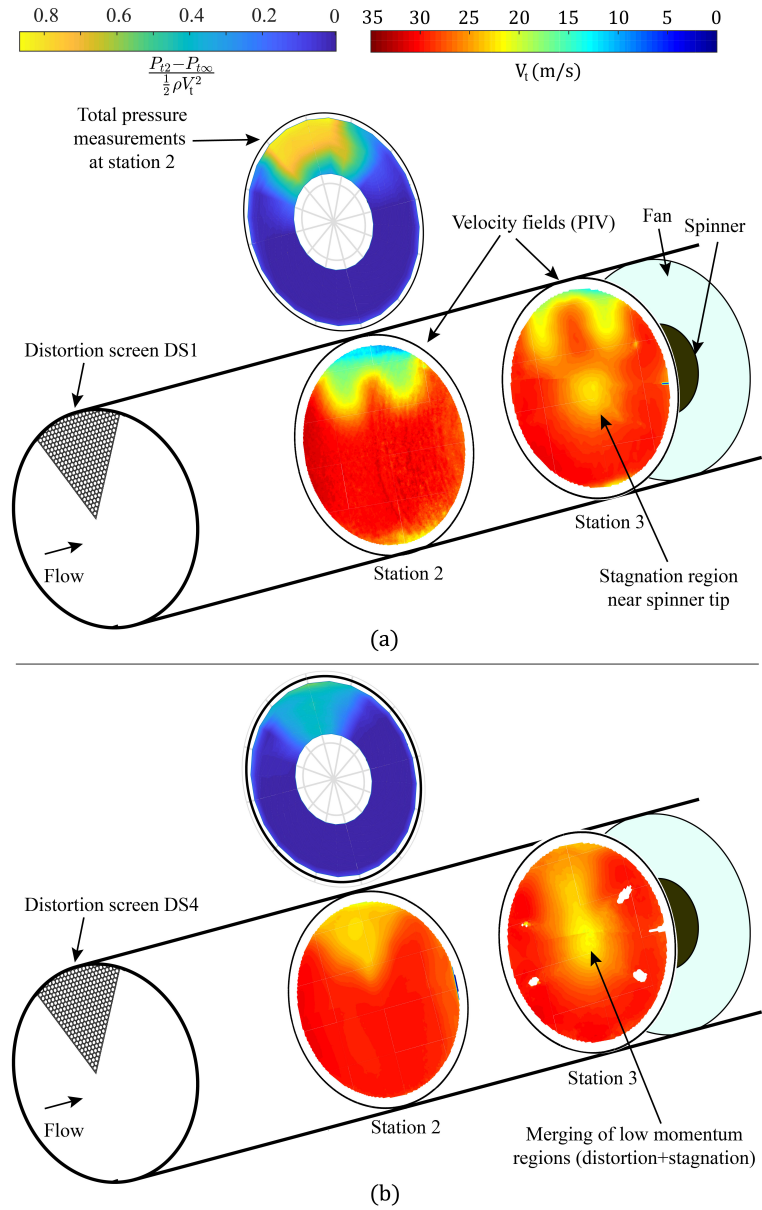


Figure 7.11: Distortion transfer upstream of the fan for two distortion screens (a) DS1 (b) DS4.

of the distortion screen. Additionally, the fan itself influences the distortion generation mechanism, however, this interaction is not explicitly studied here. It shall be noted that there is no dedicated flow straightener in the present experimental setup.

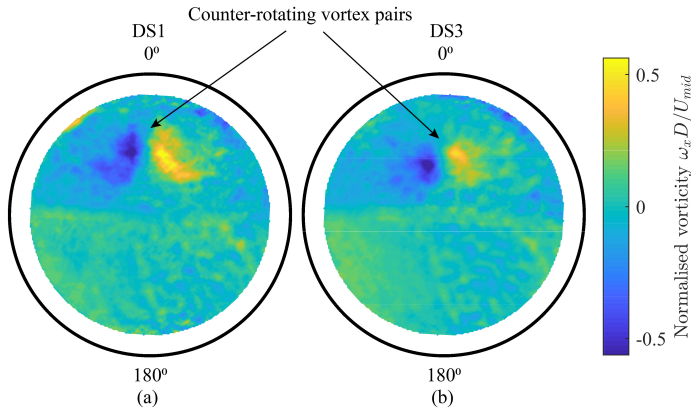


Figure 7.12: Axial vorticity field at station 2 for (a) DS1 and (b) DS3.

Screen	Normalised circulation $2\Gamma/\pi DU_{mid}$	$DC_{60}$
DS1	0.0054	0.47
DS3	0.0032	0.37

Table 7.4: Strength of stream-wise vortices downstream of the distortion screen

#### REDISTRIBUTION OF THE DISTORTION AND FLOW-FIELD ASYMMETRY AROUND THE NOSE-CONE

Past studies have shown that the fan imparts more work on the low momentum fluid in the distorted region (Jerez Fidalgo et al., 2012). This forms a localized increase in suction upstream of the rotor. As a result, the inflow undergoes a three dimensional redistribution around the nose-cone. Figure 7.13 shows slices of this redistribution region for three distortion screens. These velocity fields are obtained by merging the PIV measurements taken separately in two halves of the symmetry plane. A cross sectional view of flow at the nose-cone tip (station 3) is shown in Figure 7.11.

It is clear from Figure 7.13 that the momentum in the distorted region increases from the nose-cone tip to the fan face. This is a combined effect of three factors: area contraction, increased local work by the fan, and three dimensional flow migration from the clean to the distorted region. Clearly, this helps in reducing the circumferential asymmetry of the total pressure distribution to some extent. Although the fan drives the upstream redistribution of the distorted inflow, the asymmetry still persists at the AIP (Aerodynamic Interface Plane, chosen here at the axial location closest to the fan where the laser reflection from the fan blades are absent in PIV measurements).

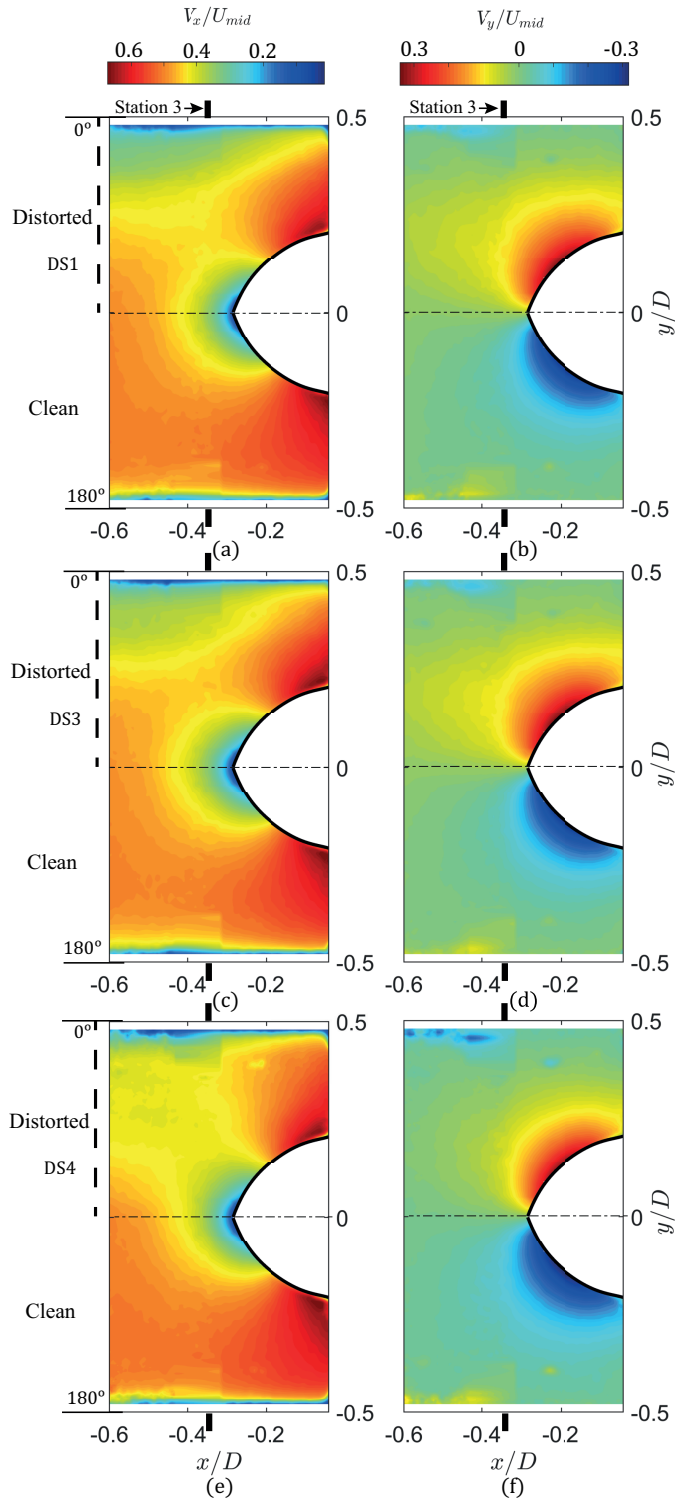


Figure 7.13: Planar PIV results in the symmetry plane with the contours of streamwise velocity (a) DS1, (c) DS3 and (e) DS4, and vertical velocity (b) DS1 (d) DS3 and (f) DS4. The results show the increase in flow momentum in the distorted region as the flow approaches the fan.

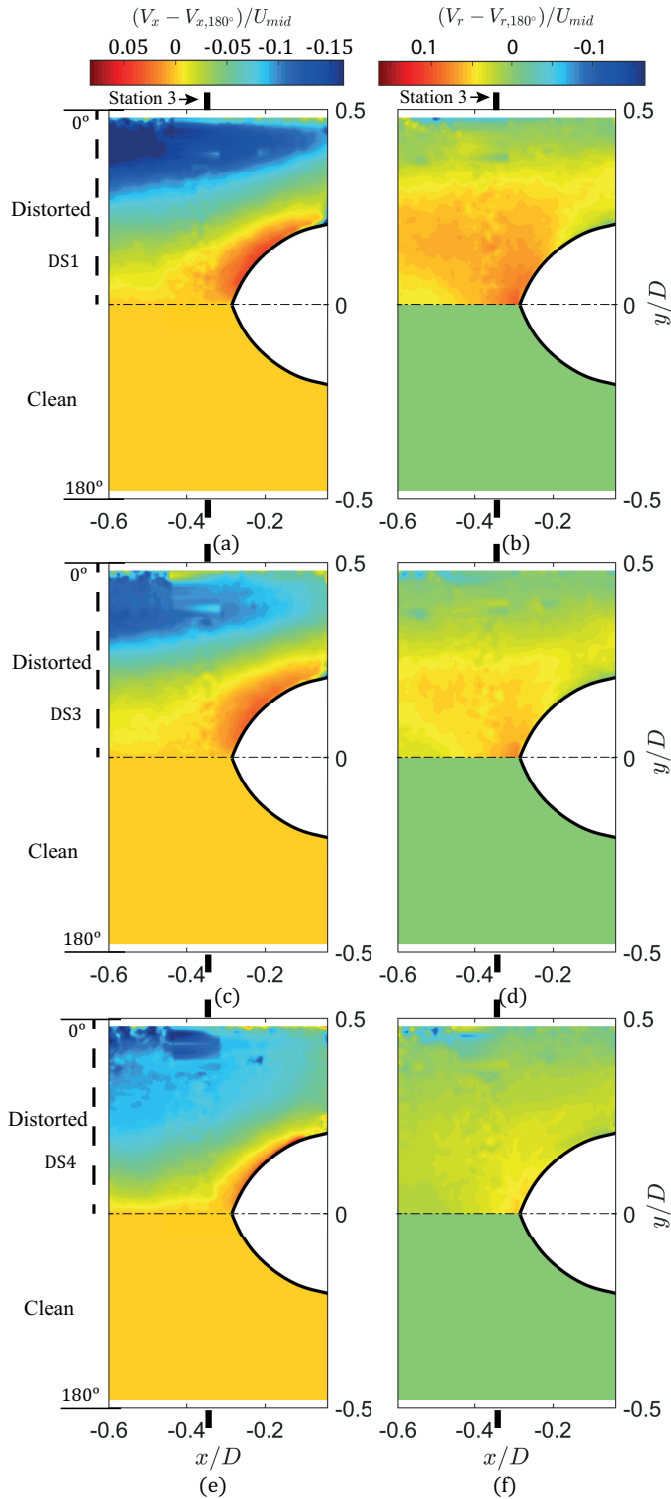


Figure 7.14: Flow asymmetry between the clean ( $180^\circ$ ) and the distorted ( $0^\circ$ ) sector (clean sector subtracted from the flow field). The contours of streamwise velocity (a) DS1, (c) DS3 and (e) DS4, and radial velocity (b) DS1 (d) DS3 and (f) DS4. The results show that the flow-field asymmetry is reduced near the nose-cone wall as the flow approaches fan.

Figure 7.14 shows the asymmetry between the clean and the distorted sectors in the symmetry plane. The contours are obtained by subtracting the velocity field of clean sector ( $180^\circ$ ) from the corresponding velocity fields shown in Figure 7.13. Therefore, the negative values of axial velocity component (Figure 7.14a, c, and e) show the momentum deficit as compared to the clean sector. Whereas, the positive values represent the additional flow acceleration caused by the non-axial flow over the nose-cone. Similar high momentum jet over the nose-cone has also been reported in the literature (Jerez Fidalgo et al., 2012). This high momentum region is present in all the cases, regardless of the upstream distortion topology. However, its strength and extent depend on the distortion index as well as topology.

Figure 7.14b, d, and f show asymmetry in the radial velocity component. It is clear that for  $DS4$ , where there is no vortex pair upstream, the radial velocity distribution is almost symmetric except near the nose-cone tip. The sharp change about the axis is an artifact of the reconstruction method, where separately measured velocity fields in two halves of the symmetry plane are merged together. The mutual up-wash (radially outwards) of the vortex pair affects the redistribution region which is clearly seen for the cases of  $DS1$  and  $DS3$ . However, the asymmetry in radial velocity decreases towards the nose-cone base.

Figure 7.14 shows that the asymmetry of the distorted flow is reduced near the nose-cone walls compared to the radially outward regions. The asymmetry is lower for the low distortion case, where there is no upstream vortex pair ( $DS4$ , figures 7.14e and f). As discussed in chapter 4, the boundary-layer instability on nose-cones can cause the growth of coherent spiral vortices in the non-axisymmetric flow field. This growth starts where the instability characteristics, i.e. spiral vortex angle and azimuthal number, do not significantly vary around the azimuth in asymmetric flow field. Therefore, as the fan reduces the asymmetry of the distorted inflow near the nose-cone walls, the conditions for the spiral vortex growth become more favourable. However, the inflow conditions will determine the sensitivity of the instability characteristics to the azimuthal flow asymmetry and whether the spiral vortices will form.

Figure 7.15 shows the velocity profiles at the AIP ( $x/D = -0.06$ ), including the clean flow (without any distortion screen). In the clean sector ( $180^\circ$ ), the velocity profiles are only slightly affected by the distortion (see Figure 7.15a and b). Whereas, the velocity profiles differ in the distorted sector ( $0^\circ$ , see Figure 7.15c and d). This suggests a different incidence angle on the fan blades in clean and distorted region.

Additionally, Figures 7.15e and f show the asymmetry between the clean ( $180^\circ$ ) and the distorted ( $0^\circ$ ) regions. Here, comparison of  $DS3$  and  $DS4$  shows that the asymmetry in  $DS3$  is recovered to a larger extent, even though the distortion of  $DS3$  is 30% stronger compared to  $DS4$  (see Figure 7.10). This shows that the presence of an upstream vortex pair has premixed the flow which leads to the reduced asymmetry in the symmetry plane. However, the asymmetry in the radial velocity is monotonically increasing with the distortion index.

Although the upstream vortex pair helps in reducing the asymmetry in the symmetry plane, the extent of recovery is not monotonic with distortion index. In Figure 7.15e, the stronger distortion  $DS1$  (therefore stronger flow migration by the vortex pair) does not lead to the larger recovery compared to  $DS3$ . This shows that the flow development in this region is complex and also depends on the properties of the distortion topology upstream.

Furthermore, this analysis is extended to the right-circular type nose-cone with half cone angle  $\psi = 15^\circ$ , same as the case of a rotating cone in non-axial inflow, investigated in chapter

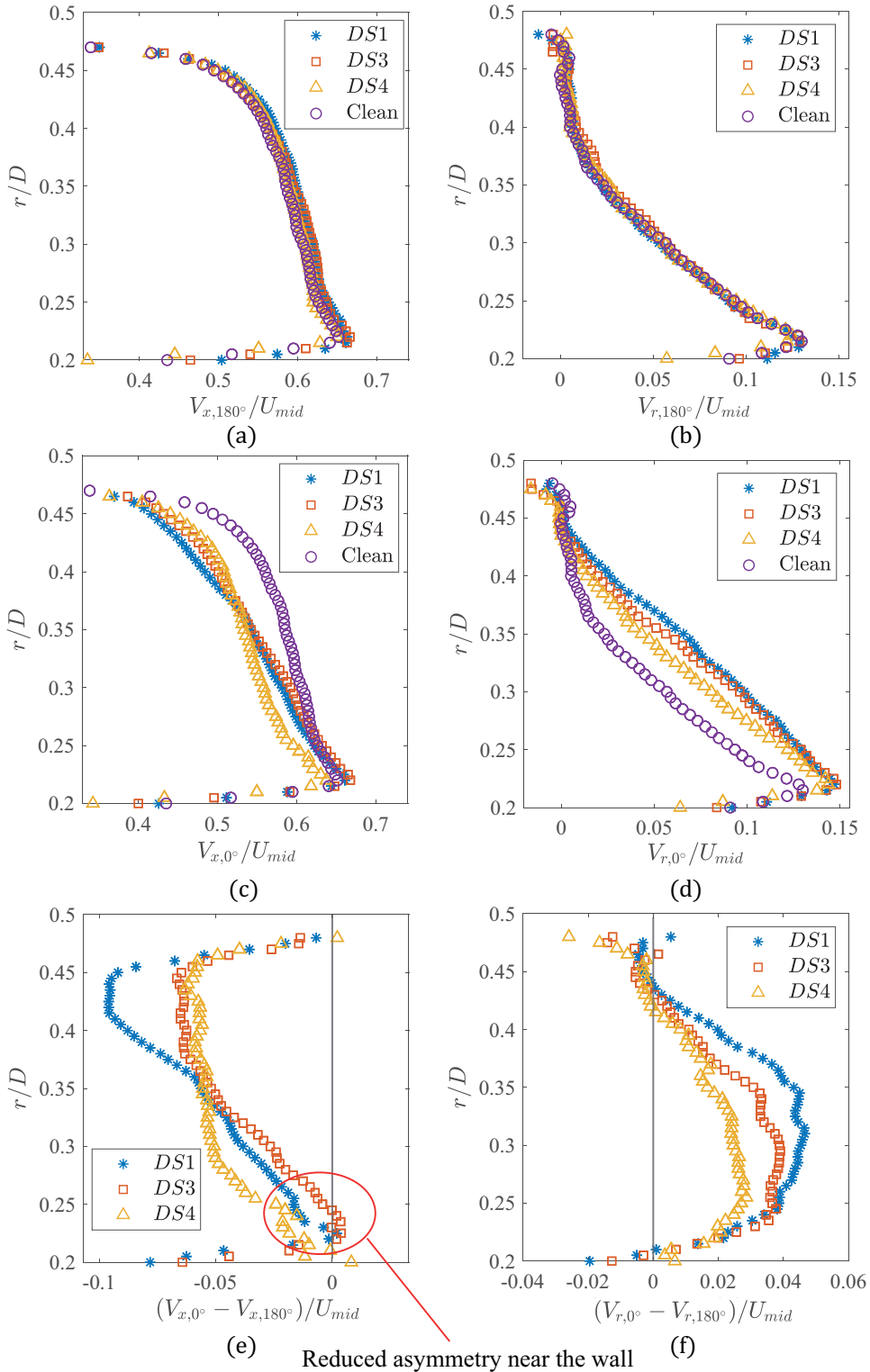


Figure 7.15: Velocity profiles at AIP. Comparison between clean and distorted inflow at (a), (b) clean sector ( $180^\circ$ ), and (c), (d) distorted sector ( $180^\circ$ ); (e), (f) asymmetry between the clean and distorted sector.

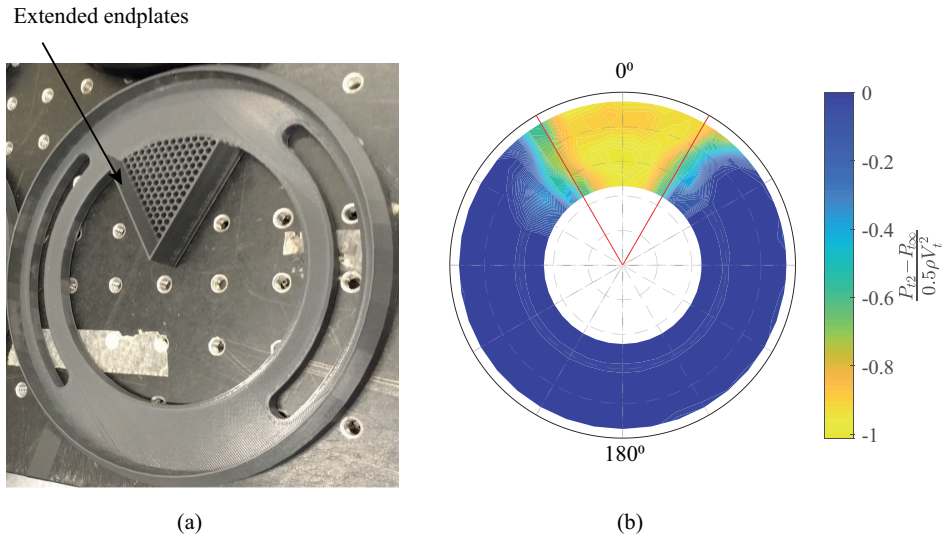


Figure 7.16: (a) Distortion screen  $DS1e$  modified from  $DS1$  by extending the edges to retain the distortion topology downstream. (b) Total pressure deficit downstream of the distortion screen  $DS1e$ , measured at station 2.

7

4. The distortion screen  $DS1e$  is used for this analysis (figure 7.16a). This distortion screen is the modified version of the  $DS1$  (figure 7.9), relating to the strongest distortion in the present study. To eliminate the stream-wise vortex pair associated with the screen  $DS1$ , its modified version  $DS1e$  features the edges extended in the stream-wise direction (as pointed in figure 7.16a), with the total edge length of  $0.12D$ . This straightens the flow and eliminates the radial transfer of the clean flow into the distorted region, see figure 7.16b. This results in the distortion index 0.47.

The PIV measurements in the symmetry plane show that the flow momentum increases in the distorted region close to the fan (figure 7.17). The overall momentum in the distorted flow is lower in figure 7.17 as compared to the case in figure 7.13. This relates to the absence of the longitudinal vortex pair downstream of the screen  $DS1e$ , unlike  $DS1$ . Therefore, there is no clean flow migration towards the distorted region upstream of the nose-cone.

Subtracting the axial and radial velocity field from those in the symmetry plane shows the asymmetry, see figure 7.18. The positive values near the nose-cone surface indicate the flow migration from the clean to the distorted region, similar to the case shown in 7.14. Figure 7.19 shows the velocity profiles extracted at the AIP ( $-0.05D$  in this case) from figures 7.17 and 7.18. Together, figures 7.17, 7.18, 7.19 show that, in the symmetry plane, the flow-field asymmetry is reduced near the surface of a nose-cone with  $\psi = 15^\circ$ . This shows that changing the nose-cone shape does not change the qualitative nature of the upstream redistribution of the distortion.

The effect of nose-cone shape on the distortion transfer across the fan is discussed in appendix D.

It is clear from the above discussion that the fan drives the redistribution of the oncoming distorted flow, and the momentum at the fan face becomes more uniform. However, the

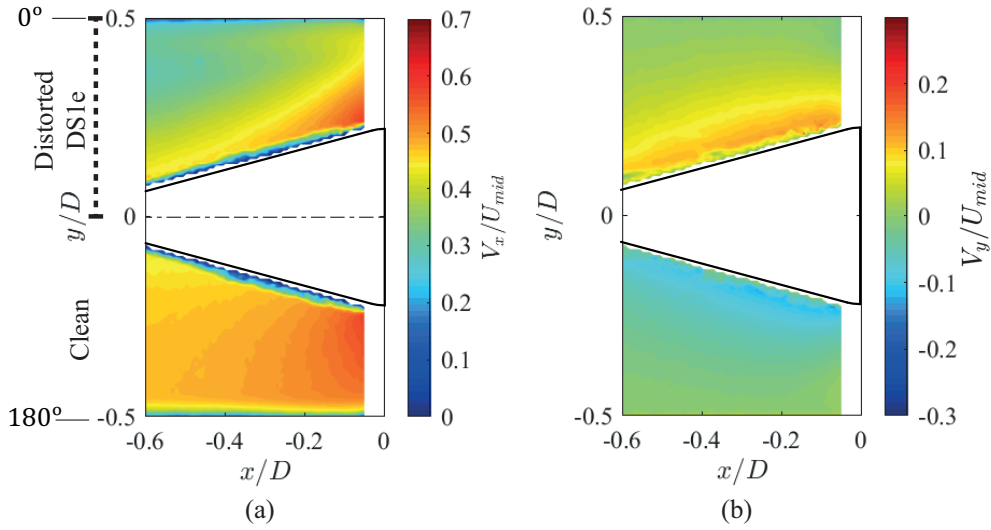


Figure 7.17: Planar PIV results in the symmetry plane with the contours of (a) streamwise velocity and (b) vertical velocity for a slender nose-cone ( $\psi = 15^\circ$ ). The results show that the momentum in the distorted region increases as the flow approaches the fan, similar to figure 7.13.

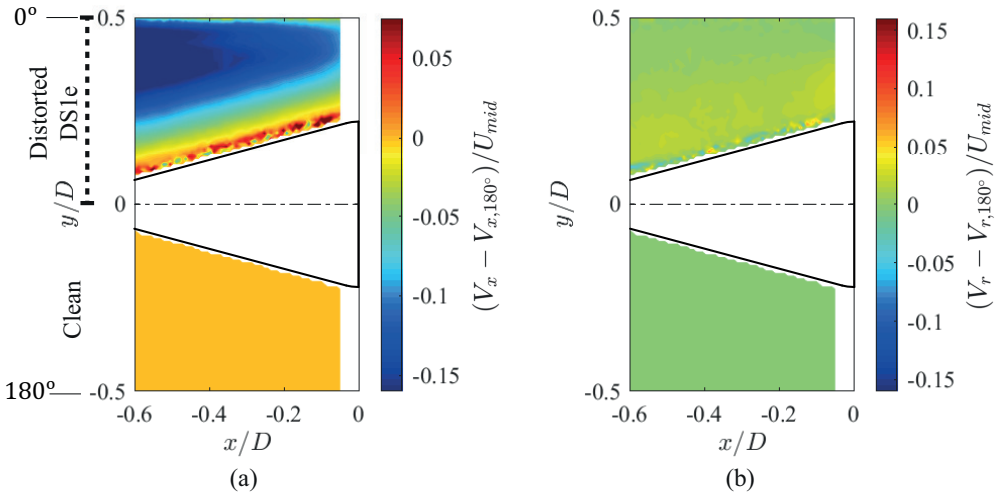


Figure 7.18: Flow asymmetry between the clean ( $180^\circ$ ) and the distorted ( $0^\circ$ ) sector (clean sector subtracted from the flow field) for a slender nose-cone ( $\psi = 15^\circ$ ). The contours of (a) streamwise velocity and (b) radial velocity component. The results show that the flow asymmetry reduces near the nose-cone surface, similar to figure 7.14.

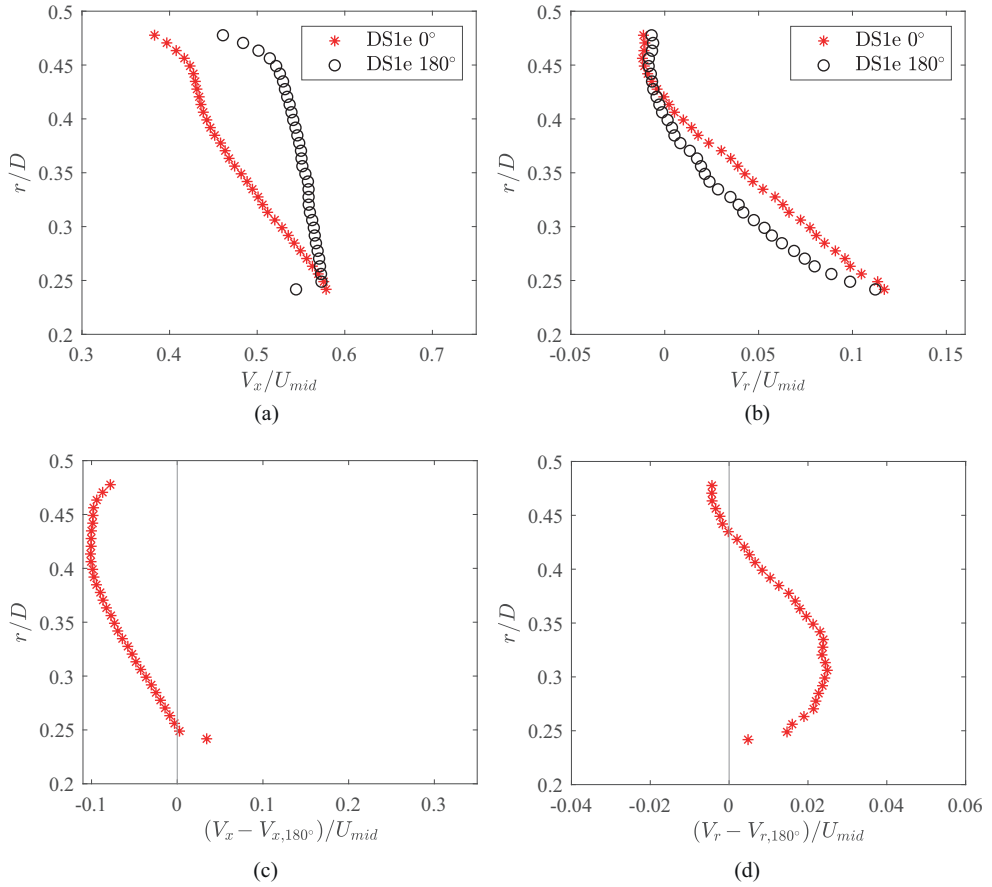


Figure 7.19: (a) Streamwise and (b) radial velocity profiles at AIP for a slender nose-cone ( $\psi = 15^\circ$ ) with the distortion screen DS1e. Flow asymmetry between the clean ( $180^\circ$ ) and the distorted ( $0^\circ$ ) sector (clean sector subtracted from the flow field) for a slender nose-cone ( $\psi = 15^\circ$ ), shown as (c) streamwise and (d) radial velocity profiles. The results show that the flow asymmetry reduces near the nose-cone surface, similar to figure 7.15.

redistribution is largely affected by distortion topology, index, and the presence of a nose-cone. Note that the presented discussion is limited to the symmetry plane. Co- and counter-rotating cross flow velocities also play an important role in the asymmetry, and govern the mechanism of losses occurring in the fan.

## 7.4. CONCLUSION

- Nose-cone shape significantly influences how the fan encounters the ingested inflow in an aero-engine.
- When operating with the distorted inflow, the fan causes increased suction in the distorted region. This causes the distorted flow to redistribute around the rotating nose-cone, causing non-axial inflow over the nose-cone. This behaviour is observed regardless of the strength, topology of a circumferential distortion, and nose-cone shape.
- As the distorted inflow approaches the fan, the flow from the clean region migrates towards the distorted region, around the nose-cone. This significantly reduces the asymmetry near the nose-cone wall in the symmetry plane. The reduced asymmetry is favourable condition for the instability characteristic to achieve the azimuthal coherence causing spiral vortex growth. However, the inflow conditions and the nose-cone shape (including the meridional curvature) will determine the boundary-layer instability behaviour and where it attains the azimuthal coherence of its characteristics. As the fan test rig did not replicate the near-flight inflow conditions, further investigation is required to characterise instability-induced flow structures on nose-cones in a distorted inflow.



# 8

## RELEVANCE OF THE NOSE-CONE BOUNDARY-LAYER INSTABILITY TO AERO-ENGINES

### 8.1. INTRODUCTION

PREVIOUS chapters 2–6 fundamentally discussed the boundary-layer instability on rotating cones in aero-engine-like inflow conditions. This chapter interprets these findings in the context of their practical relevance and their possible influence on the fan aerodynamics. Throughout the chapter, several areas of further research are identified to assess the impact of the nose-cone-boundary-layer instability on the losses in aero-engines.

Section 8.2 presents the potential interactions between the instability-induced spiral vortices on a nose-cone and fan aerodynamics near the hub. At present, the descriptions of these interactions are purely conceptual and they are based on the following: 1) present study about the spiral vortices on rotating nose-cones and 2) literature describing the near-hub aerodynamics in isolated blade passages. Moreover, this section conceptually describes the potential effects of the spiral vortex amplification on the hub-corner separation, and therefore, highlights the requirement of knowing the amplification location on the aero-engine-nose-cone.

For the practical benefit, the occurrence, growth and amplification of the spiral vortices on a nose-cone need to be interpreted in the realistic flow conditions faced by an aero-engine. Section 8.3 shows the expected occurrence of the spiral vortices on an aero-engine-nose-cone during a transonic flight. Here, the flow parameters relating to the maximum amplification of the spiral vortices (from chapter 6) are compared with those estimated on aero-engine-nose-cones at transonic cruise conditions.

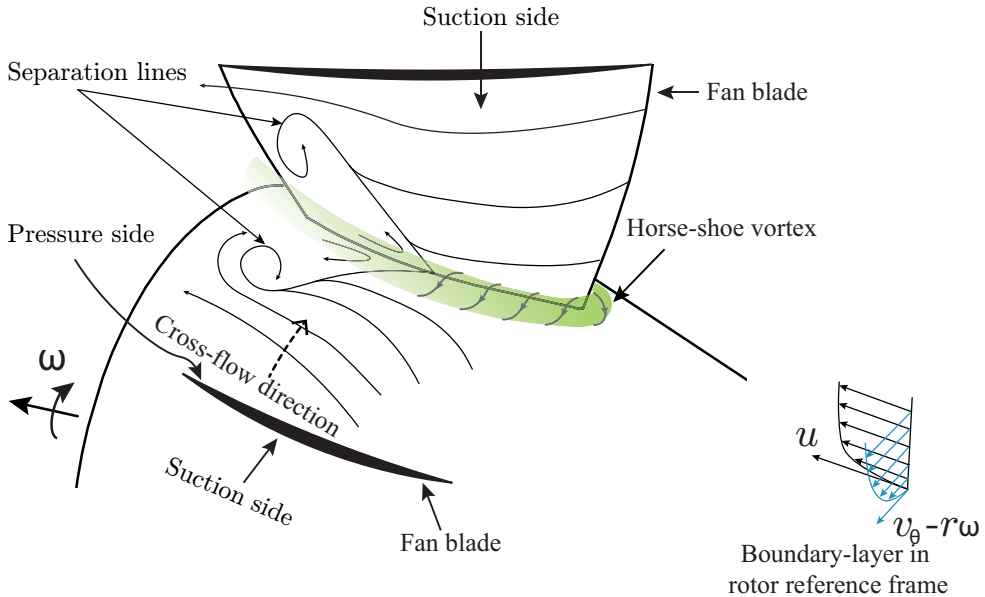


Figure 8.1: A schematic of the hub-corner separation on a fan blade (concepts adapted from Chen et al., 2014; Lei et al., 2008).

## 8.2. POTENTIAL EFFECT OF NOSE-CONE BOUNDARY-LAYER INSTABILITY ON FAN AERODYNAMICS

The instability-induced spiral vortices on the nose-cones may affect the fan aerodynamics, especially near the blade-hub junction. This junction flow is a loss-source in turbo-machinery. Gbadebo et al., 2005 suggested that almost all the compressor blades will have a separated flow at their trailing edge near the hub. Since a fan is fundamentally a compressor, a similar flow separation near the hub-blade junction exists on transonic fan rotors (Arnone, 1993; Lian & Liou, 2005; Yan et al., 2019).

Figure 8.1 schematically shows the flow separation phenomenon at the hub-blade junction (the concept is partly based on previous studies by Lei et al., 2008 and Chen et al., 2014). This phenomenon is also known as the hub-corner separation. The schematic shows a passage confined between two fan blades. The pressure is low on the suction side and high on the pressure side. This creates a cross-wise pressure gradient in the passage. The hub boundary-layer is affected by this cross-wise pressure gradient because of its low momentum near the wall. This low-momentum fluid moves across the passage towards the suction side and starts to accumulate in the hub-corner region. Here, the suction side of the blade has an adverse chord-wise pressure gradient near the trailing edge. The gathered low-momentum flow near the hub-corner cannot sustain the adverse chord-wise pressure gradient and separates. This separated region extends span-wise and in extreme cases also extends towards the pressure side in the passage. This type of separation reduces the total pressure, increases the blockage in the passage and can initiate stall (Cho et al., 2008; Gbadebo et al., 2005; Xia & Medic, 2017). Also as reported by Xia and Medic, 2017, experiments of Wei et al.,

2013; Zambonini and Ottavy, 2015; Zambonini et al., 2017 on linear compressor cascade detected three dimensional hub-corner separation at a much lower diffusion parameter (0.26) than the critical diffusion parameter (0.4) predicted by Lei et al., 2008. This shows that the hub-corner separation phenomenon is complex to predict by a simple method.

A horse-shoe vortex also exists in the hub-corner region (described in section 8.2.2). Although it is expected to play a role in hub-corner separation, a direct link between the horse-shoe vortex and hub-corner separation has not yet been established, but only tentatively suggested by previous studies (Xia & Medic, 2017). However, using Detached Eddy Simulations, Xia and Medic, 2017 found that unsteadiness in the horse-shoe vortex can cause unsteadiness in the separated hub-corner flow.

Furthermore, coherent structures in the oncoming turbulent boundary-layer can significantly alter the hub-corner separation, as evident from the experiments of Zambonini and Ottavy, 2015 on linear compressor cascades. However, past experiments on the hub-corner separation have only considered turbulent boundary-layers. But during a flight, the nose-cone boundary-layer is expected to be in the transition regime, including the coherent spiral vortices (as described in figure 8.5 in section 8.3). This is expected to have a different effect on the hub-corner separation compared to linear cascade experiments. However, this effect has not been addressed in the literature.

### 8.2.1. POTENTIAL INTERACTIONS BETWEEN THE SPIRAL VORTICES AND CROSS-FLOW IN THE BLADE PASSAGE

Figure 8.2 conceptually depicts two cases of the instability-induced spiral vortices in the blade passage of a fan with attached nose-cone: before (figure 8.2a) and after (figure 8.2b) the maximum amplification of the spiral vortices. Although the spiral vortices can be co- and counter-rotating (depending on the half-cone angle), the case of counter-rotating vortices occurring on slender cones is depicted here as an example. Before their amplification, the spiral vortices remain close to the wall and do not affect the boundary-layer as much as after their amplification (evident from figure 4.6 from chapter 4). Due to the low meridional momentum near the wall, the cross-wise pressure gradient will affect the spiral vortices and they are expected to be turned towards the suction side, as shown in figure 8.2a. This may cause a complex interaction of spiral vortices and the separation region (highlighted as interaction A in figure 8.2a).

Figure 8.2b shows the spiral vortices which have been amplified before entering the blade passage. Upon amplification the spiral vortices move away from the wall, into a region with the higher meridional velocity, evident from figure 2.13 from chapter 2, and also from figures 4.6, 4.14 and 5.8. Therefore, it is expected that the cross-wise pressure gradient has a lower effect on turning the amplified spiral vortices towards the suction side as compared to the case where the vortices have not been amplified. The two important zones have been identified (and pointed out in figure 8.2) where the spiral vortices are expected to influence the aerodynamics at the hub: (A) effect of spiral vortices on the cross-wise boundary-layer transport and (B) interaction of spiral vortices with the horse-shoe vortex.

Mean boundary-layer profiles enable understanding the typical effects of spiral vortices on the cross-wise boundary-layer transport in the passage (Interaction A, denoted in figure 8.2). Figures 8.3a and b show the meridional and cross-flow velocity, respectively, on the rotating nose-cones in an aircraft reference frame. These profiles relate to a point P upstream of the blade passage entrance, as depicted in figure 8.3. Figures 8.3c and d, show

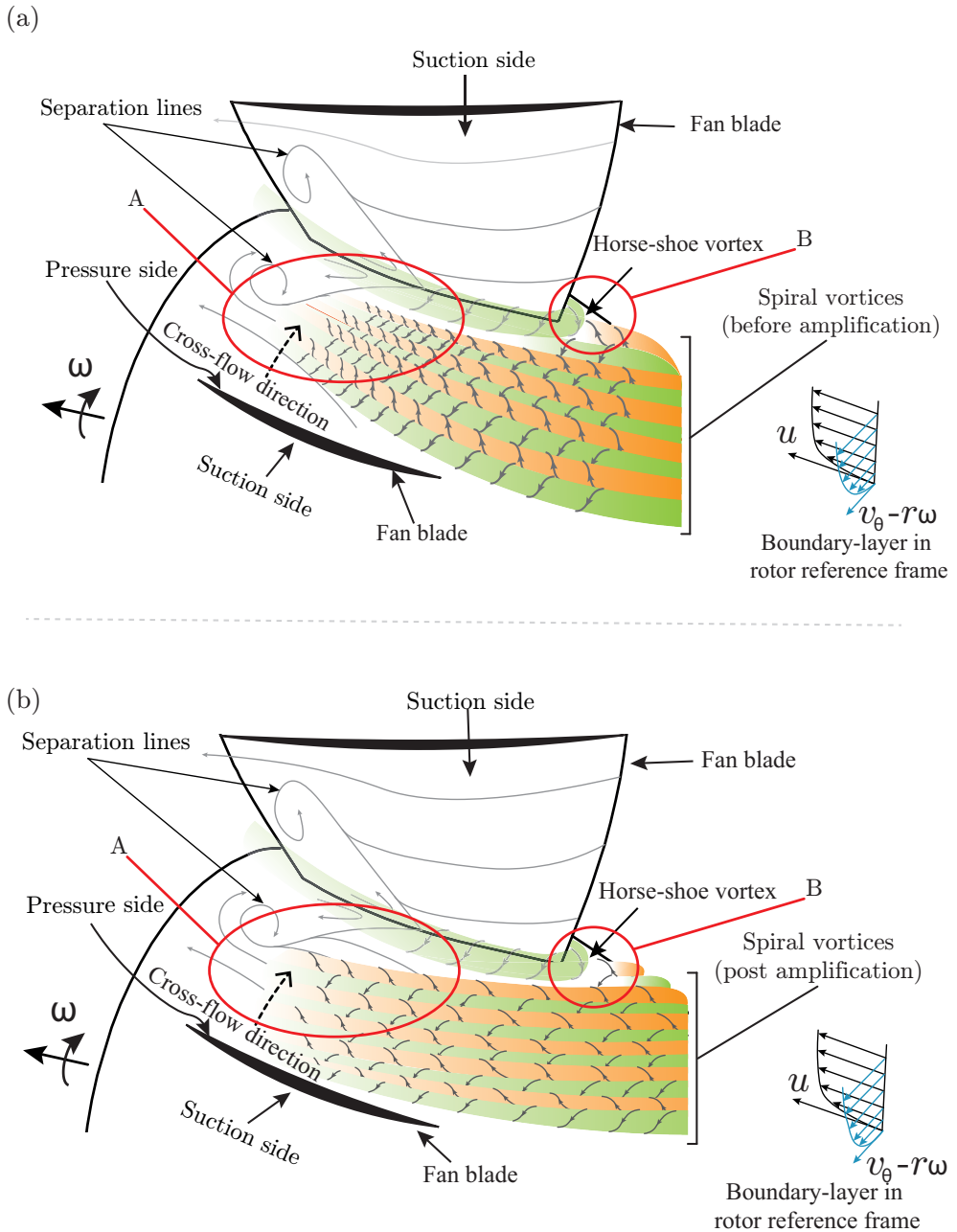


Figure 8.2: Conceptual schematics of the instability-induced spiral vortices entering a blade passage. (a) A case where spiral vortices have not reached their maximum amplification before entering the blade passage. (b) A case where spiral vortices have reached their maximum amplification before entering the blade passage.

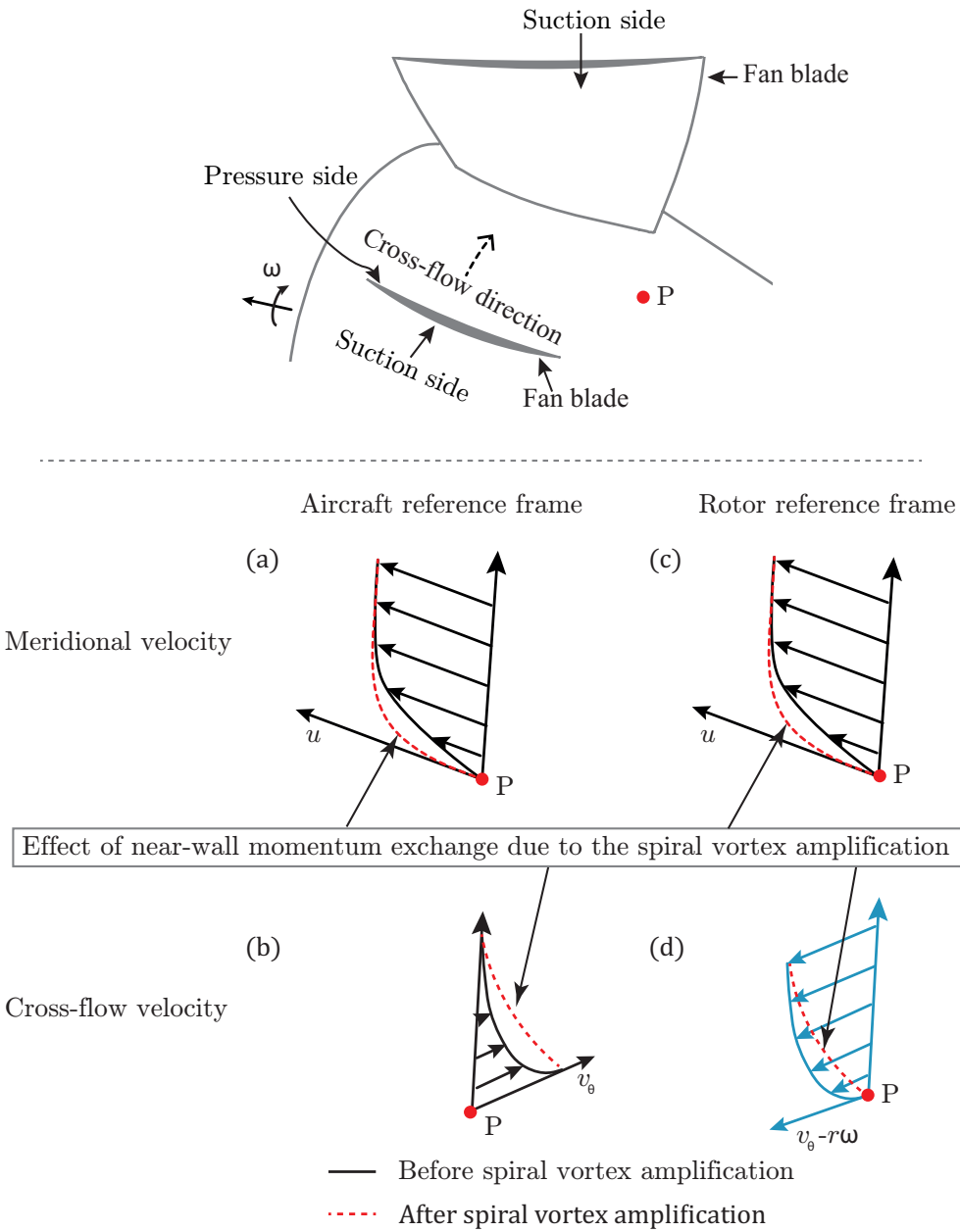


Figure 8.3: Schematics of the velocity profiles in the nose-cone boundary-layer upstream of the blade passage (at point P in a top schematic). (a),(b) are in the aircraft reference frame and (c),(d) are in the rotor reference frame. The red dotted lines show the effect of near-wall momentum exchange caused by the amplified spiral vortices (based on figure 2.13 from chapter 2, and figures 4.6, 4.14 and 5.8).

the boundary-layer velocity profiles in the reference frame of the rotor (at the same location P). Notice that the cross-flow velocity in the rotor reference frame is against the direction of the cross-wise pressure gradient in the blade passage (see figure 8.2). This suggests that, naturally, the cross-flow component of the nose-cone boundary-layer opposes the transport of the passage boundary-layer from the pressure side to suction side. However, when the spiral vortices amplify, they increase the flow momentum near the wall (evident from figure 2.13 from chapter 2). The red dotted lines in figure 8.3 show the boundary-layer profiles modified by the spiral vortex amplification. Here, the boundary-layer has increased meridional momentum closer to the wall, therefore, it is less prone to be affected by the cross-wise pressure gradient. However, the cross-flow velocity is decreased in the rotor reference frame. This will reduce the resistance to the cross-wise transport of the passage boundary-layer. The relative importance of the modified meridional velocity profile with respect to the cross-flow velocity profile will determine how much low momentum flow accumulates at the suction side of the blade. However, the increased near-wall momentum suggests that the accumulated flow near the suction side will have a higher overall momentum compared to the case without the spiral vortices, suggesting a possible delay in the separation onset.

Several past studies have investigated the effect of vortex generator rows on the cross-flow in the blade passage and the corner separation at the hub (Hergt et al., 2008; Hergt et al., 2013; Li & Ji, 2019; Ma et al., 2017). These studies used experiments on non-rotating blade cascades and RANS simulations. Therefore, their analyses did not include the instability-induced spiral vortices. However, the vortices generated by the vortex generator rows are qualitatively similar to the expected spiral vortices; therefore, these studies can be used to comprehend the extent of influence that spiral vortices can have on the hub-corner separation. Experiments of Hergt et al., 2013 showed that when vortex generators induce co-rotating vortices at the blade passage entry, they energise the boundary-layer and the separation is delayed to a further downstream location (see figure 1.4 for a conceptual adaption). They reported that the vortices entering the blade passage caused around 5% reduction in the total pressure loss. This suggests that the spiral vortices can have a beneficial effect on the fan performance near the hub. However, the orientation of the spiral vortices with respect to the blade incidence angles, strength, cross-sectional topology (co- or counter-rotating) etc. will determine whether they are beneficial or detrimental for the hub performance.

### 8.2.2. POTENTIAL INTERACTION OF THE SPIRAL VORTICES AND THE HORSE-SHOE VORTEX

Horse-shoe vortices are distinct features of the hub-blade junction flows. They contribute to the total pressure loss and their unsteadiness can cause oscillations in the hub-corner separation (Xia & Medic, 2017). Figure 8.4 schematically describes the formation of the horse-shoe vortex upstream of the blade leading edge. Here, as the boundary-layer approaches the blade leading edge, it experiences a steep adverse-pressure gradient. This leads to the boundary-layer separation. The separated flow contains the vorticity from the boundary-layer. This results in three-types of vortices as shown in figure 8.4: horse-shoe vortex (HSV), secondary vortex (SV) and tertiary vortex (TV). A corner vortex is also formed at the junction of blade and hub (Praisner & Smith, 2006).

The horse-shoe vortex system (including HSV, SV and TV) is inherently unstable (Praisner & Smith, 2006; Xia & Medic, 2017). Experiments of Praisner and Smith, 2006 showed that the coherent structures in the oncoming turbulent boundary-layer interact with the horse-shoe

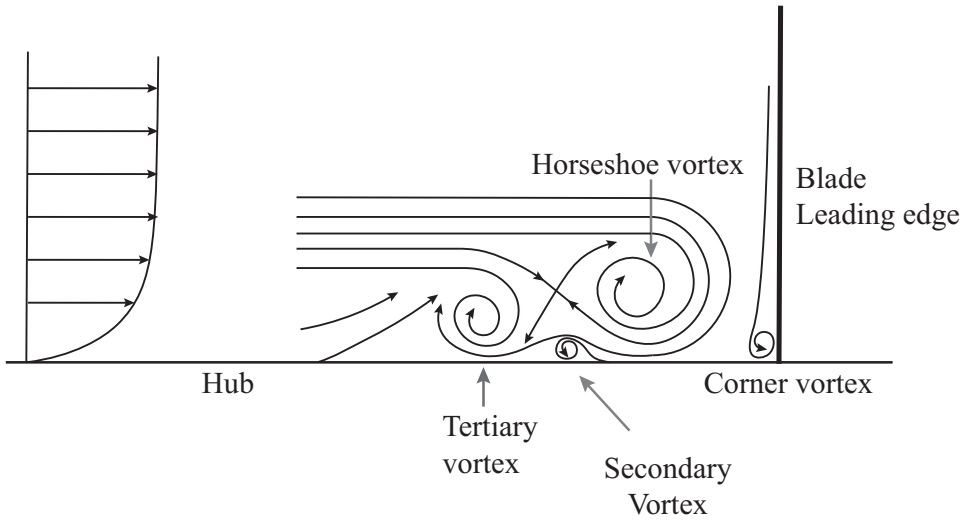


Figure 8.4: The structure of a horseshoe vortex (concept adapted from Praisner and Smith, 2006).

vortex system and cause bi-modal oscillations. Here, the secondary vortex erupts away from the wall and around the horse-shoe vortex. However, Detached Eddy Simulations (DES) of Xia and Medic, 2017 also showed bi-modal oscillations of horse-shoe vortex, but in their case the tertiary vortex moves over the horse-shoe vortex. They ascribed this difference to the absence of upstream coherent structures as their incoming modelled boundary-layer was free of any coherent structures. They also suggested that the unsteadiness in the horse-shoe vortex causes oscillations in the hub-corner separation.

This suggests that the coherent spiral vortices on nose-cones may interact with the horse-shoe vortex and consequently influence the hub-corner separation. The phase velocity of spiral vortices with respect to the nose-cone surface will play an important role. Typically, fixed disturbances on the cone-surface, e.g. surface irregularity, foreign object damage, etc. will induce spiral vortices that are stationary with respect to the cone surface. Any non-stationary modes will have an unsteady interaction with the horse-shoe vortices. Further investigation is required to better address these aspects.

### 8.3. EXPECTED OCCURRENCE OF THE SPIRAL VORTICES DURING A TRANSONIC FLIGHT

As described in the previous section 8.2, knowing the location of the spiral vortex amplification on a nose-cone is important to assess the fan performance near the hub. This section discusses how a transonic aircraft will encounter the spiral vortex growth on their nose-cones during their longest operational phase, i.e. cruise. Chapter 6 has shown the spiral vortex growth in the transitional boundary-layer on rotating cones in high-speed inflow with  $M = 0.5$  with the turbulence intensity  $u'_{RMS}/U \approx 3.4 - 4\%$ . These investigations also accounted for the area-contraction along the cone length, similar to those expected in aero-engine intakes. The resulting flow parameters relating to the maximum amplifi-

cation of the spiral vortices are compared here with the expected flow conditions on an aero-engine-nose-cone during a transonic cruise.

Currently, the majority of civil aviation consists of turbo-fan powered transonic aircraft. AIRBUS A320neo and A350-900 are two of the recent short-to-medium- and long-haul civil transport aircraft, respectively. Table 8.1 details their flight and engine specifications.

Specification	A320neo	A350-900
Cruise Mach number	0.78	0.85
Service ceiling	11900 m	13500 m
Engine	CFM Int. Leap	Rolls-Royce Trent
Assumed intake Mach number (Peters et al., 2015; Uenishi et al., 1990)	0.5	0.5
Fan diameter	1.98 m	3 m
Assumed hub to tip diameter ratio	0.28	0.28
Estimated hub-diameter	0.55m	0.84 m
Fan RPM	3894	2700

Table 8.1: Flight and engine specifications of the turbofan powered aircraft AIRBUS A320neo and A350-900 (CFM, 2013; Rolls-Royce, 2018; TCDS:EASA.A.064, 2021; TCDS:EASA.A.151, 2020).

As discussed in the previous chapters, the spiral vortex growth is governed by the local Reynolds number  $Re_l$  and rotational speed ratio  $S$ . The data in table 8.1 is used to estimate the typical range of Reynolds number and rotational speed ratio on nose-cones of A320neo and A350-900. Although these aircraft fly at high subsonic and transonic cruise Mach numbers  $M_{\text{cruise}} = 0.78 - 0.85$ , their engine intakes reduce the flow Mach number down to  $M_{\text{intake}} \approx 0.5$  to achieve the optimum fan performance (Peters et al., 2015; Uenishi et al., 1990). Using the data from table 8.1 and assuming an isentropic flow, one can estimate the range of Reynolds number and rotational speed ratio on the aero-engine-nose-cone during a flight:

$$Re_{l,\text{flight}} = \frac{lM_{\text{intake}}a\rho}{\mu}; \quad S_{\text{flight}} = \frac{l\sin(\psi)\omega}{M_{\text{intake}}a}. \quad (8.1)$$

Here,  $a$  is the sound speed,  $\rho$  is the local air density,  $\mu$  is the dynamic viscosity, and  $\omega$  is the angular velocity of the fan. The meridional length on the nose-cone varies from  $l = 0$  to  $D/(2\sin(\psi))$ . As engine manufacturers are seen to use variety of nose-cones, the present analysis considers a range of half-cone angles  $\psi = 15^\circ - 50^\circ$ . Static air properties at cruise altitude are obtained from the standard atmosphere. These are used to obtain the total air properties for the cruise Mach number  $M_{\text{cruise}}$  using isentropic relations. Due to the unavailability of the exact in-flight aerodynamic data on real aero-engine-nose-cones, both  $Re_{l,\text{flight}}$  and  $S_{\text{flight}}$  are only estimates of flow parameters governing the spiral vortex growth on the nose-cones ( $Re_l$  and  $S$ ). However, their orders of magnitude are similar.

Figure 8.5 compares the maximum amplification of the spiral vortices measured in this work with the expected flow conditions ( $Re_{l,\text{flight}}$  and  $S_{\text{flight}}$ ) on the nose-cones of A320neo (red dotted line) and A350-900 (blue dotted line), during their cruise. Figure 8.5 shows that during a typical transonic cruise the instability-induced spiral vortices will reach maximum amplification on slender nose-cones of  $\psi \lesssim 30^\circ$ . Chapter 5 discussed that the spiral vortices originate much before the experimentally detected critical and maximum amplification

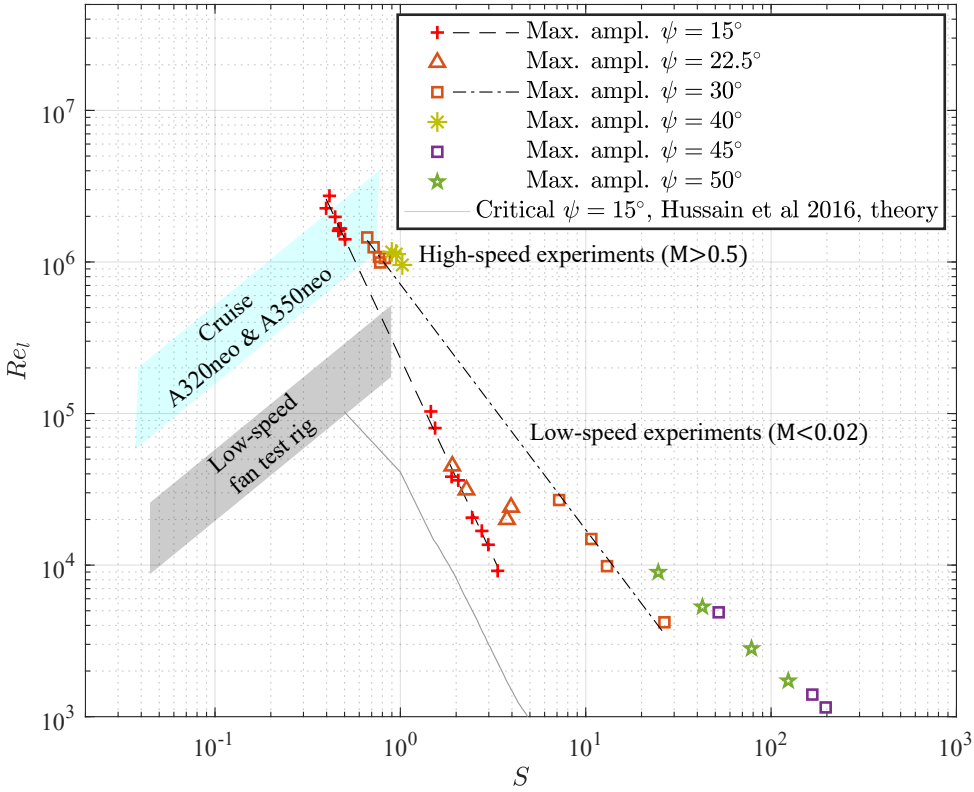


Figure 8.5: Maximum amplification of the spiral vortices on rotating cones (from figure 6.13); along with the estimated flow conditions these nose-cones would face on the aircraft A320neo and A350-900 during cruise and during experiments on a sub-scale low-speed fan test rig.

locations. Therefore, during the cruise of A320neo and A350-900, spiral vortices are also expected on the broader nose-cones of  $30^\circ < \psi \lesssim 50^\circ$ , however they will most-likely not reach their maximum amplification.

In laboratories, the detailed aerodynamics of an aero-engine fan is often studied using low-speed fan test rigs (e.g. chapter 7). These test rigs simulate a similar rotational speed ratio  $S$  as during the flight. But their Reynolds numbers are one order of magnitude of tens lower than the in-flight Reynolds numbers (see, for example, the test rig from the Whittle lab, used by Gunn and Hall, 2017; Gunn and Hall, 2014, and present test rig described in chapter 7). Figure 8.5 also shows the typical flow conditions on nose-cones in a sub-scaled ( $1/10^{th}$  of  $Re_{l,flight}$ ) low-speed fan test rig. The low Reynolds numbers in these test rigs suggest that the spiral vortices do not reach their maximum amplification on nose-cones. Numerical investigations do simulate the in-flight Reynolds numbers (Gunn & Hall, 2014; Jerez Fidalgo et al., 2012). But they are based on Reynolds Averaged Navier Stokes (RANS) equations which do not resolve the instability related phenomena. This explains why this problem of nose-cone boundary-layer transition and its effects on the fan aerodynamics might have been overlooked in the past studies. To accurately simulate the in-flight fan aerodynamics

near the hub, matching the in-flight Reynolds numbers is extremely important. For example, full-scale research engines, similar to the one used by Guimarães et al., 2015; Guimarães et al., 2018; Guimaraes Bucalo et al., 2017 with duct Reynolds number of  $2.4 \times 10^6$ , can be used to study the influence of nose-cone boundary-layer instability on fan aerodynamics. Alternatively, a numerical approach must model the nose-cone boundary-layer accurately, along with the small-scale fluctuations which can destabilise the boundary-layer and form the spiral vortices.

The present analysis (using estimated  $Re_{l,flight}$  and  $S_{flight}$ ) is based on several assumptions. First, the nose-cones are considered to be right-circular cones, without considering any meridional curvature. Some engine manufacturers use curved nose-cones while others feature right-circular cones. The effect of such curvature on the boundary-layer instability of rotating nose-cones is not addressed in this work. But the curvature is expected to alter the local pressure gradient and centrifugal force field which can affect the boundary-layer instability on rotating nose-cones. Moreover, the unavailability of the exact data on nose-cone shape and intake aerodynamics limits this analysis to order of magnitude comparisons.

This analysis is also extended to include a propeller-powered aircraft, ATR72-600. See appendix B for further details.

## 8.4. CONCLUSION

The potential interactions of the instability-induced spiral vortices with the fan aerodynamics near the hub are conceptually described. This dissertation (chapters 3–6) focused on showing how the boundary condition to the problem of hub corner separation is affected by the instability-induced spiral vortex growth. Therefore, studying hub corner stall with this boundary conditions is beyond the scope of this work and requires separate investigation.

Past experiments of Hergt et al., 2013 showed that vortices generated upstream of the compressor linear cascade re-distribute the near-wall momentum and reduce the total pressure loss by about 5%. Upon amplification, spiral vortices also increase the near-wall momentum. However, the spiral vortex strength and orientation will affect the quantity of the near-wall momentum exchange.

The past literature on the linear blade cascades has shown that the dynamics of the horse-shoe vortices is sensitive to the coherent structures in the upstream boundary-layer. This also affects the hub-corner separation. This suggests that the spiral vortices, which are the coherent structures in the boundary-layer, can influence the dynamics of the horse-shoe vortices, consequently affecting the hub-corner separation. However, the exact mechanism will depend on the spiral vortex strength, cross-sectional topology, orientation and motion relative to the cone surface.

- Instability-induced spiral vortices will most-likely appear on the right-circular nose-cones of transonic aircraft (like A320neo and A350-900), during their cruise. The vortices will also reach their maximum amplification on the slender nose-cones of  $\psi \lesssim 30^\circ$ .
- Due to the low Reynolds numbers, sub-scale low-speed testing of the aero-engines can not simulate the exact boundary-layer instability phenomenon on the rotating nose-cones that is expected to occur in the real flight.
- The effect of meridional surface curvature has not been considered in the present work

but will have an effect on the boundary-layer instability on rotating nose-cones.



# 9

## CONCLUSIONS AND RECOMMENDATIONS

**T**HIS dissertation has expanded the knowledge about boundary-layer instabilities on rotating cones in complex flow environment relevant to aero-engines. The dissertation has presented an experimental method which can be used to measure the growth of the instability-induced coherent structures on rotating bodies, and obtain their spectacular visualisations. This method overcomes the limitations of the conventional measurement techniques in the sense of capturing the instantaneous instability modes and their spatial growth on rotating cones in asymmetric and high-speed inflows. This allowed, for the first time, investigating the instability behaviour on cones rotating in asymmetric inflow, as well as, high-Reynolds number compressible inflow. Overall, this work has explored the parameter space of the boundary-layer instability on rotating cones along the following parameters: local Reynolds number  $Re_l = 0-3 \times 10^6$ , rotational speed ratio  $S = 0-250$ , inflow Mach number  $M = 0-0.5$ , inflow incidence angle  $\alpha = 0-10^\circ$  and half-cone angle  $\psi = 15^\circ-50^\circ$ .

The instabilities are found to induce coherent spiral vortices in the boundary-layer of rotating cones in asymmetric inflow, as well as, high-speed inflow. In these cases, spiral vortices grow and increase the momentum near the wall which is followed by the boundary-layer transitioning into a turbulent state. This transitional flow, in a region between the onset of spiral vortices to the onset of turbulence, is expected to influence the aerodynamic performance of the fan near its hub. The blade passages near the fan-hub host several complex aerodynamic phenomena: cross-passage turning of the low-momentum boundary-layer flow, horse-shoe vortices from the blade leading edges, three dimensional flow separation at the hub-blade junction flow on the suction side, etc. These flow phenomena increase the total pressure loss, bring down the overall engine efficiency, and can trigger the rotating stall which limits the stability margin of the fan operations. Several past attempts of studying these phenomena have assumed the hub boundary-layer as fully turbulent. The past experiments used transition strips to simulate such turbulent-boundary-layer upstream of the blade cascades. These studies reported that the coherent structures in the turbulent boundary-layer significantly affected the hub-corner separation.

However, this dissertation has shown that, during the flight, the nose-cone boundary-

layer is most likely to have the growing spiral vortices, induced by its instability. The phase of the spiral vortex growth, their orientation and azimuthal number depend on the nose-cone geometry and engine operating conditions. Therefore, the effect of the spiral vortices on the fan-hub aerodynamics will be different for different nose-cone shapes and engine operating conditions. However, this effect will be different than that reported in the past studies which assumed the boundary-layer to be fully turbulent. Therefore, this dissertation highlights that the nose-cone boundary-layer state needs to be considered to accurately assess the losses at the fan hub. Moreover, the dissertation has provided data which can be used to predict the spiral vortex growth on different rotating cones in low-speed as well as high-speed cruise conditions.

Section 9.1 summarises the new findings with regards to the boundary-layer instability on rotating cones compared to information from the available literature. The limitations of the present work are detailed in section 9.2. Recommendations for the future investigations in this subject area are listed in section 9.3.

## 9.1. NEW FINDINGS

Following are the new key findings from this work:

1. A new experimental method to investigate the coherent spiral vortices on rotating bodies is developed. This method overcomes the limitations of the previously reported methods and is suitable for both low-speed and high-speed investigations. Apart from the spectacular visualisations of spiral vortices, the method also provides quantitative data on spiral vortex growth, angle and number.
  - When the rotating cones are made of Polyoxymethylene, the foot-prints of instability induced spiral vortices on them can be measured with an infrared camera. The measurement quality can be significantly enhanced using POD approach with selective reconstruction.
  - This method allows detecting instability induced spiral vortices on rotating cones in axial inflow, non-axial inflow and high-speed turbulent inflow.
  - The r.m.s. of measured temperature-fluctuations can be used to identify the maximum amplification of the spiral vortices.
  - The POD analysis of infrared measurements allows separating two distinct types of surface temperature fluctuation patterns on rotating cones: a short azimuthal wavelength pattern of  $\lambda_\theta < \pi r/4$  relating to the spiral vortex footprints and a long azimuthal wavelength pattern of  $\lambda_\theta > \pi r/4$  overlaid on the spiral vortex footprints. The latter occurs where the spiral vortices start their rapid growth.
2. For all the investigated cones ( $\psi = 15^\circ, 22.5^\circ, 30^\circ, 45^\circ, \text{ and } 50^\circ$ ) in low-speed conditions, near their amplification point, the spiral vortices start to increase the near-wall momentum. At this location, the spatio-temporal fluctuations of surface temperature are maximum in a meridian.
3. The asymmetry caused by the non-axial inflow is found to delay the spiral vortex growth on rotating slender cone of half-cone angle  $\psi = 15^\circ$ . At low rotational speed ratio  $S$ , the asymmetric flow conditions cause growth of azimuthally-varying number of

spiral vortices at varying orientations. This inhibits the spiral vortex growth. However, the flow system allows the growth of spiral vortices in asymmetric flow conditions when the its instability characteristics become less sensitive to the azimuthal variations of the flow parameter, i.e. when the spiral vortex angle and azimuthal number do not significantly vary around the azimuth in azimuthally varying flow conditions.

4. Increasing half-cone angle stabilises the boundary-layer on the rotating cones in axial inflow.
  - As a cone gets broader the spiral vortex growth is detected at a higher rotational speed ratio  $S$  for a constant local Reynolds number  $Re_l$ . However, this effect is observed to have diminished for  $\psi = 45^\circ$  and  $\psi = 50^\circ$ .
  - The half-cone angle does not have any significant effect on the trend of spiral vortex angle with respect to the rotational speed ratio  $S$ . However, the instability on broader cones induces spiral vortices with shorter azimuthal wavelengths, i.e. higher azimuthal number.
  - The co-rotating spiral vortices are observed on rotating broad cones of half-cone angles  $\psi \gtrsim 30^\circ$  in axial inflow. However, upon their amplification the co-rotating vortices are accompanied by their counter-rotating companions.
5. Rotating cones in turbofan engines at a transonic cruise will exhibit similar boundary-layer instability behaviour as they exhibit in low-speed laboratory experiments.
  - The spiral vortices are detected on the investigated cones ( $\psi = 15^\circ, 30^\circ$  and  $40^\circ$ ) rotating in high-speed inflow conditions: Reynolds number  $Re_L > 10^6$ , rotational speed ratio  $S < 1-1.5$ , and Mach number  $M = 0.5$ .
  - The maximum amplification Reynolds number  $Re_{l,m}$  shows a well-behaved trend with respect to the rotational speed ratio  $S$ . This trend seems to follow a relation  $Re_{l,m} = CS^{a_1}$  throughout the low-speed and high-speed conditions. Here,  $a_1$  and  $C$  depend on the half-cone angle  $\psi$ . For  $\psi = 15^\circ$ ,  $a_1 = -2.62$  and  $C = 2.3 \times 10^5$ . For  $\psi = 30^\circ$ ,  $a_1 = -1.62$  and  $C = 7.1 \times 10^5$ .

Table 9.1 summarises the knowledge added by this work to the existing literature.

## 9.2. LIMITATIONS

The present study has following limitations:

1. Only right circular cones were considered for the present study as their simple geometry eases the analysis. However, many aero-engines feature ogival nose-cones with meridional curvature. As the curvature alters the centrifugal forces and pressure gradients, the boundary-layer instability behaviour is expected to be significantly affected.
2. Due to the low acquisition rates of the infrared camera (200Hz), the present experiments do not provide any information on the phase velocity of the spiral vortices w.r.t. the rotating cone surface.

Research aspect	Past literature state	Present addition
Experimental method to investigate instability-induced spiral vortices on rotating bodies	Particle-based visualisation: limited to low-speed, no information on growth. Hot-wire measurements: time-consuming, limited to single point measurements.	Enhanced application of IRT with POD approach to detect thermal footprints of the spiral vortices on rotating cones. <ul style="list-style-type: none"> <li>• snapshot visualisations with growth quantification.</li> <li>• applicable in both low- and high-Reynolds number inflow conditions.</li> </ul>
Symmetry breaking	Experimental and theoretical investigations were conducted only in axi-symmetric flow conditions.	Experiments in non-axial inflow showed that asymmetry of non-axial inflow delays the spiral vortex growth on the investigated rotating cone ( $\psi = 15^\circ$ ).
Maximum amplification of the spiral vortices	Only theoretically predicted.	Measured as the maximum RMS surface temperature fluctuations on rotating cones.
Half-cone angle	Experiments: $\psi = 7.5^\circ, 15^\circ$ , and $\psi = 30^\circ$ . Theory: $\psi = 7.5^\circ$ – $90^\circ$ .	Experiments: $\psi = 15^\circ, 22.5^\circ, 30^\circ, 40^\circ, 45^\circ$ , and $50^\circ$ .
Inflow conditions	Limited to low-speed conditions: $Re_l < 10^5$ , $S > 1$ – $1.5$ and $M \approx 0.02$ .	Experimental investigations extended in high-speed axial inflow conditions pertaining to that inside an aero-engine on a typical transonic flight: $Re_l > 10^6$ , $S < 1$ – $1.5$ and $M = 0.5$ .
Nose-cones in fan test rig	Experimental investigations limited to pressure measurements with single distortion index and a fixed nose-cone shape.	PIV measurements of the flow-field around different nose-cone shapes and for different distortion topology and indices.

Table 9.1: Body of knowledge before and after this dissertation

3. The long wave pattern of the surface temperature fluctuations is observed during the spiral vortex growth on rotating cones. But the exact origin of this long wave pattern remains unknown.
4. The present study has only conceptually discussed how the spiral vortices can affect the fan aerodynamics near the hub. The exact effect of the spiral vortices on the fan efficiency remains unknown.
5. The low-speed fan test rig of the present study (chapter 8) can not simulate the local Reynolds number on the nose-cones during transonic flight. Therefore, it does not simulate the exact fan aerodynamics of the transonic civil aircraft.
6. The present study has focused on the onset of the spiral vortices and their maximum amplification on rotating cones. After the maximum amplification of the spiral vortices, their surface temperature footprint starts to get weaker. The exact relation between this weakening surface temperature footprint and the transition of the boundary-layer to a fully turbulent state is currently unknown.

### 9.3. RECOMMENDATIONS

Following are some recommendations for the future work on this topic:

1. The surface roughness is one of the important disturbance source which can trigger or suppress the boundary-layer instability. The effect of isolated or random surface roughness on the boundary-layer instability on the cones rotating in inflow is currently unknown. A parametric study needs to be conducted with different configurations of isotropic and anisotropic roughness elements. The size and number of the elements (relative to the boundary-layer thickness) needs to be varied to observe the effect on the spiral vortex growth characteristics. The early initiation of the spiral growth in low-Reynolds numbers will allow simulating the in-flight behaviour of the spiral vortices in low-speed fan test rig. However, identifying the suppressing effect of roughness on the spiral vortex growth will aid in delaying the boundary-layer transition on rotating cones.
2. Effect of meridional surface curvature of the rotating cones on its boundary-layer instability needs to be studied in detail at both low- and high-speed conditions. The curvature affects the centrifugal forces and the local pressure gradients which can significantly affect the boundary-layer instability on rotating nose-cones.
3. The effect of instability-induced spiral vortices on the efficiency of the aero-engine needs to be estimated. This can be achieved by simulating the spiral vortices on the nose-cone of a low-speed fan test rig and measuring the changes in total pressure and torque, at constant RPM and mass flow rate. Velocity field measurements using PIV and their modal analysis will greatly aid in understanding the effect of spiral vortices on the fan aerodynamics.
4. The present study has shown that the spiral vortices can grow in a non-axisymmetric inflow at a non-zero incidence angle. Similar investigations can be extended to the

asymmetry of the non-uniform inflow found in embedded engines and ultra-high-bypass-ratio engines. Comparison of rotating and non-rotating nose-cone will greatly aid in estimating the effect of nose-cone rotation on fan-aerodynamics.

5. After the maximum amplification of the spiral vortices, the boundary-layer on a rotating cone attains a fully turbulent state. However, this process needs to be investigated further, to formulate a link between the surface temperature fluctuations and the exact location of this transition. Furthermore, the coherent spiral vortex structures are expected to be present in the fully turbulent boundary-layer. Their behaviour needs to be characterised as such coherent structures can influence the fan aerodynamics near the hub.
6. High-Reynolds number investigations are required to assess the influence of the nose-cone-boundary-layer instability on the engine performance. High-Reynolds number mid- to full-scale fan test rigs are ideal for this investigations, but they are often limited by high power requirements. A hybrid approach of combining experiments and computational fluid dynamics (CFD) will be useful. Experiments can provide data on the nose-cone-boundary-layer instability and associated spiral vortices. This can be used as a boundary-conditions for CFD studying the detailed fan-hub aerodynamics.

# A

## EFFECT OF INTEGRATION TIME ON THE SPIRAL VORTEX DETECTION USING INFRARED THERMOGRAPHY

In high-speed investigations from chapter 6, the cones are rotated at high r.p.m. (8000 to 33000) to achieve the desired rotational speed ratios in high-speed inflow. Spiral vortices are observed with an infrared camera at finite integration times, ranging from  $25\mu\text{s}$  to  $205\mu\text{s}$ . During the integration time, a cone surface rotates with respect to a stationary camera sensor plane. A sensor records the temperature of this moving surface as it passes through its field of view. For a coherent spiral vortex pattern this does not significantly alter the observed pattern. Figure A.1 shows the rotating cone at same operating conditions but observed with three integration times  $t_{int} = 205\mu\text{s}$ ,  $105\mu\text{s}$  and  $50\mu\text{s}$ . The long wave modulations do not show any significant difference, see figures A.1b, e and h. The short wavelength patterns get slightly sharper with decreasing integration time, see figures A.1c, f and i.

The locations where the spiral vortex growth is observed does not show significant changes with changing integration time, see figure A.2a. As expected, the lower integration time significantly reduces the signal strength as evident from the reduced  $I'_{RMS}$  at  $t_{int} = 50\mu\text{s}$  as compared to that at  $t_{int} = 205\mu\text{s}$  in figure A.2. The effect of integration time on the spiral vortex angle  $\epsilon$  is also minimal, as evident from figure A.2b.

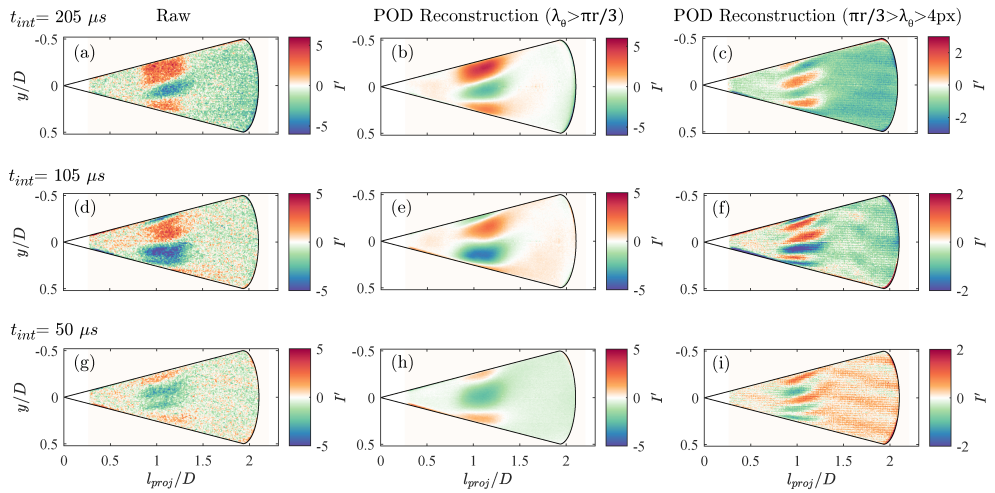


Figure A.1: Effect of integration time  $t_{int}$  on the thermal footprint measurements of the spiral vortices.

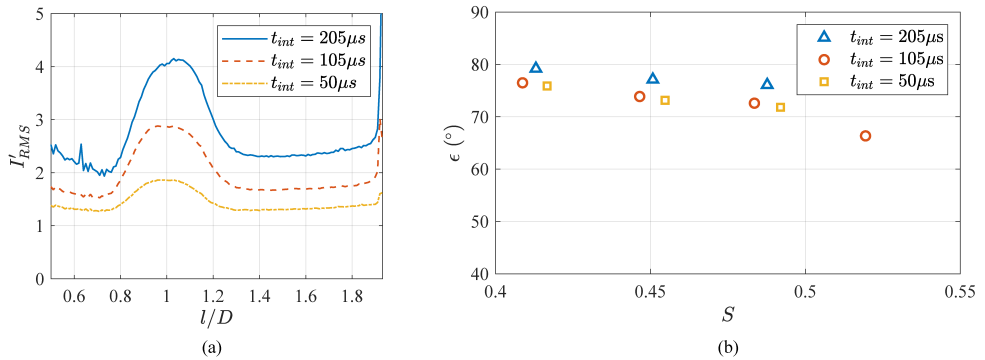


Figure A.2: Effect of integration time  $t_{int}$  on surface temperature fluctuations.

# B

## SPIRAL VORTEX GROWTH FROM THE PERSPECTIVE OF A PROPELLER AIRCRAFT

Section 8.3 from chapter 8 discussed the expected spiral vortex growth on the aero-engine-nose-cones of the transonic cruise aircraft. This section extends the analysis to a propeller powered aircraft.

The majority of regional civil air transport consists of the propeller powered aircraft because propellers are more efficient at low-speed flights ( $M_{\text{cruise}} \lesssim 0.5$ ) than turbofans. The low speeds limit the range of the propeller powered aircraft to the regional transport. ATR72-600 is one of the popular aircraft in this class. It features propellers without any intake duct, unlike turbofans. Table B.1 details the flight and engine specifications of this aircraft. Using this data, the flow conditions on the nose-cone can be estimated as per equations 8.1.

Figure B.1 compares the flow conditions on the nose-cones during the cruise phase of ATR72-600. It appears that the spiral vortices may be present on the investigated nose-cones ( $15^\circ \leq \psi \leq 50^\circ$ ) on ATR72-600. However, only a slender nose-cone of  $\psi = 15^\circ$  may experience the spiral vortex amplification. Figure B.1 also shows that a sub-scaled wind-

Specification	ATR72-600
Cruise speed	133.3 m/s
Cruise Mach number	0.43
Cruise altitude	7620 m
Engine	Pratt and Whitney Canada PW127M
Engine diameter	0.68 m
Assumed hub-diameter	0.68 m
Propeller RPM	1200

Table B.1: Flight and engine specifications of the propeller powered aircraft ATR72-600 (ATR, 2017; TCDS:EASA.IM.E.041, 2014).

## B

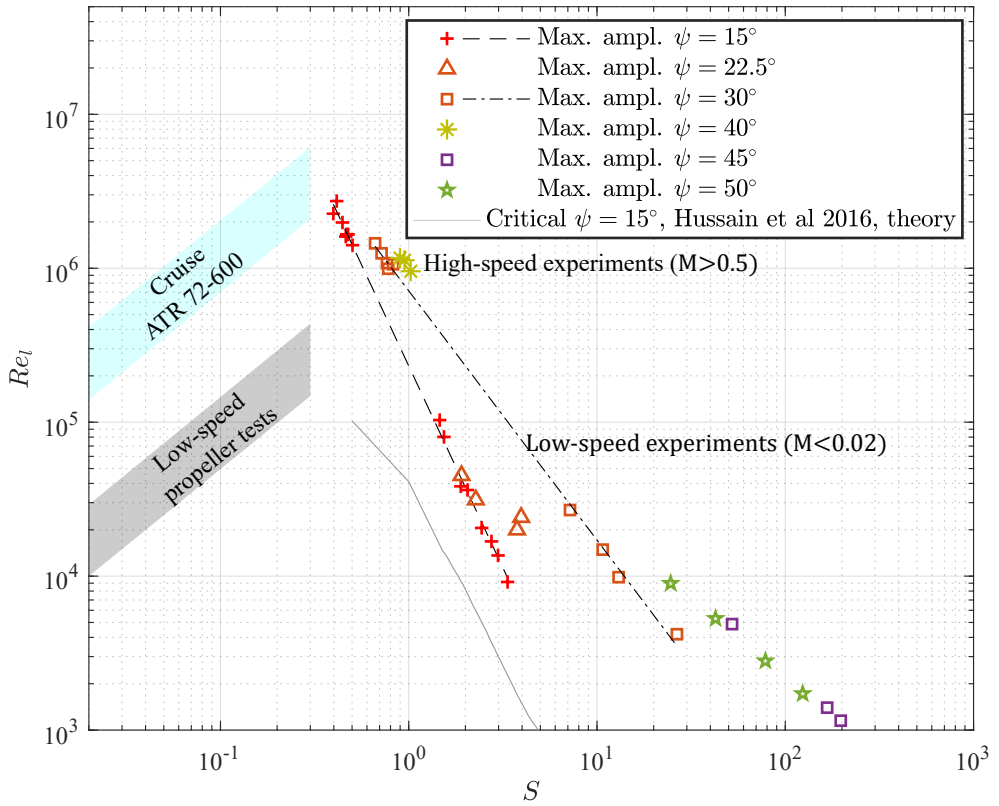


Figure B.1: Maximum amplification of the spiral vortices on rotating cones; along with the estimated flow conditions these nose-cones would face on the aircraft ATR 72-600 during cruise and during 1/10 scale wind-tunnel test.

---

tunnel experiment (for example, an isolated propeller which is  $1/10^{th}$  of the flight scale) most-likely will not simulate the spiral vortices on the nose-cones of the propellers. The influence of the spiral vortices on the near-hub aerodynamics of the propeller remains to be investigated.



# C

## FAN PERFORMANCE UNDER DISTORTED INFLOW OF VARYING DISTORTION STRENGTH

Section 7.3.2 from chapter 7 discussed the flow asymmetry around the nose-cones of a fan operating with the distorted inflow. This section presents how the fan performance and flow unsteadiness are affected due to the varying distortion strength. Figure C.1 shows the fan test rig configuration and the measurement setup.

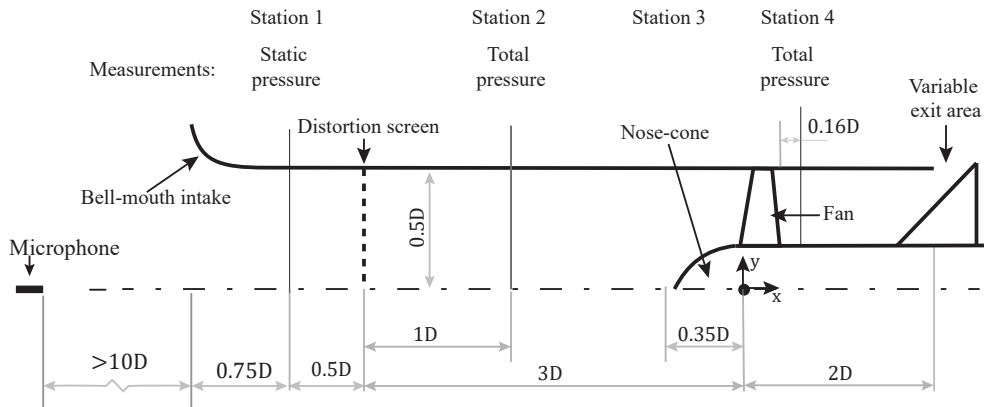


Figure C.1: Fan test rig and the measurement setup for studying the effect of different inflow distortion on the fan performance.

### C.1. FAN PERFORMANCE

Figure C.2 shows the fan performance curves for the clean as well as distorted inflow. Here, the flow coefficient ( $\phi$ ) and the loading coefficient ( $\psi_{load}$ ) are defined as

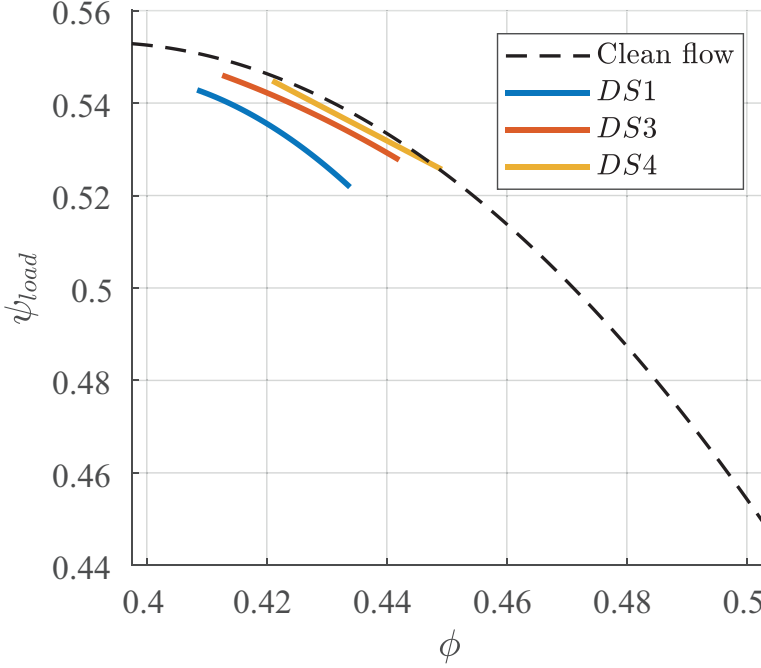


Figure C.2: Fan characteristic map showing the fan performance in clean and distorted inflows.

$$\phi = \frac{\overline{V_x}}{U_{mid}}, \quad (\text{C.1})$$

$$\psi_{load} = \frac{\overline{P_{t4}} - \overline{P_{t2}}}{0.5\rho U_{mid}^2}. \quad (\text{C.2})$$

Figure C.2 shows that the non-dimensional performance of the fan with the distortion screens DS3 and DS4 is not affected. However, the performance is reduced due to the distortion screen DS1. This results from the increased distortion index of DS1 and presence of the stronger upstream vortex.

Figure C.3 shows the total pressure measurements downstream of the fan for two flow coefficients with distortion screen DS1. One can observe that the two lobed structure of the oncoming distortion (observed in Figure 7.11 (a)) is not present in the downstream flow.

## C.2. FLOW UNSTEADINESS

Turbo-machinery operations are unsteady by definition. However, in stable operations, the unsteady pressure fluctuations occur at the blade passing frequency (BPF). Under the off-design incidence angles, the pressure fluctuations occur at lower frequencies. This shift in the power spectrum can be caused by the stall inception Perovic et al., 2019, the inflow non-uniformity, or both.

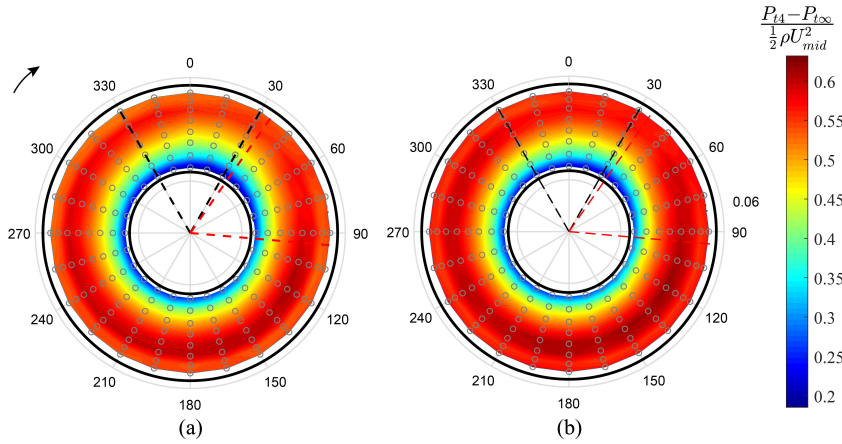


Figure C.3: Total pressure measurements downstream of the rotor at (a)  $\phi = 0.429$  and (b)  $\phi = 0.413$  for screen DS1.

Here, the flow unsteadiness is quantified from the noise spectra. The noise measurements were carried out with a Linear X microphone, located far upstream of the test rig, aligned with the centreline of the duct (see figure C.1). Each dataset was acquired for 10 seconds at 25kHz (maximum expected blade passing frequency was 3.6kHz) to satisfy the Nyquist criterion, and to ensure sufficient frequency resolution.

Figure C.4 shows the power spectra obtained by the microphone measurements for clean and distorted flow (DS1). The spectrum is obtained using Fourier transform ( $F$ ) of the signal. The power ( $|F|^2$ ) is non-dimensionalised with a cumulative energy at a reference point ( $\phi = 0.488$ ) computed as

$$E_{ref} = \sum_{0.2 \text{ BPF}}^{2 \text{ BPF}} |F|^2. \quad (\text{C.3})$$

The dotted lines in Figure C.4 show the cumulative energy

$$E_f = \sum_{0.2 \text{ BPF}}^f |F|^2 \quad (\text{C.4})$$

that is associated with a frequency  $f$ , normalised by  $E_{ref}$ .

At a reference point, the energy of the fluctuations is concentrated at the harmonics of blade passing frequency (see Figure C.4a). At a lower flow coefficient, close to the stall point, the amplitude of the fluctuations increases, and the energy is distributed among the lower frequencies (see Figure C.4b). In the distorted flow (Figure C.4c and d), the low frequency disturbances are present for all flow coefficients due to the circumferential non-uniformity. With decreasing flow coefficient, the amplitude of these disturbances increases significantly (see Figure C.4d). Furthermore, it has been observed that the disturbances start appearing around 0.7 BPF and shift towards the lower frequencies with decreasing  $\phi$ . This behaviour is

in agreement with what has been observed in literature Perovic et al., 2019. However, the exact location of the stall was not measured in the present study.

The effect of varying distortion index on the energy of the low frequency disturbances is shown in Figure C.5. The cumulative energy in the low frequency disturbances is estimated as

$$E_{f < bpf} = \sum_{0.2 BPF}^{0.9 BPF} |F|^2. \quad (C.5)$$

Figure C.5 shows that the low frequency disturbances grow exponentially with decreasing flow coefficient  $\phi$ . With increasing distortion index (at a constant  $\phi$ ), the strength of the low frequency disturbances increases monotonically, regardless of the distortion topology. The elbow of the graph shifts towards the higher flow coefficients for stronger distortions, indicating that the disturbance growth starts at higher flow coefficients. Consequently, the stability margin is reduced significantly.

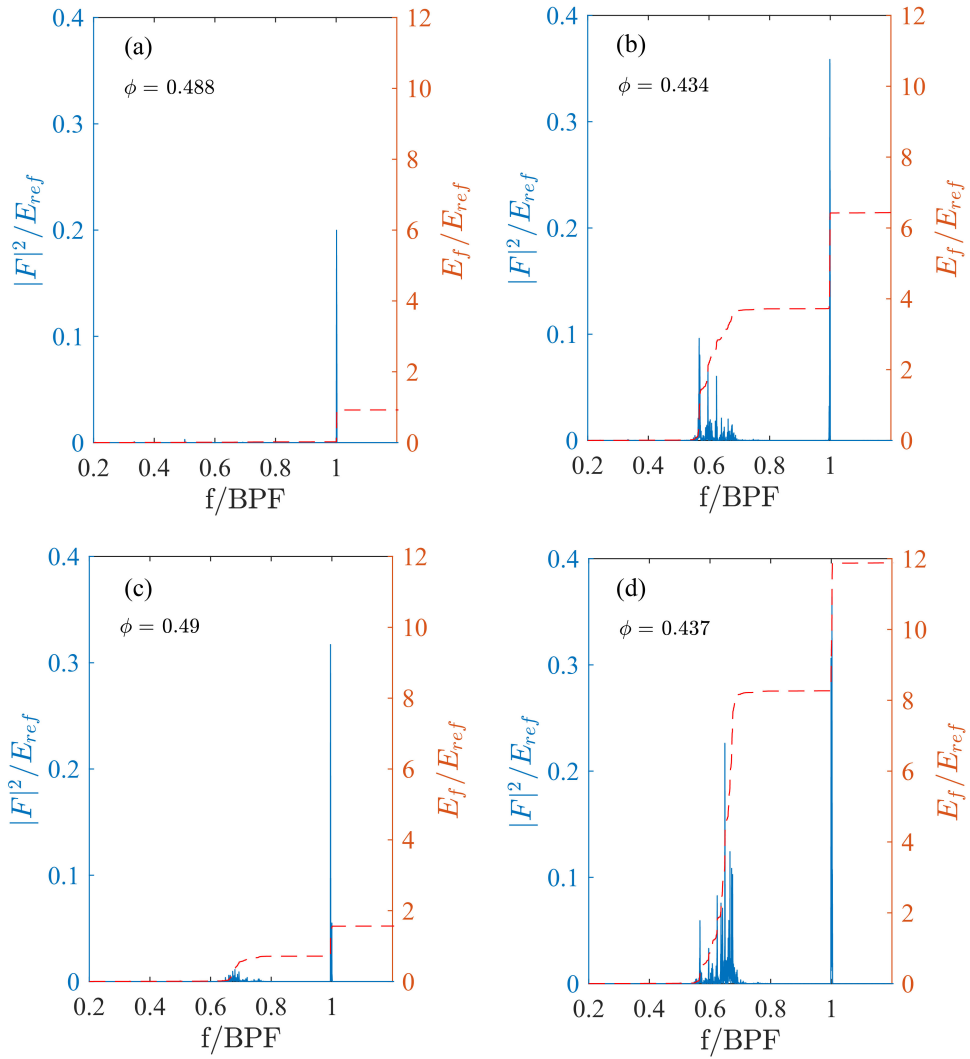


Figure C.4: Power spectra and cumulative energy of noise for (a), (b) clean flow and (c), (d) distorted flow DS1.

C

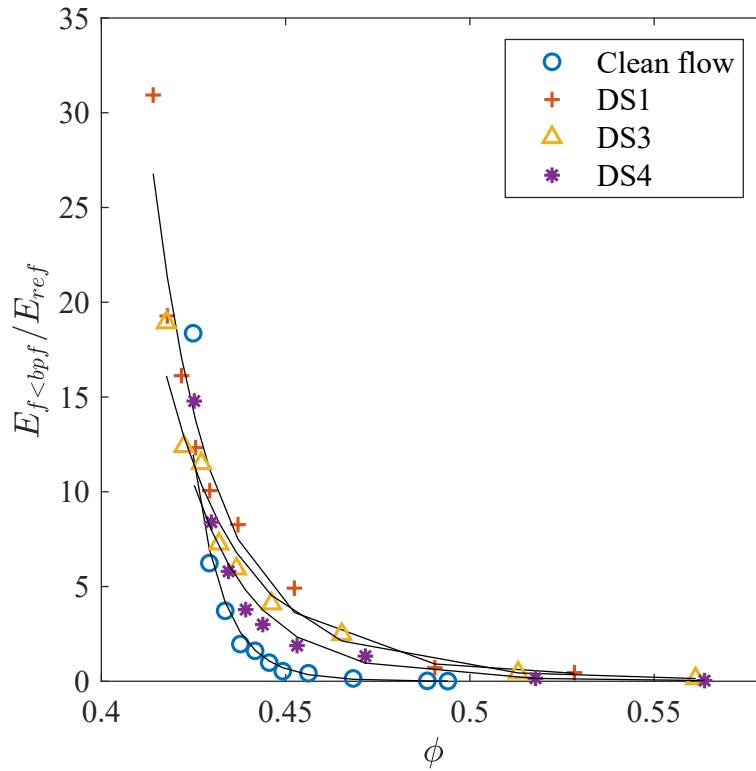


Figure C.5: Variation of the cumulative energy of low frequency disturbances with respect to the flow coefficient for clean and distorted inflows.

# D

## EFFECT OF NOSE-CONE SHAPE ON THE DISTORTION TRANSFER THROUGH THE FAN

Chapter 7 presented the upstream redistribution of the distorted flow around the nose-cone, due to the action of fan. This section shows how changing the nose-cone shape affects the distortion transfer across the fan. Figure D.1 shows the fan test rig configuration and measurement setup. The distortion screen  $DS1e$  is used to create the circumferential distortion upstream of the fan (see figure 7.16).

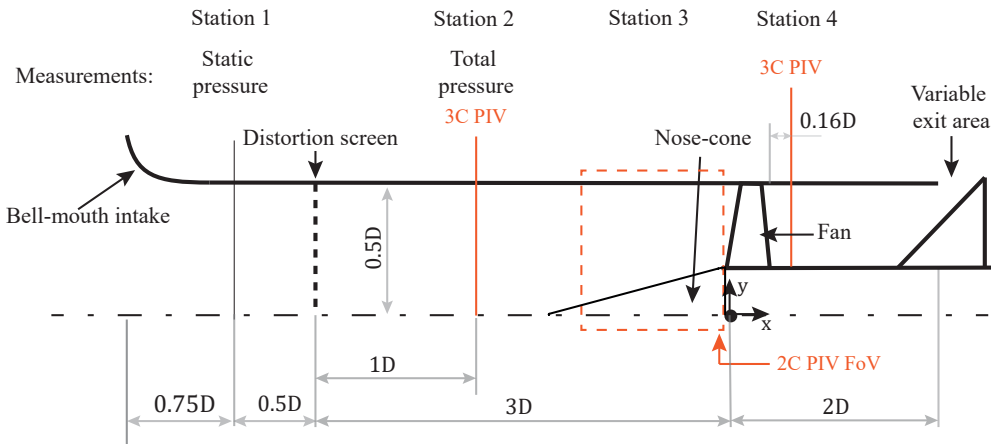


Figure D.1: Fan test rig and the measurement setup for studying different nose-cone shapes in a distorted inflow.

Figure D.2 shows two different nose-cone shapes used in the present measurements: (a) cone with half-cone angle  $\psi = 15^\circ$  (same as that investigated in chapter 4) and (b) ellipsoid

with the half-major axis equal to the minor axis. Both nose-cones have the same base diameter  $D_{hub} = 50$  mm.

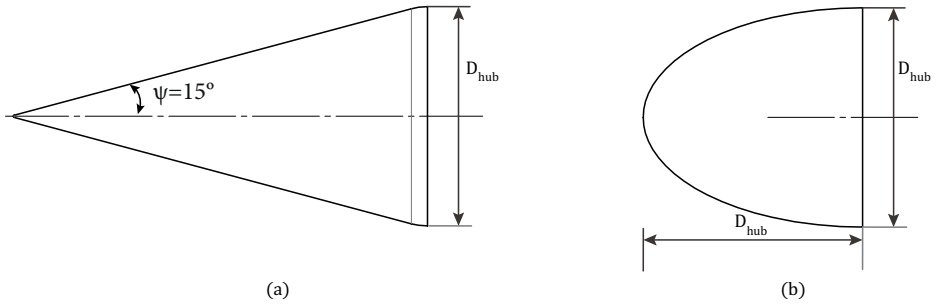


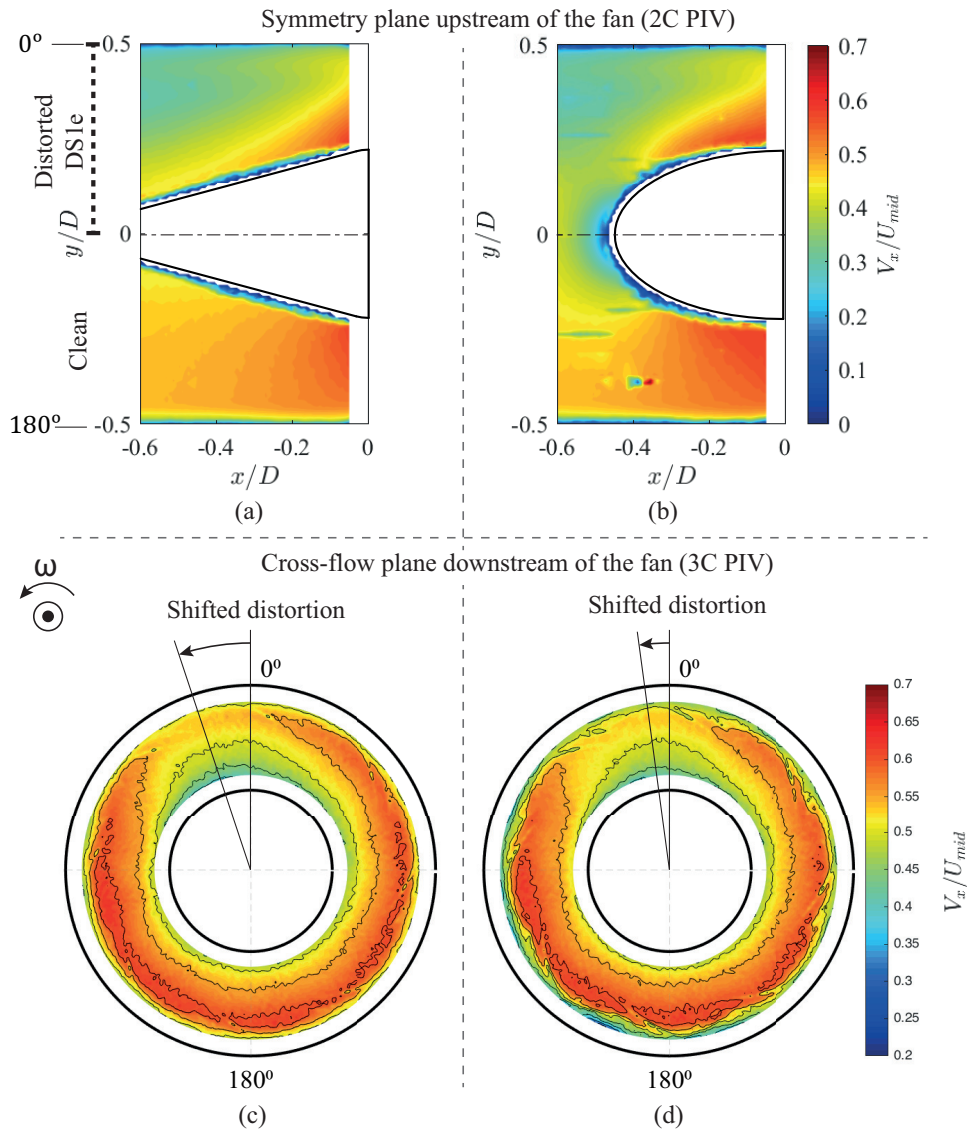
Figure D.2: Two different nose-cone shapes used in the present study: (a) cone with half-cone angle  $\psi = 15^\circ$  (same as that investigated in chapter 4) and (b) ellipsoid.

Figures D.3a and b show the axial velocity field in the symmetry plane around the nose-cone with the inflow distorted by the screen  $DS1e$ . Here, the axial momentum in the distorted region towards the fan. This results due to the upstream redistribution of the flow around the nose-cone, as discussed in section 7.3.2.

Furthermore, figures D.3 c and d, show the axial velocity field in a cross-flow plane downstream of the fan (at station 4) for the conical and ellipsoid nose-cone, respectively. In both cases, the traces of the circumferential distortion persist downstream of the fan. As the fan rotor imparts swirl, and the velocity field is measured around  $0.16D$  downstream of the fan, the low axial momentum region (relating to the distortion) appears to be shifted in the direction of the fan rotation. As the cross-flow plane is perpendicular to the constant area duct, the incompressible axial velocity directly represents the mass-flow rate. Practically, the flow field downstream of the rotor enters the stator blades. Therefore, account of the shifted distortion is crucial for designing the efficient stator blades.

The circumferential extent and shift of the low-momentum region are larger for the conical nose-cone as compared to the ellipsoid. This shift suggests the differences in the local fan performance for the two spinners. The different performances arise due to the different nose-cone shape, which affects the upstream re-distribution of the distorted flow. Figure D.4 shows the upstream velocity profiles at the AIP (Aerodynamic Interface Plane at  $-0.05D$ ), extracted in the distorted ( $0^\circ$ ) and clean ( $180^\circ$ ) regions. Overall, the ellipsoid has the higher axial velocity (figures D.4a and c) but lower radial velocity as compared to the conical nose-cone (figures D.4b and d).

As described with the velocity triangles in figure D.4, changes in the inflow velocity affects the incidence angles on the blade which changes the downstream swirl. The lower axial velocity around the conical nose-cone increases the blade incidence angle. Furthermore, the changes in radial velocity changes the radial transport of the flow through the blade passage. The higher radial velocity around the conical nose-cone suggests that the flow leaves the blade trailing edge at a higher radius, thus at a higher blade velocity  $U_2 > U_1$ , as compared to the ellipsoid. Increased incidence angle and higher radial velocity are the potential causes of the larger shift of the low-axial momentum region for the conical nose-cone, as compared to the ellipsoid.



D

Figure D.3: Axial velocity field in the fan test rig with inflow distortion generated by the screen *DS1e*. (a) and (b) show the axial velocity field in the symmetry plane around the conical and ellipsoid nose-cone, respectively. (c) and (d) show the axial velocity field in the cross-flow plane for conical and ellipsoid nose-cone, respectively. Here, the low-axial momentum region shifts by a larger extent for the conical nose-cone as compared to the ellipsoid.

D

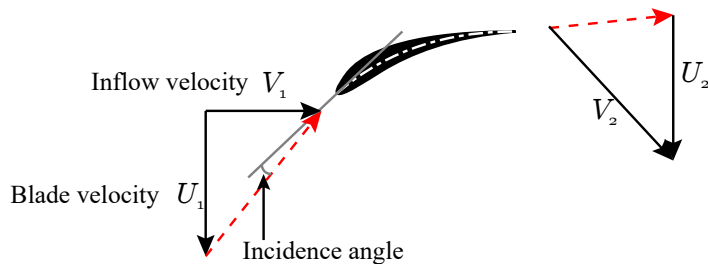
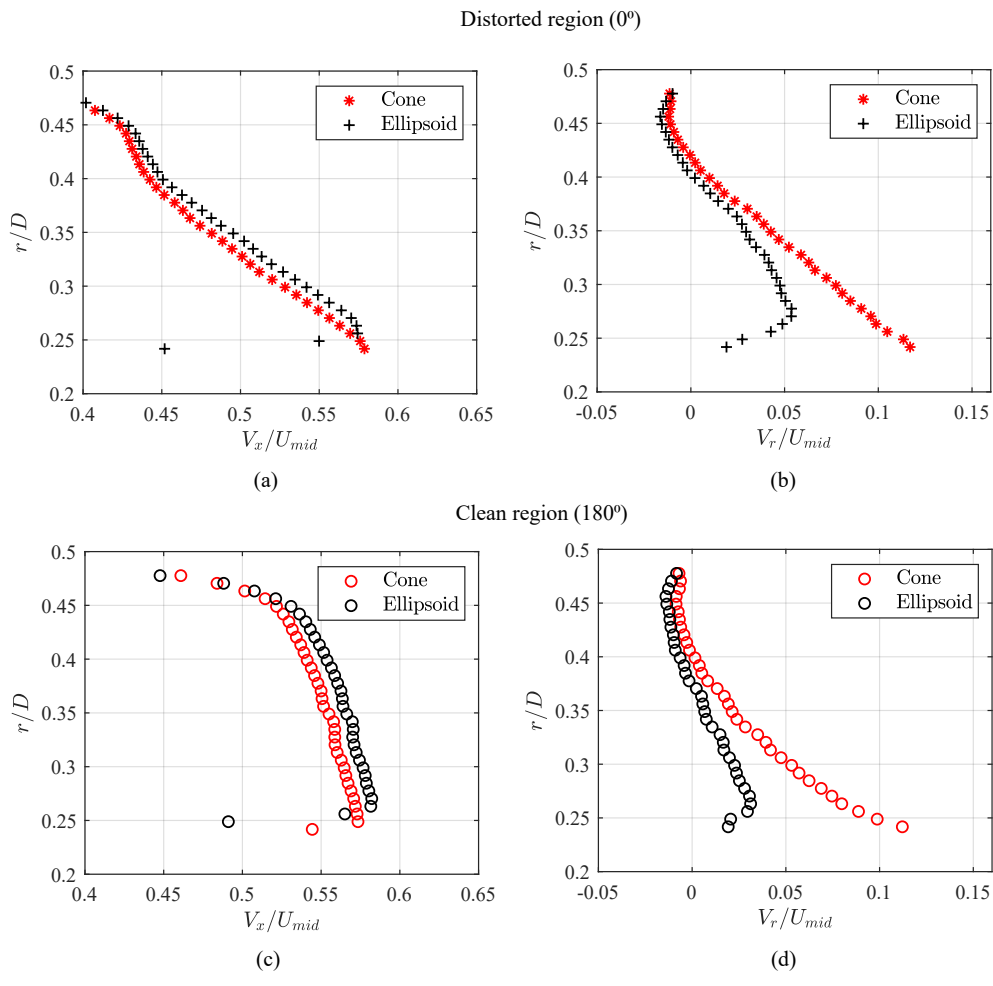


Figure D.4: (a),(c) axial and (b),(d) radial Velocity profiles extracted at the upstream of the fan AIP (at  $-0.05D$ ) for ellipsoid and conical nose-cones. (a) and (b) are obtained in the distorted region and (c) and (d) are obtained in the clean region. The bottom row shows a schematic of the velocity triangles around a 2D rotor blade.

The nose-cone shape has been found to influence the distortion transfer through the fan. Recent studies have considered non-axisymmetric stator design for improving the fan stage efficiency under the distorted inflow (Gunn & Hall, 2017). However, the present investigation shows that changing the nose-cone shape will affect how the distortion is encountered by the stators. Therefore, the present study suggests that the nose-cone shape must always be taken into account while designing efficient stator blades for a fan operating with a distorted inflow. However, the present symmetry plane flow-field shows only a limited picture of the three-dimensional redistribution around the spinner. However, due to the intense laser reflections from the fan blades, this three-dimensional re-distribution was not obtained in the present study, but must be considered for further investigations.



# BIBLIOGRAPHY

- Alveroglu, B. (2016). *The convective instability of the BEK system of rotating boundary-layer flows over rough disks* (Doctoral dissertation April). University of Leicester. <http://hdl.handle.net/2381/27576>
- Alveroglu, B., Segalini, A., & Garrett, S. J. (2016). The effect of surface roughness on the convective instability of the BEK family of boundary-layer flows. *European Journal of Mechanics, B/Fluids*, 56, 178–187. <https://doi.org/10.1016/j.euromechflu.2015.11.013>
- Arnone, A. (1993). Viscous analysis of three-dimensional rotor flow using a multigrid method. *ASME 1993 International Gas Turbine and Aeroengine Congress and Exposition, GT 1993, 1*. <https://doi.org/10.1115/93GT019>
- Astarita, T., Cardone, G., Carlomagno, G. M., & Tecchio, P. (2002). Spiral Vortices Detection on a Rotating Disk. *ICAS 2002 CONGRESS*, 1–8.
- Astarita, T., & Carlomagno, G. M. (2013). *Infrared Thermography for Thermo-Fluid-Dynamics*. Springer, Berlin, Heidelberg. <https://doi.org/10.1007/978-3-642-29508-9>
- ATR. (2017). ATR72-600. [http://www.ataircraft.com/datas/download%7B%5C\\_%7Dcenter/27/fiche72%7B%5C\\_%7D27.pdf](http://www.ataircraft.com/datas/download%7B%5C_%7Dcenter/27/fiche72%7B%5C_%7D27.pdf)
- Becker, H. A., & Massaro, T. A. (1968). Vortex evolution in a round jet. *Journal of Fluid Mechanics*, 31(3), 435–448. <https://doi.org/10.1080/03091928308209066>
- Benedict, L. H., & Gould, R. D. (1996). Towards better uncertainty estimates for turbulence statistics. *Experiments in Fluids*, 22(2), 129–136. <https://doi.org/10.1007/s003480050030>
- Berkooz, G., Holmes, P., & Lumley, J. L. (1993). The Proper Orthogonal Decomposition in the Analysis of Turbulent Flows. *Annual Review of Fluid Mechanics*, 25(1), 539–575. <https://doi.org/10.1146/annurev.fl.25.010193.002543>
- Cao, T., Vadlamani, N. R., Tucker, P. G., Smith, A. R., Slaby, M., & Sheaf, C. T. (2017). Fan-intake interaction under high incidence. *Journal of Engineering for Gas Turbines and Power*, 139(4), 1–10. <https://doi.org/10.1115/1.4034701>
- CFM. (2013). *CFM Leap - The Power for the Future* (tech. rep.). <http://www.cfmaeroengines.com/files/brochures/LEAP-Brochure-2013.pdf>
- Chen, P. P., Qiao, W. Y., Liesner, K., & Meyer, R. (2014). Location effect of boundary layer suction on compressor hub-corner separation. *Proceedings of the ASME Turbo Expo*, 2A(July). <https://doi.org/10.1115/GT2014-25043>
- Cho, M., Baek, J. H., Oh, S. H., & K, D. J. (2008). Role of hub-corner-separation on rotating stall in an axial compressor. *Transactions of the Japan Society for Aeronautical and Space Sciences*, 51(172), 93–100. <https://doi.org/10.2322/tjsass.51.93>
- Cooper, A. J., Harris, J. H., Garrett, S. J., özkan, M., & Thomas, P. J. (2015). The effect of anisotropic and isotropic roughness on the convective stability of the rotating disk boundary layer. *Physics of Fluids*, 27(1). <https://doi.org/10.1063/1.4906091>

- Davies, C., & Carpenter, P. W. (2003). Global behaviour corresponding to the absolute instability of the rotating-disc boundary layer. *Journal of Fluid Mechanics*, 486, 287–329. <https://doi.org/10.1017/S0022112003004701>
- Drazin, P. G. (2002). *Introduction to Hydrodynamic Stability*. Cambridge University Press. <https://doi.org/10.1017/CBO9780511809064>
- Fedorov, B. I., Plavnik, G. Z., Prokhorov, I. V., & Zhukhovitskii, L. G. (1976). Transitional flow conditions on a rotating disk. *Journal of Engineering Physics*, 31(6), 1448–1453. <https://doi.org/10.1007/BF00860579>
- Felder, J. L., Brown, G. V., Kim, H. D., & Chu, J. (2011). Turboelectric Distributed Propulsion in a Hybrid Wing Body Aircraft. *ISABE*, 1340.
- Fenstermacher, P. R., Swinney, H. L., & Gollub, J. P. (1979). Dynamical instabilities and the transition to chaotic Taylor vortex flow. *Journal of Fluid Mechanics*, 94(1), 103–128. <https://doi.org/10.1017/S0022112079000963>
- Frohnäpfel, D. J., Ferrar, A. M., Bailey, J. M., O'Brien, W. F., & Lowe, K. T. (2016). Measurements of fan response to inlet total pressure and swirl distortions produced by boundary layer ingesting aircraft configurations. *54th AIAA Aerospace Sciences Meeting*, (January), 1–15. <https://doi.org/10.2514/6.2016-0533>
- Garrett, S. J., Cooper, A. J., Harris, J. H., Özkan, M., Segalini, A., & Thomas, P. J. (2016). On the stability of von Kármán rotating-disk boundary layers with radial anisotropic surface roughness. *Physics of Fluids*, 28(1). <https://doi.org/10.1063/1.4939793>
- Garrett, S. J., Hussain, Z., & Stephen, S. O. (2009). The cross-flow instability of the boundary layer on a rotating cone. *Journal of Fluid Mechanics*, 622, 209–232. <https://doi.org/10.1017/S0022112008005181>
- Garrett, S. J., Hussain, Z., & Stephen, S. O. (2010). Boundary-Layer Transition on Broad Cones Rotating in an Imposed Axial Flow. *AIAA Journal*, 48(6), 1184–1194. <https://doi.org/10.2514/1.J050021>
- Garrett, S. J., & Peake, N. (2007a). The absolute instability of the boundary layer on a rotating cone. *European Journal of Mechanics B/Fluids*, 26(3), 344–353. <https://doi.org/10.1017/S0022112008005181>
- Garrett, S. J., & Peake, N. (2007b). The absolute instability of the boundary layer on a rotating cone. *European Journal of Mechanics B/Fluids*, 26, 344–353. <https://doi.org/10.1017/S0022112008005181>
- Gbadebo, S. A., Cumpsty, N. A., & Hynes, T. P. (2005). Three-dimensional separations in axial compressors. *Journal of Turbomachinery*, 127(2), 331–339. <https://doi.org/10.1115/1.1811093>
- Görtler, H. (1954). *On the Three-Dimensional Instability of Laminar Boundary Layers on Concave Walls* (tech. rep.). NACA. <https://ntrs.nasa.gov/api/citations/19930093855/downloads/19930093855.pdf>
- Govardhan, M., & Viswanath, K. (1997). Investigations on an axial flow fan stage subjected to circumferential inlet flow distortion and swirl. *Journal of Thermal Science*, 6(4), 241–250. <https://doi.org/10.1007/s11630-997-0003-8>
- Gregory, B. Y. N., Stuart, J. T., & Walker, W. S. (1955). On the Stability of Three-Dimensional Boundary Layers with Application to the Flow Due to a Rotating Disk. *Philosophical Transactions of the Royal Society of London. Series A, Mathematical and Physical Sciences*, 248(943), 155–199. <http://www.jstor.org/stable/91581>

- Greitzer, E. M., Bonnefoy, P. A., De la Rosa Blanco, E., Dorbian, C. S., Dreila, M., Hall, D. K., Hansman, R. J., Hileman, J. I., Liebeck, R. H., Lovegren, J., Mody, P., Pertuze, J. A., Sato, S., Spakovszky, Z. S., Tan, C. S., Hollman, J. S., Duda, J. E., Fitzgerald, N., Houghton, J., ... Lord, W. K. (2010). *N + 3 Aircraft Concept Designs and Trade Studies* (tech. rep. December). NASA.
- Guimarães, T., Lowe, K. T., Nelson, M., O'Brien, W. F., & Kirk, C. (2015). Stereoscopic PIV measurements in a turbofan engine inlet with tailored swirl distortion. *31st AIAA Aerodynamic Measurement Technology and Ground Testing Conference*, (June), 1–12. <https://doi.org/10.2514/6.2015-2866>
- Guimarães, T., Todd Lowe, K., & O'Brien, W. F. (2018). Complex flow generation and development in a full-scale turbofan inlet. *Journal of Engineering for Gas Turbines and Power*, *140*(8), 1–10. <https://doi.org/10.1115/1.4039179>
- Guimaraes Bucalo, T., Frohnappel, D. J., Lowe, K. T., & O'Brien, W. F. (2017). Development and Turbulence of a Twin-Vortex Type of Distortion for Turbofan Inlet Applications. *53rd AIAA/SAE/ASEE Joint Propulsion Conference*, (July), 1–16. <https://doi.org/10.2514/6.2017-4992>
- Gunn, E. J., & Hall, C. A. (2017). Non-Axisymmetric Stator Design for Boundary Layer Ingesting Fans, 1–10. <https://doi.org/10.1115/GT2017-63082>
- Gunn, E. J., & Hall, C. a. (2014). Aerodynamics of Boundary Layer Ingesting Fans. *Proceedings of ASME Turbo Expo 2014: Turbine Technical Conference and Exposition*, 1–13. <https://doi.org/10.1115/GT2014-26142>
- Gunn, E. J., Tooze, S., Hall, C. A., & Colin, Y. (2013). An Experimental Study of Loss Sources in a Fan Operating With Continuous Inlet Stagnation Pressure Distortion. *Journal of Turbomachinery*, *135*(5), 051002. <https://doi.org/10.1115/1.4007835>
- Hall, C. A., Schwartz, E., & Hileman, J. I. (2009). Assessment of technologies for the silent aircraft initiative. *Journal of Propulsion and Power*, *25*(6), 1153–1162. <https://doi.org/10.2514/1.43079>
- Hall, P. (1986). An asymptotic investigation of the stationary modes of instability of the boundary layer on a rotating disc. *Proceedings of the Royal Society A*, *406*, 93–106.
- Hergt, A., Meyer, R., Müller, M. W., & Engel, K. (2008). Loss reduction in compressor cascades by means of passive flow control. *Proceedings of the ASME Turbo Expo*. <https://doi.org/10.1115/GT2008-50357>
- Hergt, A., Meyer, R., & Engel, K. (2013). Effects of Vortex Generator Application on the Performance of a Compressor Cascade. *Journal of Turbomachinery*, *135*(2), 1–10. <https://doi.org/10.1115/1.4006605>
- Hoogreef, M. F., Vos, R., de Vries, R., & Veldhuis, L. L. (2019). Conceptual assessment of hybrid electric aircraft with distributed propulsion and boosted turbofans. *AIAA Scitech 2019 Forum*, (May 2020). <https://doi.org/10.2514/6.2019-1807>
- Hussain, Z., Garrett, S. J., & Stephen, S. O. (2014). The centrifugal instability of the boundary-layer flow over slender rotating cones. *Journal of Fluid Mechanics*, *755*, 274–293. <https://doi.org/10.1017/jfm.2014.417>
- Hussain, Z., Garrett, S. J., Stephen, S. O., & Griffiths, P. T. (2016). The centrifugal instability of the boundary-layer flow over a slender rotating cone in an enforced axial free stream. *Journal of Fluid Mechanics*, *788*, 70–94. <https://doi.org/10.1017/jfm.2015.671>

- Hussain, Z., Stephen, S. O., & Garrett, S. J. (2012). The centrifugal instability of a slender rotating cone. *Journal of Algorithms and Computational Technology*, 6(1), 113–128. <https://doi.org/10.1260/1748-3018.6.1.113>
- Hussain, Z. (2010). Stability and transition of three-dimensional rotating boundary layers. *PhD dissertation (University of Birmingham)*, (March). <http://etheses.bham.ac.uk/839/>
- Idelchik, I. E. (1986). *Handbook of hydraulic resistance (2nd revised and enlarged edition)*. Hemisphere Publishing Corp.
- Jerez Fidalgo, V., Hall, C. A., & Colin, Y. (2012). A Study of Fan-Distortion Interaction Within the NASA Rotor 67 Transonic Stage. *Journal of Turbomachinery*, 134(5), 369–380. <https://doi.org/10.1115/GT2010-22914>
- Kato, K., Alfredsson, P. H., & Lingwood, R. J. (2019). Boundary-layer transition over a rotating broad cone. *Physical Review Fluids*, 4(7), 71902. <https://doi.org/10.1103/PhysRevFluids.4.071902>
- Kato, K., Kawata, T., Alfredsson, P. H., & Lingwood, R. J. (2019). Investigation of the structures in the unstable rotating-cone boundary layer. *Physical Review Fluids*, 4(5), 1–30. <https://doi.org/10.1103/PhysRevFluids.4.053903>
- Kobayashi, R., & Izumi, H. (1983). Boundary-layer transition on a rotating cone in still fluid. *Journal of Fluid Mechanics*, 127, 353–364. <https://doi.org/10.1017/S0022112083002761>
- Kobayashi, R., & Kohama, Y. (1985). Spiral Vortices in Boundary Layer Transition on a Rotating Cone. In Kozlov V.V. (Ed.), *Laminar-turbulent transition. international union of theoretical and applied mechanics*. (pp. 573–580). Springer, Berlin, Heidelberg.
- Kobayashi, R., Kohama, Y., Arai, T., & Ukaku, M. (1987). The Boundary-layer Transition on Rotating Cones in Axial Flow with Free-stream Turbulence. *JSME International Journal*, 30(261), 423–429.
- Kobayashi, R., Kohama, Y., & Kurosawa, M. (1983). Boundary-layer transition on a rotating cone in axial flow. *Journal of Fluid Mechanics*, 127, 353–364. <https://doi.org/10.1017/S0022112083002761>
- Kobayashi, R., Kohama, Y., & Takamadate, C. (1980). Spiral vortices in boundary layer transition regime on a rotating disk. *Acta Mechanica*, 35(1-2), 71–82. <https://doi.org/10.1007/BF01190058>
- Kobayashi, R. (1994). Review: laminar-to-turbulent transition of three-dimensional boundary layers on rotating bodies. *Journal of fluids engineering*, 116(2), 200–211. <https://doi.org/10.1016/j.ymsp.2015.09.042>
- Kohama, Y. (1984a). Behaviour of spiral vortices on a rotating cone in axial flow. *Acta Mechanica*, 51(3-4), 105–117. <https://doi.org/10.1007/BF01177066>
- Kohama, Y. (1984b). Study on boundary layer transition of a rotating disk. *Acta Mech.*, 50, 193–199. <https://doi.org/10.1007/BF01170959>
- Kohama, Y. (1987). Some expectation on the mechanism of cross-flow instability in a swept wing flow. *Acta Mechanica*, 66(1-4), 21–38. <https://doi.org/10.1007/BF01184283>
- Kohama, Y. P. (2000). Three-dimensional boundary layer transition study. *Current Science*, 79(6), 800–807.
- Kosambi, D. D. (1943). Statistics in Function Space. *Journal of the Indian Mathematical Society*, 7, 76–88.
- Lee, D. S., Fahey, D. W., Skowron, A., Allen, M. R., Burkhardt, U., Chen, Q., Doherty, S. J., Freeman, S., Forster, P. M., Fuglestedt, J., Gettelman, A., De León, R. R., Lim, L. L.,

- Lund, M. T., Millar, R. J., Owen, B., Penner, J. E., Pitari, G., Prather, M. J., . . . Wilcox, L. J. (2020). The contribution of global aviation to anthropogenic climate forcing for 2000 to 2018. *Atmospheric Environment*, 244(September 2020). <https://doi.org/10.1016/j.atmosenv.2020.117834>
- Lei, V.-M., Spakovszky, Z. S., & Greitzer, E. M. (2008). A Criterion for Axial Compressor Hub-Corner Stall. *Journal of Turbomachinery*, 130(3), 031006. <https://doi.org/10.1115/1.2775492>
- Li, J., & Ji, L. (2019). Efficient Design Method for Applying Vortex Generators in Turbomachinery. *Journal of Turbomachinery*, 141(8), 1–12. <https://doi.org/10.1115/1.4042990>
- Lian, Y., & Liou, M. S. (2005). Multi-objective optimization of a transonic compressor blade using evolutionary algorithm. *Journal of Propulsion and Power*, 21(6), 979–987. <https://doi.org/10.2514/6.2005-1816>
- Lingwood, R. J. (1995). Absolute instability of the boundary layer on a rotating disk. *Journal of Fluid Mechanics*, 299, 17–33. <https://doi.org/10.1016/j.euromechflu.2006.08.002>
- Lingwood, R. J. (1996). An experimental study of absolute instability of the rotating-disk boundary-layer flow. *Journal of Fluid Mechanics*, 314, 373–405. <https://doi.org/10.1017/S0022112096000365>
- Longley, J. P., & Greitzer, E. M. (1992). Inlet Distortion Effects in Aircraft Propulsion System Integration. *AGARD Lecture Series*, 183, 7–1–7–18.
- Lumley, J. L. (1967). The structure of inhomogeneous turbulent flows. In A. M. Yaglom & V. I. Tatarski (Eds.), *Atmospheric turbulence and wave propagation* (pp. 166–78). Nauka, Moscow.
- Ma, S., Chu, W., Zhang, H., Lang, J., & Kuang, H. (2017). Numerical investigation on effect of compressor performance in single rotor with micro-vortex generator. *Proceedings of the ASME Turbo Expo, 2A-2017*, 1–10. <https://doi.org/10.1115/GT201763935>
- Malik, M. R. (1986). The neutral curve for stationary disturbances in rotating-disk flow. *Journal of Fluid Mechanics*, 164, 275–287. <https://doi.org/10.1017/S0022112086002550>
- Mayer, R. (2000). *Wall-shear stress measurements with quantitative infrared-thermography* (Doctoral dissertation). Delft University of Technology.
- Mittal, S. (2004). Three-dimensional instabilities in flow past a rotating cylinder. *Journal of Applied Mechanics, Transactions of the ASME*, 71(1), 89–95. <https://doi.org/10.1115/1.1631032>
- Mollendorf, J. C., & Gebhart, B. (1973). An experimental and numerical study of the viscous stability of a round laminar vertical jet with and without thermal buoyancy for symmetric and asymmetric disturbances. *Journal of Fluid Mechanics*, 61(2), 367–399. <https://doi.org/10.1017/S0022112073000765>
- Mueller, T. J., Nelson, R. C., Kegelman, J. T., & Morkovin, M. V. (1981). Smoke Visualization of Boundary-Layer Transition on a Spinning Axisymmetric Body. *AIAA Journal*, 19(12), 1607–1608. <https://doi.org/10.2514/3.60099>  
doi: 10.2514/3.60099
- Narayanan, V. (2007). Oscillatory thermal structures in a reattaching jet flow. *Journal of Visualization*, 10(4), 389–396. <https://doi.org/10.1007/BF03181897>
- Nelson, M. A., Lowe, K. T., O'Brien, W. F., Kirk, C., & Hoopes, K. M. (2014). Stereoscopic PIV measurements of swirl distortion on a Full-Scale turbofan engine inlet. *52nd Aerospace Sciences Meeting*, (January), 1–13. <https://doi.org/10.2514/6.2014-0533>

- Nieuwstadt, F. T. M., Boersma, B. J., & Westerweel, J. (2015). *Turbulence: Introduction to Theory and Applications of Turbulent Flows*. Springer.
- Perovic, D., Hall, C. A., & Gunn, E. J. (2019). Stall inception in a boundary layer ingesting fan. *Journal of Turbomachinery*, 141(9), 1–10. <https://doi.org/10.1115/1.4043644>
- Peters, A., Spakovszky, Z. S., Lord, W. K., & Rose, B. (2015). Ultrashort nacelles for low fan pressure ratio propulsors. *Journal of Turbomachinery*, 137(2). <https://doi.org/10.1115/1.4028235>
- Praisner, T. J., & Smith, C. R. (2006). The dynamics of the horseshoe vortex and associated endwall heat transfer - Part I: Temporal behavior. *Journal of Turbomachinery*, 128(4), 747–754. <https://doi.org/10.1115/1.2185676>
- Radi, A., Thompson, M. C., Rao, A., Hourigan, K., & Sheridan, J. (2013). Experimental evidence of new three-dimensional modes in the wake of a rotating cylinder. *Journal of Fluid Mechanics*, 734, 567–594. <https://doi.org/10.1017/jfm.2013.486>
- Raffel, M., Willert, C. E., Wereley, S. T., & Kompenhans, J. (2007). *Particle Image Velocimetry A practical Guide*. Springer Berlin Heidelberg.
- Raiola, M., Discetti, S., & Ianiro, A. (2015). On PIV random error minimization with optimal POD - based low - order reconstruction. *Experiments in Fluids*. <https://doi.org/10.1007/s00348-015-1940-8>
- Raiola, M., Greco, C. S., Contino, M., Discetti, S., & Ianiro, A. (2017). Towards enabling time-resolved measurements of turbulent convective heat transfer maps with IR thermography and a heated thin foil. *International Journal of Heat and Mass Transfer*, 108, 199–209. <https://doi.org/10.1016/j.ijheatmasstransfer.2016.12.002>
- Rao, A., Leontini, J., Thompson, M. C., & Hourigan, K. (2013). Three-dimensionality in the wake of a rotating cylinder in a uniform flow. *Journal of Fluid Mechanics*, 717, 1–29. <https://doi.org/10.1017/jfm.2012.542>
- Rao, A., Leontini, J. S., Thompson, M. C., & Hourigan, K. (2013). Three-dimensionality in the wake of a rapidly rotating cylinder in uniform flow. *Journal of Fluid Mechanics*, 730, 379–391. <https://doi.org/10.1017/jfm.2013.362>
- Reid, C. (1969). The Response of Axial Flow Compressors to Intake Flow Distortion. *ASME 1969 Gas Turbine Conference and Products Show*, 69–GT–29. <https://doi.org/10.1115/69-GT-29>
- Rolls-Royce. (2018). Trent XWB brochure.
- Saric, W. S., Reed, H. L., & White, E. B. (2003). Stability and Transition of Three-Dimensional Boundary Layers. *Annual Review of Fluid Mechanics*, 35(1), 413–440. <https://doi.org/10.1146/annurev.fluid.35.101101.161045>
- Schrijer, F. F. J. (2010). *Experimental investigation of re-entry aerodynamic phenomena* (Doctoral dissertation January).
- Scillitoe, A. D., Tucker, P. G., & Adami, P. (2017). Numerical investigation of three-dimensional separation in an axial flow compressor: The influence of freestream turbulence intensity and endwall boundary layer state. *Journal of Turbomachinery*, 139(2), 1–10. <https://doi.org/10.1115/1.4034797>
- Segalini, A., & Camarri, S. (2019). Flow induced by a rotating cone: Base flow and convective stability analysis. *Physical Review Fluids*, 4(8), 1–24. <https://doi.org/10.1103/PhysRevFluids.4.084801>
- Smith, N. H. (1947). *Exploratory investigation of laminar-boundary-layer oscillations on a rotating disk*. (tech. rep. No. 1227).

- Sreenivas, K. R., & Prasad, A. K. (2000). Vortex-dynamics model for entrainment in jets and plumes. *Physics of Fluids*, 12(8), 2101–2107. <https://doi.org/10.1063/1.870455>
- Stephen Butterworth. (1930). On the Theory of Filter Amplifiers.
- Tambe, S., Bartolom'e Oseguera, U., & Gangoli Rao, A. (2020). Performance of a low speed axial fan under distortion: an experimental investigation. *Proceedings of ASME Turbo Expo 2020: Turbine Technical Conference and Exposition June 22 - 26, 2020, London, England*.
- Tambe, S., Schrijer, F., Rao, A. G., & Veldhuis, L. (2019). An experimental method to investigate coherent spiral vortices in the boundary layer over rotating bodies of revolution. *Experiments in Fluids*, 60(7), 115. <https://doi.org/10.1007/s00348-019-2756-8>
- Tambe, S., Schrijer, F., Rao, A. G., & Veldhuis, L. (2021). Boundary layer instability over a rotating slender cone under non-axial inflow. *Journal of Fluid Mechanics*, 910(A25). [doi:10.1017/jfm.2020.990](https://doi.org/10.1017/jfm.2020.990)
- Taylor, G. I. (1923). Stability of Viscous Liquid contained between Two Rotating Cylinders. *Philosophical Transactions of the Royal Society of London. Series A, Containing Papers of a Mathematical or Physical Character*, 223(605-615), 289–343. <https://doi.org/10.1002/zamm.19590391204>
- TCDS:EASA.A.064. (2021). *TCDS EASA.A.064 AIRBUS A318, A319, A320, A321* (tech. rep. May). European Union Aviation Safety Agency.
- TCDS:EASA.A.151. (2020). *TCDS EASA.A.151 Airbus A350* (tech. rep. No. 24). European Union Aviation Safety Agency.
- TCDS:EASA.IM.E.041. (2014). EASA: Certificate Data Sheet PW 100 series engines. [https://www.easa.europa.eu/system/files/dfu/TCDS%20PW100%20series%7B%5C\\_%7D%20E%20041%7B%5C\\_%7D%20Issue%2003%7B%5C\\_%7Dfinal.pdf](https://www.easa.europa.eu/system/files/dfu/TCDS%20PW100%20series%7B%5C_%7D%20E%20041%7B%5C_%7D%20Issue%2003%7B%5C_%7Dfinal.pdf)
- Thomas, C., Stephen, S. O., & Davies, C. (2020). Effects of partial slip on the local-global linear stability of the infinite rotating disk boundary layer. *Physics of Fluids*, 32(7). <https://doi.org/10.1063/5.0012976>
- Towers, P. D., & Garrett, S. J. (2012). On the stability of the compressible boundary-layer flow over a rotating cone. *42nd AIAA Fluid Dynamics Conference and Exhibit 2012*, 44(June), 1–9. <https://doi.org/10.2514/6.2012-2693>
- Towers, P. D., Hussain, Z., Griffiths, P. T., & Garrett, S. J. (2016). Viscous modes within the compressible boundary-layer flow due to a broad rotating cone. *IMA Journal of Applied Mathematics (Institute of Mathematics and Its Applications)*, 81(5), 940–960. <https://doi.org/10.1093/imamat/hxw041>
- Towers, P. D., & Garrett, S. J. (2016). Similarity solutions of compressible flow over a rotating cone with surface suction. *Thermal Science*, 20(2), 517–528. <https://doi.org/10.2298/TSCI130408032T>
- Towers, P. D. (2013). *The stability and transition of the compressible boundary-layer flow over broad rotating cones* (Doctoral dissertation). University of Leicester.
- Uenishi, K., Pearson, M. S., Lehnig, T. R., & Leon, R. M. (1990). CFD-based 3D turdofan nacelle design system. *AIAA 8th Applied Aerodynamics Conference*, 1–18. <https://doi.org/10.2514/6.1990-3081>
- Vadlamani, N. R., Cao, T., Watson, R., & Tucker, P. G. (2019). Toward Future Installations: Mutual Interactions of Short Intakes With Modern High Bypass Fans. *Journal of Turbomachinery*, 141(8), 1–11. <https://doi.org/10.1115/1.4044080>

- Vladuchick, P. (2010). No Title. <https://www.flickr.com/photos/vladdythephotogeek/4357513581/>
- Wei, M., Xavier, O., Lipeng, L., & Francis, L. (2013). Intermittent corner separation in a linear compressor cascade. *Experiments in Fluids*, 54(6). <https://doi.org/10.1007/s00348-013-1546-y>
- Wilkinson, S. P., & Malik, M. R. (1985). Stability experiments in the flow over a rotating disk. *AIAA Journal*, 23(4), 588–595. <https://doi.org/10.2514/3.8955>
- Xia, G., & Medic, G. (2017). Hybrid RANS/LES simulation of corner stall in a linear compressor cascade. *Proceedings of the ASME Turbo Expo, 2A-2017*, 1–11. <https://doi.org/10.1115/GT201763454>
- Yan, C., Yin, Z., Shen, X., Guo, F., & Wu, Y. (2019). Axisymmetric hub-endwall profile optimization for a transonic fan to improve aerodynamic performance based on an integrated design optimization method. *Structural and Multidisciplinary Optimization*, 60(3), 1267–1282. <https://doi.org/10.1007/s00158-019-02266-y>
- Yocum, A. M., & Henderson, R. E. (1980). The effects of some design parameters of an isolated rotor on inlet flow distortions. *Journal of Engineering for Gas Turbines and Power*, 102(1), 178–186. <https://doi.org/10.1115/1.3230219>
- Zamboni, G., & Xu, L. (2009). Fan root aerodynamics for large bypass gas turbine engines: influence on the engine performance and 3D design. *ASME TurboExpo*.
- Zambonini, G., & Ottavy, X. (2015). Unsteady pressure investigations of corner separated flow in a linear compressor cascade. *Proceedings of the ASME Turbo Expo*, (June 2015). <https://doi.org/10.1115/GT2015-42073>
- Zambonini, G., Ottavy, X., & Kriegseis, J. (2017). Corner Separation Dynamics in a Linear Compressor Cascade. *Journal of Fluids Engineering, Transactions of the ASME*, 139(6). <https://doi.org/10.1115/1.4035876>

# ACKNOWLEDGEMENTS

My first and foremost gratitude goes to all those who have been involved in creating and maintaining the excellent lab facilities of AWEP without which this research was impossible.

Next, I would like to thank Leo, my promotor, for being a motivational aerodynamicist in the faculty. This, right since my MSc study at TU Delft, further fostered my curiosity in aerodynamics. Your time-efficient feedback has been instrumental in setting the tone of this research. Thank you for providing me the opportunity to conduct this research which has made my past four years really enjoyable. Also, thank you for standing up for and supporting this research when against any questions related to its worth or relevance.

I would like to thank Arvind, my copromotor, for providing me the necessary freedom to pursue the curiosity-driven research, but still ensuring its practical relevance. Thank you for sparking the idea of studying the nose-cone boundary-layer flow during our chat near the CFM56 in the aircraft hall. At that time, it wrongly appeared as a straight-forward problem to me, but a quick literature review revealed the intricacies and intriguing nature of the instability phenomenon on rotating cones. It taught me to not overlook any scientific aspect, especially those which appear too obvious. They are the ones which offer the most surprises. Thank you for this and all other subtly philosophical teachings throughout this journey, and thank you for your stubbornness. Thank you for conversing in my mother-tongue *marathi* sometimes, in my opinion, it allows one more degree of freedom for the ideas.

Next, special thanks go to Ferry, who has been supervising me since my MSc thesis, and who has also coached me in the present experiment-based research. You made it possible to quickly dissolve the unnecessary formal barriers between a student and a teacher, however your knowledge on experimental research naturally maintained your authority. Thank you for always guiding me in professional as well as personal life. The beers and jokes during our countless trips to DNW cryogenic windtunnel (KKK) in Cologne truly started the PhD journey in a right tone. Thank you for involving me in this professionally challenging experimental campaign which trained me to work in a stress-full time-limited situations where stakes are high. Also, thanks for translating their safety briefing in English, which literally was instrumental in staying alive, something that probably was necessary to finish this research. And thanks for understanding the fears of early mornings and frostbites.

I thank George Eitelberg for motivating discussions and intriguing questions during propeller group meetings. Also, thanks for the philosophical teachings during informal interactions.

I would also like to thank Bas for coaching me well in scientific research during my MSc thesis, which made the PhD journey a bit less trouble. It is always an honour to be surrounded by your intellect.

Thanks Peter, Frits, Henk-Jan, Dennis, and Eric for your technical support during the experiments. TST27 and Fan test rig experiments were impossible without you. Also thanks to Ed, Peter, and Rob from DEMO for all the non-wobbly cones.

I thank my MSc students Ugaitz, Srijan, Rahul and Bjorn for exploring the applied aspects of this research during their theses. I enjoyed supervising you and hope you keep progressing

through your profession and through personal life.

Nando and Anne-Liza reviewed the Dutch summary, bedankt!

Moving to a bit personal side, the FPP colleagues brewed a culture that made sure that I/we will forget the work week by starting de Atmosfeer sessions as quickly as Friday, and later ending up somewhere with funny stories. This helped becoming creative at work and always review the past week's work with a new perspective, as the body had to create new brain-cells after every weekend. Thanks Lucia, Andre, Nitish, and Adam for ensuring this. Also the sessions were joined after 5:30pm by the usual suspects: Reynard, Ale, Nando, Tomas, Sonia, Maurice, Sebastian, Elise, Anne-lisa, Peter-Jan, and Imco, thank you! I hope we all made some good stories and hope you remember them, because I don't, at least not completely. But I do remember being happy, which is the most important thing in my opinion.

Thanks Andre for introducing bouldering which has been a great sport for me, something to wake up for, apart from the PhD. Thanks Reynard and Nando for making the recent bouldering sessions funny. Thanks Martijn R. for occasional climbing tips and thanks Julia for the sporadic but enjoyable bouldering sessions.

After the brain-draining work week during the PhD, one can not help but find solace in being stupid. Thanks, once again, Nitish, Adam, Reynard, Lucia, Nando, Sonia and sometimes Andre and Akshay-Spoorty for all the funny non-sense conversations together during coffee breaks, in Atmosfeer, during trips, almost everywhere apart from work. I think their role in increasing work-productivity is underappreciated by the conventional society.

I would also thank my office mates Biagio, Carmine, Marco, Kushagra, Martijn, Hugo, Rishikesh, and random visitors Francesesco, good Nitish, Federica and Robert for making our 6.01 fun to work in. Thank you for coping with my spread of collectibles and for keeping them safe; thanks Carmine for leaving the office so that I could occupy another table and increase this spread.

The list just gets longer and repetitive, but it is necessary to acknowledge the family away from home. Food is the closest association and memory of the family, and I have been fortunate enough to have friends who cooked variety of cuisines all these years. Thanks for all the awesome food and time spent along with it: Adam-Max, Nando, Nitish, Andre-Elise, Lucia, Reynard-Ale, Palak-Pranav, Ashwin, Abhishek-Rucha, Jatindar, Aakarshit, Mohit, Ashish, Vibhas, Rajit, and Bala. Also, thanks Arvind-Preeti for bringing Indian home food in Delft.

The backbone is rarely seen but you know that it is always with you. Unfortunately, moving to the Netherlands has resulted parting with the awesome closest friends since the childhood: Pratik, Kedar, Nikhil, Sanket, Pratik Patil, Vineet, Pranav, Vishal, Swapnil, Naresh, Ajay, and Pranit. Thank you for the two decades full of memories and the ones that are coming next. Especially, thanks Pratik, Kedar and Nikhil for the constant support, the fun and allowing/encouraging me to be away to pursue this research. Also, thanks for always going out of your way to hangout whenever and wherever possible, including India, Europe, and Egypt. Our passionate discussions, astronomical explorations, the stubbornness of following what we really want has always kept me going, hopefully on the right path. Thanks Lavanya for allowing Pratik in these situations and also thanks for the vital dental treatments!

Finally, my deepest gratitude goes to my parents Manisha and Sunil. Your constant support has been a source of motivation and many times a relief. Thank you for all the freedom. Thank you for all that you have done for me till now.

# CURRICULUM VITÆ

## Sumit Sunil TAMBE

22-11-1991      Born in Maharashtra, India.

### EDUCATION

Aug 2009–May 2013      Bachelor of Technology (BTech.) in Aerospace Engineering  
Indian Institute of Space science and Technology (IIST), India

Sep 2015–Mar 2017      Master of Science (MSc.) in Aerospace Engineering  
Delft University of Technology, The Netherlands

Aug 2017–Jan 2022      PhD study in Aerospace Engineering  
Delft University of Technology, The Netherlands  
*Thesis:*              Boundary-layer instability on rotating cones: An experiments-based exploration  
*Promotors:*        Prof. dr. ir. L. L. M. Veldhuis  
                            Dr. A. Gangoli Rao  
*Supervisor:*        Dr. ir. F. F. J. Schrijer

## WORK EXPERIENCE

Oct 2013–Jul  
2015      Scientist/Engineer-C

Spacecraft structures group  
Indian Space Research Organisation (ISRO), Bangalore, India  
(GSAT-11, India's first 6k class satellite; moon mission Chandrayaan-2)

Jun 2012

Intern  
Human spaceflight mission  
Vikram Sarabhai Space Centre, ISRO, Thiruvananthapuram, India

Aug 2011–May  
2012

Systems engineer & Trajectory team lead  
VYOM Student sounding rocket program; 88 kg, Alt. 13.7 km.  
Indian Institute of Space science of Technology (IIST), India

# LIST OF PUBLICATIONS

1. **Tambe S.**, Schrijer F, Gangoli Rao A. & Veldhuis L., *An experimental method to investigate coherent spiral vortices in the boundary layer over rotating bodies of revolution*, *Experiments in Fluids* **60**(7), 115 (2019).
2. **Tambe S.**, Schrijer F, Gangoli Rao A. & Veldhuis L., *Boundary layer instability over a rotating slender cone under non-axial inflow*, *Journal of Fluid Mechanics* **910**, A25 (2021).
3. **Tambe S.**, Schrijer F & van Oudheusden B., *Relation Between Geometry and Wake Characteristics of a Supersonic Microramp*, *AIAA Journal* (2021).
4. **Tambe S.**, Schrijer F, Gangoli Rao A. & Veldhuis L. *Experimental study of boundary-layer instability on rotating cones in axial inflow: effect of half-cone angle*, *Journal of Fluid Mechanics* (Manuscript submitted).
5. **Tambe S.**, Schrijer F, Veldhuis L., & Gangoli Rao A. *Spiral instability modes on rotating cones in high-Reynolds-number axial flow*, *Physics of Fluids* (in preparation).
6. Unadkat J., **Tambe S.**, Fildes M., and Hussain Z., *Experimental and theoretical comparisons of the boundary-layer flow over rotating cones in axial flow. Part I: The crossflow instability*, *Journal of Fluid Mechanics* (in preparation).

## CONFERENCES

1. **Tambe S.**, Bartolomé Oseguera U., & Gangoli Rao A. *Performance of a Low Speed Axial Fan Under Distortion: An Experimental Investigation*, ASME Turbo Expo: Turbomachinery Technical Conference and Exposition, Virtual conference (2020)
2. **Tambe S.**, Schrijer F, Gangoli Rao A. & Veldhuis L. *Coherent vortex structures over a rotating spinner under non-axial inflows at low Reynolds number*, 54th 3AF International Conference AERO, at Paris, France (2019)
3. **Tambe S.**, Schrijer F & van Oudheusden B., *Effect of geometry on the downstream flow topology of a micro ramp in a supersonic turbulent boundary layer: an experimental study*, 7th European Conference for Aeronautics and Space Sciences (EUCASS), at Milan, Italy (2017)
4. **Tambe S.** & Salih A., *Numerical Study of Liquid Sloshing with Experimental Validation*, 6th Symposium on Applied Aerodynamics and Design of Aerospace Vehicles, SAROD, Hyderabad, India (2013)

